

Approaches to Lead Generation for Idiopathic Pulmonary Fibrosis Targets

Thesis submitted to the University of Strathclyde in fulfilment of the
requirements for the degree of Doctor of Philosophy

By

Emma Duffy

July 2016

Declaration of Copyright

This thesis is a result of the author's original research. It has been composed by the author and has not been previously submitted for examination which has led to the award of a degree.

The copyright of this thesis belongs to the author under the terms of the United Kingdom Copyright Acts as qualified by University of Strathclyde Regulation 3.50. Due acknowledgement must always be made of the use of any material contained in, or derived from, this thesis.

Signed:

Date: July 2016

Accordingly, a rational drug design approach was pursued with the aim of creating novel, simple molecules derived from these two progenitor compounds, whilst strategically retaining key pharmacophoric elements of AM095 and PF-8380 hypothesised to be crucial for activity

Following the design and synthesis of these novel entities, a range of biological assays were performed. The assays assessed the pharmacological potential of the compounds to disrupt the ATX-LPA signalling pathway. With regard to the hit-to-lead trajectory utilising AM095, a cross-screening approach was undertaken through simultaneously screening at both validated targets, LPA₁ and ATX. Using a scaffold hopping approach, a more minimalistic chemotype was identified with improved physicochemical properties.

In the PF-8380 derived series, a structure-based drug design approach was undertaken to fully understand binding interactions involved in ATX inhibition. Using biostructural and structure activity relationship data, the binding interactions required for ATX inhibition were defined for this chemotype. An iterative drug design cycle was employed which led to the identification of novel high quality ATX inhibitors. With suitable further biological evaluation the analogues identified in this work could be of utility as new treatment units for the intractable disease, IPF.

Acknowledgements

Firstly, I would like to express my sincere gratitude to Dr Craig Jamieson for giving me the opportunity to work as a part of his research group. My PhD has been a very positive experience and I am forever grateful for everything he has taught me. It was a pleasure and a privilege to work for him.

I would like to acknowledge my second supervisor Dr Allan Watson, and my industrial supervisors Dr Simon Macdonald and John Pritchard for their advice during the course of my PhD, and for their impact on the project as a whole. I would also like to thank GlaxoSmithKline whom funded my PhD research.

It was a pleasure to work with the technical and stores staff in the University of Strathclyde. I would also like to thank Louise Young for her expertise in the assay work presented in this thesis. Her hard work is truly appreciated.

A special thank you to "Team Fibrosis". Diana Castagna, Lisa Miller and Frances Potjewyd have been a huge support during my time in the lab. I hope your futures are filled with happiness and success.

To the past and present members of the CJ group, it has been a privilege to work with them. In particular, thank you to Morag Watson who helped with molecular modelling, she is truly a special person and mentor to the whole lab. I wish them all the very best in their careers and I hope our paths will cross in the future.

I have made many friends during my time in the University of Strathclyde. I feel extremely fortunate to have worked within the Jamieson-Watson group. The group welcomed me so warmly to Glasgow and made it my home for 3 and half years. They made my workday so enjoyable and I thank them for their kind friendship.

A very big thank to my family. I cannot thank them enough for everything they have done and continue to do for me. Their love and encouragement has made this thesis possible. Another special person in my life is John, I thank him for the love, support and understanding he has shown me.

Go raibh míle maith agaibh!

Abbreviations

#Ar	Number of aromatic rings
[s]	Substrate concentration
³ H	Tritiated
ADMET	Absorption, distribution, metabolism, excretion, toxicity
AM095	4-[3-methyl-4-((<i>R</i>)-1-phenyl-ethoxycarbonyl- amino)-isoxazol-5-yl]-biphenyl-4-yl}-acetate)
ATP	Adenosine triphosphate
ATX	Autotaxin
aVb6	Alphav beta6 integrin
BALF	Bronchial alveolar lavage fluid
bis- <i>p</i> NPP	Bis (<i>p</i> -nitrophenyl) phosphate
Boc	<i>tert</i> -Butyloxycarbonyl protecting group
CDI	1,1'-Carbonyldiimidazole
cHex	Cyclohexane
CHO-K1	Chinese hamster ovary cells derivative
Chromatographic	ChromLogD
CLND	Chemiluminescent nitrogen detection
COMU	1-[(1-(Cyano-2-ethoxy-2-oxoethylideneaminoxy) dimethylaminomorpholinomethylene)] methanaminium
Cpd	Compound number
CPF4	Coumarin fluorescein phosphodiesterase 4
d	Doublet
DCE	Dichloroethane
dd	Doublet of doublets
ddd	Doublet of doublets of doublets
DIPEA	<i>N,N</i> -Diisopropylethylamine
DMF	<i>N,N</i> -Dimethylformamide
DMSO	Dimethyl sulfoxide
DNA	Deoxyribonucleic acid
dt	Doublet of triplets
ECM	Extracellular matrix
EDG2	Endothelial differentiation gene 2
ENPP	Ectonucleotide pyrophosphatase/phosphodiesterase
eq	Equivalents
FGFR	Fibroblast growth factor receptors
FRET	Förster fluorescence resonance energy transfer
FS-3	Fluorogenic substrate 3
FTIR	Fourier Transform Infrared Spectroscopy
GPCR	G-protein coupled receptor
GSK	GlaxoSmithKline
h	Hours
HATU	<i>O</i> -(7-Azabenzotriazol-1-yl)-1,1,3,3-tetramethyluronium hexafluorophosphate

HBA	Hydrogen bond acceptor
HBD	hydrogen bond donor
HPLC	High-performance liquid chromatography
HRMS	High-resolution mass spectrometry
IC ₅₀	Half maximal inhibitory concentration
IPF	Idiopathic pulmonary fibrosis
<i>i</i> Pr	Isopropyl
K _i	$IC_{50}/(1+([s]/K_m))$
Ki16425	3-((4-(4-(3-(2-chlorophenyl)butanamido)-3-methylisoxazol-5-yl)benzyl)thio)propanoic acid
K _m	Substrate concentration at half-maximal velocity
L	Length
LogD	Octanol:water ratio @ spec pH7.4
LPA	Lysophosphatidic acid
LPAAT	LPA-acyltransferase
LPAR	Lysophosphatidic acid receptor
LPC	Lysophosphatidyl choline
LPP	Lipid phosphate phosphohydrolases
LRMS	Low resolution mass spectrometry
M	Molar
m	Multiplet
m.p.	Melting point
MAG	Monacylglycerol
MDAP	Mass directed automated purification
min	Minutes
MOE	Molecular Operating Environment
MW	Molecular weight
NHLF	Normal human lung fibroblast
NUC	Nuclease
PA	Phosphatidic acid
P _{app}	Permeability pH 7.4 assay
PC3	Human prostate cancer cells
PDB	Protein Data Bank
PDGF	Platelet derived growth factor
PF-8380	3,5-dichlorobenzyl 4-(3-oxo-3-(2-oxo-2,3-dihydrobenzo[d]oxazol-6-yl)propyl)piperazine-1-carboxylate
PFI	Property forecast indices
PLA ₁	Phospholipase A1
PLA ₂	Phospholipase A2
<i>p</i> NP-TMP	<i>p</i> -nitrophenyl thymidine 5'-monophosphate
PSA	Polar surface area
s	Singlet
SAR	Structure-activity relationship
SDS	Sodium dodecyl sulphate
SMB	Somatomedin B

Sol	Kinetic aqueous solubility assay
STAB	Sodium triacetoxy borohydride
t	Triplet
TCA	Trichloroacetic acid
TFA	Trifluoroacetic acid
THF	Tetrahydrofuran
THP	Tetrahydropyran
TLC	Thin layer chromatography
UV	Ultraviolet
VEGFR	Vascular endothelial growth factor receptors
Z	Carboxybenzyl

Table of Contents

1	Chapter 1: Introduction	1
1.1	Fibrosis and IPF	1
1.1.1	Hypothesised Pathogenesis of IPF	1
1.1.2	Abnormal Wound Healing in IPF.....	2
1.1.3	Therapeutic Targets for the Treatment of IPF	3
1.1.4	Current Treatments of IPF	4
1.2	Lysophosphatidic Acid (LPA) Signalling and IPF	7
1.2.1	LPA Production, Receptor and Degradation	9
1.2.2	LPA Receptor Antagonists.....	10
1.3	Autotaxin (ATX) and IPF.....	12
1.3.1	ATX Structure and Binding Modes.....	13
1.3.2	Determination of ATX Inhibition	15
1.3.3	ATX Inhibitors.....	19
2	Chapter 2: Project Aims.....	25
2.1	Lead Discovery Approach.....	25
2.2	Overall Project Aims	26
3	Chapter 3: Cross Screening Approach Towards New Leads for IPF Treatment	27
3.1	Design Strategy	27
3.1.1	Controlling Molecular Weight.....	29
3.1.2	Tuning cLogP and Lipophilicity	30
3.1.3	Removal of the Aminoisoxazole.....	30
3.1.4	Conservation of the Biaryl Unit	31
3.1.5	Investigation of the Acetic Acid Moiety.....	32
3.1.6	Hydantoin Series Design	33
3.1.7	Acyl Aniline Series Design.....	35
3.1.8	Aryl Indole Series Design	36
3.1.9	Overall Design Aims	37
3.2	Inhibitor Synthesis	37
3.2.1	Reductive Amination.....	37
3.2.2	Hydantoin Core Synthesis	38
3.2.3	Hydantoin Cross Coupling	38
3.2.4	Acyl Aniline and Aryl Indole Synthesis	40
3.3	Pharmacology.....	40

3.3.1	LPA ₁ Receptor Agonism/Antagonism Signalling Assay.....	40
3.3.3	[³ H]-Thymidine Incorporation Assay.....	42
3.3.4	Cytotoxicity Alamar Blue Assay	43
3.3.5	Physicochemical Measurements	43
3.3.6	Biological Evaluation of Ki16524 and AM095.....	44
3.3.7	Biological Evaluation of Hydantoin, Acyl Aniline and Aryl Indole Series	46
3.4	Summary of Hydantoin, Acyl Aniline and Aryl Indole Series.....	52
3.5	Conclusions.....	55
3.6	Future Work.....	56
4	Chapter 4: PF-8380 SAR and Hit Optimisation	58
4.1	Introduction.....	58
4.1.1	Structure-based Drug Design	61
4.2	PF-8380 Tail Assessment.....	66
4.2.1	Synthetic Access to PF-8380 Tail Analogues	67
4.2.2	Synthesis of Tail Analogues.....	68
4.2.3	PF-8380 Tail Analogues Pharmacological Evaluation.....	70
4.3	PF-8380 Zinc Binder Assessment.....	75
4.3.1	Synthetic Access to PF-8380 Zinc Binder Analogues	76
4.3.2	Synthesis of PF-8380 Zinc Binder Analogues.....	77
4.3.3	PF-8380 Zinc Binder Analogues Pharmacological Evaluation.....	78
4.4	PF-8380 Core and Linker Assessment	81
4.4.1	Synthetic Access to PF-8380 Core/ Linker Analogues.....	83
4.4.2	Synthesis of PF-8380 Core/Linker Analogues	84
4.4.3	Biological Evaluation of PF-8380 Core/Linker Analogues	86
4.5	PF-8380 SAR Overview.....	92
4.6	Structure-based Drug Design and Lead Analysis of ATX Inhibitors.....	93
4.6.1	Homospirropiperazine Structure-based.....	94
4.6.2	Truncated Series Lead Optimisation.....	105
4.7	Conclusions.....	114
4.8	Future Work.....	115
5	Chapter 5: Experimental	118
5.1	General Techniques	118
5.1.1	Experimental Details.....	118

5.1.2	General Experimental Procedures.....	119
5.2	Experimental Data.....	125
5.3	Biology.....	178
5.3.1	PathHunter® CHO-K1 EDG2 β -Arrestin Compound Screen Study...	178
5.3.2	Bis- <i>p</i> NPP ATX Inhibition Assay.....	178
5.3.3	[³ H]-Thymidine Incorporation Assay.....	179
5.3.4	Cytotoxicity Alamar Blue Assay.....	180
5.3.5	High Throughput Physicochemical Measurements.....	180
6	References.....	182

List of Figures:

Figure 1: A: Normal lung tissue and B: Fibrotic scared lung tissue.....	1
Figure 2: Proposed key events involved in abnormal wound healing IPF pathogenesis	2
Figure 3: Pirfenidone 1 and Nintedanib 2	4
Figure 4: Structure of LPA	7
Figure 5: Illustration of lung fibrosis	8
Figure 6: Structure of LPA ₁ and ligand ONO-9780307	10
Figure 7: Structure of NAEPA and DGPP	11
Figure 8: Small molecule LPAR antagonists	11
Figure 9: The crystal structure of ATX (PDB ID 2XR9).....	13
Figure 10: Schematic representation of the active site, ATX-PO ₄	14
Figure 11: Schematic representation of ATX binding site and hydrophobic pocket .	14
Figure 12: Expanded image of ATX hydrophobic pocket and tunnel.	15
Figure 13: First in class ATX inhibitors, phosphate and phosphonate analogues.	20
Figure 14: H2L-7905958 37 ATX inhibitor	20
Figure 15: Co-crystal of HA155 within the catalytic site of ATX.....	21
Figure 16: PF-8380 docked within the catalytic site of ATX.....	21
Figure 17: Exemplars from recent ATX patent application exhibiting a lipid-like layout.....	22
Figure 18: Postulated ATX non-lipid like /non-competitive inhibitors	22
Figure 19: Co-crystal of PAT-078 within ATX.....	23
Figure 20: Exemplar structures from X-Rx Discovery Inc and Galapagos patent applications.....	24
Figure 21: <i>N</i> -methylpyrazole, <i>N</i> -aryltriazole, and <i>N</i> -methyltriazole analogues.....	31
Figure 22: Represented design of hydantoin.....	33
Figure 23: Target hydantoin compounds	33
Figure 24: Design strategy of cyclopropanecarboxylic acid hydantoin derivative	34
Figure 25: Represented design of the acyl aniline series	35
Figure 26: Target acyl aniline compounds.....	36
Figure 27: Design of aryl indole series	36
Figure 28: Target aryl indole compounds.....	37
Figure 29: PathHunter [®] β -Arrestin GPCR assays	41
Figure 30: DNA synthesis cycle	42
Figure 31: Alamar Blue [®] cytotoxicity assay	43
Figure 32: Illustrating the calculated molecular weight and cLogP of I hydantoin, II acyl aniline, III aryl indole, IV ATX inhibitors.....	53
Figure 33: Active novel ATX inhibitors identified from the bis- <i>p</i> NPP assay (K _i)	54
Figure 34: PF-8380.....	58
Figure 35: Symmetrical analogues 94 and 95	60
Figure 36: Alcohol derivative 96	61
Figure 37: (S)-96 co-crystallised with ATX enzyme (ribbon structure)	62
Figure 38: Schematic representation of (S)-96 in the active site.. ..	62
Figure 39: Schematic representation of (S)-96 in the hydrophobic pocket	63
Figure 40: (S)-96 illustrated interactions with ATX.. ..	64

Figure 41: Molecular modelling of PF-8380	65
Figure 42: PF-8380 tail shaded grey, target tail SAR analogues 97-115	66
Figure 43: Overview of tail SAR	75
Figure 44: PF-8380 head group shaded blue, target altered zinc binding SAR compounds	75
Figure 45: Overview of zinc binding SAR	81
Figure 46: PF-8380 target altered core and linker SAR compounds	81
Figure 47: A matched molecular pair highlighting the differences in physicochemical and biochemical properties of piperazine rings and homospiropiperazine rings	82
Figure 48: (R)-160 and (S)-160 energy minimised against the active site of ATX	87
Figure 49: Comparison of piperazine and 2,6-diazaspiro[3.3]heptane N-N lengths	88
Figure 50: Overview of core and linker SAR	91
Figure 51: Compounds identified from SAR study for further development	94
Figure 52: Homospiropiperazine analogue 162	94
Figure 53: Molecular modelling of 162 using MOE	95
Figure 54: SAR of target homospiropiperazine zinc binders	97
Figure 55: Target homospiropiperazine tail analogue	98
Figure 56: Overview of homospiropiperazine series	104
Figure 57: Truncated analogue 164 identified from PF-8380 SAR	105
Figure 58: Molecular modelling of 164 using MOE	106
Figure 59: Molecular modelling of 213 (Z-isomer)	107
Figure 60: Target truncated compounds and target oxime analogues	109
Figure 61: Overview of truncated series	114

List of Schemes:

Scheme 1: Summary of overall project	iii
Scheme 2: Pirfenidone 1 and metabolite 5-carboxy-pirfenidone 3	5
Scheme 3: Nintedanib 2 and metabolites	6
Scheme 4: A. Synthesis of LPA	9
Scheme 5: LPA degradation pathways	10
Scheme 6: ATX catalytic hydrolysis of LPC 7 to LPA 6	12
Scheme 7: Mechanism of LPC choline release assay	17
Scheme 8: Mechanism of pNP-TMP and bis-pNPP assay	18
Scheme 9: Mechanism of FS-3 20	18
Scheme 10: Mechanism of CPF4	19
Scheme 11: Schematic representation of the three proposed series	28
Scheme 12: Retrosynthetic analysis of the hydantoin series	35
Scheme 13: Reductive amination	38
Scheme 14: Synthesis of hydantoin compounds 64 and 69	38
Scheme 15: Suzuki-Miyaura coupling and hydrolysis	39
Scheme 16: Suzuki-Miyaura coupling and hydrolysis	39
Scheme 17: Mechanism of the bis-pNPP assay	41
Scheme 18: Proposed future work of the hydantoin, acyl aniline and aryl indole series	56
Scheme 19: Hit-to-Lead optimisation process planned	60

Scheme 20: Retrosynthetic view of tail SAR analogues	68
Scheme 21: Friedel Crafts acylation and crystal structure 116.....	68
Scheme 22: Carbamate substituted piperazine synthesis	69
Scheme 23: Synthesis of urea, sulfonamide, and amide substituted piperazines....	69
Scheme 24: Carbamate analogues synthesis from intermediates 97-115.....	70
Scheme 25: Retrosynthetic view of PF-8380 zinc binding SAR analogues	77
Scheme 26: Synthesis of head group analogues 143-148	77
Scheme 27: Synthesis of benzyl analogues 149-150.....	78
Scheme 28: Retrosynthetic view of truncated analogues 71-72.....	83
Scheme 29: Retrosynthetic view of linker SAR analogues 165-166	83
Scheme 30: Retrosynthetic view of core SAR analogues 167-169,174.....	84
Scheme 31: Synthesis of truncated analogues 163-164	84
Scheme 32: Synthesis of alkanes 165 and 166	84
Scheme 33: Synthesis of acids 182 and 183	85
Scheme 34: Synthesis of amide analogues 167-169, and 174	85
Scheme 35: Overview of PF-8380 (39) SAR study	92
Scheme 36: Iterative design of the homospiropiperazine core	97
Scheme 37: Synthesis of zinc binding groups 200 and 202	99
Scheme 38: Synthesis of binding head groups 205 and 208.....	99
Scheme 39: Synthesis of homospiropiperazine intermediate 211 and 212	99
Scheme 40: Synthesis of homospiropiperazine analogues 186-190	100
Scheme 41: Synthesis of homospiropiperazine analogues 191-197	100
Scheme 42: Synthesis of tail analogue 198	101
Scheme 43: Iterative design of the truncated series.....	108
Scheme 44: Synthesis of truncated analogues 214-220	110
Scheme 45: Synthesis of truncated oxime analogues 221-225.....	110
Scheme 46: Conclusive overview of research trajectory	115
Scheme 47: Potential further SAR to be explored.....	116

List of Tables:

Table 1: Clinically advanced pharmaceutical agents for IPF	4
Table 2: ATX assay substrates and detection mode	16
Table 3: Predicted physicochemical properties of AM095 (16) and PF8380 (39)	25
Table 4: Biological data for 1-oleoyl-LPA (6), Ki16425 (15), and AM095 (16).....	44
Table 5: Biological and physicochemical data for hydantoins 49, 56-62.....	47
Table 6: Biological and physicochemical data for acyl aniline 50, 81-85	49
Table 7: Biological and physicochemical data for aryl indole 51 and 86	51
Table 8: Measured physicochemical properties of PF8380 (39).....	59
Table 9: Activity profile of compounds 97-106.....	71
Table 10: Activity profile of compounds 107-115.....	73
Table 11: Activity profile of compounds 139-150.....	79
Table 12: Activity profile of compounds 159-162.....	86
Table 13: Activity profile of compounds 163-164.....	88
Table 14: Activity profile of compounds 165-166.....	89
Table 15: Activity profile of 167-169, and 174	90

Table 16: Activity profile of compounds 186-197.....	102
Table 17: Activity profile of compounds 198.....	103
Table 18: Activity profile of compounds 214-220.....	111
Table 19: Activity profile of compounds 214-225.....	112

1 Chapter 1: Introduction

1.1 Fibrosis and IPF

Tissue injury is common throughout our lives. Following injury it is paramount that tissue architecture is restored to regain normal organ function. Injury initiates a complex series of host wound healing responses which occur by a highly coordinated sequence of events where cellular signals act in parallel to repair the injury. One such event is fibrosis, the formation of excess fibrous connective tissue in a reparative or reactive process. If successful, fibrosis restores normal tissue structure and function. If fibrosis becomes unregulated, scar tissue forms and the architectural remodelling of the tissue is severely disrupted, ultimately leading to loss of function.¹ Idiopathic pulmonary fibrosis (IPF) is the most common and devastating form of lung fibrosis, with an incidence of 6.8 per 100,000 persons.² IPF is typified by alveolar damage and subsequent lung dysfunction.³ Fibrosis in IPF is generally progressive and is intractable to current pharmacological intervention. It inevitably leads to respiratory failure due to destruction of functional alveolar units by scar tissue. This scar tissue build up affects the lung function by reducing gas exchange between the air sacs of the lung and the blood stream (Figure 1). This scar tissue build up leads to respiratory failure and death.⁴

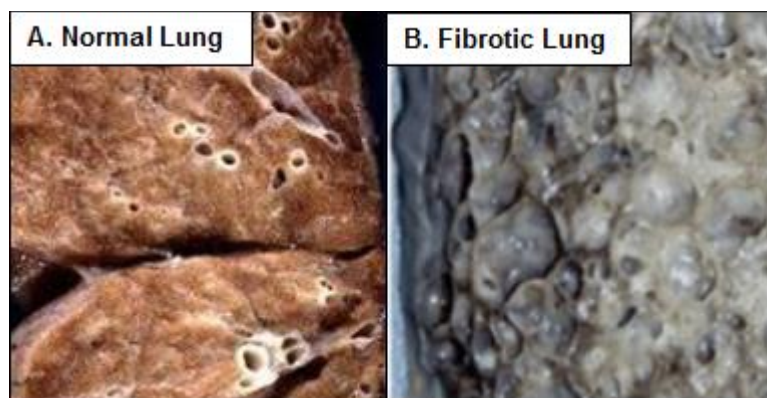


Figure 1: A: Normal lung tissue and B: Fibrotic scarred lung tissue.⁴

1.1.1 Hypothesised Pathogenesis of IPF

The word idiopathic indicates the disease in question has no known cause. The exact aetiology of IPF remains unknown, although a number of risk factors have been identified including cigarette smoking and viral infections.⁵ Three percent of IPF patients appear to have a gene polymorphism of tumour necrosis factor (TNF)- α

and transforming growth factor (TGF)- β 1 which confers an increased risk of developing IPF.⁶ As only a small number of individuals exposed to known risk factors develop IPF, the aetiology is most likely multifactorial.⁷ Although significant advances have been made towards understanding the pathogenesis of pulmonary fibrosis, the specific cellular and molecular mechanisms that contribute to disease progression remain unclear.⁷ Regardless of the uncertainty of precise IPF aetiology, it is generally accepted that abnormal wound healing is a major component of the pathogenic process.

1.1.2 Abnormal Wound Healing in IPF

Damage to the alveolar epithelium leads to endoplasmic reticulum (ER) stress. ER stress can be profibrotic and concludes in apoptotic events or the initiation of repair mechanisms. In IPF patients, these repair mechanisms are dysregulated,⁸ hence abnormal wound healing occurs (Figure 2).

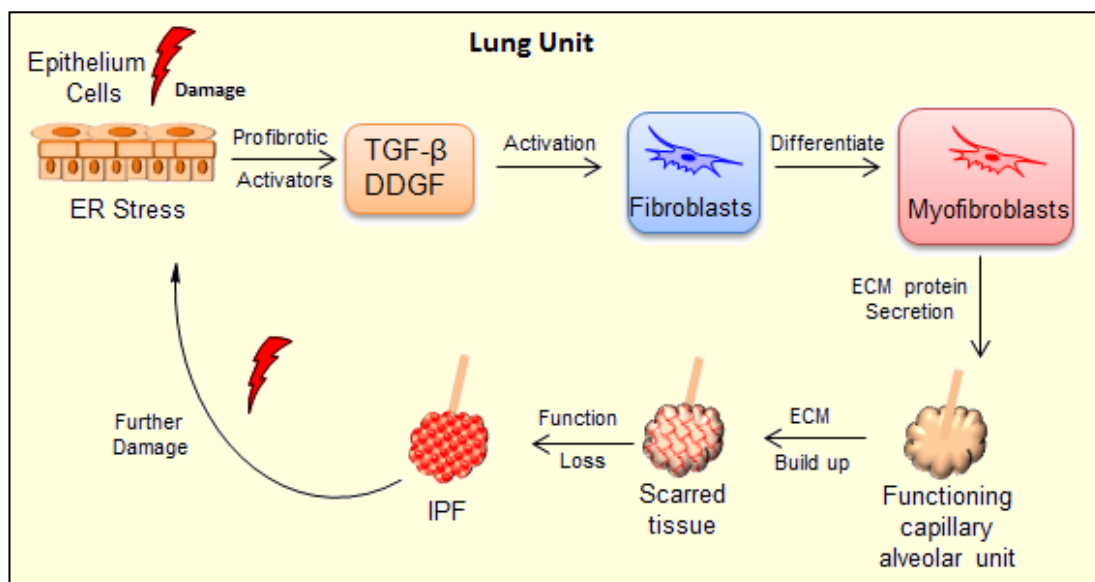


Figure 2: Proposed key events involved in abnormal wound healing IPF pathogenesis

In this repair mechanism ER stress releases transforming growth factor (TGF)- β , activated by the integrin α v β 6 (α v β 6).⁹ In response to this (TGF)- β activation the epithelium cells secrete profibrotic mediators such as platelet-derived growth factor (PDGF). PDGF triggers the recruitment of fibroblasts. Myofibroblasts, a major cell type involved in normal wound healing localise at these sites of active fibrosis, synthesise and secrete extracellular matrix (ECM) proteins.⁸ Present academic opinions suggest that myofibroblast cells have three possible origins. The first

hypothesis is that resident lung fibroblasts differentiate directly under the influence of the profibrotic microenvironment to form myofibroblasts.¹⁰ Secondly, is that epithelial cells undergo trans-differentiation to form fibroblasts and hence myofibroblasts by epithelial-to-mesenchymal transition (EMT). The third possibility is that mesenchymal cells are derived from circulating fibrocytes.¹¹ Regardless of its origin, the key effector cell in fibrogenesis is the myofibroblast, which is responsible for ECM proteins secretion. The pathogenesis of IPF is characterised by excessive ECM protein deposition into lung alveolar. This ECM protein build up leads to irreversible scarring, loss of lung function of the capillary alveolar unit, impaired gas exchange and ultimately respiratory failure and death in IPF suffers.¹²

1.1.3 Therapeutic Targets for the Treatment of IPF

Targeting IPF presents special challenges with regard to therapy. IPF appears to be characterised by abnormalities in multiple pathways involved in the wound healing process, many of which display considerable redundancy.⁹ Hence multiple therapeutic approaches have been proved for IPF.⁹ Furthermore there are no accurate animal models for IPF. Bleomycin, a glycopeptide antibiotic, is widely used in rodents to model pulmonary fibrosis. Bleomycin induces DNA strand breaks, resulting in pulmonary inflammation, injury, and subsequent interstitial fibrosis.¹³ This allows the study of mechanisms involved in fibrogenesis and for evaluation of potential therapies. It does not, however, recapitulate the underlying pathobiology of IPF.¹⁴ Over the years, numerous agents have been shown to inhibit experimentally induced lung fibrosis in mice. Yet, almost all of these compounds have failed to demonstrate comparable antifibrotic effects in humans.⁹

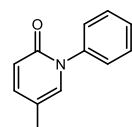
Historically, IPF was believed to result mainly from chronic inflammation, leading to persistent epithelial and vascular injury and activation/expansion of the lung mesenchyme. Conventional treatments based on this assumption involve the use of anti-inflammatory or immunosuppressive drugs. Unfortunately, none of these treatments have been shown to unambiguously alter the inflammatory process in IPF.⁸ During the past decade great progress has been made in the basic science underlying the pathogenesis of IPF. Consequently, trials targeting different pathways have been developed. Several clinical trials are currently being investigated for IPF by industry partners (Table 1).⁹

Table 1: Clinically advanced pharmaceutical agents for IPF

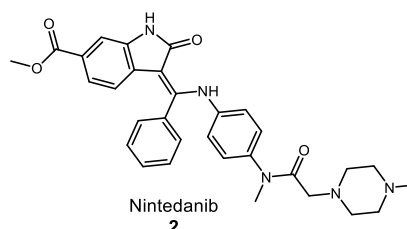
Compound	Target	Development Status
BMS-986020 (small molecule)	Lysophosphatidic acid receptor	Phase II (NCT01766817)
FG-3019 (human monoclonal antibody)	Connective tissue growth factor	Phase II (NCT01890265)
Lebrikizumab (humanized monoclonal antibody)	Interleukin-13	Phase II (NCT01872689)
SAR156597 (humanized monoclonal antibody)	Interleukin-4 and interleukin-13	Phase II (NCT01529853)
Simtuzumab (humanized monoclonal antibody)	Lysyl oxidase-like 2	Phase II (NCT0176196)
STX-100 (humanized monoclonal antibody)	Integrin $\alpha_v\beta_6$	Phase II (NCT01371035)
Tralokinumab (human monoclonal antibody)	Interleukin-13	Phase II (NCT01629667)

1.1.4 Current Treatments of IPF

Since the publication of a guideline document from the American Thoracic Society, European Respiratory Society, Japanese Respiratory Society and Latin American Thoracic Association for the diagnosis and management of IPF,¹⁵ two new drugs have consistently shown a positive effect on disease progression: Pirfenidone (**1**) and Nintedanib (**2**) (Figure 3).^{16,17}



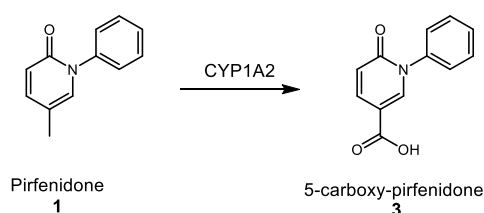
Pirfenidone
1



Nintedanib
2

Figure 3: Pirfenidone **1** and Nintedanib **2**

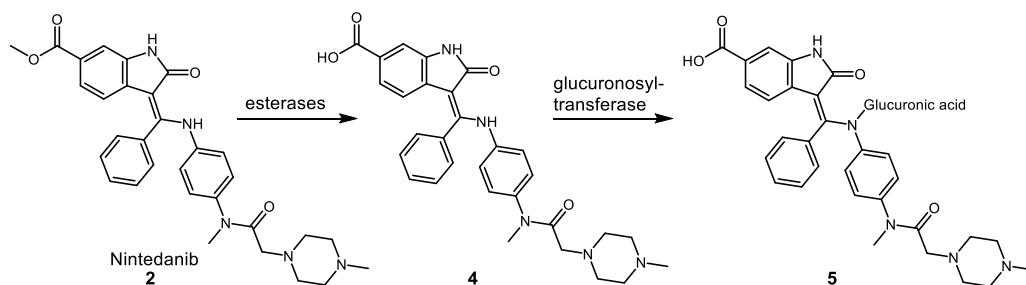
The first medication approved specifically for the treatment of IPF was Pirfenidone (**1**). Pirfenidone (**1**) is a pyridone derivative with antifibrotic, anti-inflammatory, and antioxidant properties.¹⁸ Its precise mechanism of action remains unknown but it has been associated with the inhibition of TGF- β .¹⁸ Extensive clinical trials of Pirfenidone (**1**) has led to its approval by many governing bodies worldwide including the European Medicines Agency and the Food and Drug Administration under the trade name Esbriet[®] for the treatment of IPF.¹⁹ Pirfenidone (**1**) displays an adequate safety profile with gastrointestinal upset and photosensitivity rash as the most common treatment-related adverse events.²⁰ Pirfenidone (**1**) is frequently associated with gastrointestinal upset such as dyspepsia, nausea, gastritis, gastroesophageal reflux disease, and vomiting.²¹ Approximately 70–80% of Pirfenidone (**1**) is metabolised *via* a cytochrome P450 enzyme (CYP1A2), to the inactive metabolite 5-carboxy-pirfenidone (**3**) which is also excreted in urine (Scheme 2). Accordingly, the recommended daily dose of Pirfenidone (**1**) for patients with IPF is substantial; three 267 mg capsules three times a day for a total of 2403 mg/day.²⁰ Due to its extensive metabolism and gastrointestinal side effects, Pirfenidone (**1**) has sub-optimal pharmacokinetics and is undoubtedly a poorly tolerated drug.



Scheme 2: Pirfenidone **1** and metabolite 5-carboxy-pirfenidone **3**

The second medication disclosed in the literature specifically for the treatment of IPF was Nintedanib (**2**). Nintedanib (**2**) is a multikinase inhibitor originally developed for cancer treatment.⁹ Nintedanib (**2**) inhibits multiple tyrosine kinases intracellularly, including the PDGF receptors and fibroblast growth factor receptors (FGFR)-1, 2, and 3, which have been implicated in IPF pathogenesis.²² Nintedanib (**2**) binds competitively to the adenosine triphosphate (ATP) pocket of the kinase and blocks the intracellular signalling²² which is crucial for the proliferation, migration, and transformation of fibroblasts representing essential mechanisms of the IPF pathology. Nintedanib (**2**) has been shown to exert antifibrotic activities *in vitro* human lung fibroblasts and slow IPF disease progression through clinical trials data.²³ Overall, Nintedanib (**2**) shows a generally well tolerated safety profile,

however this is not completely satisfactory with diarrhoea as the most frequent adverse event.¹⁷ Nintedanib (**2**) displays a low oral bioavailability of about 4.7%, and an effective half-life of 9.5 hours in patients with IPF. The predominant metabolic reaction for Nintedanib (**2**) is hydrolytic cleavage by esterases; resulting in the free acid moiety (**4**). The acid (**4**) is subsequently glucuronidated (**5**) by glucuronosyltransferase enzymes (Scheme 3).²⁴ Nintedanib was developed by Boehringer Ingelheim and marketed under the brand name OFEV[®] for IPF treatment.²⁴



Scheme 3: Nintedanib **2** and metabolites

Pirfenidone (**1**) and Nintedanib (**2**) are major breakthroughs for IPF patients. Nevertheless, much progress is still needed as both Pirfenidone (**1**) and Nintedanib (**2**) have side effect profiles which may lead to compliance issues. In addition, it is unknown whether the beneficial effects of these drugs are durable beyond 1 year.⁹ Most importantly neither Pirfenidone (**1**) nor Nintedanib (**2**) is a cure for IPF. Neither pharmaceutical agent improves lung function and most patients on these therapies continue to decline in lung function.

An alternative treatment for IPF is lung transplant. Unfortunately the number of patients who meet operational requirements is extremely limited. The average age at diagnosis is 66 years and many centres limit lung transplantation candidates to patients aged below 60 years. Regrettably, patients with rapidly progressive or severe IPF may die while awaiting transplantation. With a 5 year rate survival after transplantation of approximately 50-60%, the decision to list patients for transplantation is arduous.²⁵ The majority of existing care focuses on management of IPF with a combination of exercise training, education, psychosocial support, and inevitably palliative care.²⁵

In conclusion, IPF is a debilitating and devastating disease. To date there is no medical intervention able to reverse the disease, furthermore the two

pharmaceutical agents available are frequently poorly tolerated in IPF sufferers. A more complete understanding of IPF pathology is only now beginning to emerge and consequently IPF is an area of unmet clinical need.

1.2 Lysophosphatidic Acid (LPA) Signalling and IPF

Aberrant wound healing responses to injury are implicated in IPF development, but the exact pathways involved are uncertain. Equally, there is evidence in the literature that lung fibrosis is mediated by a lysophospholipid named lysophosphatidic acid (LPA).¹ LPA has also been shown to mediate the differentiation of fibroblasts into myofibroblasts, which plays a major role in fibrosis.⁸ The chemical structure of LPA consists of a phosphate head group and a single fatty acyl chain attached to a 3-carbon backbone.²⁶ LPA is generally known as a mixture of various lysophospholipids with both saturated (16 : 0, 18 : 0) and unsaturated (16 : 1, 18 : 1, 18 : 2, 20 : 4) fatty acid chains.²⁶ Throughout this thesis, LPA refers to oleoyl-L- α -lysophosphatidic acid phosphate (**6**) (18: 1) (Figure 4).

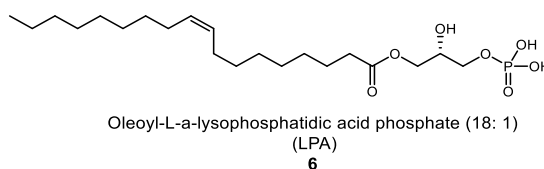


Figure 4: Structure of LPA

LPA (**6**) exerts a wide range of cellular responses, such as calcium mobilisation, cell proliferation, cell transformation through a family of membrane bound G-protein-coupled receptors (GPCRs).²⁷ To date 6 *bona fide* LPA receptors (LPAR) have been reported, and these are denoted LPA₁₋₆.²⁹ As the name indicates LPA₁ was the first LPAR to be identified. LPA 1/2/3 belong to the same endothelial differentiation gene family and share significant structural homology.²⁷ GPCRs are a large protein superfamily containing a conserved structure composed of seven transmembrane helices. GPCRs are located at the cell surface and are responsible for the transduction of an endogenous signals into an intracellular response.²⁷ These receptors are broadly expressed throughout the body and are overexpressed in pathological conditions including fibrosis (renal, liver, lung) and cancer (ovarian, breast).²⁷ Historically, the discovery of drugs acting at GPCRs has been extremely successful and remains the focus of major pharmaceutical companies.²⁸

LPA₁ receptors have been considered a therapeutic target for pathologic fibrosis for several reasons. Bronchoalveolar lavage fluid (BALF) is a technique used for retrieving fluid from lung airways; BALF is found in the lung alveoli and accordingly is a reliable representation for protein composition in the pulmonary airways.²⁹ LPA-LPA₁ signalling pathway has been linked to IPF, a significant study found that the concentration of LPA (6) levels in BALF of IPF patients was higher than would be expected.¹ Furthermore, this study found the LPA₁ receptor to be the most abundant on human IPF fibroblast tissue.¹ It was shown that LPA (6) accumulating in the alveolar and interstitial spaces attracts fibroblasts toward fibrin and activates endothelial cells through the LPA₁ receptor.¹ This endothelial contraction and remodelling causes plasma leakage from the intravascular space to the interstitial and alveolar spaces, which in turn interferes with the ability of the lungs to transfer oxygen into the bloodstream (Figure 5).

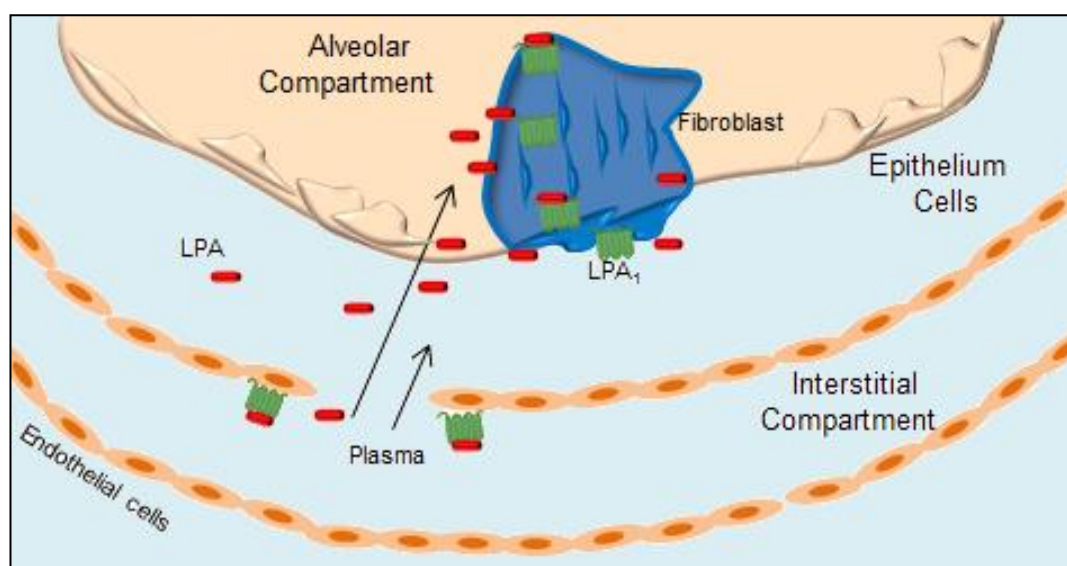
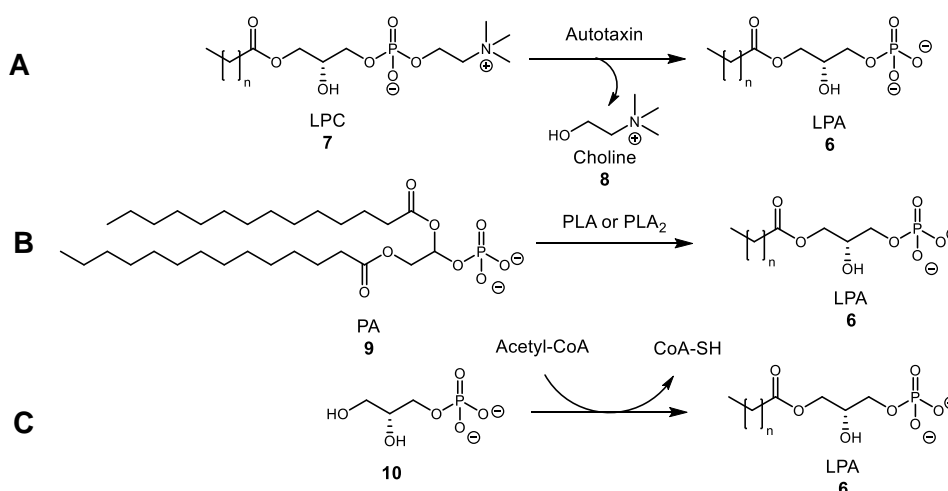


Figure 5: Illustration of lung fibrosis

It was then found that such chemotactic behaviour, i.e. likelihood of the fibroblast cells to form clusters, was found to be suppressed upon treatment with an LPA₁ antagonist.¹ LPA₁ knockout mice treated with bleomycin to induce IPF were found to exhibit a reduction in fibroblast formation and vascular leakage, increasing their survival rate.¹ This strengthens the rationale that LPA (6) is an important mediator in lung fibrosis. Along with its known profibrotic nature, these significant *in vivo* results all suggest LPA₁ to be an important drug target for the treatment of IPF.

1.2.1 LPA Production, Receptor and Degradation

LPA (**6**) is produced through several enzymatic pathways which occur in both intracellular and extracellular contexts. LPA (**6**) was initially thought to be released from activated platelets, however, the majority of extracellular LPA (**6**) has been shown to be produced from the hydrolysis of an alternative lysophospholipid; lysophosphatidic choline (**7**) (LPC). The enzyme Autotaxin (ATX) hydrolyses LPC (**7**) liberating a choline group (**8**) (A, Scheme 4).³⁰ The second major synthetic pathway for LPA (**6**) is the conversion of phosphatidic acid (PA) (**9**) into LPA (**6**) by the actions of either phospholipase A1 (PLA₁) or phospholipase A2 (PLA₂) (B, Scheme 4).³⁰ Through a separate mechanism LPA (**6**) is also *de novo* synthesised from the acylation of glycerol-3-phosphate (**10**) by the action of glycerophosphate acyltransferase (Acetyl-CoA)(C, Scheme 4).³¹



Scheme 4: A. Synthesis of LPA via hydrolysis of LPC by Autotaxin B. Synthesis of LPA via PA C. Acylation of glycerol-3-phosphate by glycerophosphate acyltransferase

LPA (**6**) exerts its cellular responses through 6 GPCRs and the expression of LPA₁ is significantly up-regulated in fibrosis.¹² The crystal structure of LPA₁ in complex with antagonist tool compound ONO-9780307 (**11**) was disclosed in 2015 (Figure 6).³² At the top of the binding pocket, the carboxylic acid of ONO-9780307 (**11**) interacts through polar and ionic bonds with residues histidine (His40), lysine (Lys39), and tyrosine (Tyr34). Across the LPAR family, both lysine (Lys39) and tyrosine (Tyr34) are highly conserved, however, histidine (His40) is unique to LPA₁ and its protonation may be important for high-affinity interactions with the carboxylic acid of ONO-9780307 (**11**).³²

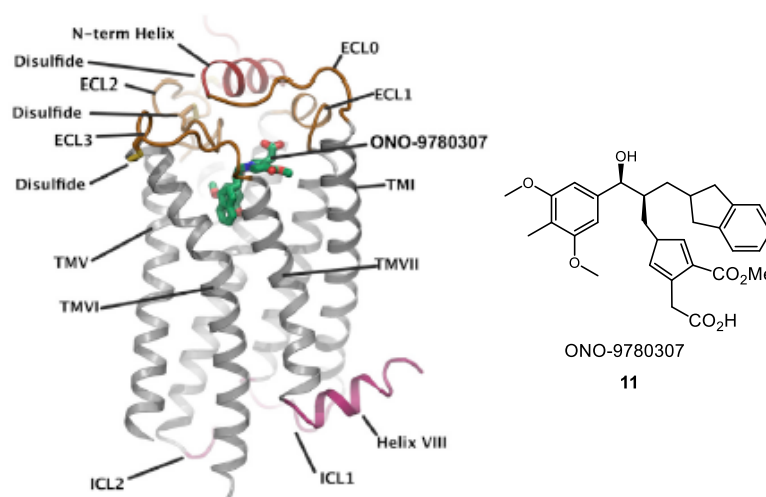
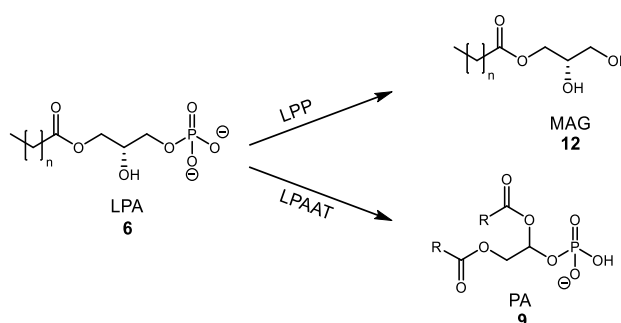


Figure 6: Structure of LPA₁ and ligand ONO-9780307 (green)³²

After successful LPA (**6**) binding to the LPA receptor and induction of downstream signalling effects, LPA (**6**) is degraded. Degradation of LPA (**6**) can occur through two main routes. In first route LPA is degraded by lipid phosphate phosphohydrolases (LPP) which irreversibly dephosphorylates LPA to monacylglycerol (MAG) **12** (Scheme 7). The second route involves the enzyme LPA-acyltransferase (LPAAT) which reversibly esterifies LPA (**6**) to phosphatidic acid (PA) **9** (Scheme 5).³³



Scheme 5: LPA degradation pathways

1.2.2 LPA Receptor Antagonists

For many GPCRs, the natural ligand can provide a good starting point in the lead finding process.²⁸ The same can be said for the history of LPAR antagonism. Among the first LPAR antagonists synthesised were lipid like structures that do not satisfy Lipinski's rule of five.³⁴ In 2001, two separate groups reported the characterisation of selective antagonists for LPAR. The first group reported the testing of a selective and competitive inhibitor of LPA₃, diacylglycerol pyrophosphate (DGPP 8:0) (**13**).³⁵ The second group reported that an *N*-acyl ethanolamide

phosphate (NAEPA) (**14**) with a benzyl-4-oxybenzyl group at the 2-position of the ethanolamine backbone and was shown to inhibit both LPA₁ and LPA₃ receptors (Figure 7).³⁶

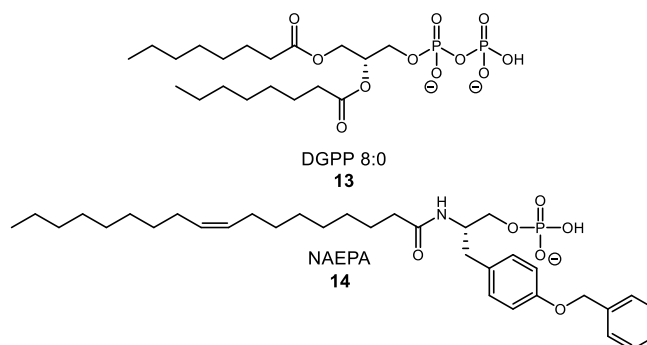


Figure 7: Structure of NAEPA and DGPP

The first non-lipid like structure acting as a LPAR antagonist was Ki16425 (**15**) (Figure 8).³⁷ This was identified through screening of 150,000 low molecular weight compounds developed by the Kirin Brewery for LPAR antagonism. They found that this isoxazole derivative inhibited LPA (**6**) induced actions in a manner highly specific to LPA₁ and LPA₃ receptor subtypes.¹² The extent of the LPA-induced inhibition seemed to depend on the cell type used. Ki16425 (**15**) was also effective against long-term responses, including DNA synthesis and cell migration in Swiss 3T3 fibroblasts.³⁷ Despite this advance, there was still need for further selectivity between LPA₁ and LPA₃ for the development of a potent drug targeting LPA signalling.

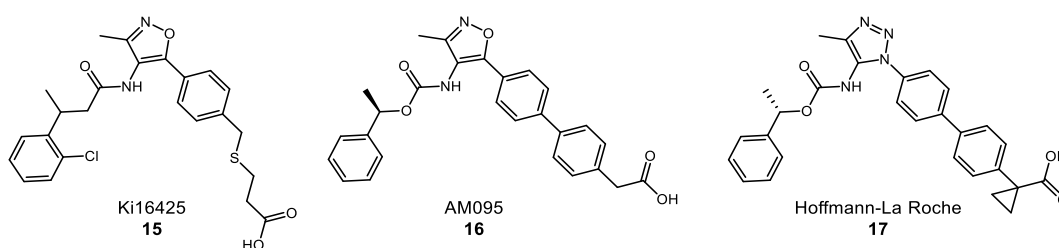


Figure 8: Small molecule LPAR antagonists

AM095 (**16**) was the first selective LPA₁ receptor antagonist reported (Figure 8). This lead compound was originally developed by Amira Pharmaceuticals Inc., and their fibrosis programme was acquired by Bristol-Myers Squibb in 2011.³⁸ *In vivo* pharmacodynamic studies demonstrated that oral administration of AM095 (**16**) reduced lung collagen, vascular leakage, and inflammation after bleomycin-induced lung injury (ED₅₀ = 10 mg/kg) in rats.³⁹ AM095 (**16**) completed phase one clinical

studies, from which data is not currently available. AM095 is now commercially available as a potent LPA₁ receptor antagonist for use in research.

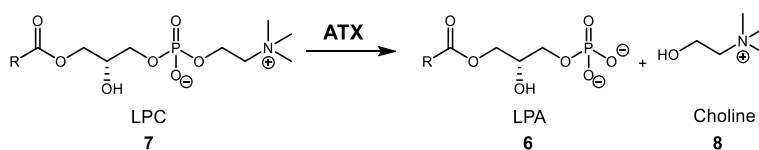
Subsequent LPA₁ receptor antagonists were disclosed from Hoffmann-La Roche.¹² In order to identify novel LPA₁-selective antagonists Hoffmann-La Roche undertook a bioisostere approach based on the AM095 (**16**) scaffold, and reported the synthesis and biological testing of a novel class of LPA₁ antagonists.¹² A selective LPA₁ antagonist (**17**) was reported by Hoffmann-La Roche (Figure 8). The antagonist (**17**) inhibited proliferation and contraction of normal human lung fibroblasts (NHLF) following LPA stimulation with a reported LPA₁ IC₅₀ of 25 nM and a LPA₃ IC₅₀ > 30 μM.¹²

In 2014, another LPA₁ antagonist, BMS-986020, whose structure has not been disclosed, began phase two clinical trials to test its efficacy on IPF (NLMID: NCT01766817).⁴⁰

Currently, no pharmaceutical agents targeting LPARs have been approved by any regulatory agency,³⁸ nevertheless the progression of LPA₁ antagonists into clinical trials strengthens the rationale of targeting LPARs for IPF. The pending clinical results will help to determine the therapeutic utility of the LPA₁ receptor as a valuable target for the treatment of IPF.

1.3 Autotaxin (ATX) and IPF

LPA (**6**) elicits a variety of biological responses including fibrosis mediation through activation of specific GPCRs. Based on this, it is hypothesised that inhibiting ATX, the enzyme responsible for LPA (**6**) synthesis will have a downstream effect, lowering LPA (**6**) concentration in plasma (Scheme 6).



Scheme 6: ATX catalytic hydrolysis of LPC 7 to LPA 6

The wide distribution of LPARs and the corresponding increase in ATX expression in IPF makes this enzyme an excellent drug target. Moreover, the drive to inhibit ATX is not restricted to the treatment of IPF. ATX up regulation has been implicated in many disease states including cardiovascular diseases, autoimmune diseases,

cancer, fibrotic diseases, inflammation, neurodegeneration, and pain amongst others.⁴¹ Consequently, selective ATX inhibitors have the potential to treat a variety of diseases that involve the LPC/LPA ATX pathway.

ATX is a 125 kDa glycoprotein with multiple domains first identified as cell motility factor.⁴² In 2005, it was discovered that ATX is synthesised in many cell and tissue types⁴³. ATX is the second member of the ectophosphodiesterase/nucleotide phosphohydrolase (ENPP) family, therefore known as ENPP2.⁴⁴ It is the only member of the ENPP family that is exclusively secreted and not found on the cell surface.⁴⁴ In humans there are four isoforms of ATX; α , β , γ and δ , which are all differentially expressed. ATX β is the most studied isoform and is mainly expressed in the peripheral tissue.^{45,46}

1.3.1 ATX Structure and Binding Modes

In 2010, the crystallisation and preliminary X-ray diffraction analysis of rat ATX was published,⁴⁷ while one year later, the crystallisation and preliminary X-ray crystallographic analysis of human ATX was reported.⁴⁸ It was revealed that rat ATX shares 93% sequence identity with human ATX. In the same year, the crystal structures of mouse ATX was presented. The structural analysis revealed that ATX consists of an *N*-terminal signal sequence, two somatomedin B (SMB)-like domains, a catalytic domain, and a nuclease-like domain (Figure 9).⁴⁹

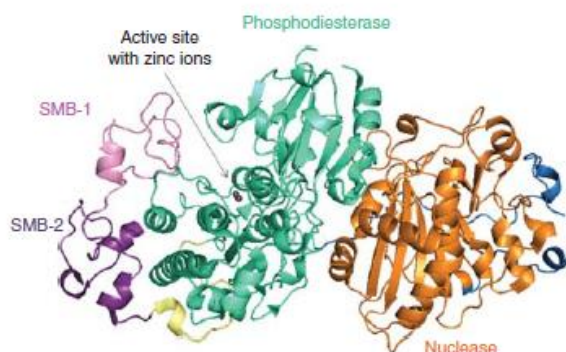


Figure 9: The crystal structure of ATX (PDB ID 2XR9), where distinct domains are represented.⁴¹

The availability of the ATX crystal structure has provided understanding of the molecular surfaces that are important for regulation of lysophospholipase enzymatic activity, in particular the catalytic domain, which comprises of the ATX binding site (catalytic site and hydrophobic pocket) and a hydrophobic tunnel within the

literature. ATX activity can be regulated by structurally diverse ligands with varied binding modes at the catalytic domain.

The catalytic site of ATX encompasses two zinc ions. The first zinc ion (Zn^{2+}) is coordinated by aspartic acid (Asp311), histidine (His315), and histidine His474, whereas the second zinc ion (Zn^{2+}) is coordinated by aspartic acid (Asp171), threonine (Thr209), and histidine (His171).⁴⁹ LPC (red) binds in the catalytic site of ATX, where it is hydrolysed by the catalytic threonine (Thr209) to LPA (Figure 10). Competitive ATX inhibitors bind to the catalytic site in the same manner as LPC, interacting with the zinc ions, which subsequently prevents LPC from being hydrolysed to LPA.

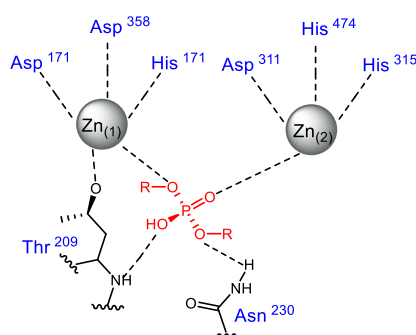


Figure 10: Schematic representation of the active site, ATX- PO_4 .

Within the ENPP family ATX is the only enzyme to contain a sequence deletion stretch of 18 amino acids, which then forms a hydrophobic pocket adjacent to the catalytic site that accommodates the glycerol backbone of the lipid products (Figure 11).⁴⁹

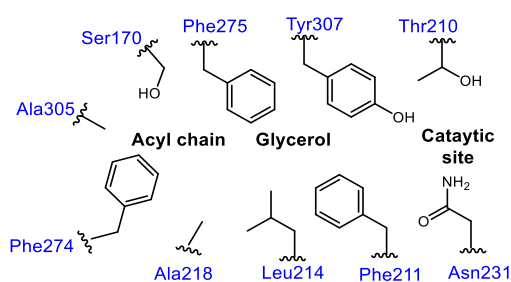


Figure 11: Schematic representation of ATX binding site and hydrophobic pocket

The residues serine (Ser170), phenylalanine (Phe211), leucine (Leu214), alanine (Ala218), phenylalanine (Phe274), phenylalanine (Phe275), alanine (Ala305), and tyrosine (Tyr307) define this hydrophobic region and it has been reported that

binding to this hydrophobic pocket remote from the catalytic site inhibits ATX activity.⁵⁰

Unique to ATX within the ENPP family is the presence of a tunnel which spans from the active site to the opposite side of ATX (Figure 12).⁵¹ A “T-junction” is formed between the hydrophobic pocket, catalytic site and this hydrophobic tunnel. It has been suggested that this tunnel may function as a second LPA product binding site.⁵² ATX has a flat molecular surface on the side of the tunnel entrance, which appears to be suitable for a molecular interaction with the plasma membrane. Therefore, ATX may also act as a lipid-carrier protein that provides hydrophobic environments for LPA products, thus allowing LPA delivery to its GPCRs, exiting *via* the tunnel.⁴⁹ This tunnel can be described as a second LPA binding site or an allosteric site. Non-competitive or allosteric compounds can bind in this tunnel and inhibit ATX, however, it is not fully understood how this inhibition occurs. A potential explanation is that allosteric binding does not affect cleavage of LPC. Instead small molecules block the recently synthesised LPA from exiting the enzyme through the hydrophobic tunnel, thereby trapping and preventing binding of a second substrate molecule. Further biochemical studies with a range of allosteric inhibitors are necessary to fully comprehend this mode of binding.

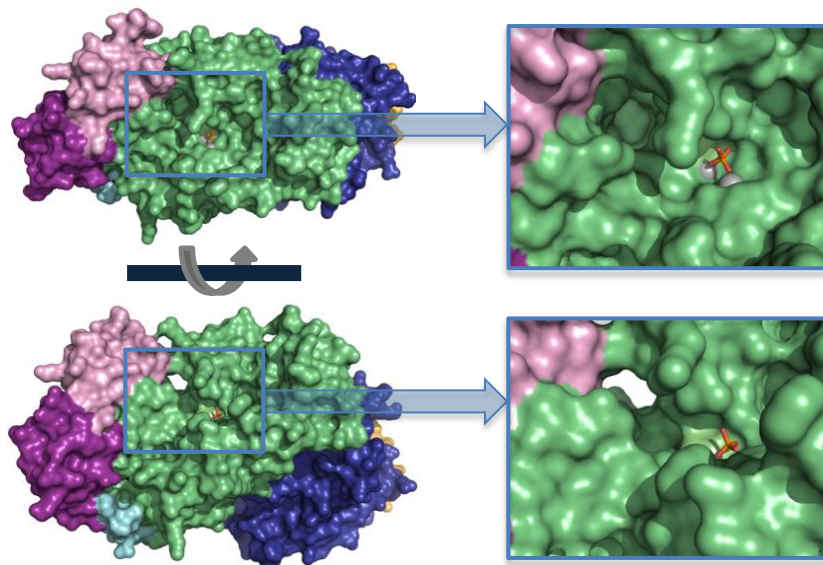


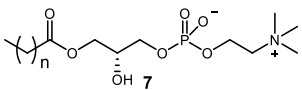
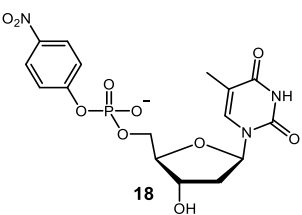
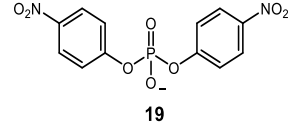
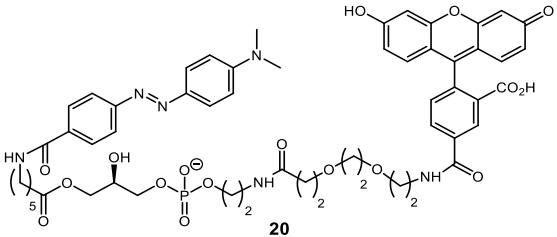
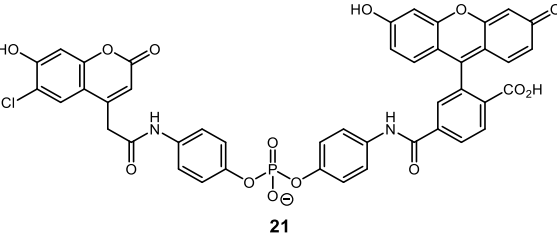
Figure 12: Expanded image of ATX hydrophobic pocket and tunnel.⁵³

1.3.2 Determination of ATX Inhibition

There are several assay protocols available in the literature to determine ATX activity *in vitro* and *in vivo*. As described earlier there are multiple molecular

surfaces, at which small molecules may exert inhibitory actions on ATX, including: (a) the catalytic site, (b) the hydrophobic pocket, and (c) the hydrophobic channel. Accordingly, different assays measure the ability of compounds to inhibit ATX in these unique inhibition modes. Assay substrates can be further sub-categorised into two main groups i) natural and ii) unnatural substrates (Table 2).

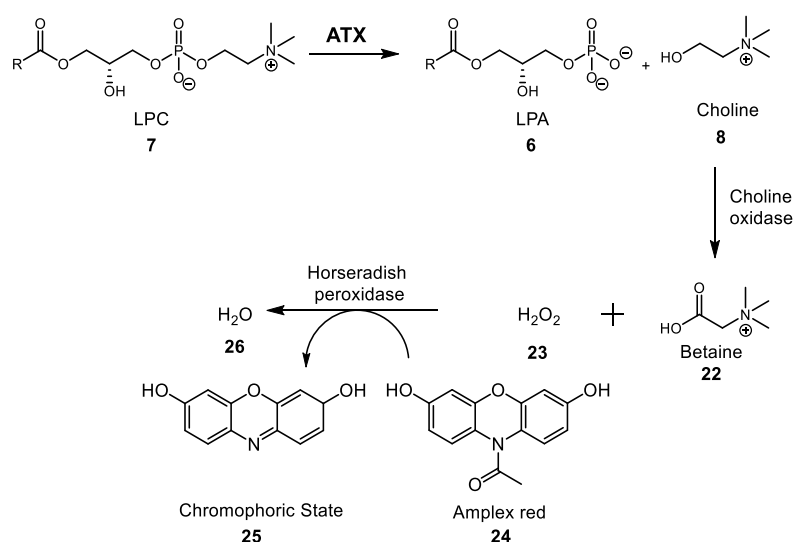
Table 2: ATX assay substrates and detection mode

Assay	Category	Substrate	Detection
LPC	Natural		LPA or choline (LCMS, radiometry, Amplex red [®])
<i>p</i> -NP-TMP	Unnatural		4-nitrophenol (UV)
Bis- <i>p</i> NPP	Unnatural		4-nitrophenol (UV)
FS-3	Unnatural		Fluorescence
CPF4	Unnatural		FRET

Competitive ATX inhibitors can be measured using a physiological ATX substrate LPC assay. LPC sits in the hydrophobic pocket of ATX. The catalytic triad of ATX facilitates hydrolysis of LPC to LPA, liberating a choline group. Assays designed using the natural substrate LPC can detect ATX inhibition by measuring either the i) LPA formed or ii) choline produced.⁵⁴

ATX activity can be determined by the measurement of LPA produced. In one such procedure the assay incubation mixture is subjected to liquid chromatography–mass chromatography (LCMS) to measure the levels of LPA present. In a different procedure, ^{14}C labelled LPC can be utilised to measure ATX activity. When ^{14}C LPC is hydrolysed by ATX a ^{14}C LPA molecule is produced. The radiolabeled LPA molecule can then be isolated and the enzyme activity quantified using radiometry.⁵⁴

ATX activity can also be determined by the measurement of choline produced, the by-product of LPC hydrolysis. A further reaction of the choline, catalysed by choline oxidase, produces betaine (**22**) and hydrogen peroxide (**23**) (Scheme 7). The concentration of hydrogen peroxide is determined by oxidising a colouring substrate to its chromophoric state in a reaction catalysed by horseradish peroxidase, one such coloring substance is Amplex[®] red (**24**).⁵⁴

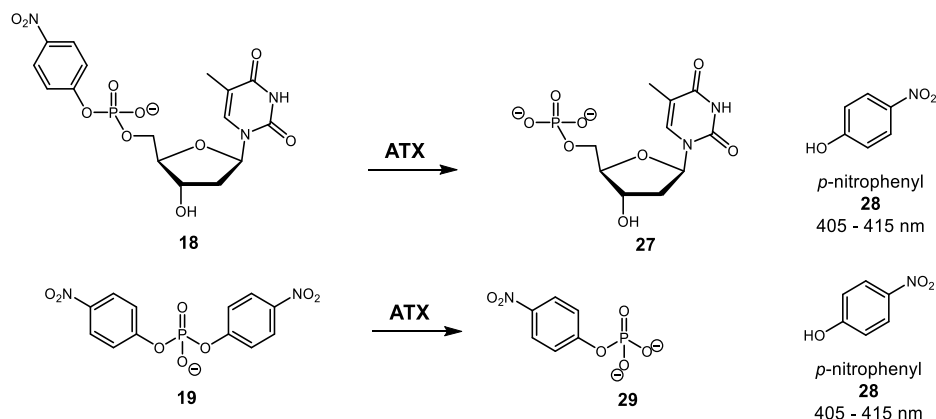


Scheme 7: Mechanism of LPC choline release assay

Even though LPC is the natural substrate and closest to an in cell environment, errors can occur in this assay. This can be the case if the ATX inhibitors being screened are active against the choline oxidase or horseradish peroxidase enzymes, or if the compounds react directly with the hydrogen peroxide being measured.⁵⁴

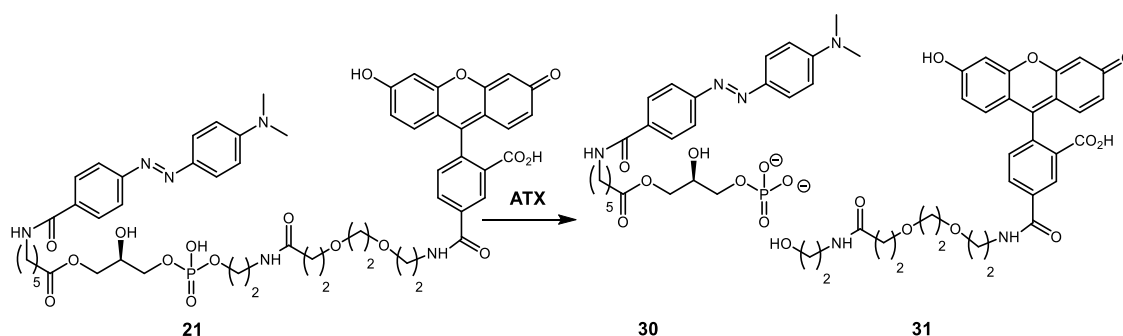
Competitive inhibition of ATX catalytic site can also be measured by the rate of hydrolysis of unnatural substrates *p*-nitrophenyl thymidine 5'-monophosphate (*p*NP-TMP) and bis (*p*-nitrophenyl) phosphate (bis-*p*NPP). ATX has the ability to hydrolyse nucleotides like other members of the ENPP family, however, it is not a

natural substrate of ATX. Both *p*NP-TMP and bis-*p*NPP when hydrolysed by ATX release 4-nitrophenol, which is readily detected using colorimetry with an absorbance of 405 - 415 nm (Scheme 8).



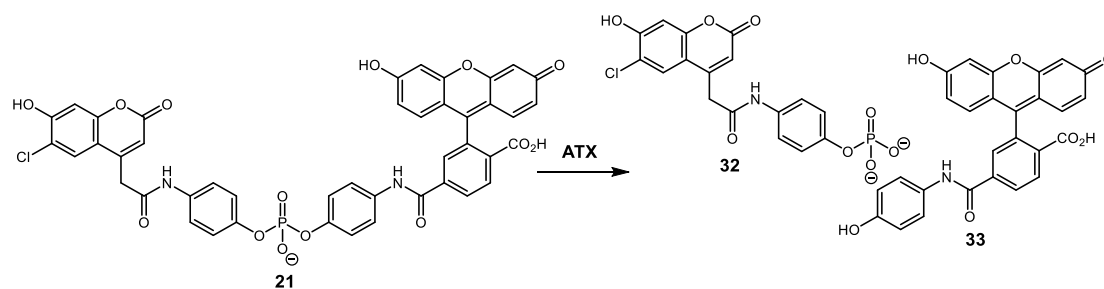
Scheme 8: Mechanism of *p*NP-TMP **18** and bis-*p*NPP **19** assay

Inhibition of the hydrophobic pocket of ATX can be measured using the natural substrate LPC assay as described previously and artificial substrates: “fluorogenic substrate 3” (FS-3) (**20**) and “coumarin fluorescein phosphodiesterase 4” (CPF4) (**21**).^{55,56} Modelling of the FS-3/ATX structure showed that the FS-3 hydrocarbon chain occupies the hydrophobic pocket and the phosphate portion of the molecule extends into the active site. As a result, compounds which bind in the hydrophobic pocket would be expected to inhibit cleavage of FS-3 (**20**). FS-3 (**20**) consists of an intermolecular quencher which is removed when ATX hydrolysis the substrate and thus the product becomes fluorescent (Scheme 9).⁵⁵



Scheme 9: Mechanism of FS-3 **20**

CPF4 (**21**) produces fluorescence prior to hydrolysis due to a Förster fluorescence resonance energy transfer (FRET). After hydrolysis of CPF4 (**21**) by ATX the FRET pair is separated thus the fluorescence is quenched, providing a sensitive readout for ATX activity (Scheme 10).⁵⁶



Scheme 10: Mechanism of CPF4 **21**

As described earlier, ATX contains a putative secondary LPA-binding site, which has also been identified as a hydrophobic channel.⁴⁰ Inhibitors that display a non-competitive mode of inhibition can be measured using the LPC assay.

The literature shows significant differences in the level of ATX inhibition exhibited between assay formats depending on the substrate utilised. Consequently attention is required when using non-native substrates to report ATX inhibition profiles, as they may not accurately reflect inhibition of native LPC substrates.

1.3.3 ATX Inhibitors

ATX is an interesting target for a plethora of disease states and conditions through modulation of multiple signalling pathways involving LPA (**6**). Moreover, inhibition of ATX leads to a reduction in LPA (**6**) production, blocking the signalling pathway that ultimately drives IPF. Encouragingly ATX is an easily accessible serum derived enzyme which sits upstream in defective signalling cascades and due to this several academic groups and pharmaceutical companies have targeted ATX in recent years. Conversely, ATX may be difficult to inhibit using small molecules due to its large, flexible and lipophilic active site and consequently no ATX inhibitor has reached the market. Despite this, significant effort has been invested in the identification of the ATX inhibitors.

1.3.3.1 Lipid Analogues Inhibitors

In 2005 identified LPA (**6**) as a negative feedback inhibitor of ATX.⁵⁷ This finding suggested that the first generation ATX inhibitors could be lipid analogues of LPA. The first patent describing ATX lipid-like inhibitors to treat cancer appeared in 2006.⁵⁸ These were described as acetal phosphate analogues (**34**) (Figure 13). The next series reported was phosphonate analogues as anti-cancer agents (**35**, **36**) (Figure 13). Structurally they were α -substituted methylene phosphonate analogues

of LPA (**6**), in which the CH_2 moiety was replaced with CHCl or CHBr .⁵⁹ They found syn- and anti- diastereomers of α -bromophosphonates (BrP-LPA) (**36**) to be pan-LPA₁₋₃ antagonists and nanomolar inhibitors of ATX.⁶⁰ Even though these inhibitors showed promising activity these lipid analogues are likely to have poor oral bioavailability as they are highly lipophilic molecules. They also possess high number rotational bonds and are rapidly degraded by hydrolytic pathways. Due to these limiting factors and potential for the LPA analogues to act as LPAR agonists, the approaches towards ATX inhibition focused on the synthesis of smaller drug like molecules.



Figure 13: First in class ATX inhibitors, phosphate and phosphonate analogues.⁶¹

1.3.3.2 Small Molecule Inhibitors of ATX

Numerous studies have recently been undertaken to evaluate new classes of ATX inhibitors which can be grouped as metal chelators and nonlipid small molecules. In 2008, prior to the ATX structure being resolved the first virtual screen for ATX inhibitors led to the discovery of H2L-7905958 (**37**) (K_i 1.9 μM , FS-3) (Figure 14).⁶¹ This pyrimidine structure was classed by its originators as a competitive ATX inhibitor. The oxocarboxylate functional group was expected to interact favorably with the active site zinc ions within the catalytic site of ATX.⁶²

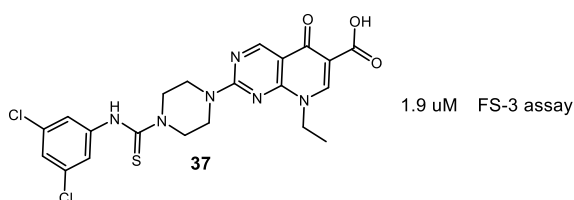


Figure 14: H2L-7905958 **37** ATX inhibitor

Following on from this work in 2010 40000 small molecules were screened and thiazolidinediones derivatives were identified as ATX inhibitors.⁶³ Development of a structure-activity relationship (SAR) in the thiazolidinedione-based series led to a boronic acid moiety, HA-155 (IC_{50} = 5.7 nM, LPC) (Figure 15).⁶⁴ The crystal structure of ATX in complex with HA-155 (**38**) revealed that it forms a reversible covalent bond with the threonine oxygen nucleophile in the ATX active site (Figure 15).⁶⁵

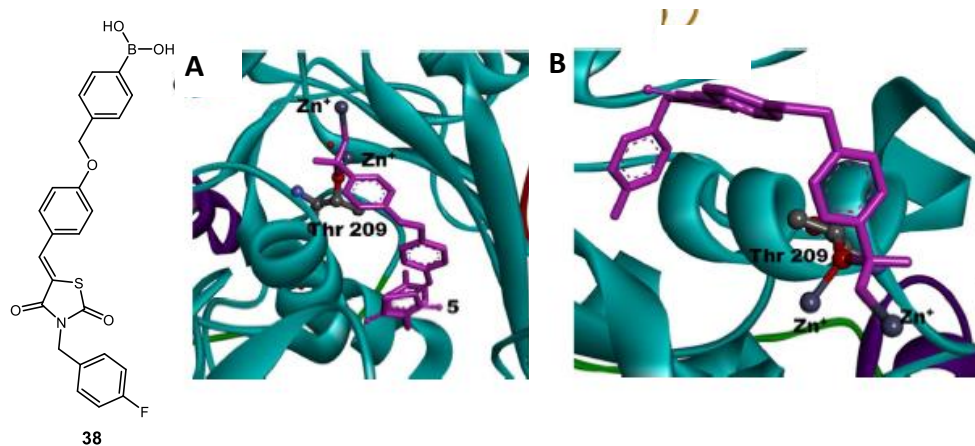


Figure 15: HA155 **38** .A. and B. Co-crystal of HA155 **38** within the catalytic site of ATX.⁶⁶

Subsequently, Merck KGaA claimed a number of piperidine and piperazine derivatives as ATX inhibitors.⁶⁷ From this patent, a key benzoxazolone derivative PF-8380 (**39**) emerged (Figure 15). In 2010 PF-8380 (**39**) was characterised by Pfizer with reported IC_{50} values of 1.7 nM in an isolated LPC enzyme assay and 101 nM in human whole blood assay.⁶³ *In vivo* studies showed an oral dose of PF-8380 (**39**) at 30 mg/kg caused > 95% reduction of rat plasma and air pouch LPA within 3 h.⁶⁴ PF-8380 (**39**) was the most potent ATX inhibitor in the literature at that time.

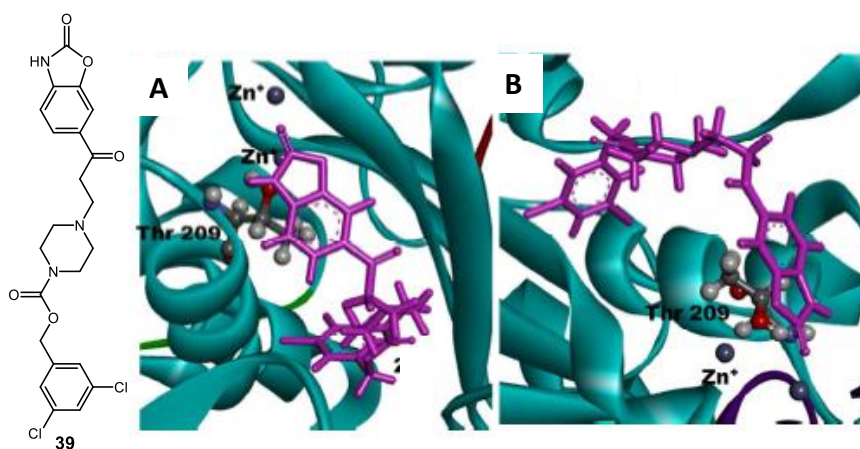


Figure 16: PF-8380 (**39**) A. and B. PF-8380 (**39**) docked within the catalytic site of ATX.⁶⁶

Consequently the patent literature was greatly influenced by HA155 (**38**) and PF-8380 (**39**). Both comprised of an acidic head group or warhead, core spacer moiety and lipophilic tail. These compounds are long linear flexible structures, similar to LPC (**7**) and LPA (**6**) and their flexibility may aid accommodation in the lipid binding site or hydrophobic pocket. The low nanomolar activity of both compounds prompted the next generation of patented ATX inhibitors to retain this

lipid-like structural layout. It is assumed this lipid-like small molecule structural layout acts in a competitive inhibition mode in the ATX active site. Multiple patent applications have been published by pharmaceutical companies, for example Eli Lilly (WO2014/143583A1)⁶⁹, Novartis (US2014/071404A1)⁷⁰, and Hoffmann La Roche (WO2014/048865A1)⁷¹ mimicking this lipid-like layout (Figure 17).

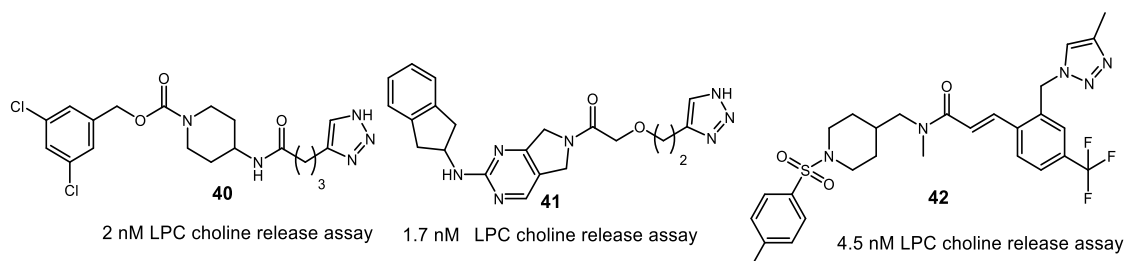


Figure 17: Exemplars from recent ATX patent application exhibiting a lipid-like layout

Additional ATX inhibitors have emerged in the literature that represent more distinct chemotypes from the lipid-like small molecule chemotype previously discussed. The structure of these compounds are, in general, less flexible, often have no apparent zinc binder, and contain more aromatic character than the lipid-like small molecules.

Amira Pharmaceuticals claimed substituted indole derivatives as ATX inhibitors,^{72,73} with IC_{50} values below 0.3 μ M (**43**) (LPC assay) (Figure 18). The applications discussed several *in vivo* experiments without reporting the efficacy of the disclosed compounds. A Pfizer patent claimed pyrimidine ATX derivatives with no overt zinc binder, exemplar (**44**) (6 nM, FS-3) (Figure 18).⁷⁴ The binding mode of both the Amira indoles and Pfizer pyrimidines has not been elucidated but it could be postulated that they are non-competitive inhibitors.

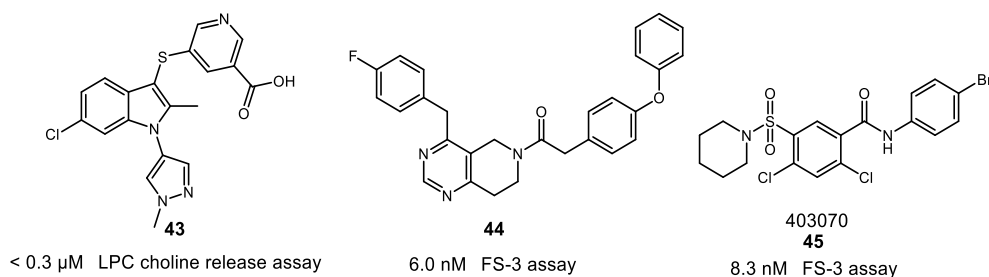


Figure 18: Postulated ATX non-lipid like /non-competitive inhibitors

In 2013, a high throughput screening study described the opportunity of using the hydrophobic pocket of ATX as an inhibitory surface.⁵⁰ The aim was to design a more focused and structurally restricted pharmacophore model binding solely to the hydrophobic binding pocket. This was achieved with a sulfonamide derivative

403070 (**45**) that displayed 8.3 nM inhibition of ATX in the FS-3 assay (Figure 18).⁷⁵ Docking studies were performed by the researchers and it was observed that the sulfonamide derivate occupied the ATX hydrophobic pocket without protruding into the catalytic cleft. The halogen occupied space deep in the hydrophobic pocket. Sulfonamide 403070 (**45**) was also found to be inactive in the *p*NP-TMP hydrolysis assay, further evidence that the compound binds in the hydrophobic pocket of ATX remote from the catalytic site.

In 2015, Pharmakea Therapeutics succeeded in co-crystallising various indole inhibitors with ATX, PAT-078 (**46**) (>0.5 μ M LPC) is an exemplar from this work. PAT-078 (**46**) was found to bind deep in the hydrophobic pocket of ATX, partially occluding the LPA (**6**) and LPC (**7**) hydrophobic binding site. This binding prevents substrate accessing the competitive site. Unlike the competitive inhibitor HA155 (**38**), which coordinates to zinc, PAT-078 (**46**) does not extend far enough to interact with the active site zinc atoms (Figure 19).⁷⁶

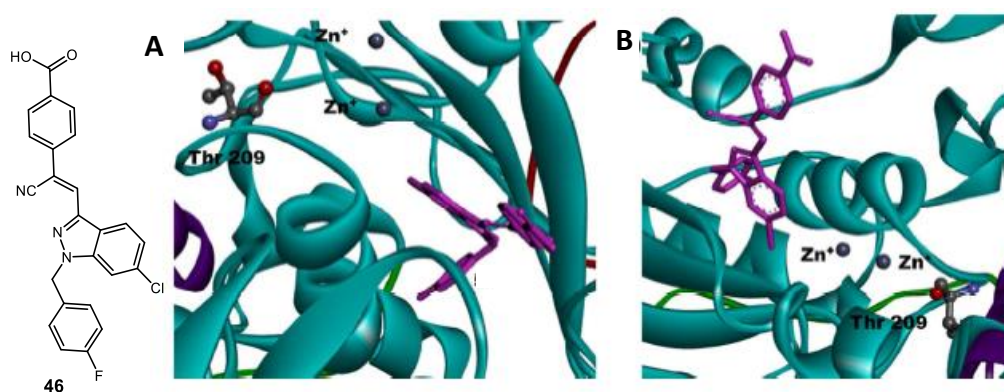


Figure 19: PAT-078 **46** A. and B. Co-crystal of PAT-078 **46** within ATX remote from the catalytic site.⁶⁶

The equivalent IC_{50} values of hydrophobic pocket, allosteric binders, and catalytic site inhibitors suggest that multiple inhibition modes of ATX are sufficient to disrupt the ATX-LPA signalling axis. It remains to be seen which binding mode will ultimately provide the most tractable compounds, however, multiple binding modes afford significant opportunities in the design of ATX inhibitors going forward.

1.3.3.3 ATX Clinical Compounds

As a result of the intensive drug discovery efforts towards identifying potent and selective ATX inhibitors currently, two separate and chemically distinct compounds have reached clinical trials; X-165 and GLPG1690. The structures of X-165 and

GLPG1690 are undisclosed. X-165 originated from a patent of substituted spirocycles, exemplar (**47**) (Figure 20)⁷⁷. GLPG1690 originated from a patent of derivatised imidazo[1,2-*a*]pyridine analogues, exemplar (**48**) (Figure 20).⁷⁸

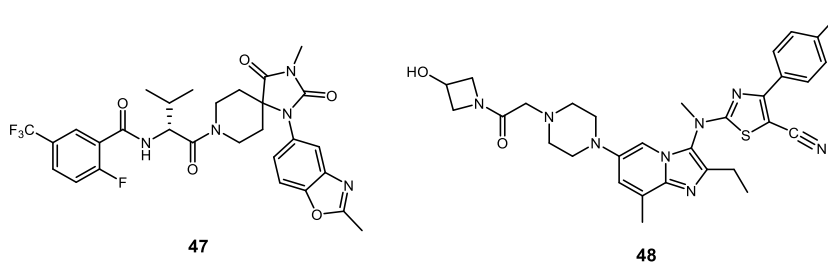


Figure 20: Exemplar structures from X-Rx Discovery Inc and Galapagos patent applications

X-Rx Discovery, Inc. identified X-165 as a potent, oral small molecule inhibitor of ATX with IC₅₀ values of 5.4 and 30 nM in isolated enzyme assays and human whole blood assays, respectively.⁷⁷ X-165 also suppressed both inflammation and fibrosis in animal model of bleomycin-induced fibrosis.⁷⁹ X-Rx Discovery, Inc then partnered with Gilead Sciences in 2015 to bring X-165 forward for clinical trials, of which results are pending.

The second clinical candidate, GLPG1690, is an ATX inhibitor discovered by Galapagos, with potential application for IPF treatment. In a phase two study in healthy human volunteers, GLPG1690 demonstrated favourable safety, tolerability and target engagement. Galapagos has decided to precede with a phase two clinical trials to test the efficiency of this oral formulation of GLPG1690 in patients with IPF.⁸⁰

This encouraging data suggests that there is significant promise in the development of ATX inhibitors for the treatment of IPF. Having stated this, only a paucity of compounds have entered clinical trials, underlining the need to develop new compounds in this therapy area.

2 Chapter 2: Project Aims

2.1 Lead Discovery Approach

Two of the most important steps in developing a new drug molecule for a particular disease are target identification and validation. Extensive literature evidence has implicated both LPA and ATX activity to be upregulated in the pathogenesis of fibrosis, and as a result a plethora of LPAR antagonists and ATX inhibitors have emerged. Hence, both the LPAR and ATX have been identified and validated as targets for the treatment of fibrosis. The LPA₁ antagonist AM095 (**16**) and ATX inhibitor PF-8380 (**39**), as discussed in Sections 1.2.2, and 1.3.3.2 respectively, are two of the most potent and selective known lead compounds in the general area of fibrosis.

Despite the relatively advanced nature of AM095 (**16**) and PF-8380 (**39**), they exhibit sub-optimal physicochemical properties for hit or lead compounds. Specifically, high molecular weight and lipophilicity, which are two factors associated with attrition in drug development.⁸¹ JChem⁸², a data analytics, reporting, and integration program for cheminformatics tasks was used to calculate standard molecular properties of AM095 (**16**) and PF-8380 (**39**) (Table 3).

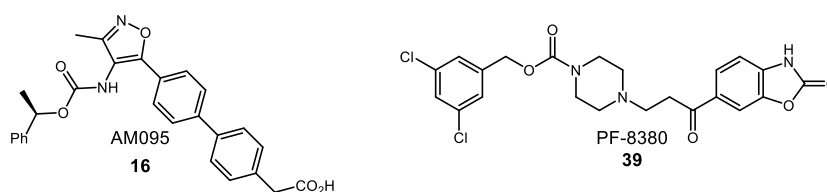


Table 3: Predicted physicochemical properties of AM095 (**16**) and PF8380 (**39**)

Entry	Cpd	MW ^a	PSA ^b	cLogP	HBD ^c	HBA ^d	#AR ^e
1	AM095 (16)	456.5	104.5	5.3	2	8	4
2	PF-8380 (39)	478.3	88.2	3.6	1	6	3

^a molecular weight (MW), ^b polar surface area (PSA), ^c hydrogen bond donor (HBD),
^d hydrogen bond acceptor (HBA), ^e number of aromatic rings (#AR)

Using AM095 (**16**) and PF-8380 (**39**) as a basis for further optimisation efforts would likely see an increase in molecular weight as analysis of recent trends reveals that the molecular weight of a molecule increases through the lead optimisation process.⁸³ This increase in molecular weight has been strongly correlated to attrition

in clinical development.⁸³ Accordingly, the current study aims to use AM095 (**16**) and PF-8380 (**39**) as starting points, to identify a lead compound with a lower molecular weight than the parent compounds, whilst maintaining chemical features which are important for respective activity. The reduced complexity lead starting point may offer a greater chance of ultimately obtaining a successful clinical candidate.

2.2 Overall Project Aims

The chemical structures of AM095 (**16**) and PF-8380 (**39**) are useful platforms in a lead discovery effort for identifying new chemical entities towards IPF treatment due to their precedented activity. The overall aims were to:

- i) use AM095 (**16**) and PF-8380 (**39**) as starting points and pursue chemical modifications and develop SAR studies of these templates
- ii) measure physicochemical parameters of selective analogues, specifically monitoring molecular weight and lipophilicity
- iii) test the analogues in pathway relevant biological assays to ultimately identify novel lead series with overall improved physicochemical profiles.

Consequently, testing a series of novel compounds against the validated targets, LPA₁ and ATX may ultimately furnish compounds with potential as future treatments for IPF.

3 Chapter 3: Cross Screening Approach Towards New Leads for IPF Treatment

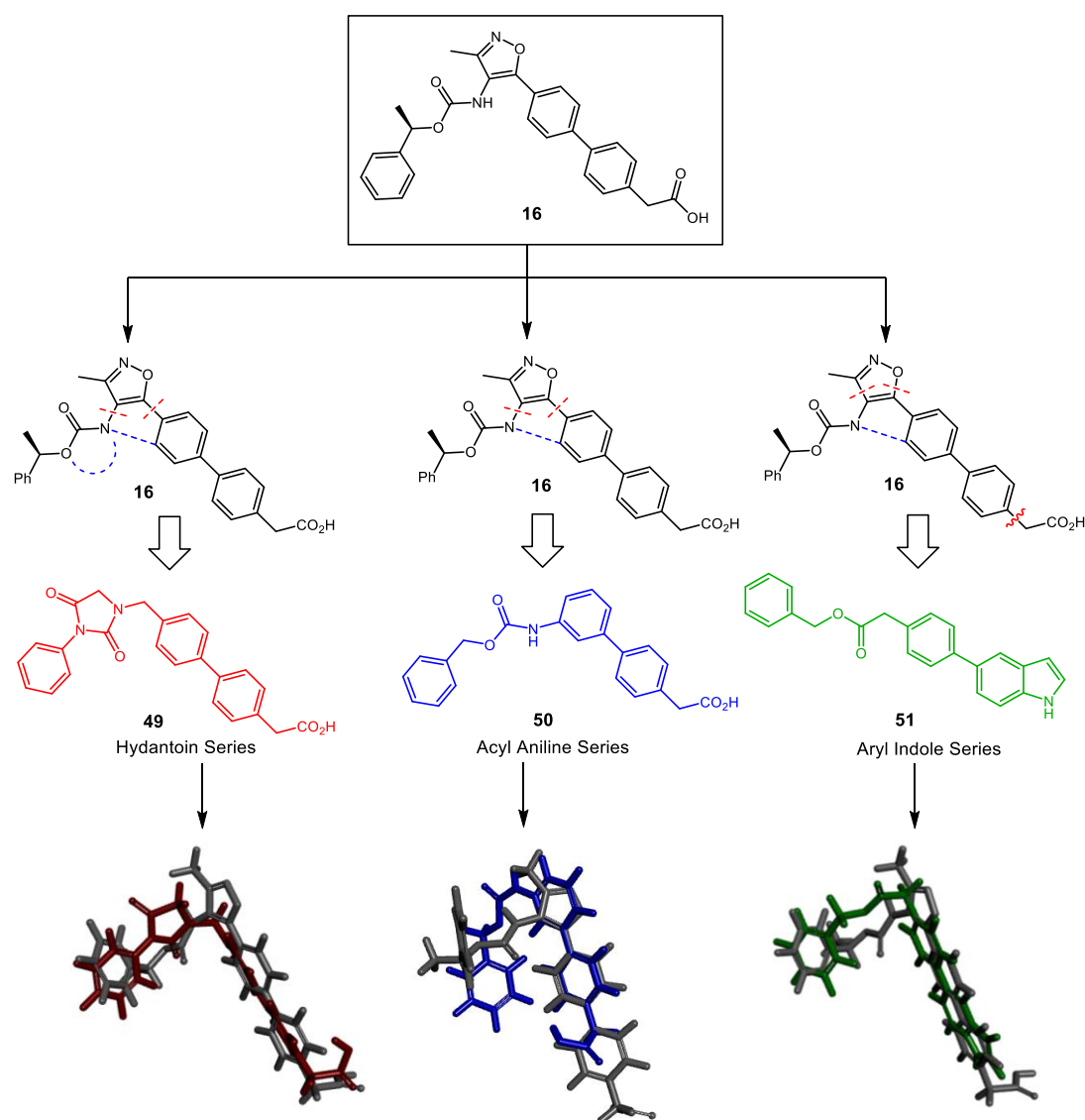
3.1 Design Strategy

AM095 is a potent and selective LPA₁ receptor antagonist which displays an IC₅₀ value of 0.98 μM for recombinant human LPA₁, and demonstrates antifibrotic activity in rodent models.³⁹ Based on the potential role of LPA₁ in a plethora of disease states, including fibrosis, AM095 (**16**) has become a noteworthy compound in this area of research. Using AM095 (**16**), as a starting point, a new lead chemotype was targeted towards LPA₁ receptor antagonism which would offer potentially improved physicochemical properties. In particular, lower molecular weight and lower cLogP were highly desirable. This lead discovery is a well validated approach as a 2002 study revealed that the majority of launched drugs were derived by modification of known drug structures or structures obtained from the scientific literature.⁸⁴ Furthermore, less complex molecules are more common starting points for the discovery of drugs.⁸⁵

Biological crosstalk refers to incidences in which a component of one signal transduction pathway affects another component.⁸⁶ Crosstalk between LPA (**6**) and ATX has been studied, and LPA (**6**) has been observed as a negative feedback inhibitor of ATX.⁵⁷ Furthermore, inhibition of both pathways has been reported in the literature using synthetic molecules which are pan-LPA₁₋₃ antagonists/nanomolar ATX inhibitors, discussed in Section 1.3.3.1. This similarity in endogenous substrates might indicate commonality in the binding site in both LPA receptor and ATX. Therefore, it was of interest to conduct cross-screening of the designed LPA₁ antagonists in the upstream target ATX, to fully investigate all potential inhibitory activity in the ATX-LPA pathway.

The medicinal chemistry strategy implemented for hit identification was a scaffold hopping approach from pharmacophores represented by AM095 (**16**). A series of ideas were generated in order to mimic the pharmacophoric features displayed by AM095 (**16**). To this end, three unique series were designed by performing simple disconnections to give the hydantoin series, acyl aniline series, and the aryl indole series. The three series possess a similar skeletal backbone to AM095 (**16**) but with potentially lower molecular weight and clogP. The aim of the three series was to design a reduced complexity (lead-like) library using simple synthetic handles

available for chemical synthesis.⁸⁷ In order to qualitatively assess the level of similarity between AM095 (**16**) and the three proposed series, a range of overlays was prepared using energy minimized structures of AM095 (**16**) and an exemplar from each series. It was hypothesised that an efficient overlap between the target compounds and AM095 (**16**) may be indicative of a similar binding mode. These novel heterocyclic biaryl compounds could potentially provide selectivity toward the LPA₁ receptor or ATX enzyme inhibition. Based on the conformational analysis, all compounds demonstrated a reasonable degree of overlap with AM095 (**16**) (Scheme 11). Accordingly, these templates were prioritised for synthesis in order to validate their biological properties against both LPA₁ and ATX.



Scheme 11: Schematic representation of the three proposed series from disconnecting AM095 (**16**) and their corresponding overlays with AM095 (**16**) (grey)

3.1.1 Controlling Molecular Weight

A set of parameters, Lipinski's rule of five have been defined to evaluate druglikeness of a compound. In these guidelines, Lipinski states that a potential drug candidate's molecular weight must be below 500 Da.³⁴ More recently, a set of simple, interpretable of rules for the absorption, distribution, metabolism, excretion, and toxicity (ADMET) for pharmaceutical agents was generated known as Gleeson's rules.⁸⁸ In these revised parameters, a molecular weight less than 400 Da was proposed for optimum drug absorption and distribution.⁸⁸ Both sets of guidelines have been widely adopted by medicinal chemists since their proposal. In relation to Lipinski's rule of five and Gleeson's rules, AM095 (**16**) is relatively large with a molecular weight of 456.5 Da, potentially indicating issues later in development.

Drug oral bioavailability, a measurement of the rate and extent to which a drug reaches the systemic circulation, is a complex pharmacokinetic (PK) parameter that is correlated to solubility and permeability.⁸⁸ AM095 (**16**) was found to have an oral bioavailability approximately of 100% in rat.³⁹ This good rat oral bioavailability profile of AM095 (**16**) may not however correspond to human oral bioavailability. It has been reported, due to the different expression levels for metabolizing enzymes between rat and human, a rat model cannot always reliably predict oral bioavailability in human.⁸⁹ Through the study of a number of key ADMET assays run within GlaxoSmithKline (GSK), it has been reported that molecular weight plays an important role in the extent of bioavailability in human.⁸⁸ From this work it was found that compounds with a molecular weight greater than 400 Da have lower bioavailability than with a molecular weight lower than 400 Da.⁸⁸ Therefore with molecular weight values of 456.5 Da for AM095 (**16**) it is likely that future lead compounds derived from this compound would likely have sub-optimum absorption, distribution and oral availability in accordance with Gleeson's rules. Accordingly, it was rationalised that a novel lead compound with a smaller weight in accordance with Gleeson's rules has a greater chance of achieving bioavailability in humans.

It has been reported that as the molecular weight of a molecule increases, solubility on average decreases and this parallels much of the reported literature.^{90,34} Molecular weight has also been shown to have a high correlation with membrane permeability. As the molecular weight of a particular chemotype increases, membrane permeability on average decreases.⁸⁸ The emphasis placed on

molecular weight through ADMET studies validates the importance of finding a lead compound with a lower molecular weight than the AM095 (**16**) system.

3.1.2 Tuning cLogP and Lipophilicity

The calculated LogP (cLogP) (calculated 1-octanol–water partition coefficient) property of a compound essentially reflects the key event of molecular desolvation in transfer from aqueous phases to cell membranes and to protein binding sites, which are mostly hydrophobic in nature.⁸³ High lipophilicity increases the likelihood of binding to multiple targets, resulting in pharmacologically based toxicology and furthermore attrition in drug development.⁸³ It has also been found that as lipophilicity increases, solubility on average decreases.⁸⁸ For these reasons cLogP has been proposed as the most important drug-like physical property.⁸³ Gleeson's rules proposed optimised physicochemical parameters in relation to cLogP, which is stated should be less than 4. The JChem⁸² predicted value for cLogP of AM095 (**16**) is 5.3, significantly above the proposed optimum of 4. Therefore this hit-to-lead optimisation approach will closely monitor the cLogP values of novel chemotypes that emerge from this work. Indeed, lipophilicity tends to increase during optimisation, so again identifying a reduced complexity starting point is a worthwhile approach.

Drug discovery has become increasingly difficult in the last few decades as a result of extra development hurdles placed in the path of pharmaceutical research programmes. The pharmaceutical industry has reacted to the changes in the development process by profiling molecules of interest earlier and more extensively using *in vitro* and *in silico* methods.⁸⁸ Taking this into consideration, all designed compounds were profiled using JChem⁸² software for their standard molecular properties. Allied to profiling and molecular modelling, key developability data such as solubility and permeability was generated for selected compounds. Access to these high throughput physicochemical measurements was possible *via* an industrial partnership with GSK.

3.1.3 Removal of the Aminoisoxazole

As discussed in previously, almost all ADMET parameters deteriorate with increasing molecular weight.⁸⁸ In a related study, replacement of the AM095 (**16**) aminoisoxazole was investigated by Hoffmann-La Roche with a series of *N*-methylpyrazole (**52**), *N*-aryltriazole (**53**), and *N*-methyltriazole (**54**) analogues

(Figure 21).¹² These researchers found each heterocyclic series to be active LPAR antagonists. Without any structural data of the LPA₁ receptor available at time of design it was reasoned from the Hoffmann-La Roche study that the aminoisoxazole was an unessential spacer moiety, and its removal may still retain LPA₁ activity/ATX inhibition whilst improving physicochemical properties. The principle modification of the AM095 (**16**) entity in the current study was removal of the large aminoisoxazole moiety with the goal of lowering the molecular weight of the three series, and reducing aromatic ring count (*vide infra*).

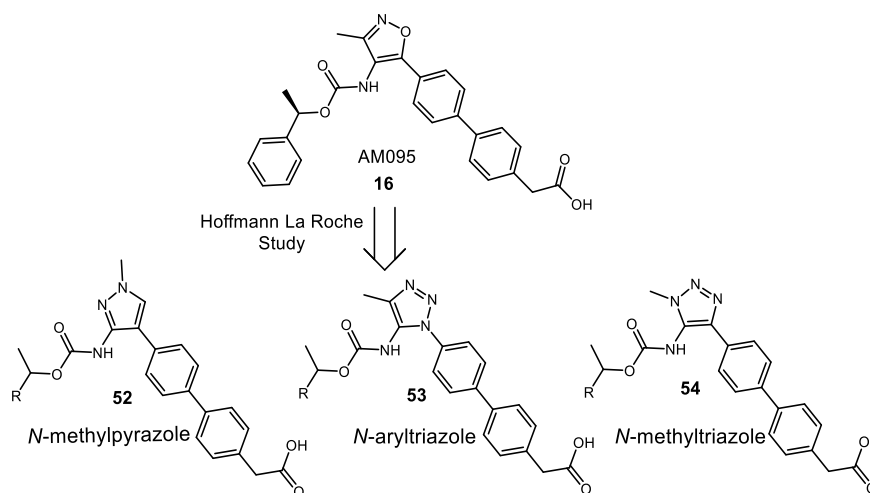


Figure 21: *N*-methylpyrazole **52**, *N*-aryltriazole **53**, and *N*-methyltriazole **54** analogues

3.1.4 Conservation of the Biaryl Unit

The physicochemical literature to date suggests that greater than three aromatic rings in a molecule correlates with poorer compound developability, thus an increased risk of attrition in development.⁸¹ Accordingly, the three novel series were designed with either two or three aromatic rings, further supporting the proposal to remove the putative isoxazole spacer. The greatest contribution toward cLogP in each series is the biaryl fragment. Conversely, conservation of the biaryl unit would likely be an acceptable strategy from the perspective of generating biological activity. Biaryl motifs represent a class of privileged structures, a term used to describe a single molecular framework able to provide ligands for diverse receptors.⁹¹ Indeed, a wide range of different pharmaceuticals including antiemetic, antifungal, anti-infective, antihypercholesteremic, anti-inflammatory antithrombotic, and antiarrhythmic components contain this motif.⁹² The fact that such activity is observed from an apparently simple structure can be readily explained through consideration of drug binding and ease of synthesis.

Interactions involved in ligand- receptor binding are often dominated through hydrophobic and aromatic binding. As aromatic groups are capable of participating in polar (e.g. π -cation interactions) and π - π stacking at receptor binding sites. Additionally, aromatic rings possess fewer degrees of freedom than chains. This generally increases the ligand-receptor binding energy (by reducing the entropy term), thus leading to increased compound potency.⁸¹

The prevalence of aromatic and heteroaromatic rings in drug molecules is also strongly allied with the fact that the chemical methodology available to assemble aryl-aryl systems is very extensive. In synthetic chemistry, a number of transformations exist to enable the synthesis of the biaryl unit in a highly robust fashion. These include Ullman, Suzuki, Stille and Negishi coupling processes.⁹³ The robustness of these transformations, combined with the ready commercial availability of building blocks make aryl-aryl couplings particularly attractive for use in drug discovery programmes.⁸¹ Combining the pharmacology aspects of the motif with the numerous and well validated synthetic processes, the biaryl unit can be considered eminently tractable, justifying its retention in the current inhibitor design.

3.1.5 Investigation of the Acetic Acid Moiety

A carboxylic acid in the para position of the biaryl unit is present in various generations of LPA receptor antagonists, Ki16425 (**15**), AM095 (**16**) and the Hoffmann-La Roche asset (**17**). This implies that an acetic acid moiety is an important functional group for drug-receptor interaction. From the Hoffmann-La Roche bioisostere approach based on AM095 (**16**), a non-carboxylic acid derivative demonstrated reasonable potency in proliferation assays.¹² In relation to the design strategy in this current study, it was aimed to probe the requirement of this acid in all three novel series and examine the position of the acetic acid moiety within the acyl aniline series.

3.1.6 Hydantoin Series Design

The first series to be identified from the analysis of AM095 (**16**) was the hydantoin based chemotype. Removal of the isoxazole ring and formation of a hydantoin moiety in place of the carbamate moiety in AM095 (**16**) gave a set of novel reduced complexity compounds (Figure 22).

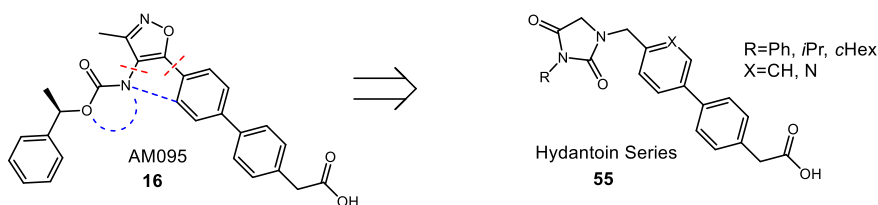


Figure 22: Represented design of hydantoin

The hydantoin is an important structural scaffold found in a number of biologically active compounds and several pharmaceutical molecules. Hydantoin derivatives have been associated with a range of biological activity including anticonvulsant, antimuscarinic, antiviral, and antiepileptic properties.^{94,95,96,97} The biaryl hydantoin designed in this research are discussed below (Figure 23).

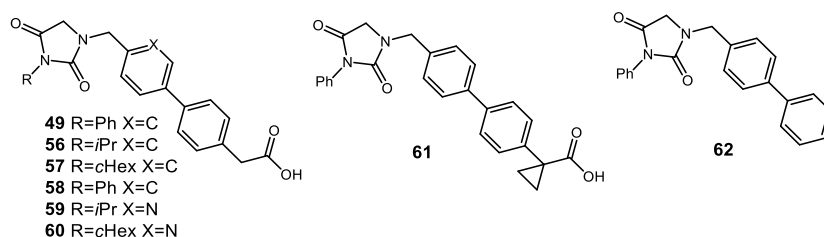


Figure 23: Target hydantoin compounds

Target hydantoin were substituted with either a phenyl (**49**, **58**, **61**, **62**), isopropyl (**56**, **59**) or cyclohexyl moieties (**57**, **60**). The rationale for synthesising hydantoin with different substituents comes from the idea of medicinal chemistry isosteres. Isosteres are defined as compounds or groups that possess near-equal molecular shapes and volumes, approximately the same distribution of electrons, and which exhibit similar physical properties.⁹⁸ The design of bioisosteres introduces structural changes that can be beneficial by improving key pharmacokinetic properties, and maintain the important pharmacophoric structure of the molecule. It was hypothesised that a phenyl, isopropyl or cyclohexyl group on the hydantoin would act as an isostere to the (*R*)-1-phenylethylcarbamate present on AM095 (**16**), acting in an equivalent way in binding to the LPA₁ receptor. Essentially, this would potentially identify compounds with reduced molecular weight and a lower cLogP

than AM095 (**16**). Furthermore, varied substitution off the hydantoin group may allow entry into new chemical space and greater diversity within this chemotype.

The hydantoin series is designed with either two or three aromatic rings in order to regulate cLogP of the novel series, as stated previously. The addition of a heteroatom to an aromatic ring decreases the cLogP of the compound compared to its carbon containing analogue. Recent literature demonstrates the advantage of isosteric -N substitution for -CH in benzene rings, resulting in compounds with lower cLogP.^{81,99} Accordingly, a set of hydantoin with a pyridyl ring system (**58-60**) was designed with the aim of further decreasing the cLogP of the final product.

The cyclopropyl group is a common structural design feature in pharmaceutically active molecules, and it is frequently included in SAR studies. Within the Hoffmann-La Roche LPAR antagonist study a cyclopropanecarboxylic acid derivative (**17**) was found to be the most potent antagonists within the series. Accordingly, the synthesis of a cyclopropanecarboxylic acid hydantoin derivative (**61**) was proposed, as it offers potential for additional receptor drug interactions similar to those observed by the Hoffmann-La Roche study (Figure 24).¹²

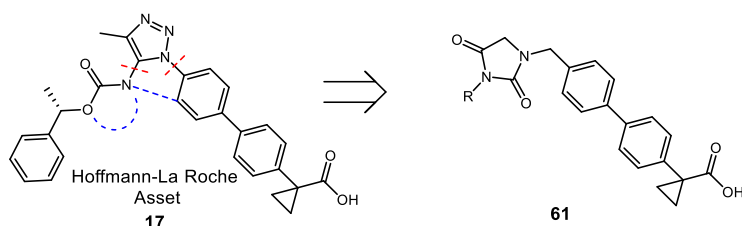
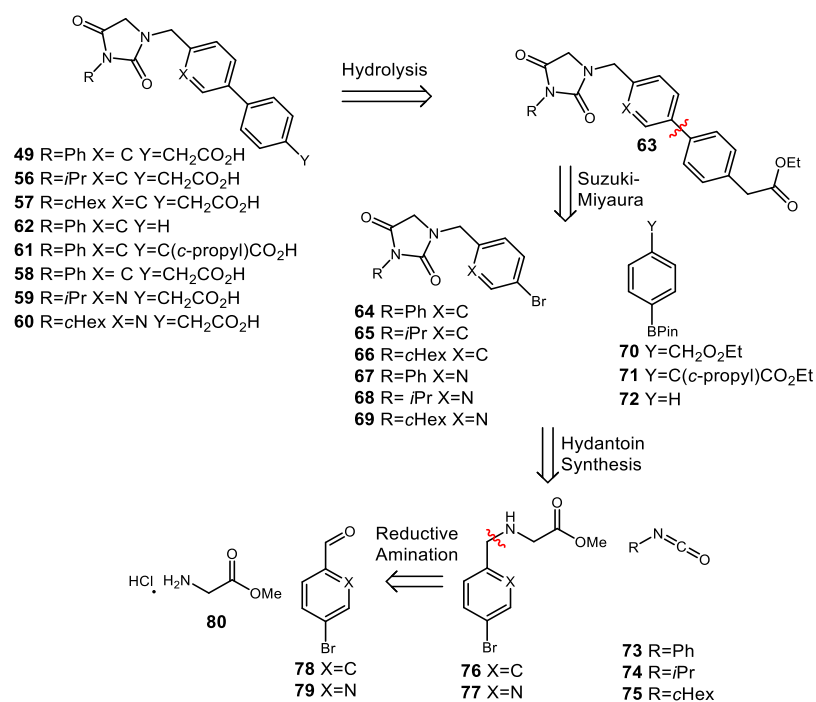


Figure 24: Design strategy of cyclopropanecarboxylic acid hydantoin derivative

In addition, it was desired to explore the role of the carboxylate group in contributing to potency within the series. Based on this a 1,1'-biphenyl hydantoin (**62**) was proposed, which lacked the carboxylate functional group.

3.1.6.1 Synthetic Access to the Hydantoin Series

The hydantoin series was prepared *via* two building blocks: i) benzyl hydantoin, and ii) pyridyl hydantoin. The synthetic route employed in order to access the target compounds was simply three primary steps (reductive amination, hydantoin formation, Suzuki coupling) yielding various substituted hydantoin analogues (Scheme 12).



Scheme 12: Retrosynthetic analysis of the hydantoin series

3.1.7 Acyl Aniline Series Design

The second series to emerge from the analysis of AM095 (**16**) was the acyl aniline chemotype. The aminoisoxazole motif was again removed with direct formation of a C-N bond to form an aniline derivative (**50**) (Figure 25).

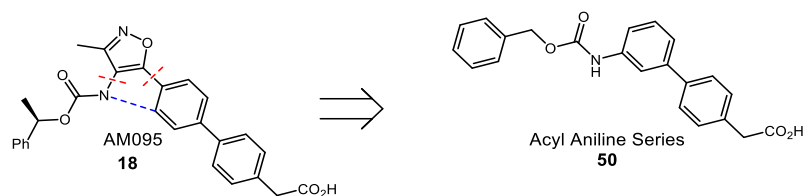


Figure 25: Represented design of the acyl aniline series

Amino aromatics such as anilines may give rise to safety concerns, as many have been shown to have mutagenic properties.¹⁰⁰ The aniline group of the acyl aniline series is however incorporated in a carbamate moiety within the final products. Carbamate-bearing molecules play an important role in modern drug discovery as they display very good chemical and proteolytic stabilities.¹⁰¹ Carbamate compounds are generally capable of permeating cell membranes and they possess a degree of conformational restriction due to the delocalization of non-bonded electrons on nitrogen into the carboxyl moiety.¹⁰¹ In addition, the carboxyl group and the backbone NH can participate in hydrogen bonding, making the carbamate group a

key structural motif in many approved drugs and prodrugs.¹⁰¹ The targeted acyl aniline analogues therefore retain this important moiety (Figure 26).

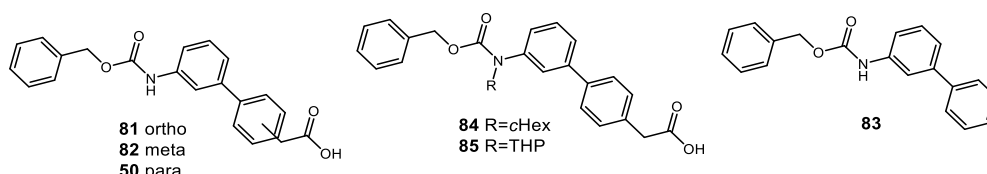


Figure 26: Target acyl aniline compounds

The acyl aniline series also retained the biaryl moiety. It was desired to explore the role and position of the carboxylate group in the acyl aniline series with ortho (**81**), meta (**82**), and para (**50**) acetic acid substituted biaryl analogues, and a benzyl [1,1'-biphenyl]-3-ylcarbamate analogue (**83**). It was also planned to substitute the nitrogen of the aniline with a cyclohexyl group (**84**) and a tetrahydropyran (**85**) group. It was hypothesised that functionalisation on the nitrogen had the potential to mimic the aminoisoxazole group present in AM095 (**16**).

3.1.8 Aryl Indole Series Design

The third series to arise from the analysis of AM095 (**16**) was the aryl indole template. The aminoisoxazole was again removed in order to focus on reduced molecular weight with direct formation of a C-C bond to form an ester moiety. The acetic acid moiety was removed and replaced with an aromatic indole group (Figure 27).

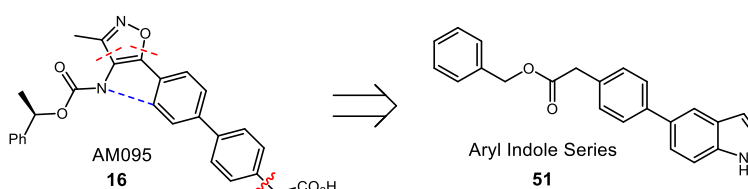


Figure 27: Design of aryl indole series

The aryl indole series was designed to challenge the original design hypothesis, as this palette of compounds do not contain an acetic acid moiety, which had been retained in the series discussed previously. The different functionalities do however retain a reasonable degree of structural overlap with AM095 (**16**), as evidenced by the overlays generated with the two energy minimised structures (Scheme 11).

The indole scaffold again represents an important structural unit in drug discovery, thus is considered a privileged structure in medicinal chemistry. Many GPCRs

possess a conserved binding pocket that is recognized by the indole scaffold in a common complementary binding domain.¹⁰² As a result, a plethora of drugs targeting GPCRs contain an indole substructure, such as indomethacin, ergotamine, frovatriptan, ondansetron, tadalafil, among many others.¹⁰² Additionally, the long linear structures of the indole series have aromatic character could potentially span the hydrophobic pocket of ATX and inhibit the enzyme. Substitution patterns of the target indoles were examined, with the benzyl 2-phenylacetate group in both the 5 (**51**) and 6 (**86**) positions (Figure 28).

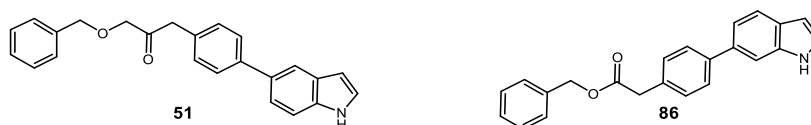


Figure 28: Target aryl indole compounds

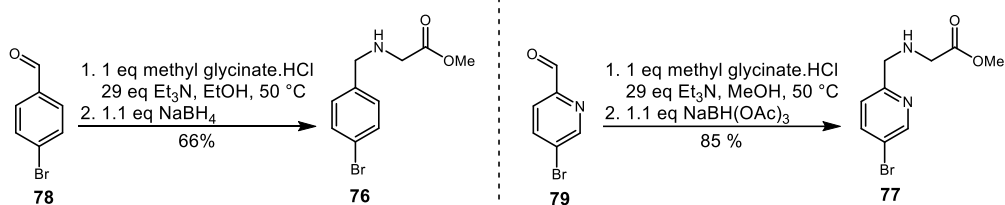
3.1.9 Overall Design Aims

In summary the overall design aims of the three series were to i) remove the isoxazole motif, ii) conserve the biaryl structure, and ii) probe the necessity and position of the acetic acid moiety to form a novel lead chemotype. An additional focus was to monitor physicochemical properties of these novel structures and test their ability to disrupt the ATX-LPA signalling pathway, through biological evaluation at both targets.

3.2 Inhibitor Synthesis

3.2.1 Reductive Amination

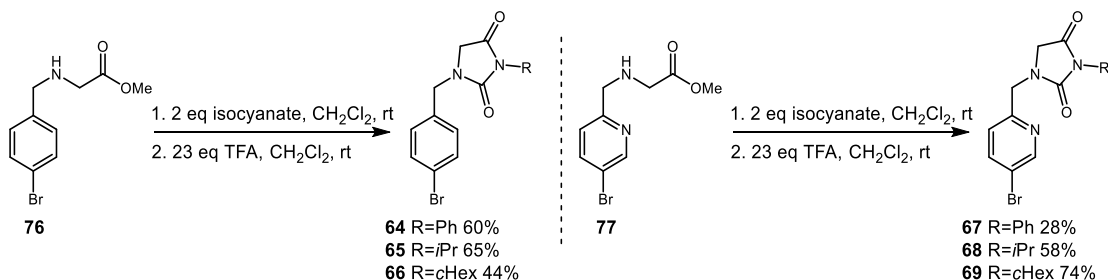
The first step in the synthesis of the hydantoin intermediate library was a reductive amination, a technique developed to alkylate amines (Scheme 13). In this case, the reductive amination consists of two successive reactions; condensation of an amine, methyl glycinate hydrochloride, with either 4-bromobenzaldehyde (**78**) or 5-bromo picolinaldehyde (**79**) to an imine in the presence of a base. This is followed by reduction of the imines to the corresponding amines (**76** and **77**) using either sodium borohydride or sodium triacetoxy borohydride (STAB).



Scheme 13: Reductive amination of 4-bromobenzaldehyde and 5-bromo picolinaldehyde

3.2.2 Hydantoin Core Synthesis

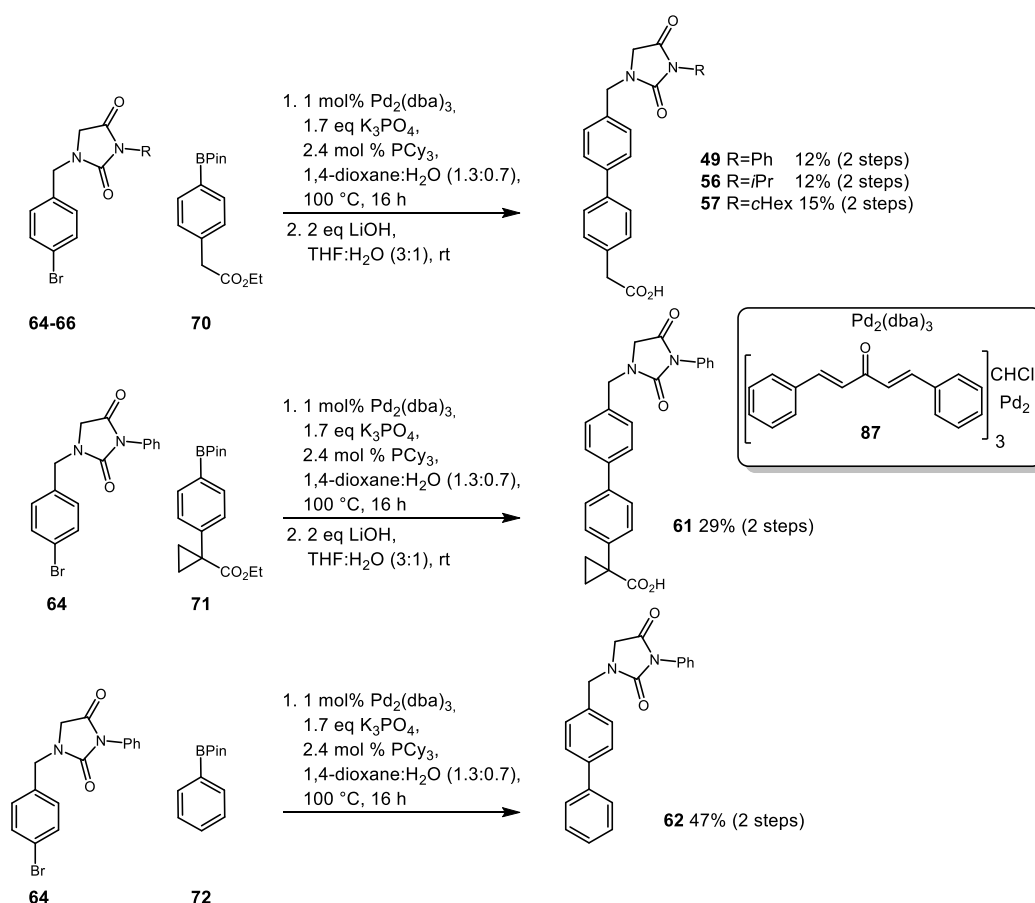
The synthesis followed in the preparation of the target hydantoins involved the reaction of the secondary amines (**76**, **77**) with an appropriate isocyanate system, yielding a urea derivative. This derivative is not isolated but can be efficiently converted to the hydantoin following treatment with a protic acid in this case, trifluoroacetic acid (TFA). This sequence was applied to the synthesis of compounds (**64-69**) (Scheme 14).



Scheme 14: Synthesis of hydantoin compounds **64** and **69**

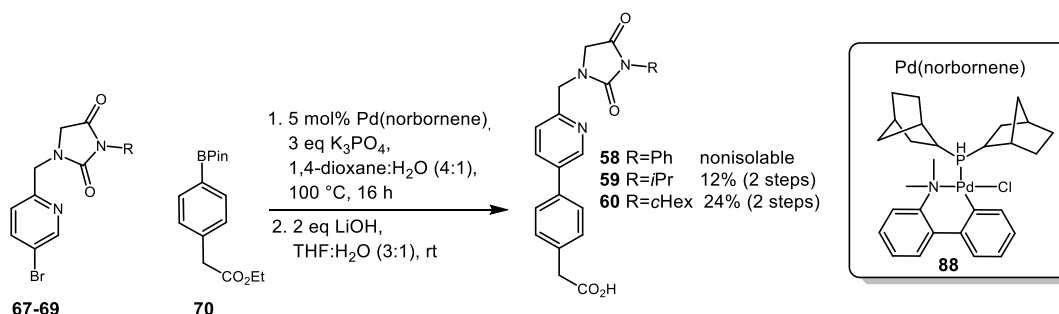
3.2.3 Hydantoin Cross Coupling

After successful generation of the hydantoin cores (**64-66**), construction of the target biaryl system was necessary. One of the most efficient means of achieving aryl-aryl bond formation is through the Suzuki-Miyaura cross-coupling reaction. In the case of the benzyl hydantoins a Suzuki reaction was carried out with 1 mol% loading of the catalyst tris(dibenzylideneacetone)dipalladium(0) ($\text{Pd}_2(\text{dba})_3$, **87**).¹⁰³ Upon workup, a Celite[®] plug was used to remove any residual palladium catalyst contaminating the isolated compounds before the compounds were smoothly converted to the carboxylic acid by base mediated hydrolysis to yield the final biaryl hydantions (**49**, **56**, **57**, **61**) (Scheme 15).



Scheme 15: Suzuki-Miyaura coupling and hydrolysis to products **49**, **56**, **57**, **61**, and **62**

The Suzuki conditions exploited for the benzyl hydantoin cross coupling were trialed in the synthesis of the pyridyl containing biaryl hydantoin. Analysis of the reaction mixture showed complete consumption of starting material however isolation of these structures proved low yielding and problematic in obtaining compounds of required purity. Thus, alternative coupling conditions were employed using 5 mol% 2'-(dimethylamino)-2'-biphenyl-palladium(II)chloride-dinorbornylphosphine (Pd(norbornene), **88**) catalyst system to gain access to the pyridyl containing biaryl hydantoin (**59** and **60**) (Scheme 16).¹⁰⁴



Scheme 16: Suzuki-Miyaura coupling and hydrolysis to products **59** and **60**

It was found that the phenyl substituted pyridyl hydantoin (**58**) could not be isolated to the required level of purity through normal phase column chromatography. Alternative purification techniques were attempted including preparative high performance liquid chromatography (HPLC), however the purity of the phenyl substituted pyridyl hydantoin was unsatisfactory for biological testing.

3.2.4 Acyl Aniline and Aryl Indole Synthesis

Synthesis of the acyl aniline series and aryl indole series were performed by another member of the laboratory.¹⁰⁵ Therefore, the details of the synthetic route undertaken will not be discussed in this thesis.

3.3 Pharmacology

After complete synthesis of the hydantoin, acyl aniline and aryl indole series, four diverse assays were employed to determine their biological activity. The analogues were assessed in a LPA₁ receptor agonism/antagonism signalling assay, the bis-*p*NPP ATX inhibition assay, and a cytotoxicity assay. The physicochemical properties of the analogues were profiled using JChem⁸² and measured using a GSK in-house high throughput physicochemical measurement assay.

3.3.1 LPA₁ Receptor Agonism/Antagonism Signalling Assay

An efficient assay used to explore GPCR biology was available externally from the global life sciences company DiscoverX. Of relevance to LPAR research is the DiscoverX PathHunter[®] β -arrestin cell line assay using cells overexpressing LPA₁ receptors.¹⁰⁶ The PathHunter[®] β -Arrestin GPCR assay is a whole cell functional assay that directly measures LPA₁ activity by detecting the interaction of β -arrestin with activated LPA₁ (Figure 29).

In this system, the LPA₁ is fused with a small enzyme fragment called ProLink[™] (a fragment of β -galactosidase). The fused LPA₁ is co-expressed with β -arrestin and an enzyme acceptor (complementing fragment of β -galactosidase.) On activation, the LPAR is phosphorylated, providing a binding site for β -arrestin. The interaction of β -arrestin and the LPAR forces the interaction of ProLink[™] and the enzyme acceptor, thus complementing the two β -galactosidase enzyme fragments. This binding results in the formation of an active β -galactosidase enzyme. The β -galactosidase enzyme is capable of hydrolyzing a substrate and generating a

chemiluminescent signal which are detected using PathHunter[®] Detection Reagents. The chemiluminescent signals are measured on a luminometer to give an accurate indication if the test compounds agonise or antagonise the LPA receptor.¹⁰⁷

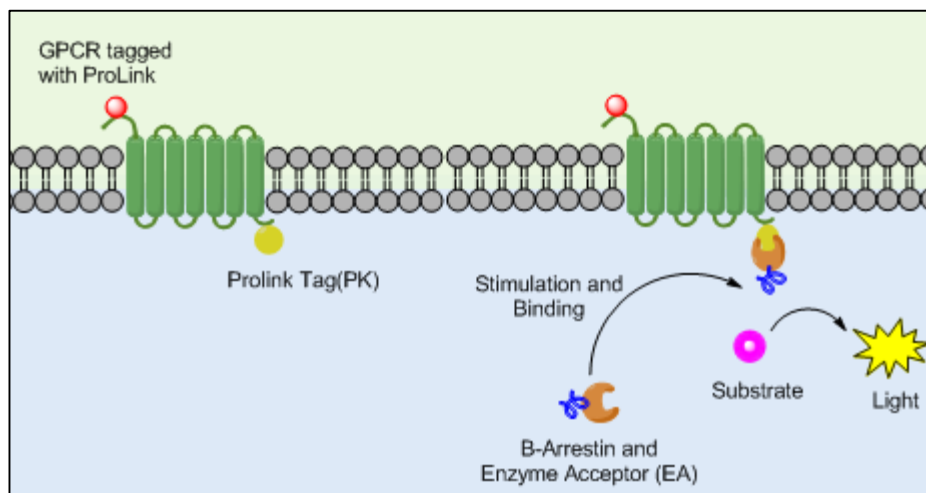
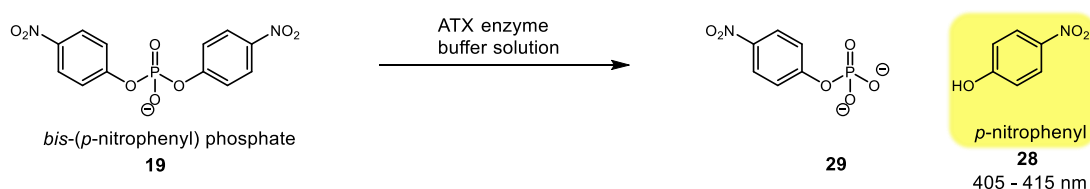


Figure 29: PathHunter[®] β -Arrestin GPCR assays

The synthesised compounds were evaluated for both LPA₁ receptor agonism and antagonism using a CHO-K1 EDG2 β -arrestin cell line in a single dose format (10 μ M). 1-oleoyl-LPA (**6**) was included as a positive agonist control. AM095 (**16**), and Ki16425 (**15**) were included as positive antagonist controls. The data obtained from the assay are described in terms of percentage of agonism where 100% refers to complete agonism and 0% refers to complete antagonism.

3.3.2 Bis-*p*NPP ATX Inhibition Assay

In parallel to the PathHunter[®] β -Arrestin GPCR assay, the three novel series, AM095 (**16**) and Ki16245 (**15**) were evaluated for ATX inhibitory activity in the bis-*p*NPP assay. Bis-*p*NPP (**19**) when hydrolysed by ATX releases 4-nitrophenol (**28**), which is readily detected using colorimetry with an absorbance of 405 nm (Scheme 17). The known ATX inhibitor PF-8380 (**39**) was used as a positive control/standard for ATX inhibition.



Scheme 17: Mechanism of the bis-*p*NPP assay

ATX inhibition is inversely proportional to the hydrolysis of the bis-*p*NPP (**19**) substrate and the production of 4-nitrophenol (**28**). The IC_{50} is calculated by plotting percentage hydrolysis versus test compound concentration. A concentration dose–response (1 nM – 30 μ M) study was performed to determine the inhibitor constants ($K_i = IC_{50} / (1 + ([S]/K_m))$) of all compounds in the three series against ATX. Compounds that displayed a K_i greater than 30 μ M in this study were deemed inactive as ATX inhibitors. The bis-*p*NPP ATX assay was carried out elsewhere in the laboratory.¹⁰⁸

3.3.3 [³H]-Thymidine Incorporation Assay

Induction of DNA synthesis is a well known action of the ATX-LPA signalling cascade.¹⁰⁹ LPAR activation is fundamental to cell proliferation; hence ATX mediated production of LPA is also fundamental to cell proliferation. DNA synthesis or cell proliferation is furthermore an integral part of the fibrosis pathway. Therefore, the observation of DNA synthesis through direct LPAR stimulation /ATX activation or reduced DNA synthesis by LPAR antagonism/ATX inhibition can provide valuable functional information with respect to identifying potential LPA antagonists and ATX inhibitors.

Metabolic incorporation of tritiated thymidine (³H-thymidine) into cellular DNA is a widely used protocol to monitor rates of DNA synthesis and cell proliferation. [³H]-thymidine is incorporated into DNA synthesis during the S-phase of DNA replication and the quantity of [³H]-thymidine measured is proportional to DNA synthesis (Figure 30).

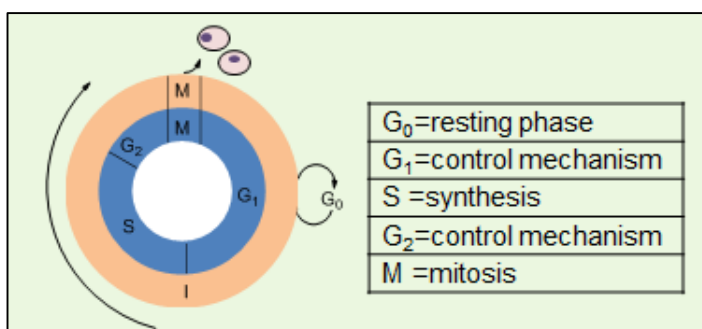


Figure 30: DNA synthesis cycle

A scintillation β -counter was used to measure the radioactivity incorporated into the DNA of the treated cells. The amount of radioactivity present determines the extent of cell division that has occurred in response to the test compounds.

3.3.4 Cytotoxicity Alamar Blue Assay

To exclude the progression of any toxic agents all synthesised compounds were studied in a cancer cell line at 30 μM using Alamar Blue[®] cytotoxicity assay, also known as Resazurin assay. Alamar Blue[®] (resazurin) (**89**) is a stain, which penetrates cellular membranes and accumulates intercellularly. Live cells incorporate resazurin (**89**). Living cells are metabolically active and are able to reduce the non-fluorescent dye to the strongly-fluorescent dye resorufin (**90**) (Figure 31). As cells begin to die, their ability to incorporate resazurin (**89**) lessens. Thus loss of resazurin (**89**) uptake corresponds to loss of cell viability in the culture. Any compounds deemed cytotoxic would be removed from further progression or testing. The Alamar Blue[®] cytotoxicity assay was carried out elsewhere in the laboratory.¹⁰⁸

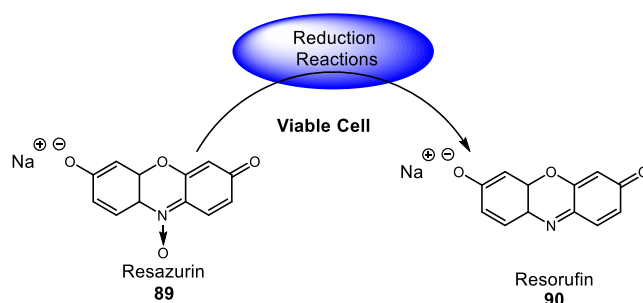


Figure 31: Alamar Blue[®] cytotoxicity assay¹⁵⁵

3.3.5 Physicochemical Measurements

The physicochemical properties of the three novel series were measured *via* an industrial partnership with GSK, in a kinetic solubility assay and an artificial membrane permeability assay.¹¹⁰ In the kinetic solubility assay, compounds are diluted up in DMSO/pH7.4 phosphate buffered saline solution. The solution is then filtered through a Millipore filter and the filtrate is quantified by a chemi-luminescent nitrogen detection. In this kinetic assay aqueous solubility $\geq 100 \mu\text{g/mL}$ is deemed excellent and $\leq 30 \mu\text{g/mL}$ is considered poor.¹¹¹ In the permeation assay, permeation rates were based on measuring how fast molecules pass from a donor cell through an artificial membrane to an acceptor cell. This artificial membrane is prepared from 1.8% phosphatidylcholine and 1% cholesterol in decane solution and the speed is expressed in nm/s. The sample concentration in both the donor and acceptor compartment is determined by LCMS. A good permeability profile for a pharmaceutical agent is $\geq 100 \text{ nm/s}$ and a poor permeability value is $\leq 30 \text{ nm/s}$.¹¹¹

Both solubility and permeability are key physicochemical properties which give a comprehensive overview of the quality of the analogues synthesised from a developability perspective.

3.3.6 Biological Evaluation of Ki16524 and AM095

Ki16425 (**15**) a LPA_{1,3} antagonist, and AM095 (**16**) a LPA₁ antagonists are commercially available materials for use in research. As stated previously, 1-oleoyl-LPA (**6**), Ki16425 (**15**), and AM095 (**16**) were utilised as controls in the PathHunter[®] β-Arrestin GPCR assay. Additionally, there is currently no literature on Ki16425 (**15**) or AM095 (**16**) acting as ATX inhibitors. Hence, their potential as ATX inhibitors was measured by evaluation in the bis-pNPP ATX inhibition assay (Table 4).

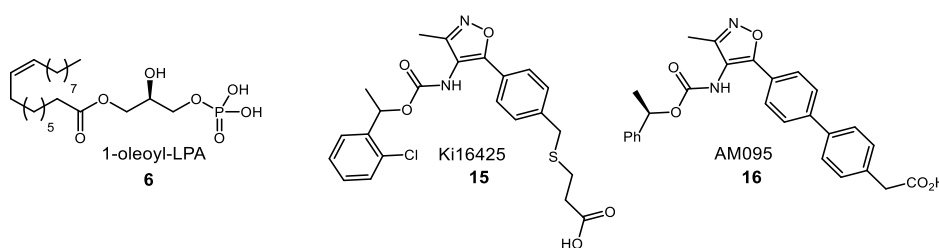


Table 4: Biological data for 1-oleoyl-LPA (**6**), Ki16425 (**15**), and AM095 (**16**)

Entry	Cpd	LPA ₁ Agonism ^a (%)	LPA ₁ Antagonism ^a (%)	ATX K _i (μM)	MW	cLogP
1	1-oleoyl-LPA (6)	100	105	n/a	436.5	5.5
2	Ki16425 (15)	-5	16	>30	473	4.9
3	AM095 (16)	4	11	>30	456	5.3

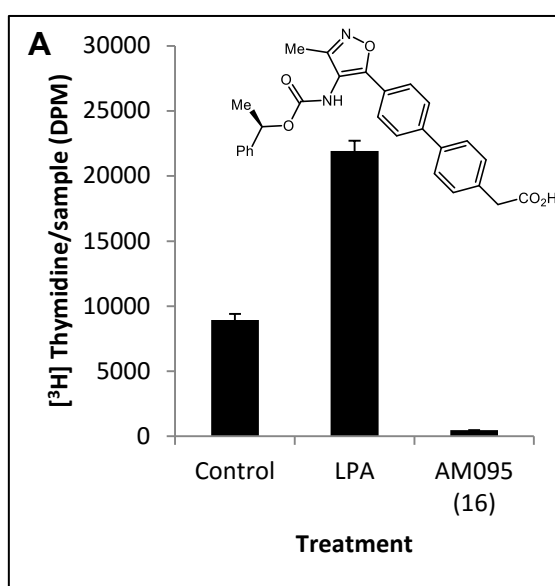
^a compounds evaluated at 10 μM concentration

To reiterate, the data obtained from the PathHunter[®] β-Arrestin GPCR assay are described in terms of percentage of agonism, where 100% refers to complete agonism and 0% refers to complete antagonism. It can be noted that 1-oleoyl-LPA (**6**, entry 1) showed complete LPA₁ agonism and no LPA₁ antagonism (105%) in the PathHunter[®] β-Arrestin GPCR assay (Table 4). Ki16425 (**15**, entry 2) and AM095 (**16**, entry 3) as expected showed LPA₁ antagonism, with percentage activity at 16% and 11%, respectively (Table 4). Ki16425 (**15**) and AM095 (**16**) did not display LPA₁ agonism in this assay, with percentage activity at -5% and 4%, respectively (Table 4). Both Ki16425 (**15**) and AM095 (**16**) were found to be inactive

as ATX inhibitors, with a K_i greater than 30 μM in the bis-*p*NPP ATX inhibition assay (Table 4). In conclusion, Ki16425 (**15**) and AM095 (**16**) were active only as LPAR antagonists. There was no cross-talk between LPAR and ATX in relation to these known antagonists, strengthening the literature assertions of these compounds being selective GPCR antagonists.^{112,37}

3.3.6.1 AM095 Effect on DNA Synthesis

AM095 (**16**) is a well characterised LPA₁ receptor antagonist that has been studied extensively for its biological responses in a range of assays. Having stated this, a direct measurement of the AM095 effect on DNA synthesis has not been reported. Consequently, it was tested in the [³H]-thymidine incorporation assay (Graph A).



Graph A: [³H]-Thymidine incorporation into LPA (2 μM), AM095 (**16**) 10 μM), stimulated prostate cancer (PC3) cell line, $n=9$, data represented as Mean \pm S.E.M

The control in this experiment contained no external stimulus, hence the basal DNA synthesis of the cells. It can be observed that DNA synthesis is triggered by LPA stimulation as the level of [³H]-thymidine incorporated into the cells is increased compared to the control. It can also be observed that AM095 (**16**) inhibits long-term DNA synthesis in prostate cancer cells. This is indicated by the reduction of [³H]-thymidine incorporation in cells stimulated with AM095 (**16**), compared to the basal level of DNA synthesis (control). AM095 (**16**) is an LPA₁ antagonist as exhibited in the PathHunter[®] β -Arrestin GPCR assay (11%, Table 4, entry 3), and displays no ATX inhibitory activity in the bis-*p*NPP assay (>30 μM , Table 4, entry 3). In

combination, this data suggests that the inhibitory effect of AM095 (**16**) on DNA synthesis in prostate cancer cells is due to the compounds blocking the LPA signalling pathway *via* specific inhibition of the receptor.

3.3.7 Biological Evaluation of Hydantoin, Acyl Aniline and Aryl Indole Series

As indicated by Tables 5-11, the data obtained from this PathHunter[®] GPCR assay indicated that none of the synthesised compounds in the hydantoin, acyl aniline or aryl indole series were acting as LPA₁ agonists or antagonists. This was somewhat disappointing given the apparent similarity which can be inferred from initial molecular overlays (Scheme 11).

From the design strategy implemented in this study, it was speculated that the isoxazole of AM095 (**16**) was a spacer between essential carbamate and biaryl acetic acid moieties. From the inactivity of the analogues displayed in the PathHunter[®] GPCR assay data, it is now clear that deletion of the isoxazole unit is not tolerated in terms of LPA₁ antagonism within this chemotype. It can, however, be derivatised to triazole and pyrazole analogues, as demonstrated by Hoffmann La Roche. There is no indication of potential binding modes from either AM095 (**16**) or the Hoffmann La Roche asset to the receptor, currently in the literature. Further exploration of the central heterocycle ring by other pharmaceutical companies has however led to potent antagonists of the LPA₁ receptor, with IC₅₀ values in the low nanomolar range.^{113,114} Therefore it can be noted that removal of this ring system is not sufficient to maintain activity at the receptor. Recently, the crystal structure of LPA₁ was reported. This progress in structural determination of LPA₁ may assist the understanding of the exact interactions required for receptor antagonism in the future, and clarify the contributions the isoxazole makes to binding.

Several of the compounds synthesised in the hydantoin, acyl aniline, and aryl indole series did however display ATX inhibition in the bis-*p*NPP assay. Gratifyingly, none of the compounds tested showed any signs of cytotoxicity in the Alamar[®] Blue assay, indicating that any cellular effects observed were not attributed to cytotoxicity.

From the data in Table 5, It can be noted that several hydantoin analogues showed significant inhibition of ATX with potencies in the range 1-4 μM, using the bis-*p*NPP ATX inhibition assay Table 5. The phenyl (**49**, entry 1), isopropyl (**56**, entry 2) and cyclohexyl (**57**, entry 3) substituted hydantoins exhibited equipotent ATX inhibitory

ability with K_i values of 3.6 μM , 1.2 μM and 1.8 μM , respectively (Table 5). The physicochemical properties of these analogues were measured and overall found to display excellent aqueous solubility but poor permeability: phenyl substituted hydantoin (**49**, 174.5 $\mu\text{g/mL}$, 3 nm/s), isopropyl substituted hydantoin (**56**, 190 $\mu\text{g/mL}$, 3 nm/s), and cyclohexyl substituted hydantoin (**59**, 186 $\mu\text{g/mL}$, 22 nm/s).

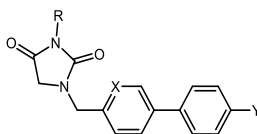


Table 5: Biological and physicochemical data for hydantoin **49**, **56-62**

Entry	Cpd	R	X	Y	LPA Ago ^a (%)	LPA Antago ^b (%)	ATX K_i (μM)	MW	cLogP
1	49	Ph	C	$\text{CH}_2\text{CO}_2\text{H}$	-2	102	3.6	400	3.7
2	56	<i>i</i> Pr	C	$\text{CH}_2\text{CO}_2\text{H}$	5	111	1.2	366	2.8
3	57	cHex	C	$\text{CH}_2\text{CO}_2\text{H}$	9	118	1.8	406	3.8
4	61	Ph	C	C(c-propyl) CO_2H	4	95	>30	426	4.3
5	62	Ph	C	H	5	98	1.3	342	4.0
6	59	<i>i</i> Pr	N	$\text{CH}_2\text{CO}_2\text{H}$	5	100	4.0	367	1.2
7	60	cHex	N	$\text{CH}_2\text{CO}_2\text{H}$	36	95	3.9	407	2.2

^aagonism ^bantagonism

The cyclopropanecarboxylic acid derivative (**61**) was found to be inactive as an ATX inhibitor (>30 μM , entry 4) (Table 5). This inactivity potentially suggests an unfavourable steric clash within the ATX active site and the constrained bulky cyclopropyl group of the hydantoin analogue (**61**). Additionally, the cyclopropyl ring system may lock the carboxylic acid into a vector which also causes a steric clash with the protein surface.

The 1,1'-biphenyl hydantoin (**62**, entry 5) was active as an ATX inhibitor with a K_i of 1.3 μM (Table 5). The absence of an acetic acid moiety may be indicative of a distinct binding mode compared to the acetic acid derivative (**49**) (3.6 μM , entry 1). Alternatively, it can be inferred that the acetic acid functional group may not be an essential pharmacophoric feature within the hydantoin series. To assess this binding mode completely, additional 1,1'-biphenyl hydantoin compounds would be required

to establish a more complete structure activity relationship and comparison with carboxylate containing analogues. The physicochemical properties of 1,1'-biphenyl hydantoin (**62**) were measured and found to display a low solubility of 7.5 µg/mL and high permeability of 540 nm/s.

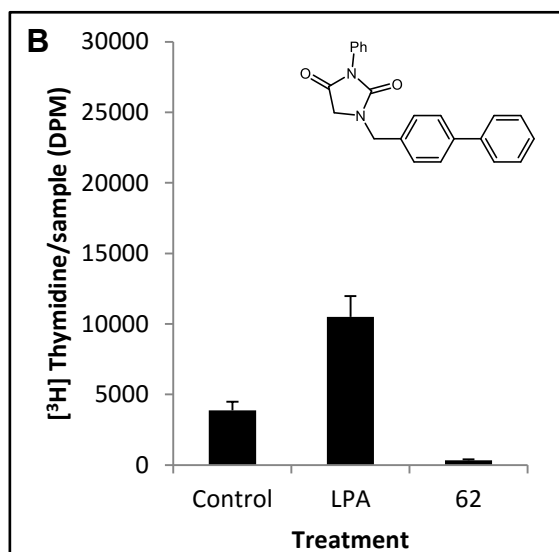
The pyridyl containing hydantoins (**59**, entry 6 and **60**, entry 7) were found to be equipotent ATX inhibitors with K_i values of 4 µM and 3.9 µM, respectively (Table 5). As discussed previously, the role of lipophilicity in determining the overall quality of candidate drug molecules is of paramount importance. Inclusion of the pyridine ring in general lowered the cLogP by 1.6 units, while retaining molecular weight in a good region. With this optimum cLogP apparent the solubility and permeability of the pyridyl containing hydantoins were measured. The heteroatom inclusion in the biaryl motif did not have a significant effect on solubility or permeability compared to the benzyl hydantoins: isopropyl substituted pyridyl hydantoin (**59**, 108 µg/mL, < 10 nm/s), cyclohexyl substituted pyridyl hydantoin (**60**, 93 µg/mL, < 30 nm/s). Overall, both the benzyl and the pyridyl containing hydantoins displayed excellent aqueous solubility but poor membrane permeability.

3.3.7.1 Hydantoin Effect on DNA Synthesis

The 1,1'-biphenyl hydantoin (**62**) was an ATX inhibitor that displayed an optimum molecular weight of 342 Da. Giving its encouraging overall profile, it was decided to examine whether the 1,1'-biphenyl hydantoin (**62**) had an impact on cell proliferation *via* ATX modulation, and accordingly this analogue was studied using the [³H]-thymidine incorporation assay (Graph B).

Examining Graph B, it can be noted that the 1,1'-biphenyl hydantoin (**62**) blocks baseline [³H]-thymidine incorporation into prostate cancer cells, compared to the basal level of DNA synthesis (control). The 1,1'-biphenyl hydantoin (**62**) is neither an LPA₁ agonist nor antagonist but displays ATX inhibitory potency (1.3 µM, Table 7, entry 1). Taken as a whole, this suggests that the inhibitory effect is due to the compound blocking the endogenous production of LPA by ATX. This can be rationalised by the fact that prostate cancer cells express significant levels of endogenous ATX that drives the generation of LPA, which in turn provides an autocrine/paracrine feedback loop to drive basal proliferation of these cells.¹⁰⁹ Visual inspection of the cells showed no apparent cell death, indicating that the

effect observed is likely to be pathway relevant and not attributed to any potential cytotoxic effect.



Graph B: [³H]-Thymidine incorporation into LPA (2 μM), **62** (10 μM), stimulated prostate cancer (PC3) cell line, n=9, data represented as Mean±S.E.M

As discussed previously, analogues of acyl aniline series (**50**, **81-85**) were inactive as LPA receptor antagonists however, four analogues displayed ATX inhibitory ability in the bis-*p*NPP assay (Table 6).

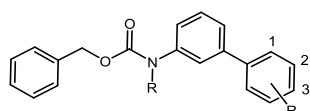


Table 6: Biological and physicochemical data for acyl aniline **50**, **81-85**

Entry	Cpd	Pos ^c R	R	R ¹	LPA Ago ^a (%)	LPA Antago ^b (%)	ATX K _i (μM)	MW	cLogP
1	81 ^d	1	CH ₂ CO ₂ H	H	-4	68	4.0	361	4.8
2	82 ^d	2	CH ₂ CO ₂ H	H	1	102	3.5	361	4.8
3	50 ^d	3	CH ₂ CO ₂ H	H	-5	88	4.5	361	4.8
4	83 ^d	-	H	H	7	101	>30	303	5.2
5	84 ^d	3	CH ₂ CO ₂ H	cHex	0	82	2.0	443	6.5
6	85 ^d	3	CH ₂ CO ₂ H	THP	0	113	>30	445	4.7

^a agonism ^b antagonism ^c position ^d analogue prepared by another member of the laboratory.¹⁰⁵

It can be noted that the acetic acid unsubstituted aniline analogues (**81**, entry 1, **82**, entry 2, **50**, entry 3) were equipotent active ATX inhibitors: 4 μM , 3.5 μM and 4.5 μM , respectively (Table 6). Their physicochemical properties were also assessed and as both compounds are positional isomers they exhibited an identical physicochemical profile with high solubility above 100 $\mu\text{g/mL}$ and satisfactory permeability; ortho analogue (**81**, 287 $\mu\text{g/mL}$, 140 nm/s), meta analogue (**82**, 221 $\mu\text{g/mL}$, 64 nm/s) para analogue (**50**, 198 $\mu\text{g/mL}$, 73 nm/s).

The 1,1'-biphenyl acyl aniline derivative (**83**, entry 4) was found to inactive as an ATX inhibitor (>30 μM) (Table 6). This infers that an acetic acid moiety is essential for ATX inhibition within the acyl aniline series. It can be reasoned that the acetic acid moiety in the aryl aniline analogues (**81**, **82**, **50**) is potentially binding to the zinc ions present in the active site of ATX, an interaction that has been noted with other acidergic groups.⁵⁴ If the acyl aniline series is acting as a competitive ATX inhibitor, this could perhaps account for why removal of the acetic acid moiety in the 1,1'-biphenyl acyl aniline derivative (**83**) led to a complete loss of ATX inhibition.

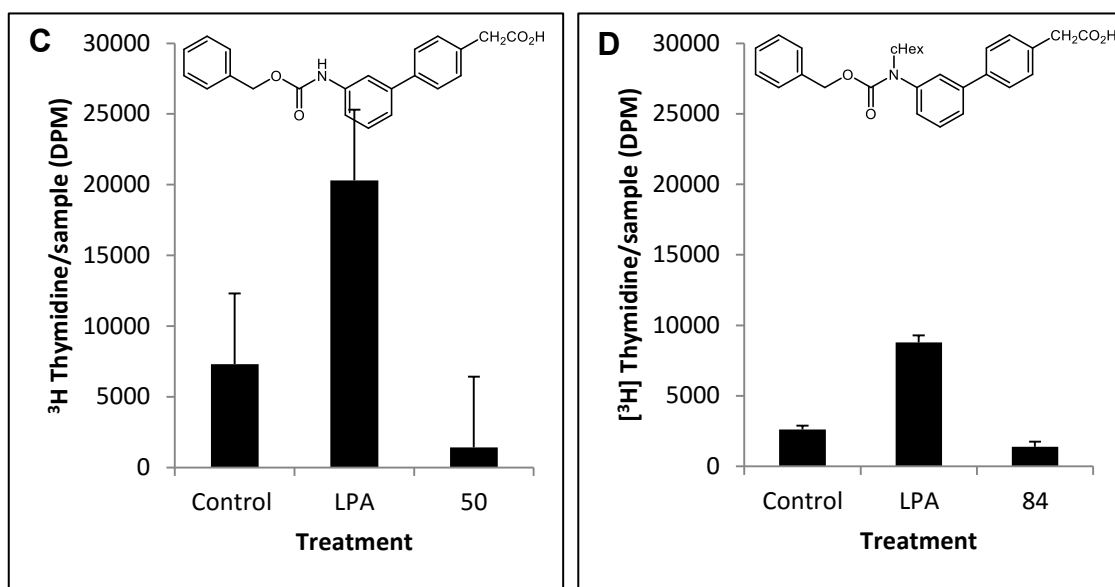
In terms of the substituted aniline analogues, the cyclopropyl analogue (**84**, entry 5) is an active ATX inhibitor with a K_i of 2 μM and the tetrahydropyran analogue (**85**, entry 6) is inactive as an ATX inhibitor with a K_i greater than 30 μM (Table 6). The activity switch between these analogues (**84**, **85**) indicates that specific substitution of the aniline nitrogen is tolerated. The inactivity of the tetrahydropyran substituted analogue (**85**) suggests an unfavourable polar interaction with the oxygen present in the tetrahydropyran group, which is absent in the cyclohexyl group. This implies that other polar functionalities may not be tolerated in this position for ATX inhibition.

The solubility and permeability of the active ATX inhibitor, cyclohexyl substituted aniline (**84**) was measured and found to exhibit an excellent solubility value of 189 $\mu\text{g/mL}$ and permeability of 150 nm/s. This analogue does however, have a sub-optimum cLogP of 6.5.

3.3.7.2 Acyl Aniline Effect on DNA Synthesis

To further confirm the potential of the acetic acid aniline analogue (**50**) and the cyclohexyl substituted analogue (**84**) as ATX inhibitors the compounds were studied in the [^3H]-thymidine incorporation assay (Graphs C and D). Examining Graphs C and D, it was concluded that both aniline analogues (**50** and **84**) also block [^3H]-

thymidine incorporation into prostate cancer cells. Both aniline analogues (**50** and **84**) were non-cytotoxic compounds in the Alamar[®] Blue assay. Furthermore, cells stimulated with the aniline analogues (**50** and **84**) were observed under the microscope and no apparent cell death was observed. Since both aniline analogues (**50** and **84**) are active only as ATX inhibitors and not LPA₁ agonists or antagonists, it can again be deduced that DNA synthesis is reduced by compounds blocking the endogenous production of LPA by ATX.



Graph C: [³H]-Thymidine incorporation into LPA (2 μM), **50** (10 μM) and **D: 84** (10 μM) stimulated prostate cancer (PC3) cell line, n=9, data represented as Mean±S.E.M

Lastly pharmacological data for the substituted acyl anilines (**51,86**) are presented in Table 7.

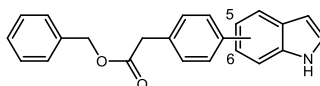


Table 7: Biological and physicochemical data for aryl indole **51** and **86**

Entry	Cpd	Pos.	LPA Agonism (%)	LPA Antagonism (%)	ATX K _i (μM)	MW	cLogP
1	51 ^a	5	-1	98	1.1	341	5.2
2	86 ^a	6	-3	88	>30	341	5.2

^a analogue prepared by another member of the laboratory.¹⁰⁵

It was noted that aryl indole positional isomers (**50**, entry 1 and **83**, entry 2) showed significantly different ATX activity. Moving the aryl carbamate from the 5 to the 6 position led to loss of activity with K_i values of 1.1 μM and greater than 30 μM , respectively (Table 7). The acid moiety previously essential for acyl aniline activity is not included in this series, therefore indicating a possible hydrophobic binding mode within the ATX pocket. This lipophilic indole analogue (**50**) has a high cLogP of 5.2 but despite this has a satisfactory solubility value of 70 $\mu\text{g/mL}$ and permeability of 445 nm/s.

3.4 Summary of Hydantoin, Acyl Aniline and Aryl Indole Series

As indicated in previous sections analogues from the hydantoins, acyl anilines, and aryl indoles series displayed the ability to inhibit the ATX enzyme. The molecular weight and cLogP values of the three chemotypes were compared against published ATX inhibitors, discussed earlier in Section 1.3.3. A guidelines commonly employed to assess developability parameters was used to assess these groups, depicted using a red line (Figure 32).⁸⁸

ATX is a highly topical area of study for both academia and industry and a substantial volume of research has been conducted into the development of novel lead inhibitors. In general, many ATX inhibitors reported in the literature exhibit a molecular weight of greater than 400 Da (Figure 32A).⁶⁶ In terms of lipophilicity, many lipid-like ATX inhibitors and a number of small molecule inhibitors also display high cLogP values (Figure 32B). It has been stated in the literature that there is a need for high quality ATX inhibitors, and focus should be placed on identification of chemotypes with improved physicochemical properties.⁶⁶ High quality analogues have been identified from the three novel series synthesised in this work which display molecular weight values below 400 Da, optimum clogP values, and display excellent aqueous solubility in addition to encouraging pharmacological attributes.

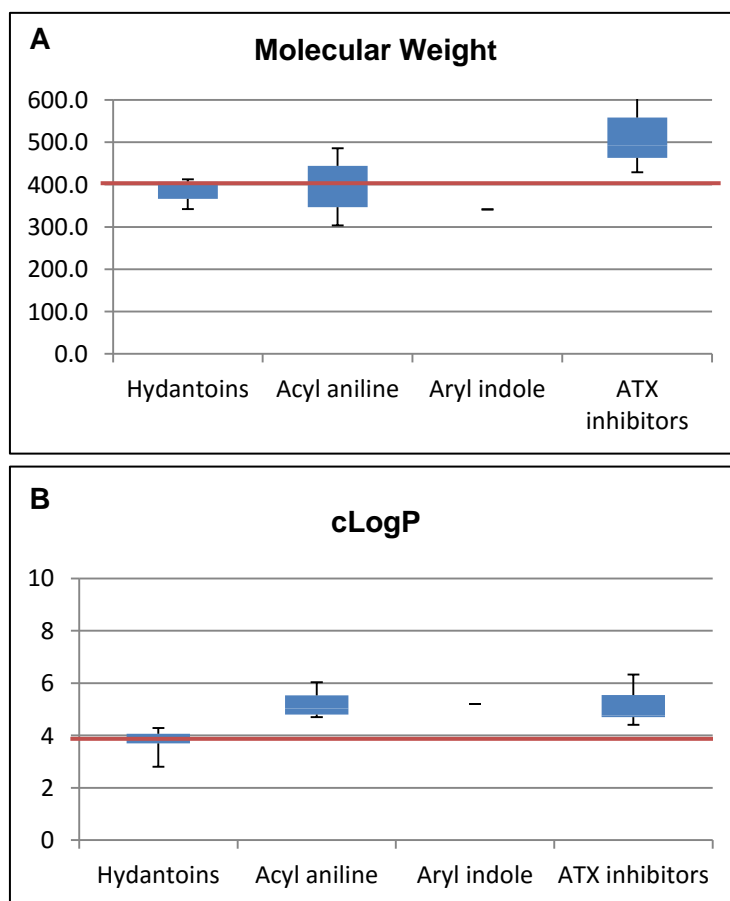


Figure 32: Illustrating the calculated molecular weight (A) and cLogP (B) of I hydantoins, II acyl aniline, III aryl indole, IV ATX inhibitors **34-38, 43, 45-48**. The red line represents the threshold in accordance with Gleeson⁸⁸ (MW <400 Da, and cLogP <4)

The hydantoins and aryl indoles series on average exhibited molecular weights just under this proposed 400 Da optimum.⁸⁸ The acyl aniline series spanned a wider range of molecular weights (361 - 445 Da), values generally considered to be acceptable. In terms of lipophilicity the hydantoin series displayed an optimum cLogP profile below 4. While the acyl anilines and aryl indoles displayed cLogP values above 4, values that are commonly considered acceptable but not optimal.⁸⁸ Generally, the hydantoin series displayed potent ATX inhibition, with an exception of the cyclopropanecarboxylic acid derivative (**61**). The series displayed optimum molecular weight, optimum cLogP, excellent solubility but limited permeability. It was inferred from the [³H]-thymidine incorporation assay that the 1,1'-biphenyl hydantoin (**62**) analogue also blocked the endogenous production of LPA by ATX in a cellular context, providing further validation of this emerging series as ATX inhibitors. Within the hydantoin series the pyridyl analogue (**59**) emerged as a potential lead compound (Figure 33). This isopropyl substituted hydantoin (**59**) has a low

molecular weight of 371 Da, good solubility of 108 $\mu\text{g/mL}$, and a favourable cLogP of 1.2. Despite these encouraging attributes, this analogue is a poorly permeable less than 10 nm/s, a feature which would require further optimisation.

Within the acyl aniline series, it was concluded that the acetic acid moiety was essential for ATX inhibition. Overall, the acyl aniline series displayed excellent solubility with the average of the active inhibitors being 235 $\mu\text{g/mL}$. It can be inferred that the cyclohexyl substituted aniline (**84**) is the most lead-like compound from the acyl aniline series (Figure 33). It displays ATX inhibition (2 μM , Table 11, entry 2) and has an impact on in-cell proliferation (Graph **D**). This aniline analogue (**84**) has an optimum solubility value of 189 $\mu\text{g/mL}$ and permeability of 150 nm/s, but has a sub-optimum cLogP value of 6.5.

From the limited exploration of the acyl indole series it was noted that substitution in the 5 position (**51**), gave ATX inhibition, hence is the lead compound within this series (Figure 33). The indole (**51**) has a satisfactory physicochemical profile with a molecular weight of 341 Da, solubility of 70 $\mu\text{g/mL}$ and permeability of 445 nm/s, however the high cLogP of 5.2 requires further optimisation as this is significant beyond the limits of what is regarded as being drug-like.

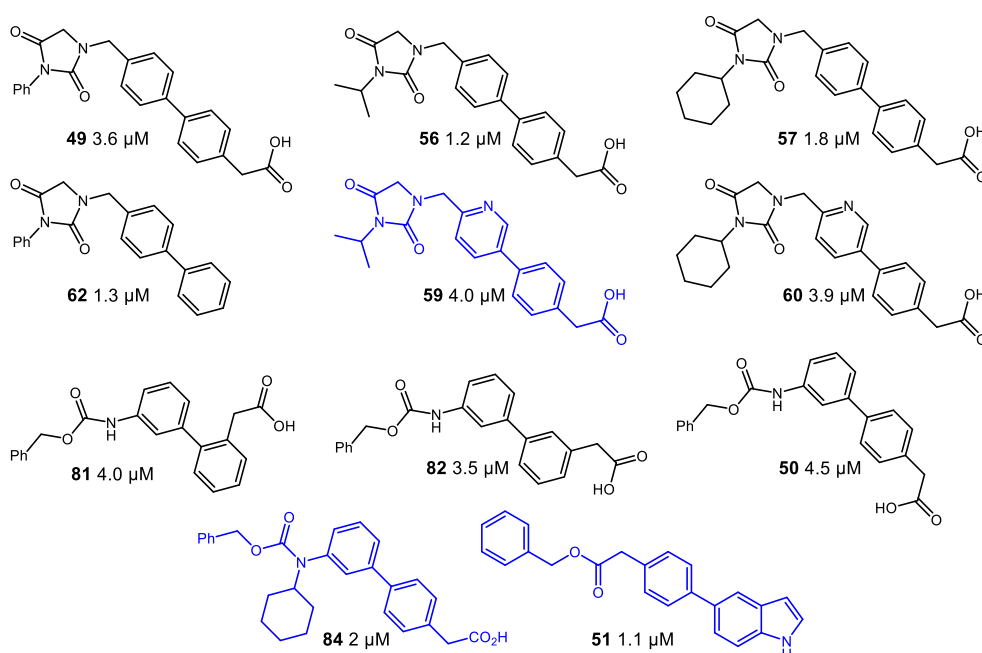


Figure 33: Active novel ATX inhibitors identified from the bis-pNPP assay (K_i)

3.5 Conclusions

Using a range of literature templates Ki12425 (**15**), AM095 (**16**) and the Hoffmann La Roche asset (**17**) as a basis to design new compounds which could interact with the ATX-LPA signalling pathway, three novel chemotypes were proposed. From consideration of modern concepts of lead-likeness, it was hypothesised that the reduction in both molecular weight and in some cases cLogP, with respect to these templates, would give rise to a more tractable and developable novel series of inhibitors at either LPA₁ or ATX. The design of the novel antagonists was based on the concept of biological isosteres, using JChem⁸² software to profile their physicochemical properties. The target compounds were successfully prepared and their solubility and permeability were measured in a high throughput assay *via* an industrial collaboration.

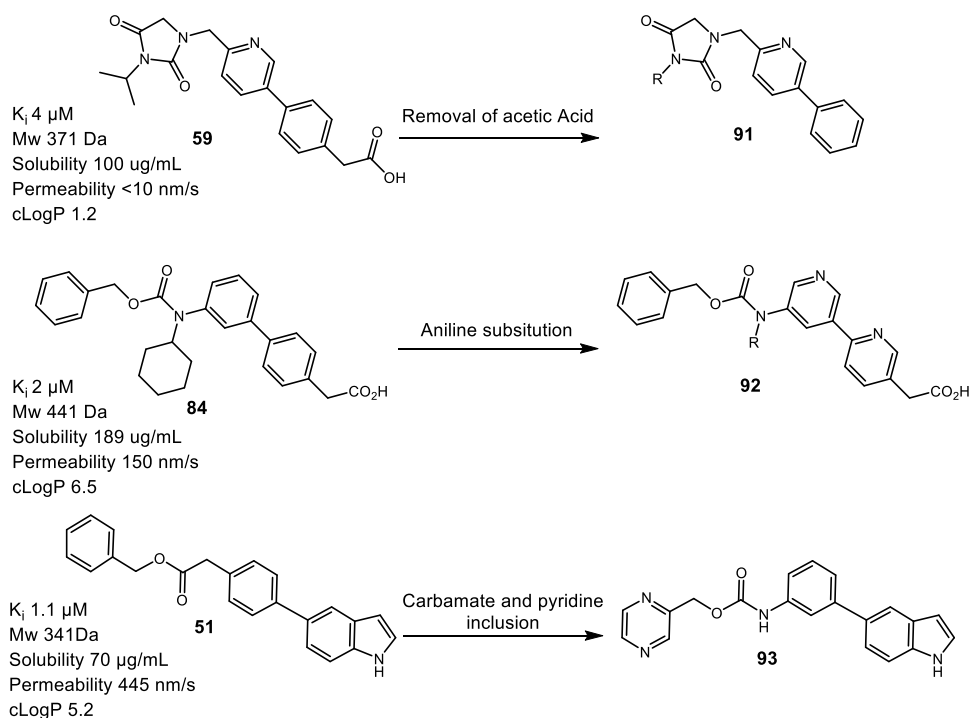
The three novel series were assessed for their ability to disrupt the ATX-LPA signalling pathway in both a cell based LPAR assay and an isolated enzyme ATX assay. None of the compounds prepared showed activity against the LPA₁ receptor, as originally designed. Encouragingly, cross-screening against ATX revealed that several exemplars had significant levels of inhibitory activity against ATX.

Additionally, a [³H]-thymidine incorporation assay demonstrated that several inhibitors had the ability to decrease DNA synthesis *via* ATX inhibition (Figure 34). This initial data is highly encouraging as it indicated the hits identified are active in a cellular context, providing additional validation for each of the series. AM095 (**16**) was also found to decrease DNA synthesis in the prostate cancer cells, data which has not been reported previously.

From this work novel ATX inhibitors were identified. Several of the hits identified had promising physicochemical profiles, suggesting that the series identified could offer potential for further optimisation. From this research it was concluded that ATX could be inhibited by three distinct and novel chemotypes further highlighting the potential of this target in addressing proliferative disorders such as IPF and cancer.

3.6 Future Work

Three compounds from this research were identified as ATX inhibitors worthy of further optimisation (Scheme 18).



Scheme 18: Proposed future work of the hydantoin, acyl aniline and aryl indole series

Within the hydantoin series the isopropyl substituted analogue (**59**) emerged as a potential lead compound. It was noted, however, to be poorly permeable <10 nm/s (optimum ≥ 100) which would require further optimisation. Interestingly, in the hydantoin series it was also noted that an acetic acid moiety was not necessary within this chemotype for ATX inhibition. Therefore removing the acetic acid moiety of lead compound (**60**) to give a phenylpyridine analogue (**91**) would lower the molecular weight further and potentially increase the permeability of the inhibitor through removal of the ionisable functionality (Scheme 18). Further SAR data around this hydantoin compound could also be investigated with substitution of the hydantoin.

It was inferred that the cyclohexyl substituted aniline analogue (**84**) was the most lead-like of the acyl aniline series but had a sub-optimum cLogP value of 6.5. Future compounds within this series could probe the substitution of the aniline with less bulky lipophilic moiety, such as a methyl, ethyl or an isopropyl group. Incorporation of heteroatoms into the biaryl motif could also be investigated to address the matter

of lipophilicity. The removal of the cyclohexyl group would also lower the molecular weight of the suggested acyl aniline analogue (**92**) (Scheme 18).

The indole analogue (**51**) was identified as the lead compound within the aryl indole series with a K_i of 1.1 μM in the bis-*p*NPP assay. This analogue, however, has a high cLogP of 5.2. To fully understand the potential of this series additional SAR exploration would be needed. Simple changes like the inclusion of a carbamate functionality and pyrazine ring could be used to improve the physicochemical properties. These alterations would also address the excessive level of lipophilicity associated with this pharmacophore, as suggested indole analogue (**93**) displays.

It would also be important to establish the binding mode of the three series within the enzyme. As discussed in Section 1.3.1 there are various inhibition modes in which compounds can inhibit ATX including catalytic site interaction and hydrophobic pocket binding. To gain this knowledge, X-ray crystallography could be employed and co-crystallography of ATX and inhibitors of interest studied.

At this point it should be reiterated that GPCRs can couple to more than one signalling pathway.¹¹⁵ Therefore, achieving the required level of efficacy through inhibition of LPA₁ receptor *in vivo* adds greater difficulty to the lead finding process. In contrast, ATX has one main function; synthesis of LPA from LPC hydrolysis. Furthermore ATX is serum derived and resides upstream in the defected signalling cascade. With these key points and the identification of ATX inhibitors from this work it was concluded that ATX is a more tractable target for this research programme. Accordingly, future efforts focused exclusively on ATX as the molecular target, and this is discussed in the following chapter.

4 Chapter 4: PF-8380 SAR and Hit Optimisation

4.1 Introduction

In Chapter 3, a cross-screening approach to disrupt the ATX-LPA pathway was described and potent ATX inhibitors were identified with novel molecular pharmacophores. It was also noted that attaining selective antagonism of the LPAR family is a challenge within this area of research, and it was concluded that ATX is a potentially more tractable target than LPA towards the aim of disrupting the ATX-LPA signalling cascade. Once ATX was established as a suitable target within this research programme, a deeper understanding of the key pharmacophoric elements required for inhibition was needed. This knowledge would ultimately aid in the design of ATX inhibitors with greater efficacy than the compounds identified in Chapter 3.

The aim of this chapter was to study the potent ATX inhibitor and tool compound PF-8380 (**39**) (Figure 34). PF-8380 (**39**) is an attractive molecule to initiate further lead finding efforts towards novel and developable ATX inhibitors. In 2010 PF-8380 (**39**) was reported by researchers at Pfizer to have IC_{50} ATX inhibition values of 1.7 nM in an LPC isolated enzyme assay, and 101 nM in a human whole blood assay.⁶³ Through direct ATX inhibition, PF-8380 (**39**) was found to be capable of blocking inflammation-induced LPA synthesis, both in plasma and at the site of inflammation.⁶⁸ This data attracted significant interest as PF-8380 (**39**) was the most potent ATX inhibitor reported in the literature at that point.

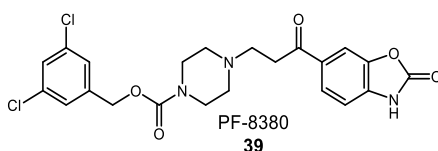


Figure 34: PF-8380 (**39**)

ATX is also over-expressed in various cancers and, due to the potent ATX activity of PF-8380 (**39**), it has been employed in multiple cancer research studies.⁴¹ Despite the immense potential of PF-8380 (**39**) as a drug compound there is no apparent evidence of PF-8380 (**39**) moving beyond animal models or reaching the clinic. It is, however commercially available for use in research. Academic groups have used PF-8380 (**39**) as a positive control in ATX assay studies. One such comprehensive enzyme kinetic study found that PF-8380 (**39**) showed maximal inhibition of the bis-*p*NPP cleavage assay with average IC_{50} values of 0.007-0.001 μ M, and

0.004 μM inhibition within the FS-3 assay.⁷⁶ Although there is extensive use of PF-8380 (**39**) within the scientific literature, there is no ATX co-crystallisation data available and only a paucity of SAR studies reported to date. Based on the above, PF-8380 (**39**) was of interest to this work and a valid starting point for the design of novel ATX inhibitors for the treatment of IPF.

Chromatographic LogD (chromLogD) is the measured lipophilicity value of a molecule at pH7.4.¹¹⁶ There is a strong relationship between lipophilicity and solubility, and it has been found that as lipophilicity increases, solubility on average decreases.⁸⁸ Property forecast index (PFI) is defined as the chromlogD plus the number of aromatic rings, and is an effective guide to predicting solubility. Considerable emphasis is placed on maximizing solubility in lead generation in the pharmaceutical industry as solubility is a key element in attaining orally available drugs.⁸⁸ PF-8380 (**39**) was tested in a series of physicochemical measurement assays *via* collaboration with an industrial partner, GSK (entry 2, Table 8). Its physicochemical properties were compared to the optimum solubility, chromlogD, human serum albumin (HSA) binding and PFI for a drug compound, as reported in the medicinal chemistry literature (entry 1, Table 8).⁸⁸

Table 8: Measured physicochemical properties of PF8380 (**39**)

Entry	Cpd	MW	ChromLogD	Solubility ($\mu\text{g/mL}$)	HSA (%)	PFI
1	Optimum ¹¹¹	≤ 350	≤ 4	≥ 100	≤ 90	≤ 5
2	PF-8380 (39)	478	5.5	24	97.55	7.54

PF-8380 (**39**) displays a high molecular weight (478 Da), a high chromlogD (5.5), poor solubility (24 $\mu\text{g/mL}$), a high level of protein binding (HSA) (97.55%), and a sub-optimum PFI (7.54) in comparison to optimum literature values (Table 8).¹¹¹ Overall the physicochemical properties of PF-8380 (**39**) are unsatisfactory as a hit compound particularly with regard to its high molecular weight and poor solubility.

In 2013, a rudimentary SAR study of PF-8380 (**39**) found that ATX inhibitory activity was fundamentally attributed to the presence of two fragments, a 3,5-dichlorobenzyl carbamate moiety and a benzo[d]oxazolone group.¹¹⁷ The researchers came to this conclusion as the two most active inhibitors identified in this study were symmetrical analogues; (**94**, 1.8 μM) and (**95**, 0.8 μM) when measured in the bis-pNPP assay (Figure 35). None of the compounds included in this study exhibited a potency which

approached that of PF-8380 (**39**), and the exact interactions' made between the compound and ATX were not fully elucidated in the study. Accordingly, one aim of this research was to further explore the exact contributions to binding within the active site of ATX. A SAR study in conjunction with structure-based drug design approach to PF-8380 (**39**) was adopted to gain full understanding of the binding mode of PF-8380 (**39**) in the catalytic site of ATX. The initial design strategy was to identify which essential components of hit compound PF-8380 (**39**) were responsible for activity through deletion analogue synthesis and the synthesis of closely related analogues.

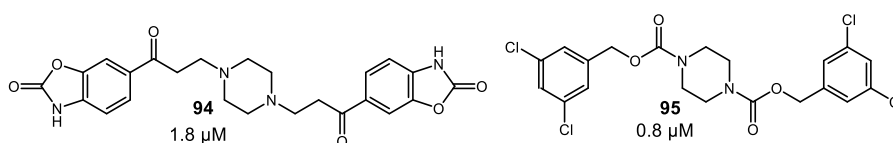
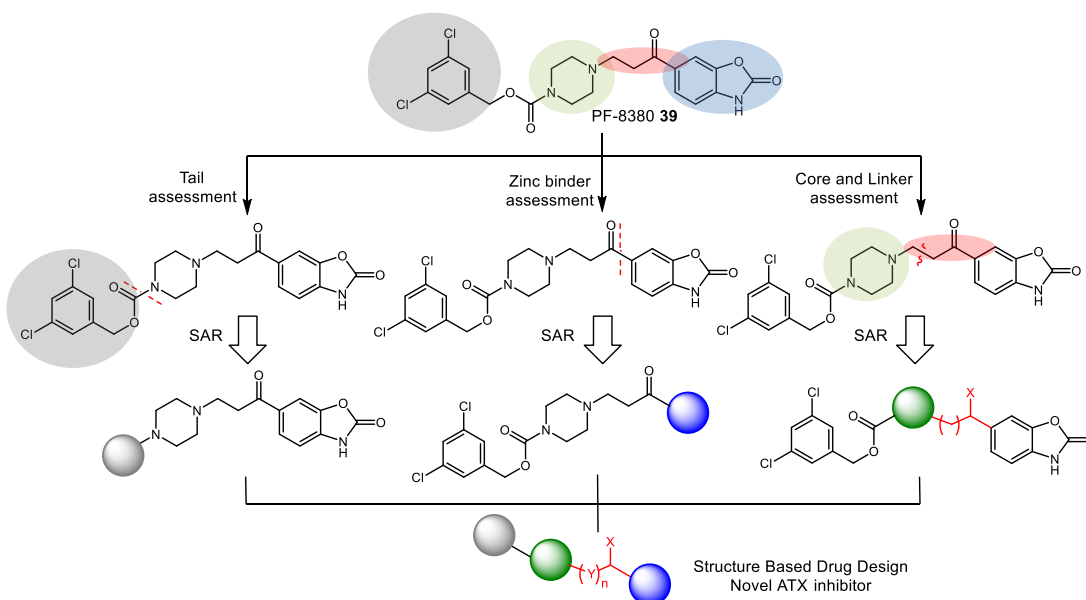


Figure 35: Symmetrical analogues **94** and **95**

PF-8380 (**39**) is categorised as a lipid-like small molecule ATX inhibitor; its long linear flexible structure contains an acidic end or head group and lipophilic tail, which was proposed to make similar interactions to LPC with the enzyme.⁶⁶ It was decided to group PF-8380 (**39**) analogue target molecules into classes addressing this structural layout through modification of three main areas: the lipophilic tail (grey shading), zinc chelators (blue shading) and core/linker moiety (green/red shading) (Scheme 19).



Scheme 19: Hit-to-lead optimisation process planned

A modular approach was taken to this SAR study, examining the three sections of the molecule independently. Single point changes were made to PF-8380 (**39**) to probe both activity and pharmacological properties in each of the three areas of modification. New inhibitors were designed with two key factors in mind; controlling molecular weight and cLogP, using JChem⁸² to profile synthesised analogues. In order to identify compounds with potentially improved physicochemical properties as well as developing a more complete structure activity relationship for this series.

4.1.1 Structure-based Drug Design

Structure-based drug design using X-ray crystallography is a common approach in pharmaceutical development.¹¹⁸ The ATX enzyme is ideal for structure-based design due to the availability of multiple ATX crystal structures in the literature.⁶⁶ The binding mode of ATX/PF-8380 (**39**) in the literature is postulated to be competitive at the catalytic site. Reports suggest that the benzo[*d*]oxazol-2(3*H*)-one of PF-8380 (**39**) makes an essential interaction with one of the zinc ions present in the active site of ATX, and the long lipophilic portion of the molecule resides in the hydrophobic pocket adjacent to the catalytic site. The exact interactions, however, are not explicitly stated in the literature and have not been shown through co-crystallisation with ATX.^{66,76}

An additional objective of this research programme was to obtain crystallographic data of ATX in complex with either PF-8380 (**39**) or a derivative by working in collaboration with the Perrakis group in the Netherlands Cancer Institute. To this end a racemic alcohol derivate (**83**) was synthesised elsewhere in our laboratory and found to have a K_i value of 0.002 μM in the bis-*p*NPP ATX inhibition assay (Figure 36).¹¹⁹

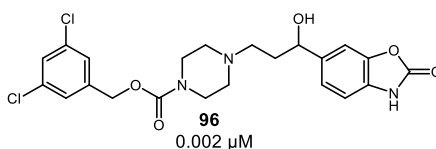


Figure 36: Alcohol derivative **96** (Synthesised by another member of the laboratory.¹¹⁹)

Pleasingly, successful co-crystallisation of alcohol derivate (**96**) and ATX (rat ATX produced in HEK 293 Flp-In cells) was achieved by a collaborative effort with the Perrakis group.⁵³ The alcohol derivative (**96**) was crystallised as a racemate,

however the co-crystallised data obtained shows only the (*S*)-enantiomer ((*S*)-**96**) of the alcohol bound to the active site of ATX. This crystallographic data obtained between the alcohol analogue ((*S*)-**96**) and ATX is the first to be reported containing the PF-chemotype (Figure 37).

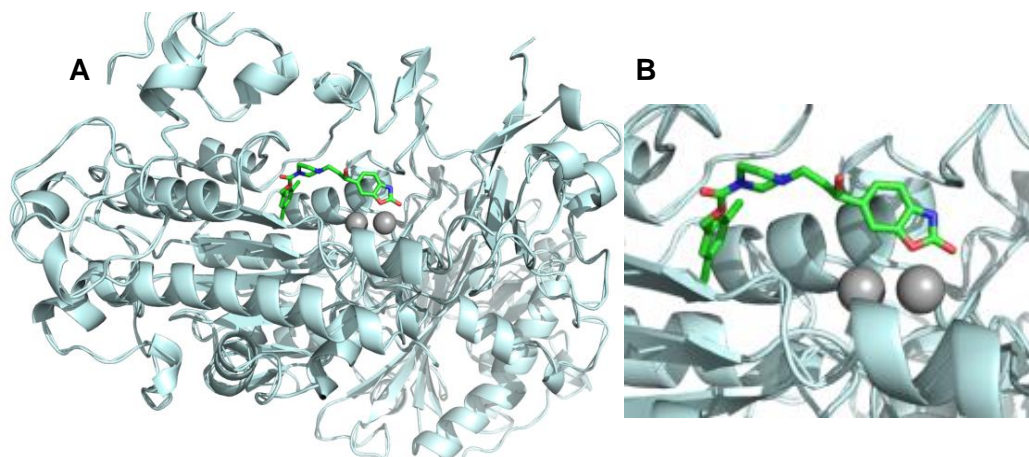


Figure 37: A: (*S*)-**96** (green) co-crystallised with ATX enzyme (ribbon structure)⁵³ B: (*S*)-**96** (green), focusing on catalytic site⁵³

From the analysis of the co-crystallised ATX/compound ((*S*)-**96**) structure, the benzo[*d*]oxazol-2(3*H*)-one group of alcohol ((*S*)-**96**) does indeed act as a head group pointing towards the catalytic site as suggested in the literature.⁶⁶ The benzo[*d*]oxazol-2(3*H*)-one carbonyl interacts with the zinc through an associated water molecule (Figure 38). Furthermore, the ring oxygen of the benzo[*d*]oxazol-2(3*H*)-one chelates to a zinc ion. The nitrogen of the benzo[*d*]oxazol-2(3*H*)-one is orientated towards a lysine residue (Lys208), interacting *via* hydrogen bonding through a water molecule (HOH127). This water molecule also forms a hydrogen bond with the key asparagine residue (Asn230).

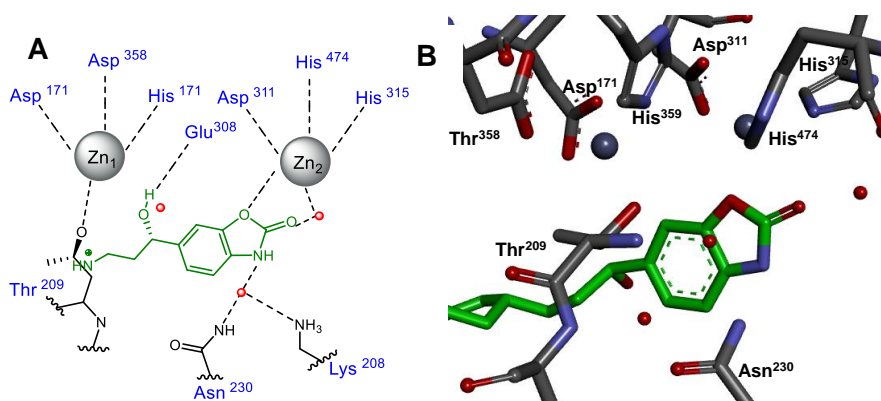


Figure 38: A: Schematic representation of (*S*)-**96** in the active site. B: Co-crystal structure of (*S*)-**96** in the active site. (ligand=green, water molecules=red).

In the final resolved crystal structure the position of the hydrogen on the alcohol is undefined. The rotatable nature of this hydrogen means multiple conformations could be postulated. A putative interaction of the alcohol hydrogen is that it forms a hydrogen bond with a glutamate (Glu308) (Figure 38). In order to confirm this interaction the single enantiomers of the alcohol (**96**) could be isolated through chiral separation and co-crystallised with ATX, a task undertaken by another member of our laboratory with results pending.

The piperazine core of the alcohol analogue ((*S*)-**96**) sits in a twisted boat conformation in which the tertiary amine of the piperazine is protonated. The saturated ring has hydrophobic interactions with a tyrosine (Tyr306) molecule. The carbamate carbonyl of the tail region hydrogen bonds to a tryptophan residue (Trp275) and the proton of the benzyl carbon hydrogen bonds with a phenylalanine residue (Phe273) (Figure 39).

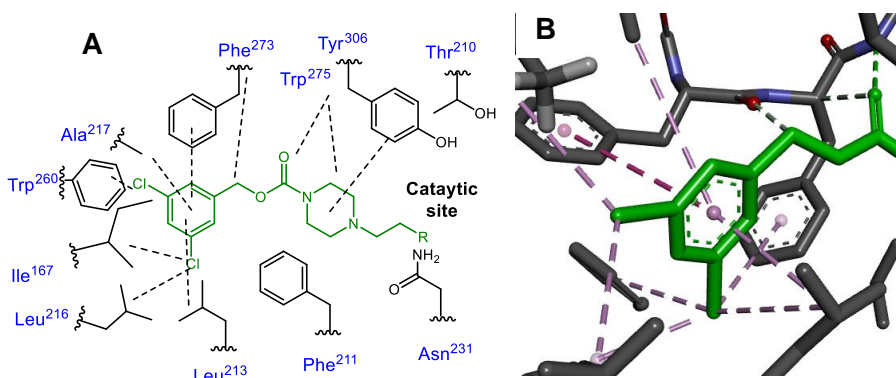


Figure 39: A: Schematic representation of (*S*)-**96** in the hydrophobic pocket. B: Co-crystal structure of (*S*)-**96** in the hydrophobic pocket (ligand=green).

The 3,5-dichlorobenzyl moiety or tail of the alcohol analogue ((*S*)-**96**) resides, as predicted, in the hydrophobic pocket of ATX (Figure 40). The benzene ring forms π - π stacking interactions with a phenylalanine (Phe273) and π -alkyl hydrophobic interactions with a leucine (Leu213). The chlorine atoms of the 3,5-dichlorobenzyl moiety make a range of hydrophobic interactions; one chlorine interacts with a leucine (Leu216) and isoleucine (Ile167), and the second chlorine interacts with phenylalanine (Phe274), and leucine (Leu213). This chlorine also has a π -alkyl interaction with a tryptophan (Trp260).

From consideration of this data, the binding mode of PF-8380 (**39**) chemotypes, elucidated in the literature, is accurate. In conclusion, the alcohol analogue ((*S*)-**96**)

spans the active site of ATX from the catalytic site and zinc ions to the hydrophobic pocket (Figure 40).

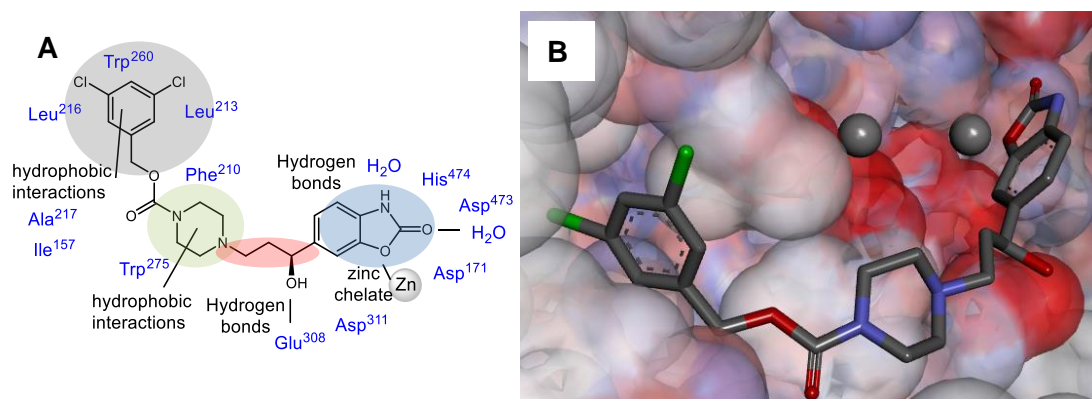


Figure 40: A: (S)-96 (shading consistent with key discussed in text) illustrated interactions with ATX. B: Image of (S)-96 co-crystallised with ATX generated using DS Visualizer.¹²⁰

A standard practice in structure-based drug design is to use the initial small molecule inhibitor to determine the target binding site of an enzyme.¹¹⁸ Utilising the co-crystal structural data of ATX/alcohol analogue ((S)-96) molecular modelling was implemented to study likely PF-8380 (39) binding interactions in ATX. Furthermore, this work allowed evaluation of how effective the molecular modelling data was able to accurately recapitulate the crystal data. The ligand alcohol ((S)-96) was used to define the binding site and Molecular Operating Environment (MOE)¹²¹ software was used to dock and study PF-8380 (39) into the binding site of ATX (Figure 41).

From molecular modelling analysis of ATX/PF-8380 (39), the benzo[*d*]oxazol-2(3*H*)-one group of PF-8380 (39) was again shown to act as a head group pointing towards the catalytic site, as proposed by the literature. The benzo[*d*]oxazol-2(3*H*)-one carbonyl in this case directly chelates with a zinc ion (Figure 41). The ring oxygen of the benzo[*d*]oxazol-2(3*H*)-one hydrogen bonds to a water molecule (HOH126). This water composes of a network of hydrogen bonds to the catalytic site residues asparagine (Asn230), histidine (His474), and threonine (Thr209). This interaction with the catalytic site differs from the co-crystallised ATX/compound ((S)-96) complex, where the ring oxygen of the benzo[*d*]oxazol-2(3*H*)-one of the alcohol analogue ((S)-96) chelates directly with the zinc ion. Furthermore, the ring nitrogen of the benzo[*d*]oxazol-2(3*H*)-one of PF-8380 (39) does not seem to make any interactions in the model. Additionally, the carbonyl adjacent to the benzo[*d*]oxazol-2(3*H*)-one head group of PF-8380 (39) does not appear to make any significant interactions with the ATX side chain in this model.

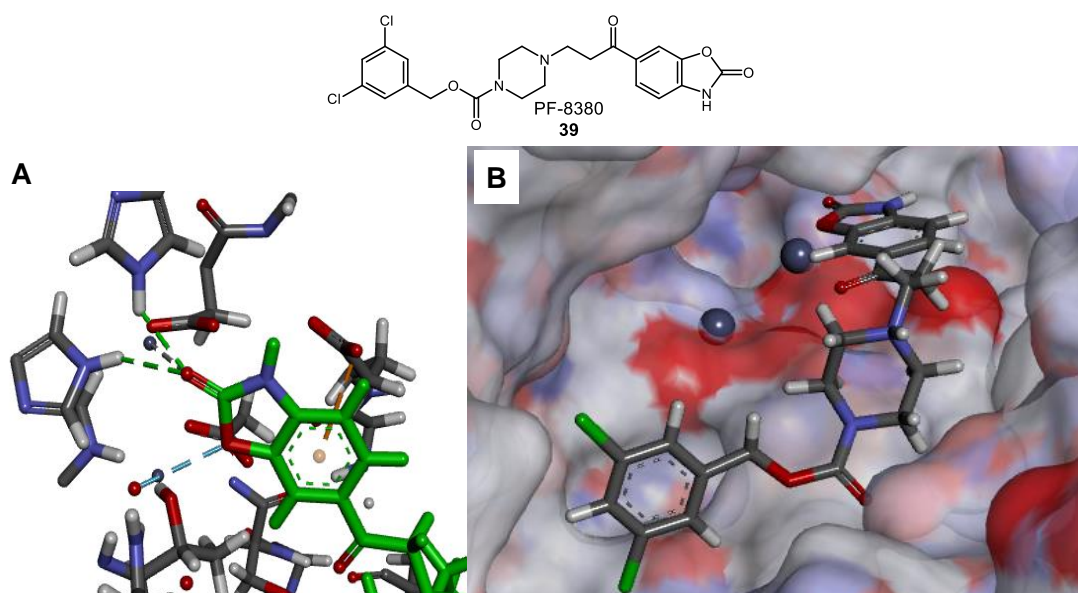


Figure 41: Molecular modelling of PF-8380 (**39**) using MOE and diagrams prepared using DS Visualizer.¹²⁰ A: PF-8380 (**39**) interacting with catalytic site (dotted lines, hydrogen bonds blue and green, chelation grey) B: PF-8380 (**39**) spanning the active site of ATX

In this molecular model of ATX/PF-8380 (**39**), the piperazine acts as a spacer moiety, displaying no significant interactions within the active site of ATX. A tryptophan (Trp275) residue of ATX forms a hydrogen bond to the carbamate carbonyl of the tail region. The 3,5-dichlorobenzyl moiety of the PF-8380 (**39**) model structure again resides in the hydrophobic pocket of ATX (Figure 16). The benzene ring forms π -alkyl hydrophobic interactions with alanine (Ala304) and leucine (Leu213). The chlorine atoms on the benzene rings make a range of hydrophobic interactions; one chlorine atom makes hydrophobic interactions with an alanine (Ala304), isoleucine (Ile167), and phenylalanine (Phe273). The second chlorine makes hydrophobic interactions with a tryptophan (Trp260), alanine (Ala217), and leucine (Leu213).

Overall, the molecular modelling of the ATX/PF-8380 (**39**) docked structure displayed globally similar interactions with ATX compared to the defined co-crystallised structure ATX/ alcohol analogue ((*S*)-**96**). The only significant difference between the docked structure of PF-8380 (**39**) and the co-crystal structure of ATX/ alcohol analogue ((*S*)-**96**) was in relation to the placement of the benzo[*d*]oxazol-2(3*H*)-one head group in the active site. Both the modelled ATX/PF-8380 complex and co-crystallised ATX/alcohol analogue ((*S*)-**96**) indicate the benzo[*d*]oxazol-2(3*H*)-one moiety acts as a head group interacting at the catalytic site. Both

analogues span ATX to the hydrophobic pocket, with the 3,5-dichlorobenzyl making lipophilic interactions.

At this point, a robust molecular model of PF-8380 (**39**) was established. The biostructural data could then be confidently related to emerging SAR information, to fully understand the binding contributions of the PF-8380 (**39**) chemotype. The eventual aim was to use this understanding of ATX to design novel drug compounds, with good physicochemical properties, to inhibit the ATX-LPA signalling pathway. Throughout this SAR study, continuous efforts were made to attain additional ATX co-crystal structures to build further confidence in the SAR picture being developed.

4.2 PF-8380 Tail Assessment

In this study of the structure activity relationship around PF-8380 (**39**), the 3,5-dichlorobenzyl moiety was defined as the tail region, and first section of the PF-8380 (**39**) chemotype examined. As discussed previously, molecular weight and cLogP are crucial properties of a successful drug candidate.⁸⁸ The most significant contributions to molecular weight and cLogP of PF-8380 (**39**) can be attributed to the 3,5-dichlorobenzyl moiety. Single point changes were made to PF-8380 (**39**) tail region to probe both activity and associated physicochemical properties of the analogues (Figure 42).

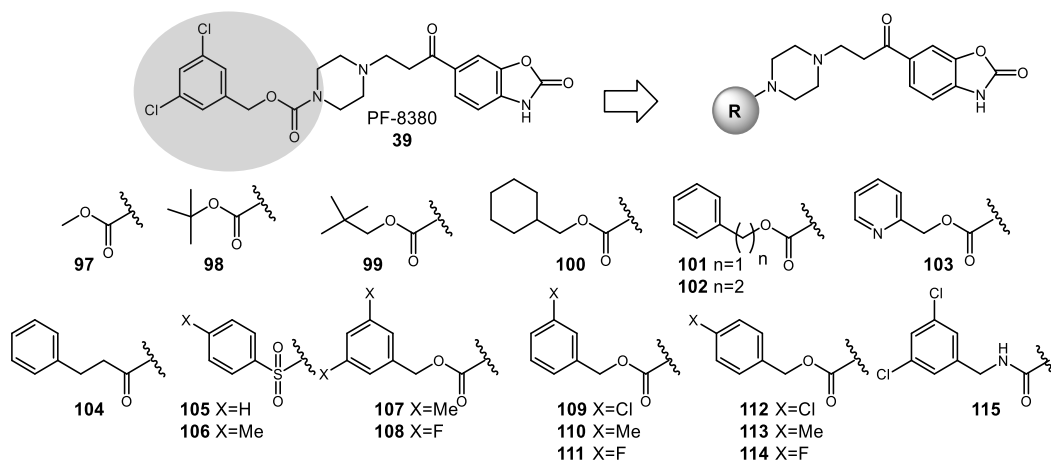


Figure 42: PF-8380 (**39**) tail shaded grey, target tail SAR analogues **97-115**

The initial compounds proposed for synthesis in this SAR study were truncated PF-8380 analogues. This involved the removal of the aromatic ring and replacement with aliphatic methyl, butyl, neopentyl, and cyclohexyl groups (**97-100**) to access the

effect on ATX potency. It was anticipated that the decrease in aromatic ring count would have a positive lowering effect on cLogP and ultimately be favourable in terms of PFI.

The next set of SAR analogues would investigate the need for the chlorine atoms, with an unsubstituted benzene ring in its place (**101**). Assuming the benzyloxycarbonyl analogue (**101**) was active, two point changes could then be studied with the inclusion of an amide derivative (**104**), to study the contributions to binding of the carbamate oxygen. A pyridine containing analogue (**103**) was proposed for synthesis to decrease cLogP from 3.6 to 1.4. An elongated carbamate (**102**) was also prioritised for synthesis in order to understand the importance of length and flexibility within the tail region of the PF-series. Additionally, sulfonamides are commonly employed in SAR studies,¹²² and therefore analogues (**105** and **106**) containing this group were included in the proposed compound list.

Removing the 3,5-dichlorobenzyl ring or replacing the chlorines with alternative isosteres was an important consideration in controlling molecular weight of the potential lead compounds. Methyl groups are monovalent bioisosteric replacements for chlorine as they have similar lipophilicity values, hence a 3,5-dimethylbenzyl analogue (**107**) was also suggested.¹²³

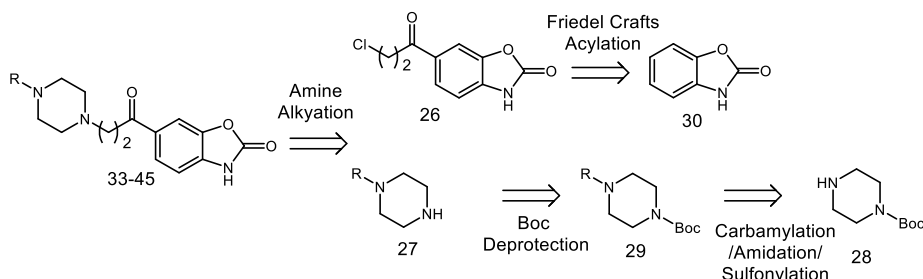
Replacement of chlorines with fluorine molecules is also a known medicinal chemistry practice.¹²⁴ Fluorine can positively influence conformation, potency, membrane permeability, metabolic pathways, and pharmacokinetic properties, so accordingly a 3,5-difluorobenzyl (**108**) was planned for synthesis.¹²⁴ Furthermore, to investigate the position of the halogen and methyl groups around the ring, meta and para-substituted chlorine, fluorine, and methyl analogues (**109-114**) were also identified for synthesis.

Replacement of the carbamate oxygen to a nitrogen was also suggested. This urea tail analogue (**115**) would determine if a hydrogen bond donor in place of a hydrogen bond acceptor would improve ATX potency.

4.2.1 Synthetic Access to PF-8380 Tail Analogues

The retrosynthetic analysis of tail SAR analogues led to the identification of a set of key building blocks: 6-(3-chloropropanoyl)benzo[*d*]oxazol-2(3*H*)-one (**116**) and mono-substituted piperazine (**120**). The mono-substituted piperazine is derived from

1-Boc-piperazine (**120**), functionalised by carbamylation/amidation or sulfonylation (**119**) and subsequently deprotected to the free amine. 6-(3-chloropropanoyl)benzo[*d*]oxazol-2(3*H*)-one (**116**) is derived from a Friedel Crafts acylation of benzo[*d*]oxazol-2(3*H*)-one (**117**) and reacted with the functionalised amines to afford the final products (**97-115**) (Scheme 20).¹¹⁷

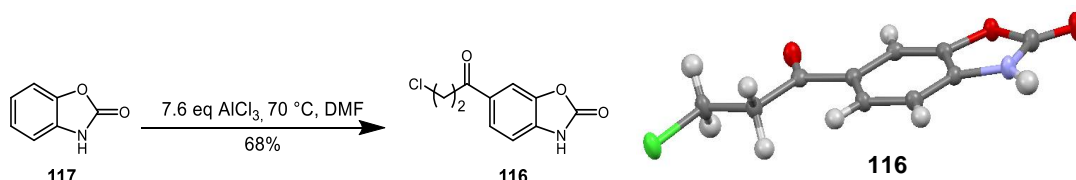


Scheme 20: Retrosynthetic view of tail SAR analogues

4.2.2 Synthesis of Tail Analogues

4.2.2.1 Friedel Crafts Acetylation

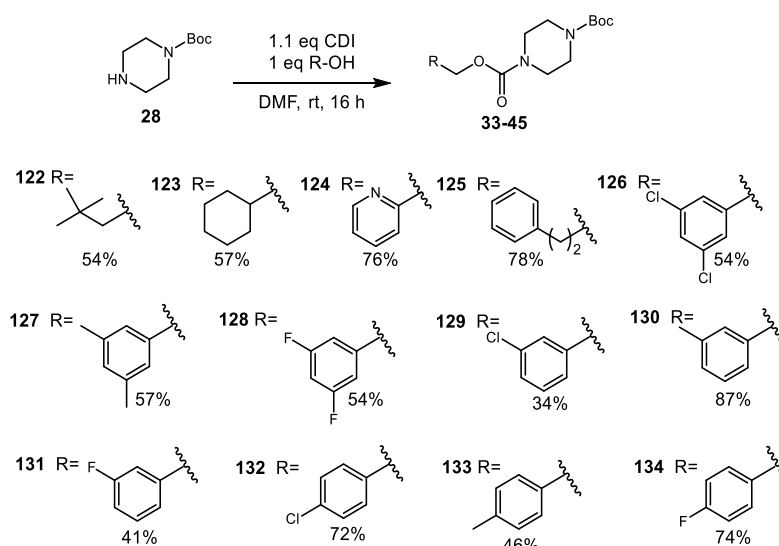
As shown in the retrosynthetic analysis, the initial reaction required for the first SAR library was a Friedel Crafts acylation of benzo[*d*]oxazol-2(3*H*)-one (**117**) using 3-chloropropyl chloride. Purification by recrystallisation in EtOH yielded the desired two carbon linked acylated chloroalkane (**116**). To confirm acylation occurs para to the nitrogen of benzo[*d*]oxazol-2(3*H*)-one a crystal structure of the chloroalkane was obtained. The crystal structure clearly indicated the correct regiochemistry was present (**121**) (Scheme 21).¹²⁵



Scheme 21: Friedel Crafts acylation and crystal structure **116**

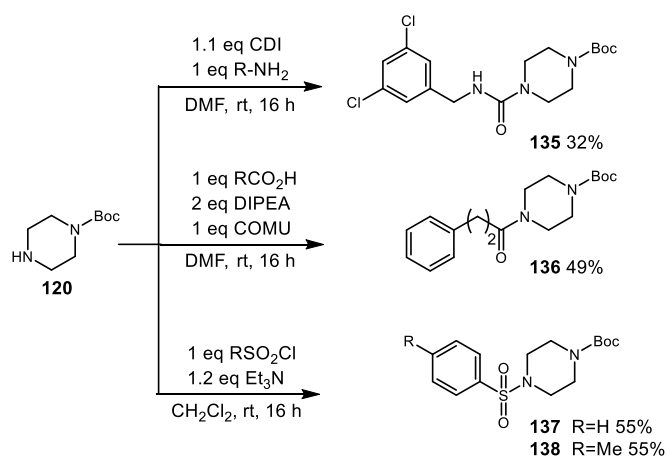
4.2.2.2 *N*-Substituted Piperazine Preparation

The second component required for generating a PF-8380 (**39**) SAR library was various *N*-substituted piperazines. Starting from 1-Boc-piperazine (**120**) a one pot reaction of 1,1'-carbonyldiimidazole (CDI) in dimethylformamide (DMF) with a secondary alcohol provided an efficient general method for the preparation of the carbamate analogues (**122-134**) (Scheme 22).



Scheme 22: Carbamate substituted piperazine synthesis

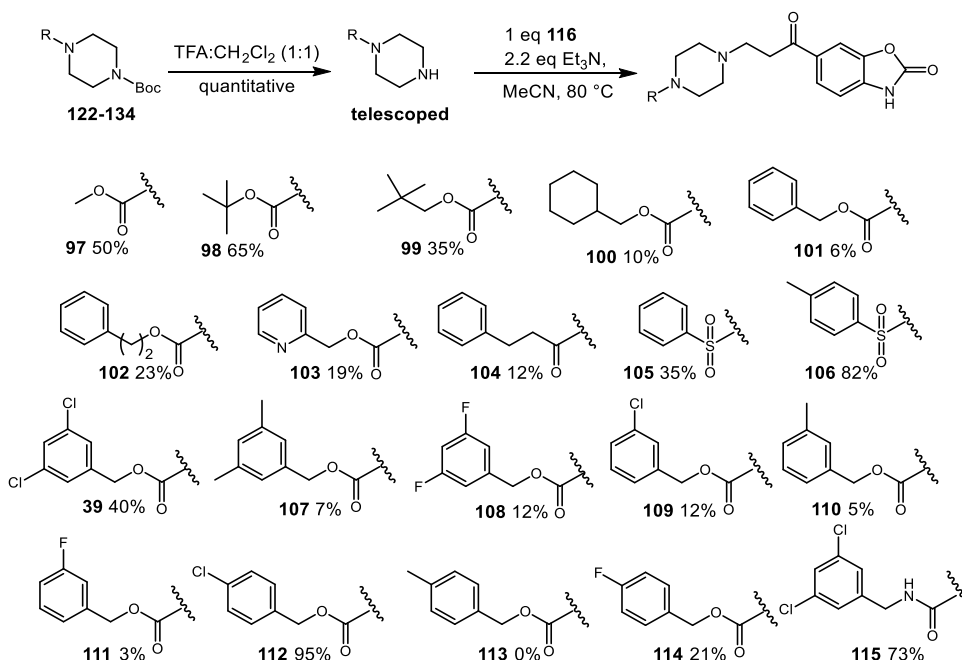
The one pot reaction of CDI in DMF with a secondary amine was also utilised to yield the urea derivative (**135**) (Scheme 23). Amidation of 1-Boc-piperazine (**120**) with 3-phenylpropanoic yielded the amide derivative (**136**) (Scheme 23). The safe and efficient coupling reagent 1-[(1-(cyano-2-ethoxy-2-oxoethylideneamino)oxy)] (COMU) was used for this procedure. COMU is an ideal coupling reagent as it is non-explosive, has fast coupling efficiency, and the by-products formed by COMU are water-soluble and easily removed by aqueous extraction.¹²⁶ Benzenesulfonyl chloride and 4-methylbenzenesulfonyl chloride were reacted with 1-Boc-piperazine in the presence of triethylamine to yield the sulfonamide derivatives (**137-138**) (Scheme 23).



Scheme 23: Synthesis of urea, sulfonamide, and amide substituted piperazines

4.2.2.3 PF-8380 Tail Analogue Preparation

Once the appropriate substituted piperazines were isolated the target final compounds were then accessed. The Boc protecting group was removed using trifluoroacetic (TFA) in dichloromethane, in quantitative yields. The mono substituted piperazines were then telescoped into an amine alkylation reaction with the key building block 6-(3-chloropropanoyl)benzo[d]oxazol-2(3H)-one (**116**) (Scheme 24). Preparation of amines *via* nucleophilic displacement is utilised extensively in this SAR study.

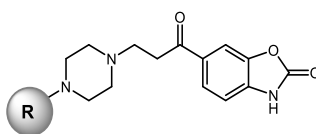


Scheme 24: Carbamate analogues synthesis from intermediates **97-115**

PF-8380 tail analogues (**97-112**, **114** and **115**) were isolated successfully and purified using normal phase column chromatography. The 4-methylbenzyl analogue (**113**) was found to be insoluble in aqueous and organic solvents, therefore isolation and purification were unsuccessful.

4.2.3 PF-8380 Tail Analogues Pharmacological Evaluation

Following successful synthesis of PF-8380 (**39**) tail analogues, their utility as ATX inhibitors was evaluated in the bis-*p*NPP ATX inhibition assay. Compounds were initially screened at a single concentration of 30 μM. A concentration dose-response (30 nM - 30 μM or 1 nM - 30 μM) study was performed to calculate the inhibitor constant (K_i) values of the tail analogues (Tables 9 and 10).

**Table 9:** Activity profile of compounds **97-106**

Entry	Cpd	R	ATX K _i (μM)	MW	cLogP
Standard	PF-8380 (39)	-	0.008	478	3.6
1	97^a		3.187	333	0.7
2	98^a		7.800	375	1.8
3	99^a		2.169	389	2.3
4	100^b		0.265	415	2.8
5	101^a		0.067	409	2.4
6	104^b		0.932	407	2.4
7	103^a		1.400	410	0.5
8	102^b		0.421	423	2.7
10	105^b		8.527	415	1.7
11	106^b		5.375	429	2.2

^a concentration dose-response (1 nM - 30 μM) ^b concentration dose-response (30 nM - 30 μM)

Generally, modifications to the tail region lowered the molecular weight of the PF-chemotype, and simultaneously reduced the cLogP of the corresponding analogues. It can be noted that aliphatic tail analogues of the PF-scaffold (**97-99**, entry 1-3) tend to be less active than those with aromatic substitution (Table 9). The bulky neopentyl substitution (**99**, entry 3) is the most active of the acyclic aliphatic groups at 0.9 μM. The cyclohexyl substituted PF-8380 analogue (**100**, entry 5)

shows greater activity than acyclic derivatives, with a K_i of 0.265 μM (Table 9). The inclusion of this saturated ring also lowered the molecular weight to 415 Da, and significantly improved the clogP to 2.8 compared to PF-8380 (**39**).

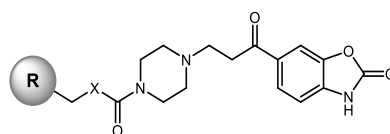
With the removal of the chlorine atoms and reinstatement of aromaticity in the carboxybenzyl derivative (**101**, entry 4), there is a tenfold loss in activity at 0.067 μM compared to PF-8380 (**39**) which has a K_i value of 0.008 μM (Table 9). This highlights the potential importance of the hydrophobic interactions of the chlorine atoms within this binding pocket of ATX.

Further activity is lost upon the removal of the benzyl oxygen to form an amide (**104**, entry 6) with a K_i value of 0.932 μM (Table 9). In both the molecular modelling data of PF-8380 and the analysis of the co-crystal structure ATX/analogue ((S)-**96**), this benzyl oxygen does not appear to make any interactions with the ATX hydrophobic pocket. The requirement of this moiety can be rationalised in that carbamates possess a further degree of conformational restriction compared to ketones or amides. This conformational restriction is due to the delocalization of non-bonded electrons on nitrogen into the carboxyl moiety. The conformational constriction provided by the carbamate group might be required for the placement of the tail moiety into the hydrophobic pocket of ATX.

The substitution of a pyridine ring (**103**, entry 7) in place of the 3,5-dichlorobenzyl moiety decreases activity further to 1.400 μM despite the significant lower cLogP (Table 9). This result implies that polar character is not tolerated in this region of ATX, which is consistent with the nature of the binding site identified in the molecular modelling of PF-8380 (**39**).

Homologation of the carbamate (**102**, entry 8) decreases the activity to 0.420 μM (Table 9). This suggests that overall analogue length is an important feature of this chemotype to fit into the hydrophobic pocket of ATX.

The sulfonamide analogues (**105**, entry 10 and **106**, entry 11) are shorter than PF-8380 (**39**) and are the least active of all tail analogues at 8.527 μM and 5.375 μM , respectively (Table 9). The altered geometry of the sulfonamide compared to the carbamate of PF-8380 (**39**) could potentially cause the sulfonyl benzene moiety and sulfonyl-4-methylbenzene moiety to clash with the hydrophobic pocket of ATX.

**Table 10:** Activity profile of compounds **107-115**

Entry	Cpd	R	X	ATX K_i (μM)	MW	cLogP
Standard	PF-8380 (39)	-	-	0.008	478	3.6
1	115^a		N	0.175	477	2.9
2	108^a		O	0.076	445	2.7
3	107^a		O	0.115	438	3.5
4	109^a		O	0.132	444	3.0
5	111^a		O	0.100	427	2.6
6	110^a		O	0.009	423	2.9
7	112^a		O	0.001	444	3.0
8	114^a		O	0.100	427	2.6

^a concentration dose-response (30 nM - 3 μM)

The substituted benzyl derivatives showed varied ATX inhibition in the bis-*p*NPP assay, with mono substituted analogues displaying lower molecular weight and cLogP than the progenitor PF-8380 (**39**).

It was noted that the urea analogue (**115**, entry 1) is less active than the carbamate containing PF-8380 (**39**) (Table 10). This indicates that a hydrogen bond donor is not as well tolerated in this position again being consistent with the hydrophobic nature of the ATX binding pocket.

Halogen substitution and position on the aromatic ring has a significant effect on ATX inhibition. The 3,5-difluoro analogue (**108**, entry 2) has a K_i of 0.080 μM , equipotent to the unfunctionalised benzene ring, (**101**, entry 5) (Table 10). This is expected when considering steric effects. The influence of fluorine is anticipated to be marginal; fluorine is a small atom with a van der Waals radius of 1.47 Å, close to

the 1.20 Å value for hydrogen.¹²⁴ This trend is also observed with the 3-fluoro analogue (**101**, 0.100 µM entry 5), and 4-fluoro analogue (**114**, 0.100 µM, entry 8), both equipotent to the benzene analogue (**101**, 0.100 µM, Table 10, entry 5).

The 3,5-dimethyl analogue (**107**, entry 3) has a K_i value of 0.115 µM which is significantly less active than PF-8380 (**39**) (Table 10). As mentioned previously, methyl groups are monovalent bioisosteric replacements for chlorine atoms in terms of their lipophilicity values, however methyl groups have a slightly larger van der Waals radius of 1.80 Å, compared to that of chlorine at 1.73 Å.¹²³ The additional steric bulk of the methyl groups may then inhibit binding in the hydrophobic pocket.

Both the 3-chloro analogue (**109**, entry 4) and the 3-fluoro analogue (**111**, entry 5) are mono substituted by halogens, and these are less active than their di-substituted counterparts (Table 10). The removal of one substituent lowers the lipophilicity which may then affect hydrophobic binding to the enzyme, leading to the observed lower activity. By contrast the 3-methyl analogue (**110**, entry 6) is a potent ATX inhibitor with a K_i of 0.009 µM. It is more potent than the di-methyl substituted analogue (**107**, entry 3) and equipotent to PF-8380 (**39**) (Table 10). This difference in activity between mono and di-substituted methyl analogues infers that the hydrophobic pocket is not large enough to accommodate the 3,5-dimethylbenzyl moiety. Furthermore, the 3-methyl analogue (**110**) has the lowest molecular weight, 423 Da, within this substituted tail series and an acceptable cLogP of 2.3, making it a compound of interest with respect to its physicochemical properties. The 4-chloro substituted analogue (**112**, entry 7) is also equipotent to PF-8380 (**39**) (Table 10). This analogue is also a potential lead compound within this sub series as it is 34 Da less than PF-8380 (**39**) and 1 log unit less than the hit compound in terms of lipophilicity.

Summarising the PF-8380 (**39**) tail analogue SAR, and comparing the biostructural data of the ATX hydrophobic pocket it can be stated that tails with aromatic character are most beneficial for ATX inhibition (Figure 43). Moreover, mono substitution of this benzene ring is optimum with regard to potency, molecular weight, and cLogP. 3-methyl substitution and 4-chlorine substitution are the most active tail SAR analogues. To link the piperazine and the tail region of these PF-8380 (**39**) analogues, the SAR data suggests a carbamate moiety is optimal. In both the molecular modelling data of PF-8380 (**39**) and the analysis of the co-crystal structure ATX/analogue ((S)-**96**) the carbonyl of the carbamate hydrogen bonds with

a tryptophan (Trp 275). Carbamate-bearing molecules, as mentioned earlier, are key structural motifs in many approved drugs due to their good chemical and proteolytic stabilities and they are generally capable of permeating cell membranes.¹⁰¹ Therefore retaining this carbamate motif in future PF-8380 (**39**) analogues is potentially advantageous.

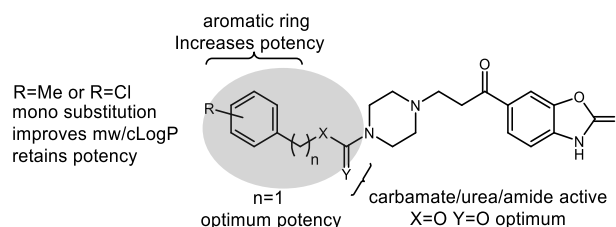


Figure 43: Overview of tail SAR

4.3 PF-8380 Zinc Binder Assessment

From consideration of both crystallographic and modelling data it was hypothesised in this SAR study that the benzo[*d*]oxazol-2(3*H*)-one portion of PF-8380 (**39**) acted like an acidic head group interacting with the catalytic site. Based on this it was decided to substitute the benzo[*d*]oxazol-2(3*H*)-one with diverse functional groups to confirm the nature of the catalytic site interaction (Figure 44).

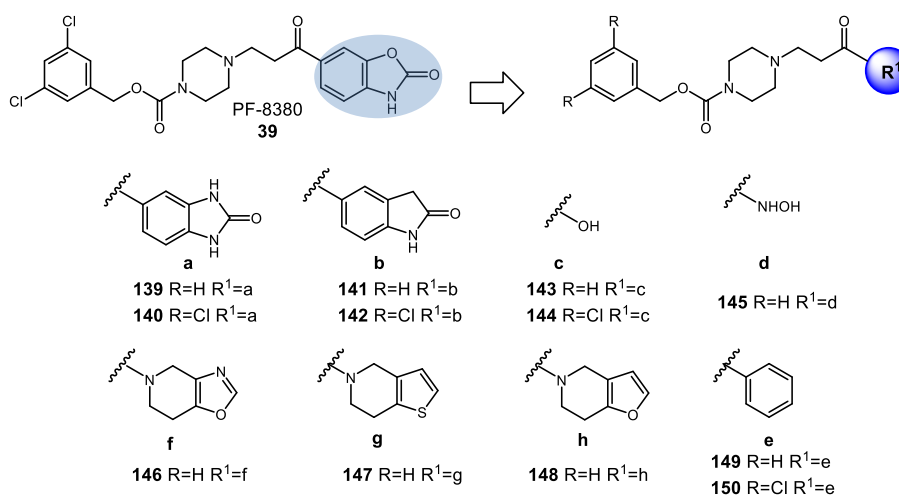


Figure 44: PF-8380 (**39**) head group shaded blue, target altered zinc binding SAR compounds

Firstly, full understanding of the benzo[*d*]oxazol-2(3*H*)-one moiety was desired. In order to establish if the nitrogen or oxygen portion of the benzo[*d*]oxazol-2(3*H*)-one head group had an importance for zinc chelation or active site interaction, the urea and oxindole analogues were proposed (**139-142**).

The pKa of the benzo[d]oxazol-2(3*H*)-one is relatively acidic at 9.33, calculated using JChem.⁸² Therefore, replacement of the benzo[d]oxazol-2(3*H*)-one with carboxylic acid analogues (**143** and **144**) was considered to be of interest. This increase in acidity and decrease in molecular weight of acids (**143** and **144**) compared to PF-8380 (**39**) may give important insight into the pharmacophoric features needed to interact with the catalytic site.

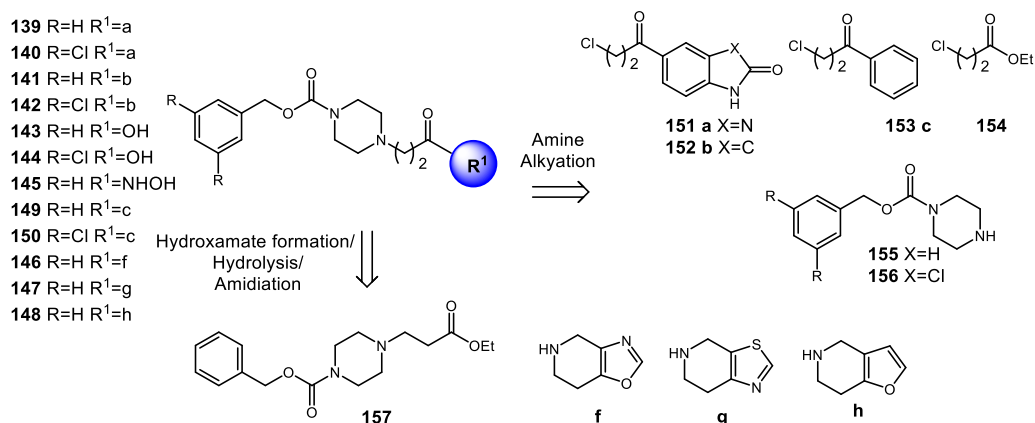
Hydroxamates are among the most effective zinc binding group known in the literature.¹²⁷ In an effort to improve the zinc-chelating portion of the PF-series the widely used hydroxamic acid moiety was included in this SAR study (**145**). Based on a similar hypothesis, and in a further effort to potentially tune the interaction with the catalytic site, alternative heterocyclic head groups were included (**147-148**). The inclusion of these heterocycles in the core template decreases both molecular weight and cLogP compared to PF-8380 (**39**), and therefore are of interest.

As stated above, the binding hypothesis of PF-8380 (**39**) to ATX involved the benzo[d]oxazol-2(3*H*)-one moiety acting like an acidic head group; interacting with the catalytic site. To challenge this hypothesis, two deletion analogues were proposed (**149** and **150**). This removed any polar functionality and replaced it with a benzene ring, in order to investigate if a hydrophobic group would be tolerated in the catalytic site.

4.3.1 Synthetic Access to PF-8380 Zinc Binder Analogues

The synthesis of the urea and oxindole analogues (**139-142**) was carried out by another member of the laboratory.¹¹⁹ Accordingly, the synthetic route followed will not be elaborated in this thesis.

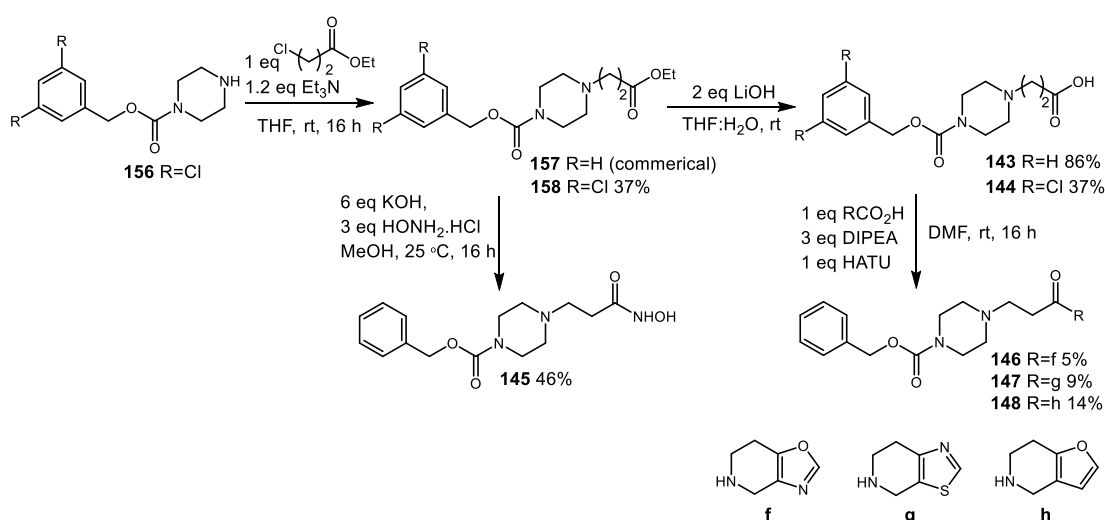
The retrosynthetic analysis of analogues (**139-150**) involves an amine alkylation of intermediates (**155**) and (**155**) (Scheme 25). The commercially available ester (**157**) can also be used for the direct synthesis of hydroxamic acid (**145**). Hydrolysis of this ester provides an intermediate for the formation of amides (**146-148**) with the piperidine derivatives **f**, **g**, and **h**.



Scheme 25: Retrosynthetic view of PF-8380 zinc binding SAR analogues **139-150**

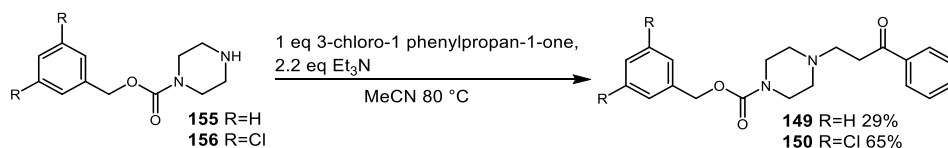
4.3.2 Synthesis of PF-8380 Zinc Binder Analogues

The requisite carboxylic acid analogue (**143**) was prepared by a base mediated hydrolysis of the commercially available ester (**157**) (Scheme 26). The 3,5-dichloro-substituted carboxylic acid derivative (**144**) was synthesised by an amine alkylation reaction and the ester intermediate (**158**) telescoped and hydrolysed to the acid (**144**) (Scheme 26). Synthesis of the hydroxamate (**145**) utilised the commercially available ester (**66**), using hydroxylamine hydrochloride and potassium hydroxide (Scheme 25). An amidation reaction was then performed using the previously prepared carboxylic acid (**143**) and coupling reagent *O*-(7-Azabenzotriazol-1-yl)-1,1,3,3-tetramethyluronium hexafluorophosphate (HATU) with *N,N*-Diisopropylethylamine (DIPEA) as base to yield the heterocyclic final products (**146-148**) (Scheme 26).¹²⁸



Scheme 26: Synthesis of head group analogues **143-148**

Substituted piperazine intermediates (**64-65**) were employed in an alkylation reaction with 3-chloro-1-phenylpropan-1-one to yield the target benzyl derivatives with no zinc binder (**60-61**) (Scheme 27).

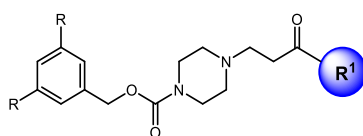


Scheme 27: Synthesis of benzyl analogues **149-150**

4.3.3 PF-8380 Zinc Binder Analogues Pharmacological Evaluation

Following the synthesis of PF-8380 (**39**) zinc binder analogues (**50-59**), the analogues were evaluated in the bis-*p*NPP assay (1 nM - 30 μM) (Table 11).

Recurrently, modifications to the zinc binding region of the PF-chemotype generally lowered the molecular weight and cLogP, whilst increasing the lead-like properties of the analogues. The majority of zinc binder substitutions, however rendered the PF-8380 (**39**) analogues inactive as ATX inhibitors (<30% percentage hydrolysis at 30 μM concentration, entry 5-12, Table 11). In the case of entries 5-7, the acids and hydroxamic acid derivatives (**143-145**) were significantly shorter in length compared to PF-8380 (**39**). This implies that the length of the analogues is an important factor, suggesting that inhibitors must sufficiently bridge the active site from the zinc ions to hydrophobic pocket. Likewise, the benzene analogues used as replacements of the benzo[*d*]oxazol-2(3*H*)-one (**149**, entry 8 and **150**, entry 9) are shorter analogues to PF-8380 (**39**) (Table 11). These analogues also lack any heteroatoms, and their inactivity supports the proposed binding mode, suggesting that it is necessary to chelate with the zinc ions present or interact with the polar residues in the active site to inhibit ATX. This result indicates that exclusively hydrophobic interactions are not sufficient for ATX inhibition within this compound series. Furthermore, the bicyclic head group analogues (**146-148**, entry 10-12) were also found to be inactive as ATX inhibitors (Table 11). This potentially suggests that an acidic head group with a hydrogen bond donor is needed for ATX inhibition within this chemotype.

**Table 11:** Activity profile of compounds **139-150**

Entry	Cpd	R ¹	R	ATX K _i (μM)	MW	cLogP
Standard	PF-8380 (39)	-	-	0.008	478	3.6
1	139 ^a		H	5.375	408	2.3
2	140 ^a		Cl	0.003	477	3.5
3	141 ^a		H	2.280	407	2.2
4	142 ^a		Cl	0.016	476	3.4
5	143		H	<30*	292	-1.4
6	144		Cl	<30*	361	-0.1
7	145		H	<30*	307	0.5
8	149		H	<30*	352	3.1
9	150		Cl	<30*	421	4.3
10	146		H	<30*	398	0.3
11	147		H	<30*	413	1.6
12	148		H	<30*	396	1.6

^a analogue prepared by another member of the laboratory. ¹¹⁹ * % hydrolysis at 30 μM concentration.

By contrast the urea (**139-140**, entries 1-2) and oxindole (**141-142**, entries 3-4) derivatives show potent ATX inhibition (Table 11). As the molecular modelling data of PF-8380 (**39**) predicted chelation to the zinc occurred *via* the carbonyl of the benzo[*d*]oxazol-2(3*H*)-one, it was expected that the urea and oxindole derivatives would chelate to the zinc in the same mode.

The benzyloxycarbonyl substituted urea analogue (**139**, entry 1) has a K_i of 5.375 μM , a reduction in potency compared to the corresponding benzo[*d*]oxazol-2(3*H*)-one derivative (**101**, Table 9, entry 12). 3-5-dichlorobenzyl substituted urea analogue (**140**, entry 2) shows an almost identical potency and physicochemical profile in terms of molecular weight and cLogP compared to PF-8380 (**39**). Similarly, the benzyloxycarbonyl substituted oxindole analogue (**141**, entry 3) has a K_i of 2.280 μM , a reduction in potency compared to the corresponding benzo[*d*]oxazol-2(3*H*)-one derivative (**101**, Table 9, entry 12). The 3-5-dichlorobenzyl substituted oxindole analogue (**143**, entry 4) also displays a reduction in potency with a K_i 0.016 μM compared to PF-8380 (**39**). The oxindole analogues (**141** and **142**) also display equal physicochemical properties to their analogous benzo[*d*]oxazol-2(3*H*)-one derivatives (**101** and PF-8380 (**39**)). The solubility of the oxindole derivatives (**141** and **142**) were measured *via* a GSK solubility assay, described previously in Section 3.3.5. The benzyloxycarbonyl urea analogue (**141**) showed an increased aqueous solubility of 396 $\mu\text{g/mL}$ compared to benzyloxycarbonyl analogue (**101**, 67.5 $\mu\text{g/mL}$). No increase in aqueous solubility was observed for the 3,5-dichlorobenzyl analogue (**142**, 69 $\mu\text{g/mL}$) compared to PF-8380 (**39**, 24 $\mu\text{g/mL}$).

In the molecular modelling analysis of PF-8380 (**39**), the ring oxygen of benzo[*d*]oxazol-2(3*H*)-one hydrogen bonds to a water molecule (HOH126). This water molecule sits in a network of hydrogen bonds to the catalytic site residues asparagine (Asn230), histidine (His474), and threonine (Thr209). Therefore, the reduction in potency of the urea analogue (**140**), and oxindole analogue (**141**) compared to the benzo[*d*]oxazol-2(3*H*)-one derivative (**101**) potentially supports this putative interaction. It can also be noted that potency can be recovered in both the urea and oxindole derivatives with the additional hydrophobic interactions of the 3-5-dichlorobenzyl group (entry 2 and 4, Table 11). This recovery of potency highlights the importance of the lipophilic tail within the PF-chemotype.

To summarise the SAR generated around this focused set of zinc binding analogues of PF-8380 (**39**), it was noted that heteroaromatic character was essential for good levels of ATX inhibition (Figure 45). Acid functionalities, hydroxamic acids and carboxylic acids, were not sufficient zinc binders to retain potent ATX inhibition. These chemotypes potentially require additional length to span active site from the catalytic site to the hydrophobic pocket to inhibit the enzyme. Furthermore, a hydrogen bond donor is potentially needed to interact with residues in the catalytic

site. The benzo[d]oxazol-2(3H)-one, urea, and oxindole moieties were identified as the best zinc binders in this study, with the oxindole group's potential to increase solubility highlighted. The alteration of the urea and oxindole templates with the active site decreased inhibition, and the lipophilic 3,5-dichlorobenzyl moiety was required to restore potency. It was also recognised that this 3,5-dichlorobenzyl moiety negatively impacts on the solubility of corresponding substituted analogues.

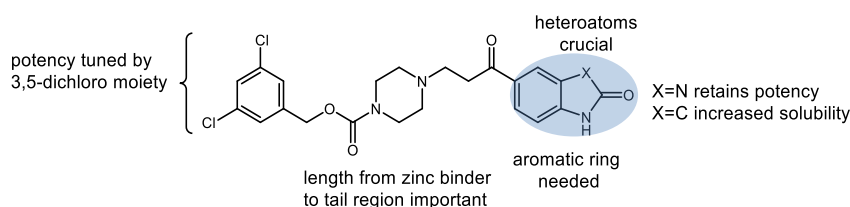


Figure 45: Overview of zinc binding SAR

4.4 PF-8380 Core and Linker Assessment

An initial objective of this SAR study was to probe the activity and pharmacological properties of each region of PF-8380 (**39**). The piperazine ring was defined as the core region and the propan-1-one moiety defined as the linker region of the PF-8380 (**39**) template. A range of altered core and linker analogues of PF-8380 (**39**) were designed in order to understand optimum length, rigidity, and structure of the PF-8380 (**39**) core for ATX inhibition (Figure 46).

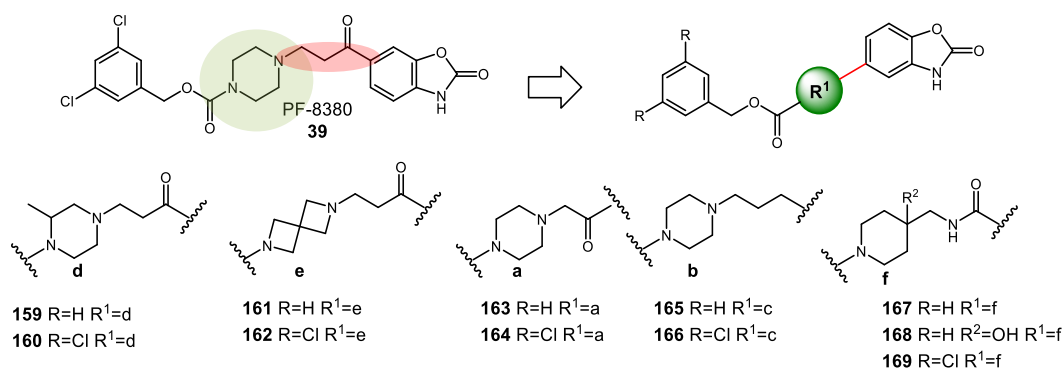


Figure 46: PF-8380 (**39**) core region shaded green, linker region shaded red, target altered core and linker SAR compounds

The first modification proposed was substitution on the 2 position of the piperazine core with a methyl group (**159** and **160**). This analogue was proposed to add additional lipophilic interactions to the core region as the binding site is relatively hydrophobic in nature.

A commonly used approach to rigidify ligand conformation is the introduction of another ring, hence a compound containing a spirocyclic ring system was identified as being of interest. 2,6-Diazaspiro[3.3]heptane also known as homospiropiperazine, is an intriguing ring system which was introduced into the PF-8380 (**39**) scaffold to replace the piperazine ring. Homospiropiperazine is considered a structural surrogate or isostere for piperazine ring systems.¹²⁹ The resulting cyclic analogue would potentially benefit from a reduced conformational entropy penalty upon binding to the ATX enzyme.¹³⁰ Literature precedent has shown that replacing a six-membered monocyclic unit in a drug candidate by a corresponding spiro[3.3]heptane analogue may increase the aqueous solubility, reduce lipophilicity and reduce metabolic degradation (Figure 4).¹³¹ This three-dimensional alteration may give novelty and potentially improved physical properties to the corresponding analogues (**161** and **162**).¹³⁰

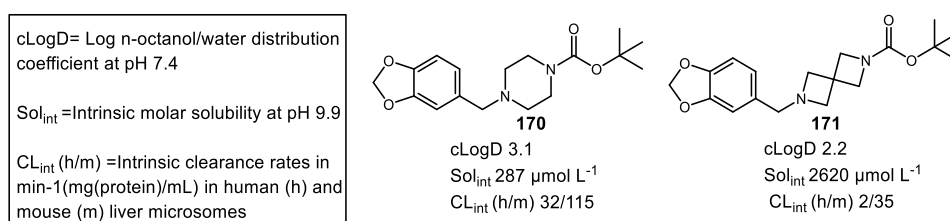


Figure 47: A matched molecular pair highlighting the differences in physicochemical and biochemical properties of piperazine rings and homospiropiperazine rings.¹³¹

Moving on from core modifications, in order to gain information about the optimum length of the linker or space needed between the head group and tail portion of PF-8380 (**39**), a limited number of truncated analogues were prioritised for synthesis. These were targeted both with and without the 3,5-dichlorobenzyl carbamate tail (**163** and **164**).

The second modification to the linker proposed was removal of the ketone to yield simple alkane derivatives (**165** and **166**). The alkane increases flexibility within the active site, mimicking the LPC natural substrate to potentially offer an increase in activity, albeit potentially at an entropic cost. Additionally, the molecular modelling data of PF-8380 (**39**) indicated that ketone adjacent to the benzo[*d*]oxazol-2(3*H*)-one didn't make any specific interactions within the ATX catalytic site. Therefore the removal of this group was of further interest.

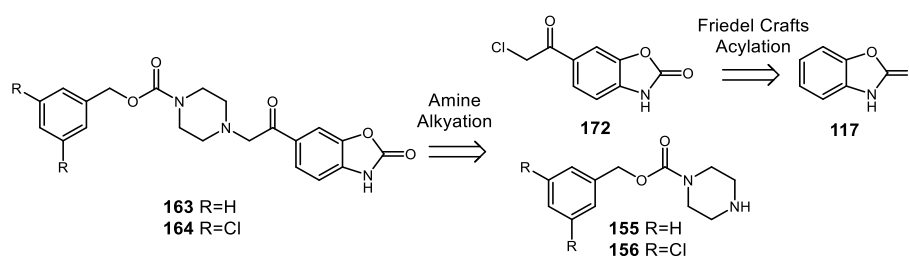
An amide derivative was also proposed, which meant the core was altered from a piperazine to an amino-methyl piperidine. The addition of a hydrogen bond donor

into the linker may add to potency within the series (**168-169**), as well as tuning physicochemical properties such as cLogP and solubility.

4.4.1 Synthetic Access to PF-8380 Core/ Linker Analogues

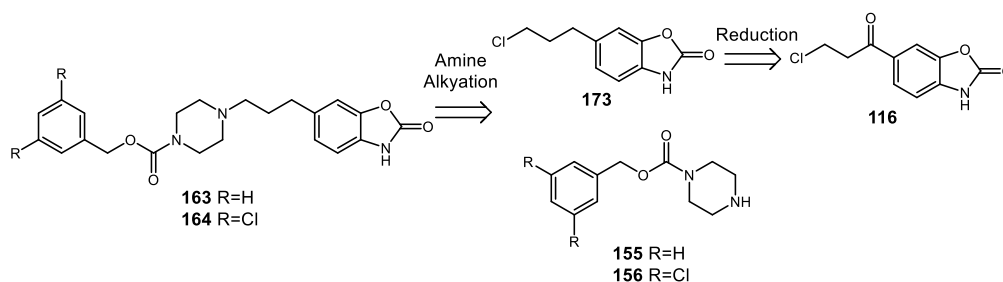
Synthesis of the 2-methylpiperazine analogues (**159-160**), and homospiro-piperazine core analogues (**161-162**) were performed by another member of the laboratory.¹¹⁹ Therefore, the details of the synthetic route undertaken will not be discussed in this thesis.

The retrosynthetic analysis of the truncated analogues (**163** and **164**) suggests that these targets could be prepared through amine alkylation using intermediates (**155** and **156**) and intermediate (**172**), derived from a Friedel Crafts acylation of benzo[*d*]oxazol-2(3*H*)-one (**117**) (Scheme 28).



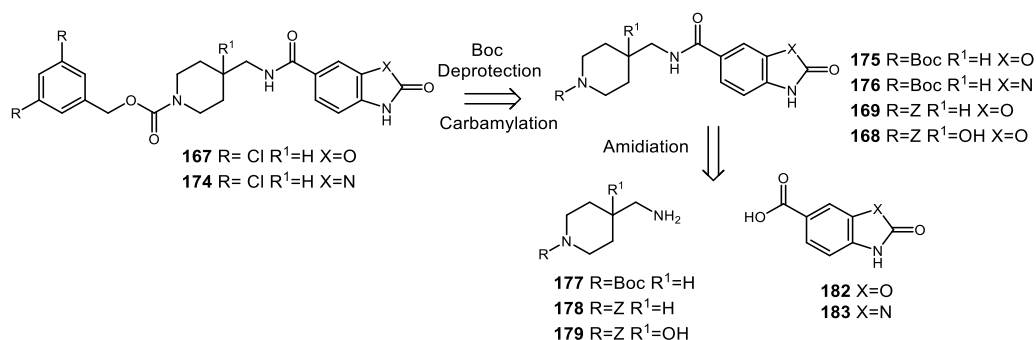
Scheme 28: Retrosynthetic view of truncated analogues **71-72**

The retrosynthetic analysis of the target alkane analogues involved the formation of key alkane intermediate (**85**) *via* reduction of the ketone (**26**). Subsequent amine alkylation follows using (**64** and **65**) to yield final product (**73** and **74**) (Scheme 29).



Scheme 29: Retrosynthetic view of linker SAR analogues **165-166**

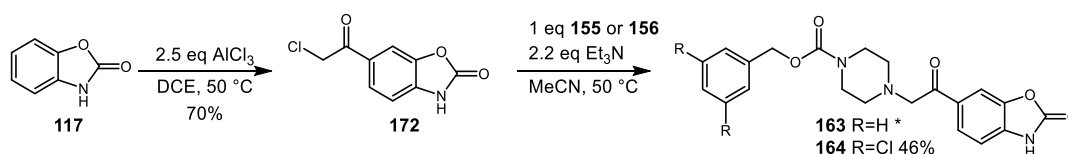
The retrosynthetic analysis of 4-(aminomethyl) piperidine analogues suggested formation of key intermediate **177** and **178** *via* amidation with acids **182** and **183**. Boc removal and carbamylation would then follow to yield final products **167-169**, and **174** (Scheme 30).

Scheme 30: Retrosynthetic view of core SAR analogues **167-169,174**

4.4.2 Synthesis of PF-8380 Core/Linker Analogues

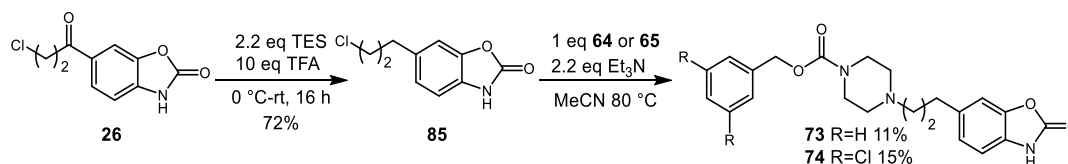
4.4.2.1 Truncated Analogues

To access the one carbon linked acylated chlororalkane (**172**), a Friedel Crafts acylation was performed on benzo[*d*]oxazol-2(3*H*)-one (**116**), and the resulting product (**172**) was used without further purification.⁶⁷ Truncated analogues (**163-164**) were then prepared *via* nucleophilic displacement with the chlororalkane (**172**) (Scheme 31).

Scheme 31: Synthesis of truncated analogues **163-164** (* Analogue prepared by another member of the laboratory.¹¹⁹)

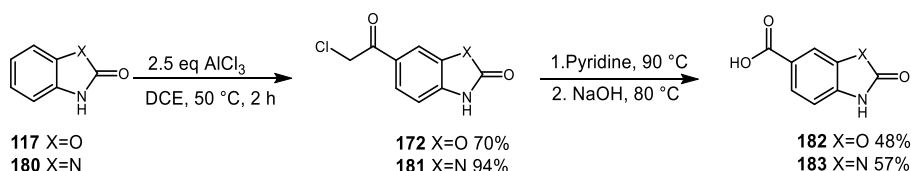
4.4.2.2 Alkane Analogues

6-(3-chloropropanoyl)benzo[*d*]oxazol-2(3*H*)-one (**116**) was reduced using triethyl silane (TES) and trifluoroacetic (TFA) to afford the alkane building block (**173**) (Scheme 32).¹³² The alkane (**172**) was then used in an alkylation reaction with key substituted piperazines (**155-165**) to yield the desired target compounds (**165-166**).

Scheme 32: Synthesis of alkanes **165** and **166**

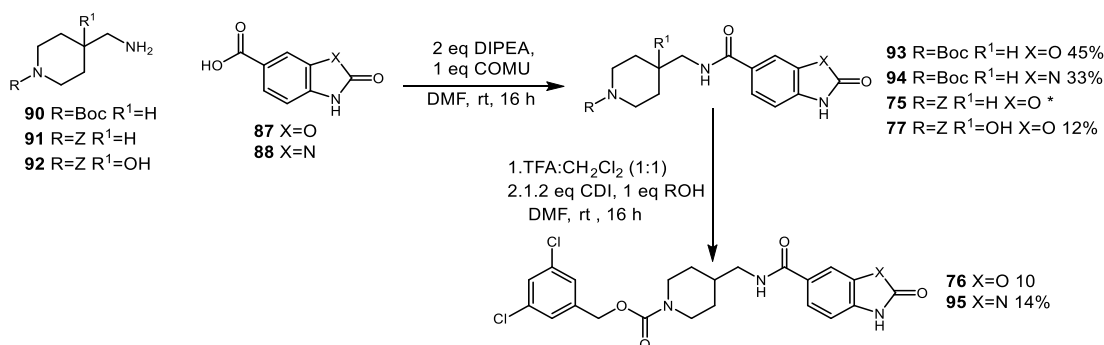
4.4.2.3 4-(Aminomethyl)piperidine Analogues

Synthesis of the 4-(aminomethyl)piperidine analogues started with the preparation of requisite acid derivatives (**182** and **183**). This involved the Friedel Crafts acylation of benzo[*d*]oxazol-2(3*H*)-one (**117**) and 1,3-dihydro-2*H*-benzo[*d*]imidazol-2-one (**180**). The intermediates (**172** and **182**) were heated in pyridine for three hours. The solution was cooled and filtered, and the residue submitted to heating in sodium hydroxide for two hours, followed by an acidic work-up to afford the carboxylic acids (**87** and **88**) (Scheme 33).¹³³



Scheme 33: Synthesis of acids **182** and **183**

Amidation of the commercially available *tert*-butyl 4-(aminomethyl)piperidine-1-carboxylate (**177**), benzyl 4-(aminomethyl)piperidine-1-carboxylate (**178**) and benzyl 4-(aminomethyl)-4-hydroxypiperidine-1-carboxylate (**179**) with carboxylic acids (**182** and **183**) using the coupling reagent COMU in the presence of DIPEA yielded derivatives (**175-169**). The Boc protecting group of intermediates (**175** and **176**) was subsequently removed with TFA and a carbamylation reaction performed using (3,5-dichlorophenyl)methanol to afford the final carbamates (**167** and **174**).



Scheme 34: Synthesis of amide analogues **167-169**, and **174** (* Analogue prepared by another member of the laboratory).¹³⁴

4.4.3 Biological Evaluation of PF-8380 Core/Linker Analogues

The biological activity of 2-methylpiperazine and homospiropiperazine core analogues (**159-162**) were assessed in the bis-*p*NPP assay (1 nM - 30 μ M) (Table 12).

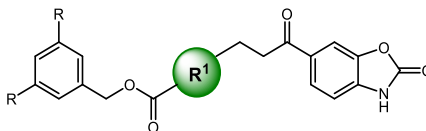


Table 12: Activity profile of compounds **159-162**

Entry	Cpd	R ¹	R	ATX K _i (μ M)	MW	cLogP
Standard	PF-8380 (39)	-	-	0.008	478	3.6
1	159 ^a		H	0.036	423	2.9
2	160 ^a		Cl	0.002	492	4.1
3	161 ^a		H	0.002	421	2.1
4	162 ^a		Cl	0.002	490	3.3

^a analogue prepared by another member of the laboratory.¹¹⁹

Potent ATX inhibition was observed when the 2-methylpiperazine core is included in the PF-8380 (**39**) template as displayed by both the carboxybenzyl analogue (**159**) (0.036 μ M, entry 1) and the 3,5-dichlorobenzyl analogue (**160**) (0.002 μ M, entry 2) (Table 12). The methyl group increases the potency of the unsubstituted analogue (**159**), when compared to the benzyloxycarbonyl analogue (**101**) (0.067 μ M, entry 5, Table 9). The carboxybenzyl analogue (**159**), has an improved physicochemical profile in comparison with PF-8380 (**39**), with 55 Da lower molecular weight and almost one logP unit decrease in cLogP, thus representing an attractive lead. The 3,5-chlorobenzyl containing 2-methylpiperazine analogue (**160**) is almost equipotent to PF-8380 (**39**) at 0.002 μ M (entry 2, Table 12). Despite this the 2-methylpiperazine analogue (**160**) is considered a poor lead compound, as it displays a high molecular weight and cLogP of 492 Da and 4.06 units, respectively.

The 2-methylpiperazine core increases the lipophilic interactions of this template with ATX. Using MOE to analyse both the (*R*)- and (*S*)- enantiomers of 2-methylpiperazine analogue (**160**), it can be inferred that both enantiomers have the potential to hydrophobically interact with a leucine (Leu213) and tyrosine (Try306) (Figure 48). Molecular modelling of these enantiomers infers that the benzo[*d*]oxazol-2(3*H*)-one and 3,5-dichlorobenzyl moieties make identical interactions as PF-8380 (**39**) with ATX, however the chiral methyl group causes an altered conformation of the piperazine ring. The large ATX active site is predicted to accommodate both enantiomers, and vector the methyl group towards this hydrophobic cleft of leucine (Leu213) and tyrosine (Try306).

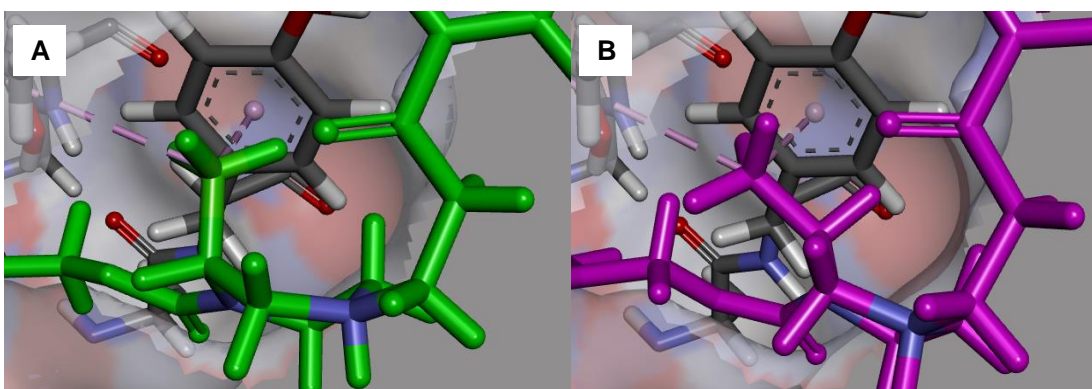


Figure 48: A: (*R*)-**160** (ligand green, piperazine nitrogen blue) B: (*S*)-**160** (ligand pink, piperazine nitrogen blue), energy minimised using MOE against the active site of ATX. Hydrophobic interactions (pink lines) with Leu213 and Tyr306

Potent ATX inhibition is also observed when the homospirropiperazine core is included in the PF-8380 (**39**) template. The carboxybenzyl analogue (**161**) has a K_i of 0.017 μM (entry 3) and the 3,5-dichlorobenzyl analogue (**162**) has a K_i of 0.002 μM (entry 4) (Table 12). The benzyloxycarbonyl analogue (**161**) is of interest with nanomolar activity and improved physicochemical properties of 423 Da molecular weight and a cLogP of 2.9. From consideration of this data, the carboxybenzyl analogue (**161**) is also an attractive lead compound, and accordingly its aqueous solubility was measured and found to be excellent at 353 $\mu\text{g/mL}$ which compares favourably with PF-8380 (**39**). As mentioned earlier homospirropiperazine is considered a structural surrogate for piperazine, however N-N distances have been determined to be longer in the homospirropiperazine structure (Figure 49).

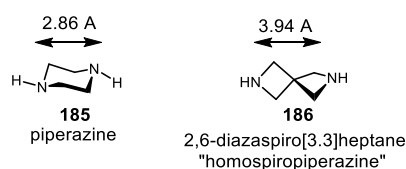


Figure 49: Comparison of piperazine and 2,6-diazaspiro[3.3]heptane N-N lengths

The increase in activity of the homospirpiperazine analogue (**161**) compared to the piperazine analogue (**101**, entry 5, Table 12) implies that the homospirpiperazine core represents the optimum length for this chemotype. The homospirpiperazine analogues (**161** and **162**) are theoretically capable of spanning the active site to the hydrophobic pocket, and the increase in length of the carboxybenzyl analogue (**161**) potentially compensates for the lack of hydrophobic chlorine interactions.

As stated previously, the truncated PF-8380 analogues (**163-164**), were synthesised to probe if a shorter length linker would be tolerated for ATX inhibition in the PF-8380 template (Table 13).

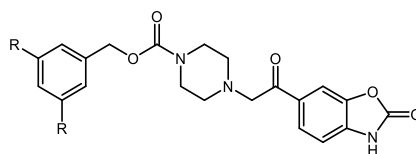


Table 13: Activity profile of compounds **163-164**

Entry	Cpd	R	ATX K_i (μM)	MW	cLogP
Standard	PF-8380 (39)	-	0.008	478	3.6
1	163 ^a	H	3.900	395	2.2
2	164	Cl	0.009	465	3.4

^a analogue prepared by another member of the laboratory¹¹⁹

It can be noted that the 3,5-dichlorobenzyl analogue (**164**, entry 2); the direct analogue of the hit PF-8380 (**39**) is equipotent to PF-8380 (**39**) at 0.009 μM (Table 13). The corresponding carboxybenzyl analogue (**163**) has a significantly lower activity, with a K_i of 3.9 μM (entry 1, Table 13). It is possible this shorter analogue length may need the lipophilic interactions of the chlorines to enhance activity within the hydrophobic pocket in order to compensate for the sub-optimal interactions made with the catalytic site.

In the molecular modelling analysis of PF-8380 (**39**) it was hypothesised that the ketone adjacent to the benzo[*d*]oxazol-2(3*H*)-one does not make any interactions

within the catalytic site of ATX. To establish the significance of this moiety in the PF-template the ketone was removed and analogues (**165-166**) tested in the bis-*p*NPP assay (Table 14).

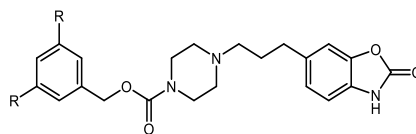


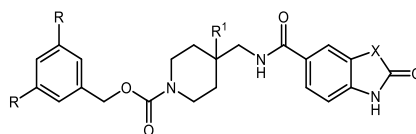
Table 14: Activity profile of compounds **165-166**

Entry	Cpd	R	ATX K_i (μM)	MW	cLogP
Standard	PF-8380 (39)	-	0.008	478	3.6
1	165	H	<30*	395	2.8
2	166	Cl	<30*	463	4.6

*% hydrolysis at 30 μM concentration

The corresponding alkane analogues (**165-166**) were both found to be inactive as ATX inhibitors (<30% hydrolysis, entry 1-2, Table 14). The increase in flexibility designed to mimic the natural substrate LPC did not translate to an increase in ATX inhibition. This inactivity suggests that the ketone adjacent to the benzoxazolone is an important SAR moiety for ATX inhibition. As previously stated, molecular modelling of PF-8380 (**39**) suggested that this ketone did not make any interactions within ATX. Therefore, it can be hypothesised that this ketone potentially acts as structural lock, to vector the position of the benzo[*d*]oxazol-2(3*H*)-one in to the active site. Furthermore both alkane analogues (**165-166**) were poor lead compounds from a physicochemical perspective: having an increased cLogP compared to their direct analogues PF-8380 (**39**, cLogP 3.6) and carboxybenzyl analogue (**101**, cLogP 2.4).

To probe the linker region further and potentially increase the number of hydrogen bond interactions between the linker region and ATX, 4-(aminomethyl) piperidine amide derivatives were synthesised. The 4-(aminomethyl) piperidine amide linked analogues (**167-169**, **174**) in general displayed promising ATX inhibition, therefore the solubility of these analogues were measured (Table 15).

**Table 15:** Activity profile of **167-169**, and **174**

Entry	Cpd	X	R ¹	R	ATX K _i (μM)	MW	cLogP	Solubility (μg/mL)
Standard	PF-8380 (39)	-	-	-	0.008	478	3.6	24
1	167	O	H	H	0.032	409	2.5	238
2	168	O	OH	H	0.122	425	1.3	>459
3	169	O	H	Cl	<30*	478	3.7	33
4	174	N	H	Cl	0.003	477	3.5	71

*% hydrolysis at 30 μM concentration

The carboxybenzyl 4-(aminomethyl) piperidine analogue (**167**, entry 1) has potent ATX inhibition with a K_i of 32 nM (Table 15). This analogue (**167**) is reasoned to be the best lead compound within this sub-series as it has a lower molecular weight of 409 Da, significantly decreased cLogP of 2.5, and increased solubility of 238 μg/mL compared to the progenitor compound PF-8380 (**39**, 24 μg/mL, Table 8). The hydroxyl containing 4-(aminomethyl) piperidine analogue (**168**, entry 2) also has an increased solubility of 459 μg/mL, presumably due to the incorporation of the hydroxyl which could serve as a solubilising group.¹³⁵ Furthermore, this hydroxyl group decreases the cLogP to 1.3. This hydroxyl containing analogue (**168**) is, however, fifteenfold less potent than PF-8380 (**39**) at 0.122 μM and approximately threefold less potent than its corresponding carboxybenzyl analogue (**167**).

The benzo[d]oxazol-2(3*H*)-one amide derivative (**169**, entry 3) containing the 3,5-chlorobenzyl moiety is inactive as an ATX inhibitor with a bis-*p*NPP hydrolysis greater than 30% at 30 μM (Table 15). This result is an outlier within this sub series and potentially could be explained by the poor solubility within aqueous media (33 μg/mL) of this benzo[d]oxazol-2(3*H*)-one amide analogue (**169**), which may interfere with detection in the assay medium.

The 1,3-dihydro-2*H*-benzo[d]imidazol-2-one or urea derivative (**174**, entry 4) containing the the 3,5-chlorobenzyl moiety is however active as an ATX inhibitor with a K_i of 0.003 μM (Table 15). This urea analogue (**174**) does not represent any significant improvement over the hit compound PF-8380 (**39**) as its physicochemical

profile is essentially identical to PF-8380 (**39**), including poor solubility values of 71 µg/mL and a comparatively high cLogP of 3.5.

In conclusion, a 4-(aminomethyl) piperidine amide linker is tolerated within this SAR study of ATX. The 4-(aminomethyl) piperidine amide offers the potential to fine tune both the solubility and cLogP of these analogues when the 3,5-chlorobenzyl moiety is replaced with a simple benzyl moiety.

To recapitulate the SAR data observed for the core/linker region of the PF-template, it was observed that a 2-methylpiperazine increases the hydrophobic interactions of the core (Figure 50). The methyl group on the piperazine ring is chiral; therefore synthesis of the separate enantiomers has the potential to double the activity, making the 2-methylpiperazine analogue (**159**) an interesting lead in this study so far. The homologation of the homospiropiperazine core compared to the piperazine core of PF-8380 (**39**) also increases lipophilic interactions and hence ATX inhibition. Additionally, the overall length of molecule appears to be important in terms of spanning both the catalytic site and hydrophobic pocket of the enzyme. By contrast, the truncated analogues retain activity but the removal of the 3,5-dichlorobenzyl moiety considerably decreases ATX inhibition in this sub series. Removal of the ketone adjacent to the benzo[d]oxazol-2(3H)-one head group is not tolerated but the addition of a 4-(aminomethyl) piperidine amide into the linker retains ATX activity while fine tuning solubility and cLogP of the sub-series.

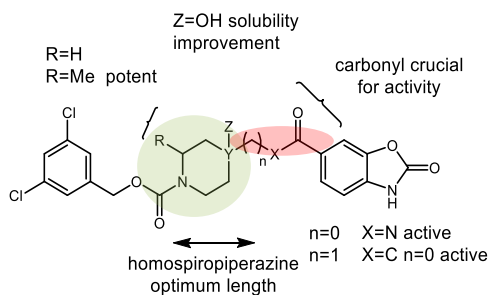
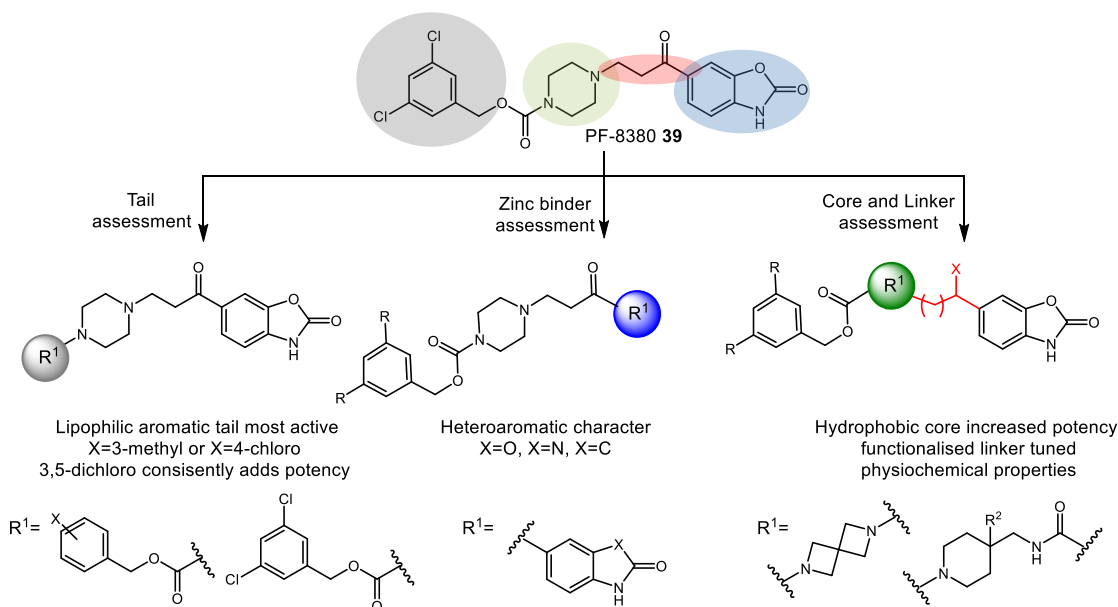


Figure 50: Overview of core and linker SAR

4.5 PF-8380 SAR Overview

In conclusion, an extensive SAR study of PF-8380 (**39**) was conducted which addressed the structural layout of this chemotype; tail region, head group and core functionality. This SAR study highlighted the moieties essential for ATX inhibition and also identified analogues with improved physicochemical properties: increased solubility, decreased molecular weight, and lower cLogP. The structure-activity relationship which ensued was also compared to the modelling and biostructural information for the PF-chemotype. The overall summary of this SAR study is discussed below (Scheme 35).



As discussed in Section 4.3.3, tails with lipophilic aromatic character are essential to efficiently interact with the hydrophobic pocket and inhibit ATX. 4-chloro substitution or 3-methyl substitution of this benzene ring is the minimum determinant likely to retain lipophilic interactions. Going forward, it was necessary to accept that a degree of lipophilicity was needed within the series to achieve good levels of ATX inhibitory activity. Therefore, the 3,5-dichlorobenzyl moiety remained a useful functionality to attain potency.

Molecular modelling and biostructural data suggests that a carbamate moiety linking the piperazine ring to the tail functionality is beneficial. This is probably due to the hydrogen bonds formed between the carbamate carbonyl and tryptophan (Trp275).

In terms of head group interactions with the catalytic site of ATX, simple aliphatic acids and hydroxamic acids are insufficient for ATX inhibition and head groups with heteroaromatic character are superior. The substitution of the ring oxygen in the benzo[*d*]oxazol-2(3*H*)-one moiety for nitrogen to form a urea derivative retains potent ATX inhibition. The removal of the ring oxygen in the benzo[*d*]oxazol-2(3*H*)-one moiety to form an oxindole head group was also identified as an efficient ATX inhibitor. Furthermore, the oxindole moiety increased aqueous solubility of carboxybenzyl derivatives. In the case of the urea and oxindole analogues, the carbonyl of the head group is postulated to chelate to the zinc.

The optimum core moiety identified in this SAR study was the homospiropiperazine bringing novelty to this chemotype. The linker moiety of the PF-8380 (**39**) chemotype is relatively flexible in nature. ATX inhibition was attained with truncated analogues and particular 4-(aminomethyl) piperidine amide derivatives. Specific 4-(aminomethyl) piperidine amide analogues demonstrated an excellent balance of potency and physicochemical properties, including aqueous solubility. Based on biostructural data, functionality in the linker region of the PF-chemotype has the potential to interact with polar amino acids arginine (Arg244) and glutamate (Glu308) of ATX.

This SAR study is the first comprehensive overview of the tool compound PF-8380 (**39**) and builds greatly on the paucity of SAR information reported in the literature to date.¹¹⁷ With the identification of essential components of the PF-chemotype and an understanding of the inhibitory binding of ATX, an iterative structure-based drug design programme proceeded.

4.6 Structure-based Drug Design and Lead Analysis of ATX Inhibitors

The process of structure-based drug design is an iterative one and often proceeds through multiple cycles before an optimised lead is identified for further evaluation.¹¹⁸ Molecular modelling is frequently used within these cycles to dock potential drug molecules into the active site of the target in order to evaluate potential interactions and assist in prioritising analogues for synthesis. In the second cycle structure determination of the target in complex with a lead from the first cycle reveals sites on the compound that can be optimised to increase potency. After several cycles of the drug design process, the optimised compounds usually show marked improvement in the binding to the target and improved physicochemical

properties.¹¹⁸ From the extensive SAR study of PF-8380 (**39**), two interesting ATX inhibitors emerged for further development through application of structure based drug design: the homospirpiperazine analogue (**162**) and the truncated PF-8380 analogue (**164**) (Figure 51).

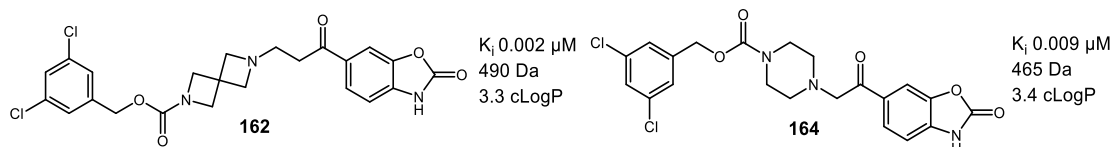


Figure 51: Compounds identified from PF-8380 (**39**) SAR study for further development

A prerequisite for structure based drug design is an understanding of the principles of molecular recognition in protein-ligand complexes. From molecular modelling of PF-8380 (**39**) and comparison with information obtained from the co-crystallisation of ATX/alcohol analogue ((*S*)-**96**), confidence was established that the molecular docking of ensuing analogues reliably recapitulated actual ligand ATX-interactions.

4.6.1 Homospirpiperazine Structure-based

The incorporation of the homospirpiperazine or four-membered heterocycles into the PF-8380 scaffold provides an opportunity to uniquely tune the physicochemical and biochemical properties of the series while entering novel chemical space.

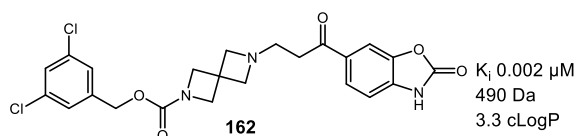


Figure 52: Homospirpiperazine analogue **162**

The homospirpiperazine analogue (**162**) has a K_i value of 0.002 μM , equipotent to PF-8380 (**39**). The molecular weight of homospirpiperazine (**162**) is 478 Da, a moderate increase from PF-8380 (**39**), and cLogP marginally decreased to 3.3. The potential of this homospirpiperazine functionality was highlighted in the PF-8380 (**39**) SAR study, when this scaffold increased the potency and solubility of carboxybenzyl homospirpiperazine derivative (**161**) (0.002 μM , 353 $\mu\text{g/mL}$) compared to its piperazine analogue (**101**) (0.076 μM , 67 $\mu\text{g/mL}$). The 3,5-dichlorobenzyl homospirpiperazine analogue (**162**) is one point change away from PF-8380 (**39**). It was decided to progress the development of a homospirpiperazine series using this single point change analogue. Whilst accepting the physicochemical issues the 3,5-dichlorobenzyl group presents, this hydrophobic moiety gives potency to the

series. By utilising analogue (**162**) as a lead compound direct comparisons can be made with SAR data obtained in the study of PF-8380 (**39**), thus a more sequential and stepwise progression of ATX inhibition can be assessed. Once a potent novel compound inhibitor was identified within this series the physicochemical properties could be optimised by potentially removing the 3,5-dichlorobenzyl moiety and replacement with an aromatic moiety with more favourable chemical properties.

4.6.1.1 Molecular Modelling of Homospirropiperazine Analogue

Having established the similarities in the binding modes between the crystal structure of ATX and docked structures. MOE¹²¹ software was employed by the author to study the novel homospirropiperazine lead compound (**162**) (Figure 53).

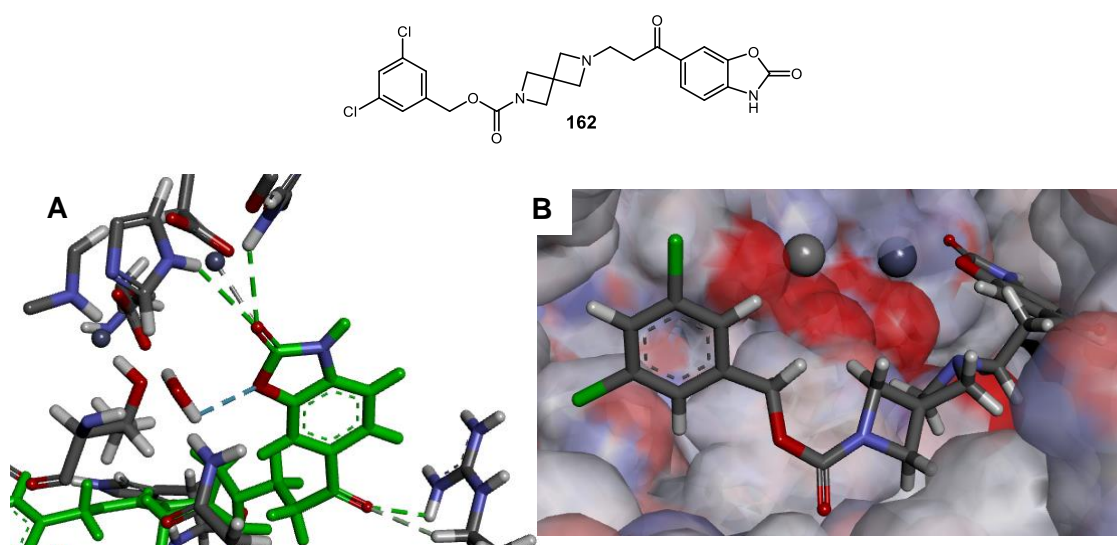


Figure 53: Molecular modelling of **162** using MOE and diagrams prepared using DS Visualizer.¹²⁰ A: **162** interacting with catalytic site (dotted lines, hydrogen bonds blue and green, chelation grey) B: Pose of **162** spanning the active site of ATX.

From the molecular modelling study it was inferred that the carbonyl of the benzo[*d*]oxazol-2(3*H*)-one chelates to the catalytic zinc ion (grey lines, Figure 18) and hydrogen bonds to the two histidine residues (His474 and His315) present in the catalytic site. The ring oxygen of the benzo[*d*]oxazol-2(3*H*)-one hydrogen bonds with a water molecule (HOH129) (blue lines, Figure 18), which is coordinated to the catalytic threonine (Thr209) and asparagine (Asn310). This slightly altered orientation of the benzo[*d*]oxazol-2(3*H*)-one, in comparison with co-crystal structure ATX/alcohol analogue ((*S*)-**96**), may be due to the ketone adjacent to the benzo[*d*]oxazol-2(3*H*)-one. This ketone possibly locks the benzo[*d*]oxazol-2(3*H*)-one

into a specific vector and orientates the benzo[d]oxazol-2(3*H*)-one into the catalytic site. The oxygen of this ketone can then hydrogen bond with the proximal arginine (Arg 244) (green lines, Figure 53).

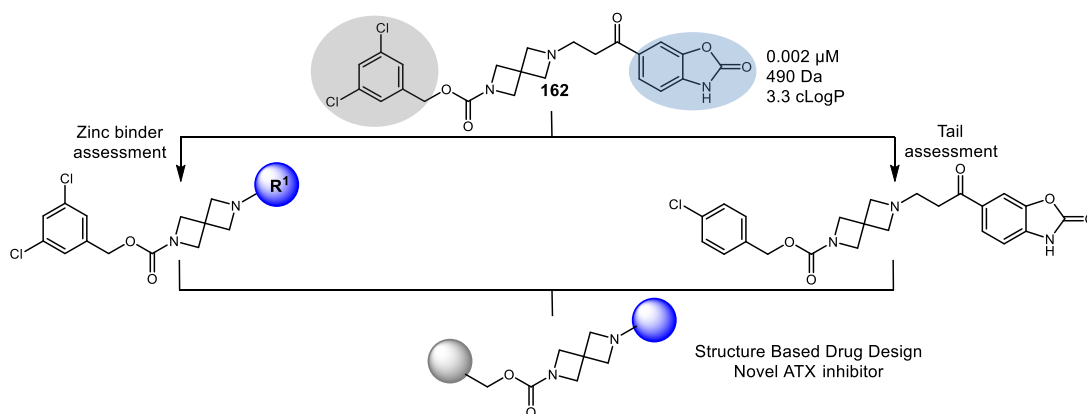
By modelling analysis it appears that the homospiropiperazine core of the lead analogue (**162**) makes identical interactions compared to the piperazine core of progenitor analogue (**96**) (co-crystal structure, Section 4.2.2). The saturated homospiropiperazine ring has hydrophobic interactions with a tyrosine (Tyr306) residue.

In terms of the tail region of this homospiropiperazine analogue (**162**), the carbonyl of the carbamate moiety forms a hydrogen bond with a phenylalanine (Phe274). The 3,5-dichlorobenzene moiety makes hydrophobic interactions with phenylalanine (Phe273), alanine (Ala304), leucine (Leu213), leucine (Leu216) isoleucine (Ile167), alanine (Ala217), phenylalanine (Phe274), and tryptophan (Trp260) similar to co-crystal structure ATX/ alcohol analogue ((*S*)-**96**).

Overall, the binding pose of the homospiropiperazine is similar to the co-crystallised analogue ((*S*)-**96**). The benzo[d]oxazol-2(3*H*)-one interacts with the catalytic site through zinc chelation and the inhibitor spans the length of the ATX active site, from the zinc ions in the catalytic domain to the hydrophobic pocket.

4.6.1.2 Homospiropiperazine SAR Design Strategy

Further elaboration of the SAR around homospiropiperazine analogue (**81**) was developed using knowledge gained in the PF-8380 (**39**) SAR study and molecular modelling data. The SAR of this homospiropiperazine series focuses on the zinc binding aspect of ATX inhibition to increase potency and gain further novelty. In addition to optimising interactions with the ATX binding site, a second objective was to investigate if SAR trends observed in the PF-8380 (**39**) study were transferable in this novel homospiropiperazine series with respect to the tail region (Scheme 36).



Scheme 36: Iterative design of the homospiropiperazine core

The targeted homospiropiperazine analogues with modified zinc binding motifs are discussed below (Figure 54). Molecular modelling data of homospiropiperazine lead analogue (**162**) suggested that the ketone adjacent to the benzo[*d*]oxazol-2(3*H*)-one head group hydrogen bonded to a proximal glutamate (Glu308) residue. Therefore this hydrogen bond acceptor moiety was retained in the subsequent homospiropiperazine inhibitors (**186-197**). Moreover, PF-8380 (**39**) SAR suggested that an aromatic ring attached to the zinc binding group was also beneficial, therefore a benzene moiety is retained in the homospiropiperazine analogues (**186-197**).

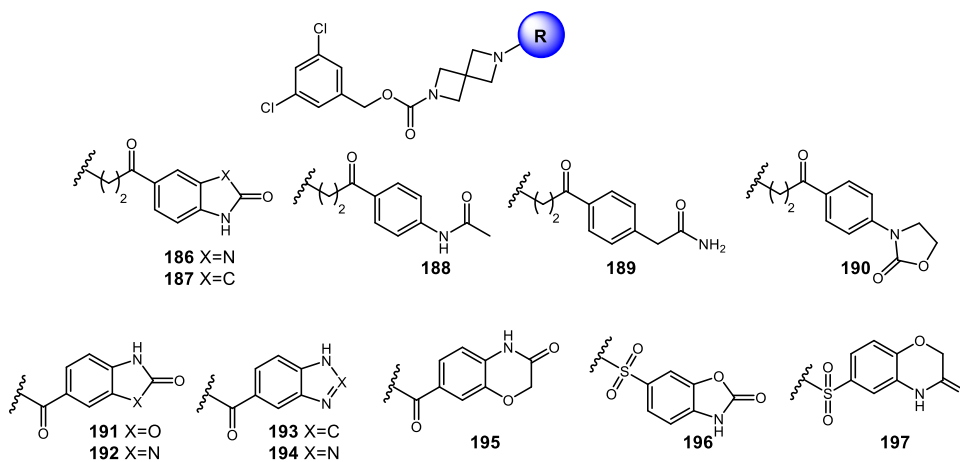


Figure 54: SAR of target homospiropiperazine zinc binders

Molecular modelling of analogue (**162**) also projected the ring carbonyl moiety of benzo[*d*]oxazol-2(3*H*)-one to interact with a zinc ion in the active site. Therefore, modified head group analogues (**186-192**, **195-197**) were designed with this carbonyl retained. Urea and oxindole based head groups (**186-187**) were included

for synthesis as these motifs were found to be important in contributing to potency from the earlier studies in this series. Furthermore, the oxindole derivate has the potential to increase aqueous solubility of its parent compound as previously noted. Acetamides (**188-189**) and oxazolidinone (**190**) derivatives were proposed for synthesis to potentially gain potency and to enhance novelty of the homospiropiperazine template.

It was also planned to attach a zinc binding group directly to the homospiropiperazine core (**191-197**). Deletion of the linker region (ethyl spacer) with a zinc binding group directly bonded to the core would decrease molecular weight and cLogP of the corresponding analogues. It was hypothesised that these analogues could retain the ability to span the active site, from the catalytic site to the hydrophobic pocket. Additionally the PF-8380 (**39**) study highlighted in the need for an acidic zinc binder, and therefore the acid isosteres, imidazole (**193**) and triazole (**194**) analogues were suggested for synthesis.

A 4-chlorobenzyl carbamate analogue (**198**) was also planned for synthesis in this homospiropiperazine series (Figure 55). The 4-chlorobenzyl moiety was found to be active within the PF-8380 (**39**) SAR study, with improved physicochemical properties compared to the 3,5-dichlorobenzyl moiety.

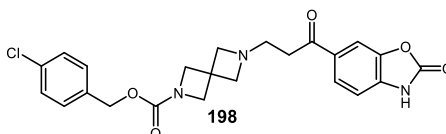
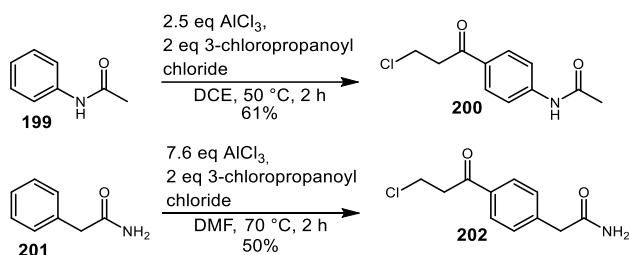


Figure 55: Target homospiropiperazine tail analogue

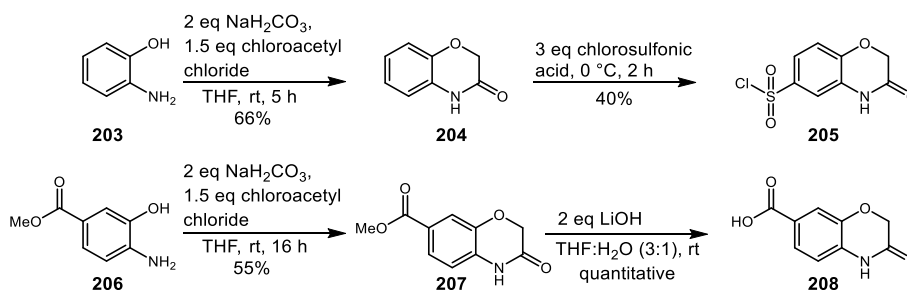
4.6.1.3 Homospiropiperazine Analogues Synthesis

Study of the homospiropiperazine analogues began with the preparation of the zinc binding head groups, carried out in conjunction with another member of the laboratory.¹¹⁹ The potential acetamide zinc binders (**200** and **200**) were prepared *via* a Friedel Crafts acylation of commercially available *N*-phenylacetamide (**199**) and 2-phenylacetamide (**201**) (Scheme 37).



Scheme 37: Synthesis of zinc binding groups **200** and **202**

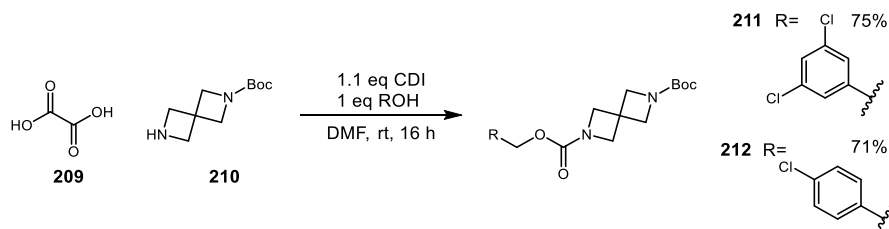
The formation of sulfonyl halide (**205**) and carboxylic acid (**208**) began with an alkylation and *in situ* cyclisation of 2-aminophenol and methyl 4-amino-3-hydroxybenzoate, to form intermediates (**204** and **207**), respectively.¹³⁶ Intermediate (**204**) was reacted with chlorosulfonic acid to form the sulfonyl chloride (**205**), and intermediate (**207**) was hydrolysed under basic conditions to afford the carboxylic acid (**208**) (Scheme 38).



Scheme 38: Synthesis of binding head groups **205** and **208**

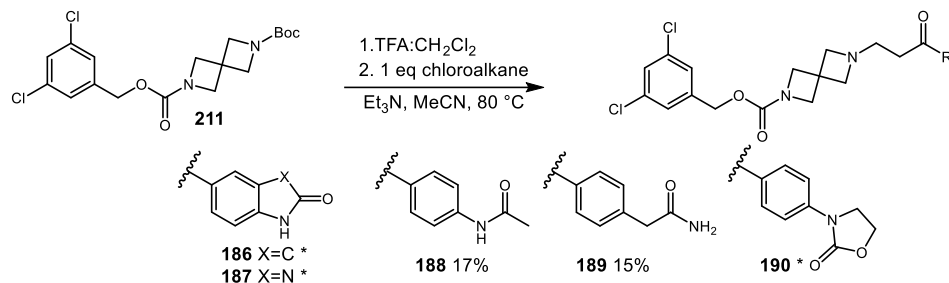
The remaining zinc binding building blocks were either synthesised as previously reported or prepared by another member of the laboratory.¹¹⁹

Synthesis of homospirropiperazine analogues was analogous to the chemistry applied to the PF-8380 (**39**) SAR study. Commercially available 2,6-diazaspiro[3.3]heptane-2-carboxylic acid *tert*-butyl ester hemioxylate (**110**) was reacted with CDI and (3,5-dichlorophenyl)methanol or (4-chlorophenyl)methanol in DMF to provide the corresponding carbamates (**111,126**) (Scheme 19c).



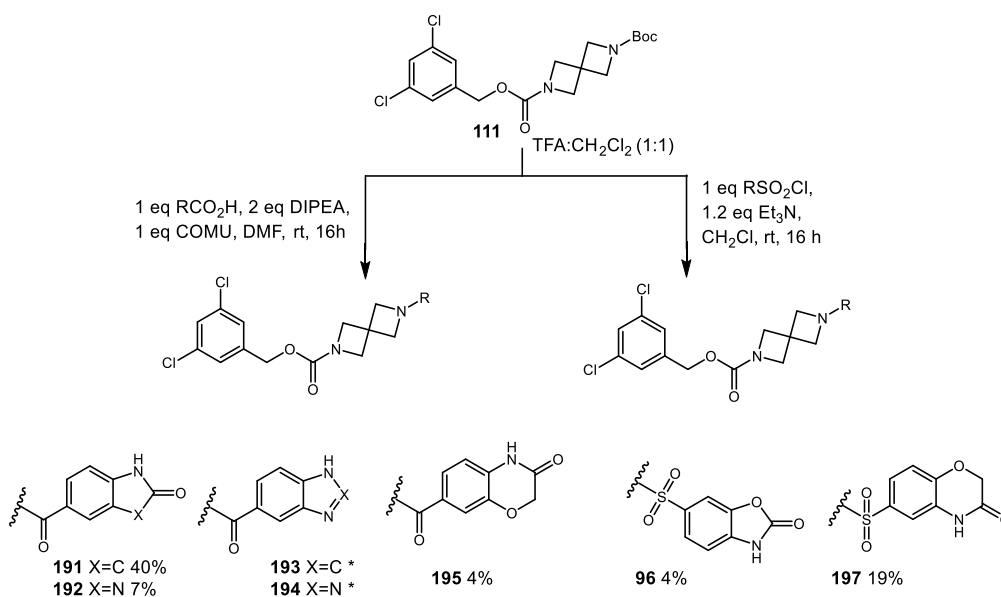
Scheme 39: Synthesis of homospirropiperazine intermediate **211** and **212**

The Boc protected homospirropiperazine intermediate (**211**) was treated with trifluoroacetic (TFA) in dichloromethane to remove the protecting group. The revealed amine was telescoped into an alkylation reaction with various chlororalkanes to yield analogues (**186-190**) (Scheme 40).



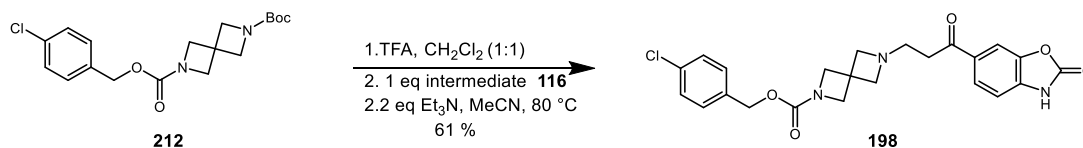
Scheme 40: Synthesis of homospirropiperazine analogues **186-190** (* Analogue prepared by another member of the laboratory. ¹¹⁹)

The Boc protected homospirropiperazine intermediate (**211**) was treated with trifluoroacetic (TFA) in dichloromethane to remove the protecting group. The free amine was utilised in two processes: an amidation reaction with various acids to yield analogues (**191-194**), and sulfonamide formation to yield analogues (**196** and **197**) (Scheme 41).



Scheme 41: Synthesis of homospirropiperazine analogues **191-197** (* Analogue prepared by another member of the laboratory. ¹¹⁹)

The targeted 4-chlorobenzyl carbamate analogue (**198**) was prepared *via* an alkylation reaction using 6-(3-chloropropanoyl)benzo[d]oxazol-2(3*H*)-one intermediate (**116**) and 4-chlorobenzyl 2,6-diazaspiro[3.3]heptane-2-carboxylate, generated from intermediate (**212**) (Scheme 42).



Scheme 42: Synthesis of tail analogue **198**

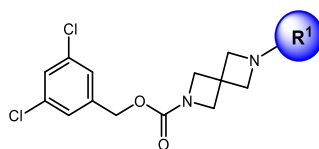
4.6.1.4 Homospiropiperazine Analogues Biological Evaluation

Following the synthesis of the homospiropiperazine analogues (**186-197**), each of the compounds were evaluated in the bis-*p*NPP ATX assay (Table 11).

It can be noted that the novel homospiropiperazine analogues generally followed the trends observed in the PF-8380 (**39**) series. The oxindole analogue (**187**, entry 2), with a K_i of 0.122 μM , is essentially less active than the urea derivative (**186**, entry 1) with a K_i of 0.067 μM (Table 16).

The novel homospiropiperazine analogues (**188**, entry 3), (**189**, entry 4), (**190**, entry 5) with novel head groups are inactive as ATX inhibitors at <30% hydrolysis of the bis-*p*NPP substrate (Table 16). From this it can be deduced that these moieties do not chelate to the zinc ions present in ATX or interact with the catalytic site of ATX.

The acid isosteres imidazole (**193**, entry 6) and triazole (**194**, entry 7) are active ATX inhibitors with K_i values of 0.074 μM and 0.028 μM , respectively (Table 16). It is noteworthy that the novel triazole (**194**) stands out as an interesting and potent ATX inhibitor. Triazole (**194**) has an acceptable molecular weight of 446 Da and an improved clogP value of 2.9, two logP units lower than lead homospiropiperazine analogue (**162**). Moreover, the triazole compound (**194**) has a chemical structure that is altered extensively from lead homospiropiperazine analogue (**162**) and can be further differentiated from the original hit compound PF-8380 (**39**), with only the 3,5-dichlorobenzyl motif remaining. Accordingly, multiple point changes from hit compound PF-8380 (**39**) have allowed entry to entirely novel chemical space.

**Table 16:** Activity profile of compounds 186-197

Entry	Cpd	R ¹	ATX K _i (μM)	MW	cLogP
1	186^a		0.067	489	3.1
2	187^a		0.122	488	2.9
3	188		<30*	490	3.2
4	189		<30*	490	2.8
5	190^a		<30*	518	3.5
6	193^a		0.074	445	2.7
7	194^a		0.028	446	2.9
8	191		0.038	462	2.9
9	192		0.118	461	2.8
10	195		8.191	476	2.4
11	196^a		0.100	496	2.4
12	197		0.105	512	2.1

^a analogue prepared by another member of the laboratory. ¹⁹ *% hydrolysis at 30 μM concentration

The benzo[*d*]oxazol-2(3*H*)-one derivative (**191**, entry 8) and the 1,3-dihydro-2*H*-benzo[*d*]imidazol-2-one derivative (**192**, entry 9), directly linked to the homospirropiperazine core *via* an amide bond are both active with K_i of 0.038 μM and 0.118 μM , respectively (Table 16). These shortened analogues are however less active than their extended counterparts **161** (0.0017 μM , Table 12, entry 3) and **162** (0.002 μM , Table 12, entry 4). From this decrease in activity, it can be inferred that inhibitor length is an important parameter within the homospirropiperazine series, in parallel to the PF-8380 (**39**) series. The molecular modelling data also supports this result as both the piperazine and homospirropiperazine rings make identical interactions within the active site of ATX.

The benzo[*b*][1,4]oxazin-3(4*H*)-one analogue (**195**, entry 10), showed only modest ATX inhibition with a K_i of 8.191 μM (Table 16). The sulfonamide linked analogues (**196**, entry 11, and **197**, entry 12) are by comparison more potent ATX inhibitors with K_i values of 0.253 μM and 0.105 μM , respectively (Table 16). Comparing the benzo[*d*]oxazol-2(3*H*)-one derivative (**191**, 0.038 μM) with its sulfonamide equivalent (**196**, 0.253 μM) it can be seen that the sulfonamide is less potent; hence a sulfonamide linker is not optimum for this chemotype. This decrease in activity could potentially be explained by an unfavourable interaction with the arginine (Arg244) of the ATX active site.

The activity and physicochemical profile of 4-chlorobenzyl homospirropiperazine analogue (**198**) are discussed below (Table 17).

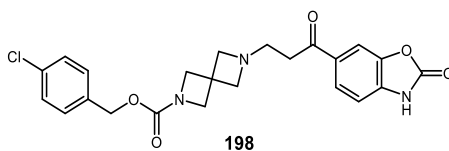


Table 17: Activity profile of compounds **198**

Entry	Cpd	ATX K_i (μM)	MW	cLogP
1	198	0.135	455	2.7

The 4-chlorobenzyl homospirropiperazine analogue (**189**, entry 2) is less active than homospirropiperazine analogue lead (**162**) at 0.135 μM (Table 17). In the PF-series the 4-chlorobenzyl moiety was equipotent to the 3,5-dichlorobenzyl moiety, this equivalent potency trend is not observed in the homospirropiperazine series. The

chlorine of of 4-chlorobenzyl moiety potentially makes an unfavourable clash with the hydrophobic pocket of ATX, which may be attributed to the increase in length associated with the homospiropiperazine spacer.

In conclusion, removal of the ethyl linker moiety homospiropiperazine analogues (**193** and **194**) retained the ability to inhibit ATX, with encouraging K_i values in the range of 0.118-0.028 μM . This suggests that these analogues have the ability to span ATX from the catalytic site to the hydrophobic pocket resulting in good levels of potency. It was reasoned in the molecular modelling data that the carbonyl of the benzo[*d*]oxazol-2(3*H*)-one moiety binds to the zinc ions present in the active site of ATX. Potent ATX inhibition was attained, however, with a triazole analogue (**194**), lacking this carbonyl moiety. This triazole analogue emerges as a compound for further optimisation. As stated earlier the triazole analogue (**194**) has optimum physicochemical properties: molecular weight 446 Da and clogP 2.9. To fully understand the binding interactions of the triazole (**194**), work is on-going to obtain a co-crystal structure of this analogue in complex with ATX.

Concluding the SAR around the homospiropiperazine series, the oxindole derivative (**187**) was less active than the lead benzo[*d*]oxazol-2(3*H*)-one derivative homospiropiperazine (**162**). Expansion of the heterocyclic ring of the head group to form the benzo[*b*][1,4]oxazin-3(4*H*)-one analogue (**195**) also decreased activity. Removal of this cyclic ring system in compounds (**188-189**) resulted in complete loss of activity. One altered tail analogue (**198**), with a 4-chlorobenzyl carbamate moiety in place of the 3,5-dichlorobenzyl moiety resulted in decreased ATX inhibition (Figure 56). Further investigation of this tail region is needed within this homospiropiperazine lead series.

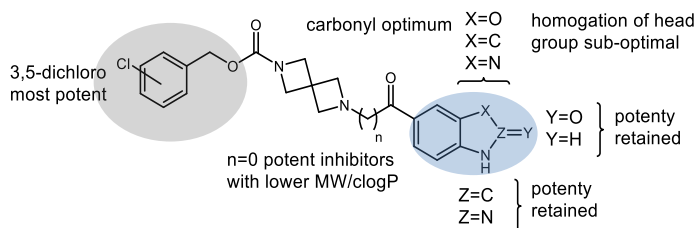


Figure 56: Overview of homospiropiperazine series

4.6.2 Truncated Series Lead Optimisation

As discussed earlier, the process of structure-based drug design is iterative and often proceeds through multiple cycles examining several lead compounds. In this process each lead series is considered in an attempt to produce more potent and selective compounds which possess favourable pharmacokinetic properties to increase the probability of finding a candidate molecule for further development.¹¹⁸

The extensive SAR study of PF-8380 (**39**) highlighted a lead compound, which was a truncated analogue of PF-8380 (**164**) (Figure 57). This truncated analogue (**164**) is noted to be equipotent to PF-8380 (**39**), hence displaying maximal inhibition of bis-*p*NPP cleavage assay. It exhibits marginally improved physicochemical properties in comparison with PF-8380 (**39**), with a molecular weight of 465 Da, cLogP of 3.4. The truncated analogue (**164**) is claimed within the original Merck KGaA patent but no SAR data is available in the literature with regards to this analogue.⁶⁷

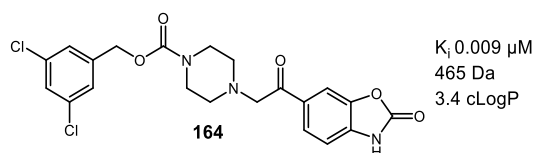


Figure 57: Truncated analogue **164** identified from PF-8380 (**39**) SAR

The truncated lead analogue (**164**) remained structurally similar to PF-8380 (**39**), therefore it was decided that this lead was an ideal compound for further structure based drug design and lead optimisation. A series of PF-8380 (**39**) truncated SAR compounds were proposed for further study. The aim of this stage of the work was to refine the lead compound and further improve its developability profile. Moreover, it was assumed that structural data obtained from the SAR of PF-8380 (**39**) would be reflected in a truncated lead series, allowing expedient identification of novel, highly potent analogues.

4.6.2.1 Molecular Modelling of Truncated Lead Analogue

Molecular modelling software was employed to study the truncated lead (**164**), using MOE¹²¹. The aim of the molecular modelling was to fully assess the potential binding interactions made by the truncated analogue (**164**) with the ATX active site (Figure 58).

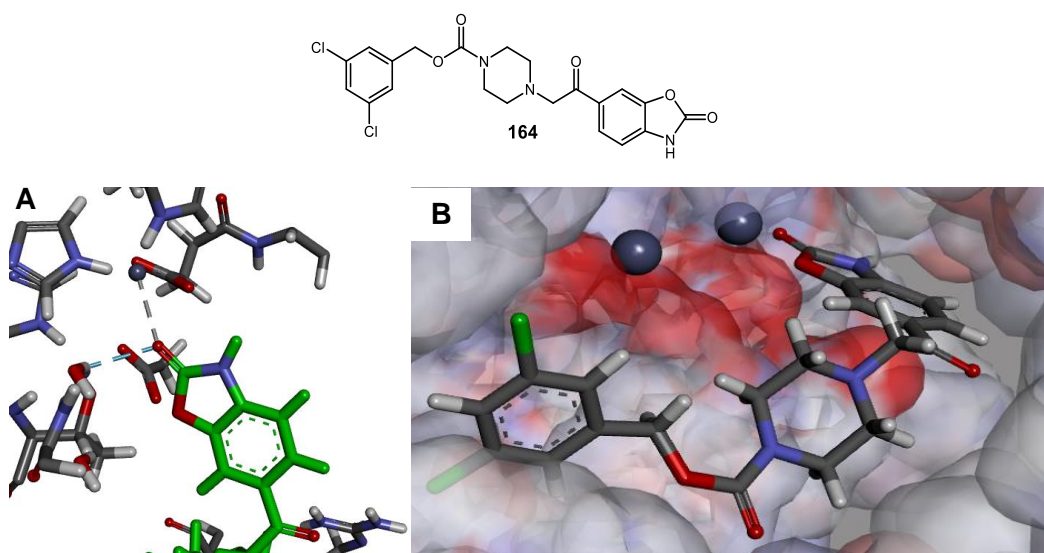


Figure 58: Molecular modelling of **164** using MOE and diagrams prepared using DS Visualizer. A: **164** interacting with catalytic site (dotted lines, hydrogen bonds blue and green, chelation grey) B: **164** spanning the active site of ATX.

From the molecular modelling, it was determined that the carbonyl of the benzo[*d*]oxazol-2(3*H*)-one again chelates to the catalytic zinc ion (grey lines, Figure 58) and hydrogen bonds to a bound water molecule. In this instance, the ring oxygen of the benzo[*d*]oxazol-2(3*H*)-one does not appear to make any interactions with the active site in this model. The ketone adjacent to the benzo[*d*]oxazol-2(3*H*)-one also is predicted to be 3.5 Å away from an arginine (Arg244) residue which could result in a weak hydrogen bond.¹³⁷

The piperazine ring resides in a chair conformation making the same hydrophobic interactions with tyrosine (Tyr306) and hydrogen bond with tryptophan (Trp275), as noted in the co-crystal structure of alcohol analogue ((*S*)-**96**). Furthermore, the 3,5-dichlorobenzyl moiety of the truncated analogue (**164**) also makes identical hydrophobic interactions as co-crystallised alcohol analogue ((*S*)-**96**).

As discussed above, the ketone adjacent to the benzo[*d*]oxazol-2(3*H*)-one could potentially make weak electrostatic interactions with an arginine (Arg244) (Figure 20). The possibility of transforming this ketone into another functional group to gain further interactions was interesting, and accordingly an oxime derivative was proposed. The corresponding oxime analogue (**213**) of the truncated lead analogue (**164**) was docked into the active site of ATX using MOE¹²¹ and the potential for additional interactions was assessed (Figure 59).

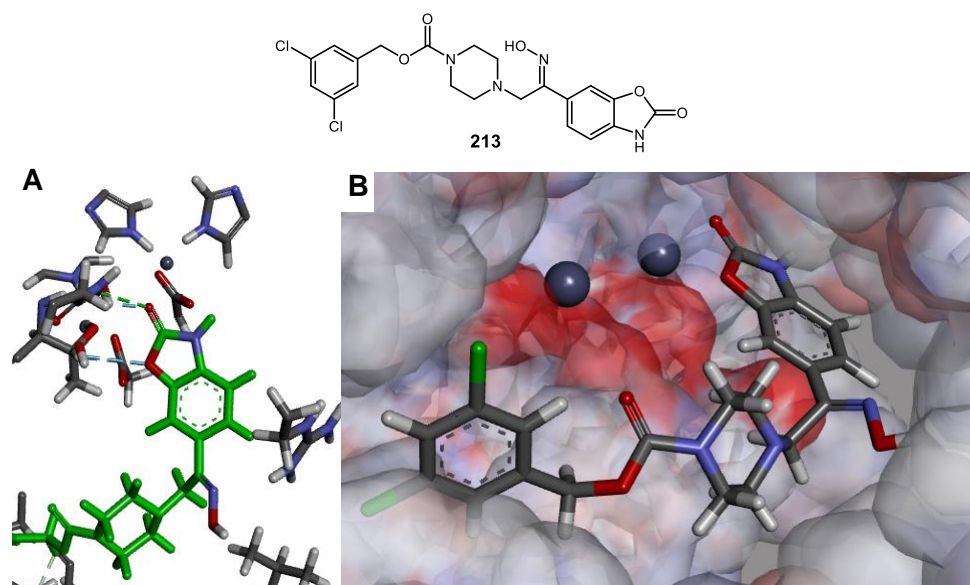


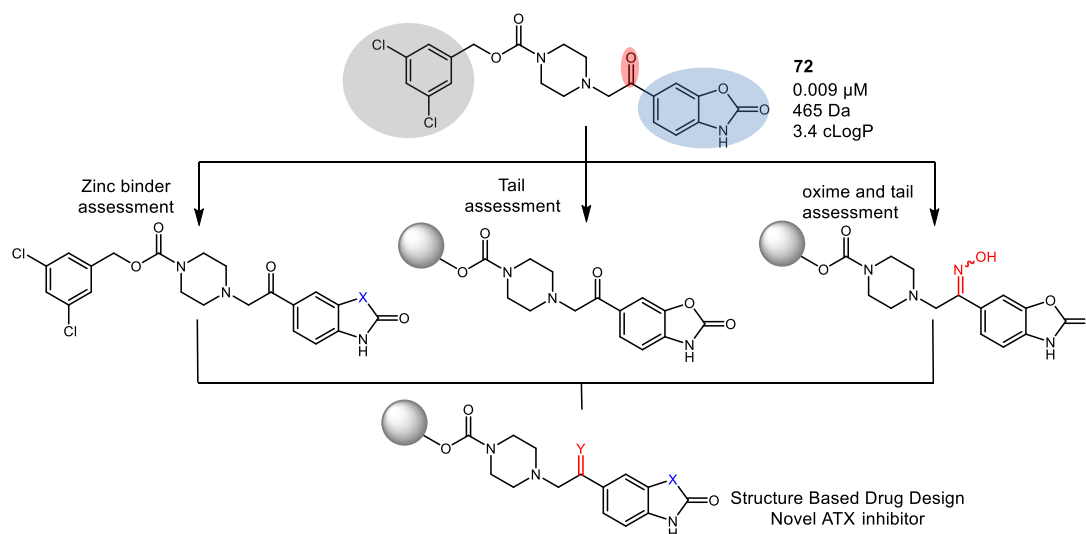
Figure 59: Molecular modelling of **213** (Z-isomer) using MOE and diagrams prepared using DS Visualizer.¹²⁰ A: Analogue **213** interacting with catalytic site (dotted lines, hydrogen bonds blue and green, chelation grey) B: Diagram of **213** spanning the active site of ATX.

From the molecular modelling data it was deduced that the benzo[*d*]oxazol-2(3*H*)-one head group of the oxime analogue (**213**) resides in an altered pose compared to the progenitor truncated analogue (**164**) (Figure 22). In the case of the oxime (**213**), the carbonyl of the benzo[*d*]oxazol-2(3*H*)-one hydrogen bonds to the asparagine (Asn230) in the catalytic site, compared to the benzo[*d*]oxazol-2(3*H*)-one carbonyl of lead analogue (**164**) interacting with a zinc ion. The ring oxygen of the benzo[*d*]oxazol-2(3*H*)-one of the oxime analogue (**213**) hydrogen bonds to the backbone of the catalytic threonine (Thr209). Furthermore, the oxime moiety appears to point towards the solvent in this model. This may increase the solubility of the oxime analogue (**213**). Oximes generally form a mixture of geometric isomers, therefore depending on the orientation of the oxime, it could potentially hydrogen bond to a proximal valine (Val277) or salt bridge to the arginine (Arg244).

The piperazine ring also resides in a chair conformation like its parent analogue truncated lead (**164**), making a hydrophobic interaction with tyrosine (Tyr306). Additionally, the tail or 3,5-dichlorobenzyl moiety of the oxime analogue (**213**) makes identical hydrophobic interactions compared to those proposed for the truncated analogue (**164**).

4.6.2.2 Truncated Series SAR Strategy

The SAR strategy of the truncated series again leveraged knowledge gained from the PF-8380 (**39**) series. The zinc binding and tail regions of this truncated series would be altered, incorporating functionalities associated with activity and favourable physicochemical properties that were identified in the previous PF-8380 (**39**) SAR study. As described in Section 4.7.2.1 an oxime moiety was also proposed to be included in this truncated series, similarly the zinc binding region and tail region of truncated oxime analogues would be probed (Scheme 43).



Scheme 43: Iterative design of the truncated series

The target analogues identified are discussed below (Figure 60). It was decided to firstly probe the acidic head group and binding mode of this truncated series, with a urea and an oxindole derivative (**113-116**). The oxindole moiety was identified as having potent ATX inhibition ability within the PF-8380 (**39**) SAR study. It was also identified as improving the aqueous solubility of analogues containing this head group. Therefore, an oxime analogue incorporating the oxindole functionality was intended for synthesis (**121**). The inclusion of the oxindole may aid in clarifying the binding hypothesis of the oxime analogue (**213**): that the ring oxygen atom of the benzo[*d*]oxazol-2(3*H*)-one makes central hydrogen bonds with the catalytic threonine (Thr209).

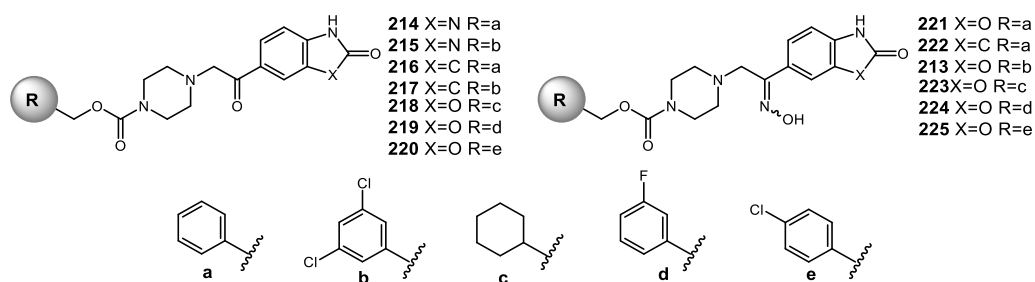
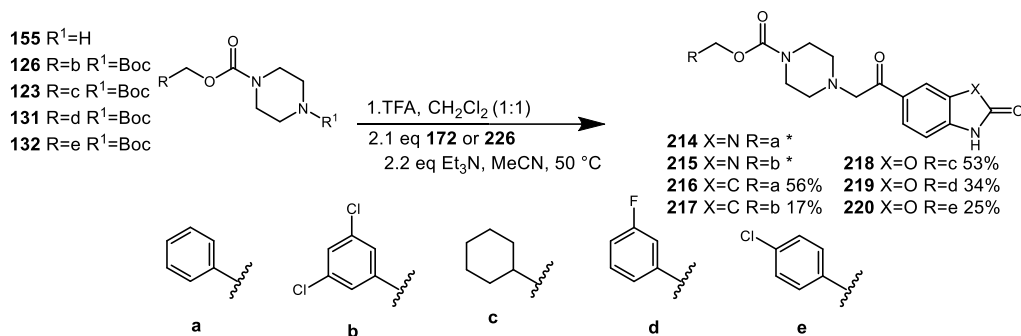


Figure 60: Target truncated compounds **214-220** and target oxime analogues **213, 221-225**

It was decided to fine tune the physicochemical properties of the truncated series by removing the 3,5-dichlorobenzyl moiety and replacement of this functional group with alternative tails. The tails selected showed both ATX inhibition or improved lipophilicity in the PF-8380 (**39**) series. The piperazine ring was functionalised with a cyclohexylmethyl carbamate (c), 3-fluorobenzyl carbamate (d), and 4-chlorobenzyl carbamate (e). The cyclohexylmethyl carbamate analogue (**218**) has the lowest molecular weight in this sub series of 401 Da, 63 Da lower than the progenitor compound (**164**). In the binding hypothesis of the truncated lead (**164**), it was inferred that alkyl hydrophobic interactions can occur between the aromatic ring of the ligand and a leucine (Leu213), and alanine (Ala304) in the hydrophobic pocket of ATX. The aliphatic cyclic analogue (**218**) would challenge this binding hypothesis. The 3-fluoro analogue (**219**) would reinstate the aromatic character of the tail but lower the clogP by 1 unit from the truncated lead compound (**164**). The 4-chloro analogue (**220**) was also proposed, as this motif was seen to retain activity in the PF-8380 (**39**) SAR study, while lowering molecular weight and cLogP. It was anticipated this motif would also preserve activity within the truncated series. Oxime analogues (**213, 121-125**) were planned, mirroring the modifications made in the truncated series.

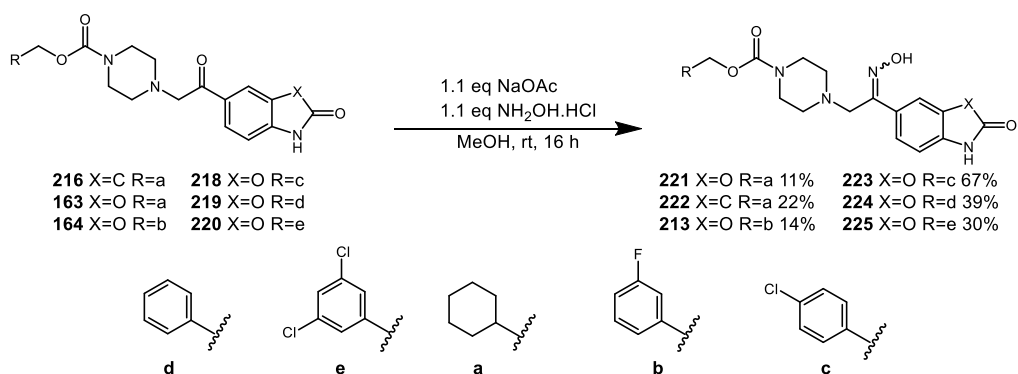
4.6.2.3 Truncated Series Analogue Synthesis

The Boc protecting group of substituted piperazine intermediates (**123, 126, 131, and 132**), to yield amine intermediates. Commercially available 1-Z-piperazine and the amine intermediates were utilised in nucleophilic displacement reactions with chloroalkane building blocks (**172 and 226**) to form truncated analogues (**214-220**) (Scheme 44).



Scheme 44: Synthesis of truncated analogues **214-220** (Analogue prepared by another member of the laboratory.¹¹⁹)

Attention then turned to the oxime analogue synthesis. Ketones (**163**, **164**, **218-220**) were reacted with hydroxylamine hydrochloride to give corresponding oximes (**221-225**) assumed to be equal mixtures of E- and Z- isomers (Scheme 45).

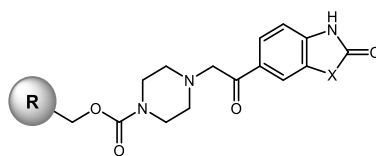


Scheme 45: Synthesis of truncated oxime analogues **221-225**

4.6.2.4 Truncated Series Analogue Biological Evaluation

Following synthesis of the target compounds, the utility of the truncated series (**214-220**) as ATX inhibitors was evaluated in the bis-*p*NPP ATX inhibition assay (Table 18).

It was observed that the urea containing compound (**214**, entry 1) is an active ATX inhibitor with a K_i of 1.946 μ M (Table 18). The corresponding 3,5-dichlorobenzyl urea containing analogue (**215**, entry 2) is inactive with inhibition greater than 30% hydrolysis of the bis-*p*NPP substrate (Table 18). The lack of activity of the 3,5-dichlorobenzyl moiety with the urea analogue (**215**) does not follow the general trend observed previously: that the lipophilic chlorines make significant hydrophobic interactions which contribute majorly to the overall potency, inferring a potential difference in binding mode.

**Table 18:** Activity profile of compounds **214-220**

Entry	Cpd	X	R	ATX K_i (μM)	MW	cLogP
1	214	N ^a		1.946	394	2.0
2	215	N ^a		<30*	463	3.2
3	216	C		1.400	393	1.9
4	217	C		0.115	462	3.2
5	218	O		0.115	401	2.6
6	219	O		0.291	413	2.3
7	220	O		0.074	429	2.8

^a analogues prepared by another member of the laboratory *% hydrolysis at 30 μM

The oxindole derivatives (**216**, entry 3 and **217**, entry 4) are active inhibitors with K_i values of 1.4 μM and 0.115 μM , respectively (Table 18). This supports the molecular modelling data in which the ring oxygen of the benzo[d]oxazol-2(3*H*)-one of the oxime analogue (**213**) does not appear to make any interactions with the active site of ATX.

The cyclohexylmethyl carbamate containing ketone (**218**, entry 5) and 3-fluorobenzyl carbamate containing ketone (**219**, entry 6) are also active ATX inhibitors, with K_i values of 0.115 μM and 0.291 μM , respectively (Table 18). The 4-chloro analogue (**220**, entry 7) is the most active within this sub series with a K_i of 0.074 μM (Table 18). This analogue also has highly desirable physicochemical properties with a molecular weight of 429 Da and cLogP of 2.8.

From the exploration of the truncated series no inhibitor was identified that matched the potency of the lead truncated analogue (**164**, 0.0094 μM). Overall the truncated analogues (**214-220**) are less active than the lead truncated analogue (**164**), however these compounds generally tend to have better physicochemical properties, specifically being of lower molecular weight and cLogP.

Oximes (**214-225**) were also accessed for their ability to inhibit ATX using the bis-*p*NPP inhibition assay (Table 15).

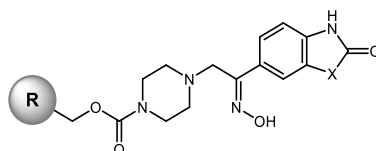


Table 19: Activity profile of compounds **214-225**

Entry	Cpd	R	X	ATX K_i (μM)	MW	cLogP
1	221		O	1.100	410	2.0
2	222		C	<30*	408	1.8
3	213		O	0.003	478	3.2
4	223		O	0.261	416	2.4
5	224		O	0.103	428	2.2
6	225		O	0.100	445	2.6

*% hydrolysis at 30 μM concentration

A range of ATX inhibition activities were seen for the novel oxime compounds. The benzo[*d*]oxazol-2(3*H*)-one containing analogue (**221**, entry 1) was active with a K_i of 1.1 μM (Table 19). This is an increase in potency compared to the truncated carboxybenzyl analogue (**163**, 3.900 μM , Table 13, entry 1). Furthermore, this oxime carboxybenzyl analogue (**221**) was found to have excellent solubility of 157 $\mu\text{g/mL}$.

By contrast, the oxindole containing analogue (**222**, entry 2) was inactive and showed a percentage hydrolysis of the bis-*p*NPP substrate greater than 30% (Table 19). This infers that the ring oxygen of the benzo[*d*]oxazol-2(3*H*)-one makes a significant interaction within the catalytic site within this oxime series, as hypothesised by the binding mode, discussed in Section 4.6.2.1.

The cyclohexyl containing analogue (**223**, entry 4), 3-fluoro containing analogue (**224**, entry 5), and 4-chloro containing analogue (**225**, entry 6) are less active than the truncated lead (**164**) with K_i values of 0.261 μM , 0.103 μM and 0.100 μM , respectively (Table 19). This may be due to the loss of hydrophobic interactions in the pocket region of ATX, which is known to contribute to potency.

The most active analogue within this series is the benzo[*d*]oxazol-2(3*H*)-one containing oxime (**213**, entry 3) with a K_i value of 0.003 μM (Table 19). To fully determine the inhibition potential of this analogue (**213**) and assess the quality of this novel analogue as a drug compound its physicochemical properties were measured in a series of physicochemical assays within GSK. It was found to have a chromlogD of 3.4 (optimum ≤ 4), LLE of 0.337 (optimum ≤ 0.3), and a PFI of 5.4 (optimum ≤ 6). The solubility of this analogue was measured also and found to be sub-optimal at 33 $\mu\text{g/mL}$ (optimum ≥ 100 $\mu\text{g/mL}$). Comparing the oxime carboxybenzyl analogue (**221**, 1.100 μM , 157 $\mu\text{g/mL}$) with the 3,5-dichlorobenzyl (**213**, 0.003 μM , 33 $\mu\text{g/mL}$) the importance of the lipophilic 3,5-dichloro moiety is once again highlighted. This hydrophobic moiety significantly increases potency at the expense of good aqueous solubility, and increases the cLogP by one log unit.

Overall, the addition of the oxime moiety into the truncated series retained ATX inhibition (Figure 61). The molecular modelling of the oxime moiety implied that the oxime feasibly points towards solvent in the ATX structure. Therefore, this functional group potentially improves the solubility of analogues of the truncated template, substituted with alternative tails than the 3,5-dichlorobenzyl moiety. It would be important to test these oxime analogues in the kinetic solubility assay, described previously, to clarify this theory. The 3,5-dichlorobenzyl significantly increases potency, with increased clogP and decreased solubility. It was hypothesised that carbonyl of the benzo[*d*]oxazol-2(3*H*)-one containing oxime analogues hydrogen bonds to the asparagine (Asn230) in the catalytic site. Additionally, it was postulated that the ring oxygen of the benzo[*d*]oxazol-2(3*H*)-one containing oxime analogues hydrogen bonds to the backbone of the catalytic threonine (Thr209). To

prove the binding model of the oxime analogues efforts are on-going to attain a co-crystal structure of an oxime analogue with ATX.

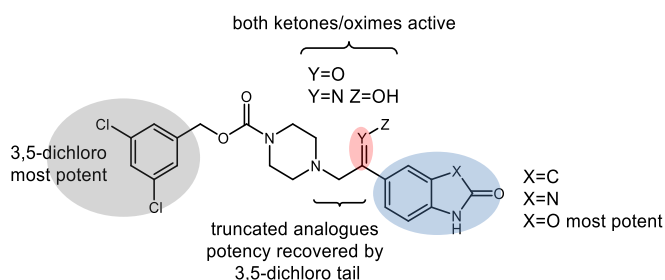


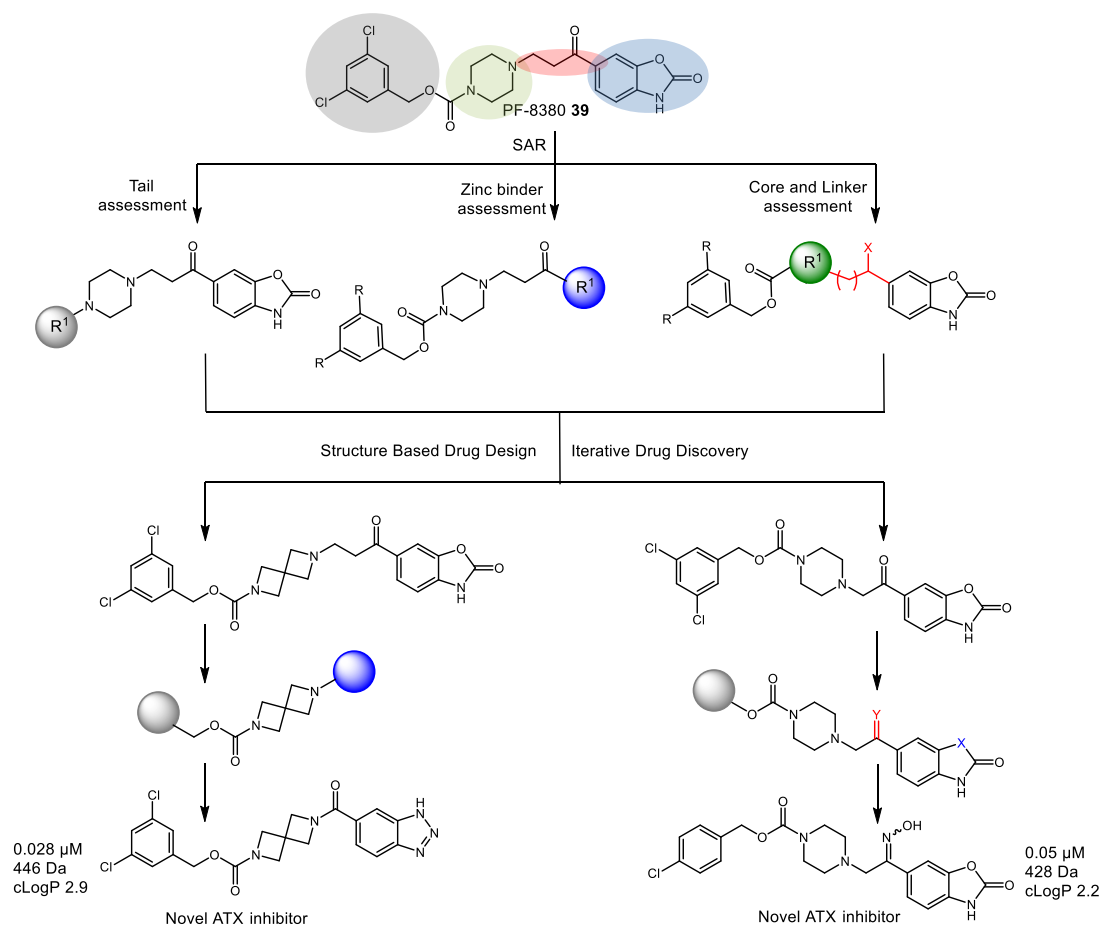
Figure 61: Overview of truncated series

4.7 Conclusions

In summary 42 PF-8380 (**39**) analogues were designed, synthesised and their biological activity evaluated against the ATX enzyme. The SAR study conducted suggested that the most effective ATX inhibitor should contain both a zinc binding moiety and a large bulky lipophilic tail group. Multiple core and linker moieties retained potent ATX inhibition. It was found that alterations of the core and linker region affected the physicochemical properties of the analogues, specifically improving cLogP and solubility. An iterative drug design cycle was then pursued in which additional ATX inhibitors were identified, with improved lead-like properties (Scheme 46).

This work reported, for the first time, the co-crystal structure of ATX in complex with a PF-8380 (**39**) analogue. The X-ray crystallography data was used to help guide productive interactions within the ATX enzyme. A model of PF-8380 (**39**) binding with ATX was consistent with both the X-ray data and information obtained from the PF-8380 (**39**) SAR study. Two potent ATX inhibitors were identified from the SAR study for further improvement. Using X-ray crystallography data, molecular modelling and biological data gained within this research programme the two lead compounds were refined in an iterative process. X-ray crystal structures often reveal active sites which contain hydrophobic pockets, as in the case of ATX.¹³⁸ A misguided but common design tactic in structure-based drug design focuses only on potency and automatically increases molecular weight and generally increases the lipophilicity of the inhibitors to fill these hydrophobic pockets.¹³⁹ Therefore, the refinement of these lead compounds concentrated on controlling molecular weight and cLogP as well as retaining potent ATX inhibition. In conclusion, novel potent

ATX inhibitors were identified through this research with lead compounds that can be clearly differentiated from the hit compound PF-8380 (**39**).



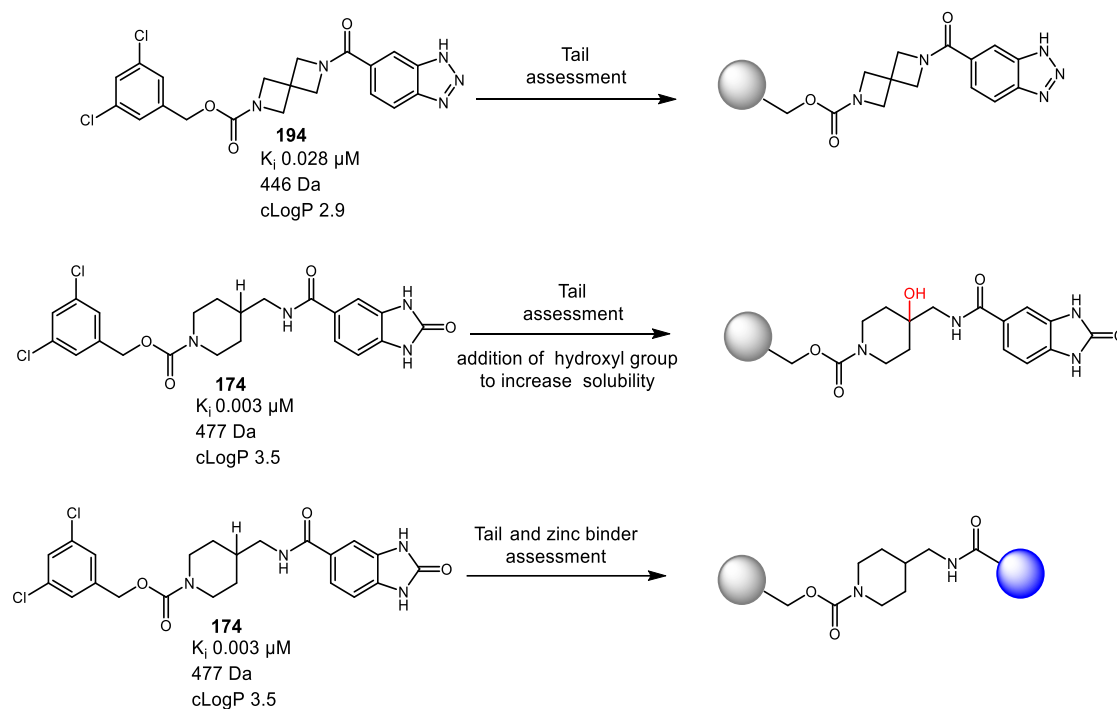
Scheme 46: Conclusive overview of research trajectory

4.8 Future Work

Investigation of the tool inhibitor PF-8380 (**39**) led to the identification of novel, potent ATX inhibitors with improved physicochemical properties. Returning to the iterative drug design process, several inhibitors could be placed back into the design cycle; three exemplars are discussed below .

The homospiropiperazine analogue (**194**) has a triazole head group directly linked to the core region, attaining potency and novelty (0.028 μM). The physicochemical properties of this homospiropiperazine analogue (**194**) should be measured to assess its druglikeness. Efforts should also be made to attain a co-crystal structure of this homospiropiperazine analogue (**194**) and ATX, to fully understand its contributions to binding and compare it to the benzo[*d*]oxazol-2(3*H*)-one moiety binding modes. Moreover, further exploration of the tail region of this analogue (**194**)

could advance the physicochemical properties of this ATX inhibitor, through tuning lipophilicity and retaining ATX inhibitory activity (Scheme 47).



Scheme 47: **Potential further SAR to be explored**

The 4-(aminomethyl) piperidine analogue (**174**) is also a potent ATX inhibitor (0.003 μ M) with poor aqueous solubility of 71 μ g/mL. To increase the aqueous solubility of this analogue a hydroxyl group could be included into its structure, as a hydroxyl group has previously been proven to increase solubility within this chemotype. Additionally, the tail region of this analogue could also be assessed to lower the molecular weight (Scheme 47). Removal of the 3,5-dichlorobenzyl moiety would also potentially improve aqueous solubility, as observed in the PF-8380 (**39**), homospiropiperazine, and truncated templates. It would also be of interest to further explore the 4-(aminomethyl) piperidine template with regards to zinc binders. Potent head groups with improved physicochemical properties identified from the modifications of the homospiropiperazine series could be combined with this 4-(aminomethyl) piperidine template. In particular a triazole group could be prioritised for synthesis. This amalgamation of potent zinc binders, a 4-(aminomethyl) piperidine core and tail groups with increased solubility may lead to superior ATX inhibitors, with regards to potency and physicochemical properties than inhibitors currently in the literature.

Several potent ATX inhibitors have been established in this research programme using the unnatural ATX assay substrate bis-*p*NPP. It would be worthwhile to assess these active ATX inhibitors using the natural substrate assay: the LPC choline release assay. Accompanying this it would be important to evaluate these inhibitors in cells, potentially fibroblast cells to measure their potential as lead compounds which could be of utility as new treatment units for IPF.

5 Chapter 5: Experimental

5.1 General Techniques

All reagents and solvents were obtained from commercial suppliers and were used without further purification.

5.1.1 Experimental Details

- i) Air-sensitive reactions were carried out using oven-dried glassware and purged with N₂ before use.
- ii) Purging refers to a vacuum/nitrogen-refilling procedure.
- v) Reactions were carried out at 0 °C using ice/water baths.
- vi) Room temperature was generally *ca.* 18 °C.
- vii) Reactions were carried out at elevated temperatures using a temperature-regulated hotplate/stirrer.

5.1.1.1 Purification of Products

- i) Thin layer chromatography was carried out using Merck silica plates coated with fluorescent indicator UV254. These were analysed under 254 nm UV light or developed using potassium permanganate solution.
- ii) Flash chromatography was carried out using ZEOprep 60 HYD 40-63 µm silica gel or IST Isolute Flash silica cartridges.
- iii) Mass directed automated purification (MDAP) was conducted on an XBridge C18 column (100 mm x 30 mm i.d., 5 µm packing diameter) at room temperature. Purifications were performed using a gradient method range of 0-99% MeCN in H₂O over 25 min at a flow rate of 40 mL/min.
- iv) Reverse-phase HPLC purification was carried out using a Gilson preparative HPLC system of 322 pumps coupled to a 151 UV/Vis spectrometer, 234 Autoinjector and a GX-271 liquid handler using a Agilent Zorbax SB-C18, 21.2 x 100 mm, 5µ column at room temperature. Purifications were performed using a gradient method range of 5 - 90% MeCN in H₂O over 15

min at a flow rate of 10 mL/min. Analysis was carried out using Gilson Trilution software.

5.1.1.2 Analysis of Products

- i) Fourier Transformed Infra-Red (FTIR) spectra were obtained on a Shimadzu IRAffinity-1 instrument.
- ii) ^1H and ^{13}C NMR spectra were obtained on a Bruker DRX 500 spectrometer at 500 and 126 MHz, respectively; or on a Bruker AV3 400 spectrometer at 400 and 101 MHz, respectively. Chemical shifts are reported in ppm and coupling constants are reported in Hz with CDCl_3 referenced at 7.27 (^1H) and 77.23 ppm (^{13}C), DMSO-d_6 referenced at 2.50 (^1H) and 39.51 ppm (^{13}C) and MeOD referenced at 3.31 (^1H) and 49.15 ppm (^{13}C)
- iii) High-resolution mass spectra were obtained on a Thermofisher LTQ Orbitrap XL instrument at the EPSRC National Mass Spectrometry Service Centre (NMSSC), Swansea.
- iv) LCMS data was obtained on an Agilent 1200 series LCMS with a 6130 single quadrupole.

5.1.2 General Experimental Procedures

General Procedure A: Hydantoin synthesis

For example, for the preparation of 1-(4-bromobenzyl)-3-phenylimidazolidine-2,4-dione, **64**.

To a round-bottomed flask was added methyl 2-((4-bromobenzyl) amino) acetate (**76**, 0.4 g, 1.55 mmol), CH_2Cl_2 (38 mL) and phenyl isocyanate (0.3 mL, 3.08 mmol). The clear solution was stirred at room temperature for 16 h. The reaction mixture was concentrated and azeotroped three times with CH_2Cl_2 (10 mL). The mixture was redissolved in CH_2Cl_2 (15 mL). TFA (3.16 mL, 41 mmol) was added and the solution stirred for 2 h at room temperature. The reaction was quenched with saturated NaHCO_3 (20 mL) and extracted using CH_2Cl_2 (3 x 20 mL). The organics were collected, dried (hydrophobic frit) and concentrated under vacuum to a residue that was purified using silica gel chromatography (30% EtOAc in petroleum ether) to afford the desired product as a yellow amorphous solid (0.34 g, 60%).

General Procedure B: Suzuki-Miyaura and hydrolysis

For example, for the preparation of 2-(4'-((2, 4-dioxo-3-phenylimidazolidin-1-yl)methyl)-[1,1'-biphenyl]-4-yl)acetic acid, **49**.

To a round-bottomed flask was added 1-(4-bromobenzyl)-3-phenylimidazolidine-2,4-dione (**64**, 0.18 g, 0.52 mmol), methyl 2-(4-(4,4,5,5-tetramethyl-1,3,2-dioxaborolan-2-yl)phenyl)acetate (0.16 g, 0.57 mmol), Pd₂(dba)₃ (1 mol%, 5 mg, 0.01 mmol), K₃PO₄ (0.19 g, 0.89 mmol) and PCy₃ (2.4 mol %, 4 mg, 0.01 mmol). The flask was purged with N₂ before adding 1,4-dioxane (4 mL) and H₂O (1.3 mL). The reaction was stirred for 16 h at 100 °C. The reaction mixture was allowed to return to room temperature and concentrated under vacuum to a residue that was filtered through a silica plug (EtOAc). The filtrate and washings were collected, concentrated under vacuum to a residue that was purified using silica gel chromatography (50 % EtOAc in petroleum ether) to afford methyl 2-(4'-((2,4-dioxo-3-phenylimidazolidin-1-yl)methyl)-[1,1'-biphenyl]-4-yl)acetate as a white solid (41 mg, 19%). Methyl 2-(4'-((2,4-dioxo-3-phenylimidazolidin-1-yl)methyl)-[1,1'-biphenyl]-4-yl)acetate (41 mg, 0.10 mmol) was dissolved in THF:H₂O (3:1, 3 mL), LiOH (8 mg, 0.2 mmol) was added and the reaction stirred for 3 h at room temperature. The solution was acidified using HCl (1M, 2 mL) and extracted using EtOAc (2 x 15 mL), and washed with brine (10 mL). The organics were collected, dried (hydrophobic frit) and concentrated under vacuum to afford the desired product as a white powder (25 mg, 12%).

General Procedure C: Carbamylation

For example, for the preparation of 1-(*tert*-butyl) 4-neopentyl piperazine-1,4-dicarboxylate, **122**.

To a round-bottomed flask was added 2,2-dimethylpropan-1-ol (0.24 g, 2.68 mmol) and CDI (0.52 g, 2.68 mmol) were dissolved in DMF (2.00 mL) and stirred for 30 min. *tert*-Butyl piperazine-1-carboxylate (0.5 g, 2.68 mmol) was added to the reaction mixture and stirred for 16 h at room temperature. H₂O (5 mL) was added and the precipitate was filtered and washed with H₂O to afford the desired product as a white solid (0.44 g, 54%).

General Procedure C: Sulfonylation

For example, for the preparation of *tert*-butyl 4-(phenylsulfonyl)piperazine-1-carboxylate, **137**.

To a round-bottom flask was added benzenesulfonyl chloride (0.31 mL, 1.47 mmol), *tert*-butyl piperazine-1-carboxylate (0.25 g, 1.34 mmol), Et₃N (0.23 mL, 1.61 mmol), CH₂Cl₂ (3 mL) and stirred for 16 h at room temperature. The reaction mixture was diluted with EtOAc (10 mL) and washed with H₂O (5 mL). The organics were collected, dried (hydrophobic frit) and concentrated under vacuum to a residue that was purified using silica gel chromatography (50% EtOAc in petroleum ether) to afford the desired product as a white solid (0.24 mg, 55%).

General Procedure E: Boc removal and subsequent alkylation

For example, for the preparation neopentyl 4-(3-oxo-3-(2-oxo-2,3-dihydrobenzo[*d*]oxazol-6-yl)propyl)piperazine-1-carboxylate, **99**.

To a round-bottomed flask was added (**122**, 1-(*tert*-butyl) 4-neopentyl piperazine-1,4-dicarboxylate (0.2 g, 0.67 mmol) and dissolved in TFA:CH₂Cl₂ (1:1, 2 mL). The solution was stirred at room temperature until no starting material remained by TLC analysis. The reaction mixture was concentrated under vacuum to afford amine intermediate TFA salt. The amine intermediate was redissolved in MeCN (3 mL). 6-(3-chloropropanoyl) benzo[*d*]oxazol-2(3*H*)-one (0.14 g, 0.6 mmol) and Et₃N (0.4 mL, 1.46 mmol) were added and the solution was refluxed until no starting material remained by TLC analysis. The reaction mixture was concentrated under vacuum to a residue that was purified using silica gel chromatography (0-100% EtOAc in petroleum ether) to afford the desired product as white solid (15 mg, 65%).

General Procedure F: Amidation using COMU

For example, for the preparation of *tert*-butyl 4-((2-oxo-2,3-dihydrobenzo[*d*]oxazole-6-carboxamido)methyl)piperidine-1-carboxylate **176**.

To a round-bottom flask was added 2-oxo-2,3-dihydrobenzo[*d*]oxazole-6-carboxylic acid (**182**, 1.2 g, 6.7 mmol), DMF (10 mL). DIPEA (2.33 mL, 13.4 mmol) was added and the reaction stirred for 5 min. COMU (2.87 g, 6.7 mmol) was added and reaction mixture stirred for a further 5 min before *tert*-butyl 4-(aminomethyl)piperidine-1-carboxylate (1.42 mL, 6.7 mmol) was added. The reaction mixture was stirred for 16 h at room temperature before being diluted with EtOAc (50 mL) and washed with

H₂O (30 mL). The organics were collected, dried (hydrophobic frit) and concentrated under vacuum to a residue that was purified using silica gel chromatography (50% EtOAc in petroleum ether) to afford the desired product as a white solid (1.13 g, 45%).

General Procedure G: Amidation using HATU

For example, for the preparation of benzyl 4-(3-(6,7-dihydrooxazolo[4,5-*c*]pyridin-5(4*H*)-yl)-3-oxopropyl)piperazine-1-carboxylate, **146**.

To a round-bottom flask was added 3-(4-((benzyloxy)carbonyl)piperazin-1-yl)propanoic acid (**143**, 0.15 mg, 0.51 mmol), DMF (3 mL). DIPEA (0.27 mL, 1.54 mmol) was added and the reaction mixture stirred for 5 min. HATU (0.22 g, 0.51 mmol) was added and reaction mixture stirred for a further 5 min before 5,6,7-tetrahydrooxazolo[4,5-*c*]pyridine hydrochloride (0.06 mL, 0.51 mmol) was added. The reaction mixture was stirred for 16 h at room temperature before being diluted with EtOAc (10 mL) and washed with H₂O (5 mL). The organics were collected, dried (hydrophobic frit) and concentrated under vacuum to a residue that was purified using MDAP to afford the desired product as a yellow gum (10 mg, 5%).

General Procedure H: Friedel Crafts acylation

For example, for the preparation of 6-(2-chloroacetyl)benzo[*d*]oxazol-2(3*H*)-one, **172**.

To a round-bottomed flask was added AlCl₃ (12.2 g, 92.51 mmol) and DCE (2.5 mL) was added dropwise at 0 °C. After 15 min chloroacetyl chloride (5.86 mL, 74.2 mmol) was added followed by benzo[*d*]oxazol-2(3*H*)-one (5 g, 37 mmol) portion wise at 0 °C. The reaction mixture was heated to 50 °C and stirred for 2 h. The solution was cooled and poured onto ice (300 g) and the precipitate filtered to afford the desired product as a beige solid (5.48 g, 70%).

General Procedure I: Nucleophilic substitution with NaOH

For example, for the preparation of 2-oxo-2,3-dihydro-1*H*-benzo[*d*]imidazole-5-carboxylic acid, **182**.

To a round-bottom flask was added 5-(2-chloroacetyl)-1,3-dihydro-2*H*-benzo[*d*]imidazol-2-one (**172**, 1 g, 4.75 mmol), pyridine (10 mL) and stirred for 3 h at 90 °C. The reaction mixture was allowed to cool to room temp and filtered. The solid

obtained was dissolved in 2.5 M NaOH (10 mL) and heated for 2 h at 80 °C. The reaction mixture was allowed to cool to room temp and acidified with 1 M HCl. The precipitate was filtered to afford the desired product as a brown solid (0.39 g, 37%).

General Procedure J: Boc removal and subsequent carbamylation

For example, for the preparation of, 3,5-dichlorobenzyl 4-((2-oxo-2,3-dihydro-1*H*-benzo[*d*]imidazole-5-carboxamido)methyl)piperidine-1-carboxylate **174**.

To a round-bottomed flask was added *tert*-butyl 4-((2-oxo-2,3-dihydro-1*H*-benzo[*d*]imidazole-5-carboxamido)methyl)piperidine-1-carboxylate (**176**, 0.2 g, 0.73 mmol) and dissolved in TFA:CH₂Cl₂ (1:1, 2 mL). The solution was stirred at room temperature until no starting material remained by TLC analysis. The solution was quenched with saturated Na₂CO₃ (5 mL) and extracted into CH₂Cl₂ (10 mL). The organics were then collected, dried (hydrophobic frit), and concentrated under vacuum to afford amine intermediate. To a round-bottomed flask was added (3,5-dichlorophenyl)methanol (0.1 g, 0.55 mmol) and CDI (0.1 g, 0.55 mmol) were dissolved in DMF (2 mL) and stirred for 30 min. The amine intermediate (0.15 g, 0.55 mmol) was added to the reaction mixture and stirred for 16 h at room temperature. After this time H₂O (5 mL) was added and the precipitate was filtered and washed with H₂O to afford the desired product as a white solid (0.04 g, 14%).

General Procedure K: Alkylation

For example, for the preparation of benzyl 4-(3-oxo-3-phenylpropyl) piperazine-1-carboxylate, **149**.

To a round-bottom flask was added 3-chloro-1-phenylpropan-1-one (0.25 g, 1.48 mmol) MeCN (12 mL), Et₃N (0.23 mL, 1.63 mmol), benzyl piperazine-1-carboxylate (0.32 mL, 1.63 mmol) and the reaction mixture refluxed for 2 h. The reaction mixture was concentrated under vacuum to a residue that was purified using silica gel chromatography (10-50% EtOAc in petroleum ether) to afford the desired product as a yellow gum (15 mg, 29%).

General Procedure I: Boc removal and subsequent amidation

For example, for the preparation of 3,5-dichlorobenzyl 6-(2-oxo-2,3-dihydro-1*H*-benzo[*d*]imidazole-5-carbonyl)-2,6-diazaspiro[3.3]heptane-2-carboxylate, **192**.

To a round-bottomed flask was added 2-(*tert*-butyl) 6-(3,5-dichlorobenzyl) 2,6-diazaspiro[3.3]heptane-2,6-dicarboxylate (**111**, 0.15 g, 0.37 mmol), and dissolved in TFA:CH₂Cl₂ (1:1, 2 mL). The solution was stirred at room temperature until no starting material remained by TLC analysis. The reaction mixture was concentrated under vacuum to afford amine intermediate TFA salt. To a round-bottomed flask was added 2-oxo-2,3-dihydro-1*H*-benzo[*d*]imidazole-5-carboxylic acid (**181**, 0.06 g, 0.33 mmol) and DMF (1 mL). DIPEA (0.12 mL, 0.66 mmol) was added and the reaction stirred for 5 min before COMU (0.14 g, 0.33 mmol) was added and reaction mixture stirred for a further 5 min before amine intermediate TFA salt was added to the reaction mixture and the reaction was stirred for 16 h at room temperature. After this time the reaction was diluted with EtOAc (10 mL) and washed with H₂O (10 mL). The organics were collected, dried (hydrophobic frit) and concentrated under vacuum to a residue that was purified using silica gel chromatography (80% EtOAc in petroleum ether) to afford the desired product as a white solid (10 mg, 7%).

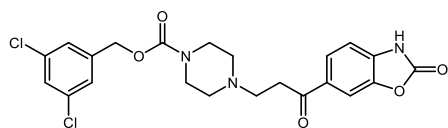
General Procedure M: Oxime formation

For example, for the preparation of benzyl (*E*)-4-(2-(hydroxyimino)-2-(2-oxo-2,3-dihydrobenzo[*d*]oxazol-6-yl)ethyl)piperazine-1-carboxylate, **221**.

To a round-bottom flask was added benzyl 4-(2-oxo-2-(2-oxo-2,3-dihydrobenzo[*d*]oxazol-6-yl)ethyl)piperazine-1-carboxylate (**214**, 0.18 g, 0.46 mmol), NaOAc (0.04 g, 0.5 mmol), HONH₂·HCl (0.04 g, 0.5 mmol) and MeOH (3 mL). The reaction mixture was stirred for 16 h at room temp. After this time the reaction mixture was concentrated under vacuum to a residue that was purified using silica gel chromatography (50-100% EtOAc in petroleum ether) to afford the desired product as a yellow gum (21 mg, 11%).

5.2 Experimental Data

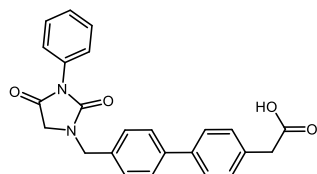
Compound 39: 3,5-dichlorobenzyl 4-(3-oxo-3-(2-oxo-2,3-dihydrobenzo[*d*]oxazol-6-yl)propyl)piperazine-1-carboxylate



Chemical Formula: C₂₂H₂₁Cl₂N₃O₅
Molecular Weight: 478.33 Da

Prepared according to general procedure K at 80 °C using 3,5-dichlorobenzyl piperazine-1-carboxylate (**156**, 0.7 g, 2.44 mmol), 6-(3chloropropanoyl)benzo[*d*]oxazol-2(3*H*)-one (**116**, 0.5 g, 2.21 mmol), MeCN (8 mL), Et₃N (0.34 mL, 2.44 mmol) to afford the desired product as a white solid (0.57 g, 54%). MPt: 148 – 150 °C; ν_{\max} (neat): 1766, 1674 cm⁻¹; ¹H NMR (500 MHz, DMSO-*d*₆) δ 12.15 (s, 1H), 7.96 – 7.82 (m, 2H), 7.59 (t, *J* = 1.9 Hz, 1H), 7.47 (d, *J* = 1.9 Hz, 2H), 7.25 (d, *J* = 8.2 Hz, 1H), 5.12 (s, 2H), 4.28 – 4.00 (m, 2H), 3.67 – 3.38 (m, 6H), 3.35 – 3.08 (m, 4H); ¹³C NMR (101 MHz, DMSO-*d*₆) δ 195.0, 154.3, 153.8, 143.3, 140.7, 135.3, 134.0, 130.1, 127.5, 126.3, 125.1, 109.5, 108.9, 65.2, 51.0, 50.7, 40.6, 32.6; HRMS: exact mass calculated for [M+H]⁺ (C₂₂H₂₂Cl₂N₃O₅) requires *m/z* 478.0931, found *m/z* 478.0926; Consistent with previously reported data.¹¹⁷

Compound 49: 2-(4'-((2, 4-dioxo-3-phenylimidazolidin-1-yl)methyl)-[1,1'-biphenyl]-4-yl)acetic acid

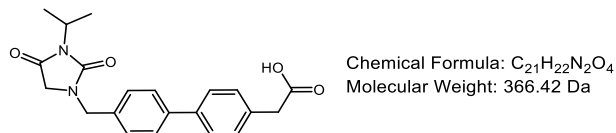


Chemical Formula: C₂₄H₂₀N₂O₄
Molecular Weight: 400.43 Da

Prepared according to general procedure B using 1-(4-bromobenzyl)-3-phenylimidazolidine-2,4-dione (**65**, 0.18 g, 0.52 mmol), methyl 2-(4-(4,4,5,5-tetramethyl-1,3,2-dioxaborolan-2-yl)phenyl)acetate (0.16 g, 0.57 mmol), Pd₂(dba)₃ (1 mol%, 5 mg, 0.01 mmol), K₃PO₄ (0.19 g, 0.89 mmol), PCy₃ (2.4 mol%, 4 mg, 0.01 mmol), 1,4-dioxane (1.3 mL) H₂O (0.7 mL), LiOH (8 mg, 0.20 mmol) to afford the desired product as a white solid (25 mg, 12%). MPt: 165 – 167 °C; ν_{\max} (neat): 3415 (broad), 1600, 1485 cm⁻¹; ¹H NMR (400 MHz, CDCl₃): δ 7.65 – 7.33 (m, 13H), 4.69 (s, 2H), 3.96 (s, 2H), 3.73 (s, 2H), 1.71 (s, 1H); ¹³C NMR (126 MHz, CDCl₃): δ 168.8, 155.7, 141.0, 139.6, 134.3, 131.9, 130.0, 129.2, 128.9, 128.3, 127.9, 127.4,

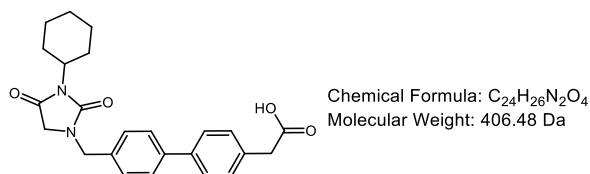
126.2, 49.2, 46.8, 15.3, 2xC coincident; HRMS: exact mass calculated for $[M+H]^+$ ($C_{24}H_{21}N_2O_4$) requires m/z 401.1496, found m/z 401.1499.

Compound 56: 2-(4'-((3-isopropyl-2,4-dioxoimidazolidin-1-yl)methyl)-[1,1'-biphenyl]-4-yl)acetic acid



Prepared according to general procedure B using 1-(4-bromobenzyl)-3-phenylimidazolidine-2,4-dione (**65**, 0.25 g, 0.8 mmol), methyl 2-(4-(4,4,5,5-tetramethyl-1,3,2-dioxaborolan-2-yl)phenyl)acetate (0.24 g, 0.09 mmol), $Pd_2(dba)_3$ (1 mol%, 8 mg, 0.01 mmol), K_3PO_4 (0.29 g, 1.37 mmol) and PCy_3 (2.4 mol%, 5 mg, 0.19 mmol), 1,4-dioxane (1.3 mL) H_2O (0.7 mL), LiOH (44 mg, 1.05 mmol) to afford the desired product as a white solid (70 mg, 23%). MPt: 148 – 150 °C; ν_{max} (neat): 1701, 1460, 1134 cm^{-1} ; 1H NMR (400 MHz, $CDCl_3$): δ 7.55 (t, $J = 8.5$ Hz, 4H), 7.37 (d, $J = 8.2$ Hz, 2H), 7.31 (d, $J = 8.2$ Hz, 2H), 4.57 (s, 2H), 4.36 (sept, $J = 7.0$ Hz, 1H), 3.70 (d, $J = 3.2$ Hz, 4H), 1.44 (d, $J = 7.0$ Hz, 6H), OH proton not observed; ^{13}C NMR (101 MHz, $CDCl_3$): δ 169.9, 156.8, 140.7, 139.4, 134.7, 130.0, 128.7, 127.7, 127.3, 49.0, 46.4, 44.2, 19.8, 3xC coincident; HRMS: exact mass calculated for $[M+H]^+$ ($C_{21}H_{23}N_2O_4$) m/z 367.1652, found m/z 367.1654.

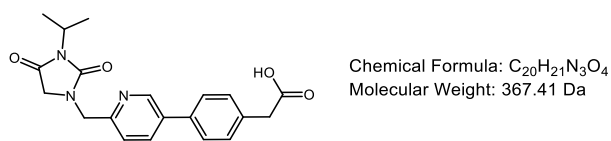
Compound 57: 2-(4'-((3-cyclohexyl-2,4-dioxoimidazolidin-1-yl)methyl)-[1,1'-biphenyl]-4-yl)acetic acid:



Prepared according to general procedure B using 1-(4-bromobenzyl)-3-cyclohexylimidazolidine-2,4-dione (**66**, 0.35 g, 1 mmol), methyl 2-(4-(4,4,5,5-tetramethyl-1,3,2-dioxaborolan-2-yl)phenyl)acetate (0.3 g, 1.1 mmol), $Pd_2(dba)_3$ (1 mol%, 9 mg, 0.01 mmol), K_3PO_4 (0.36 g, 1.7 mmol) and PCy_3 (2.4 mol%, 7 mg, 0.02 mmol), 1,4-dioxane (1.3 mL), H_2O (0.7 mL), and LiOH (22 mg, 0.52 mmol) to afford the desired product as a white solid (63 mg, 15%). MPt: 151 – 152 °C; ν_{max} (neat): 3371, 1699, 1114 cm^{-1} ; 1H NMR (500 MHz, $CDCl_3$): δ 7.55 (dd, $J = 9.7$,

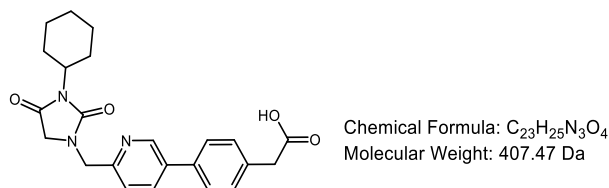
8.2 Hz, 4H), 7.37 (d, $J = 8.2$ Hz, 2H), 7.31 (d, $J = 8.1$ Hz, 2H), 4.57 (s, 2H), 3.94 (tt, $J = 11.0, 3.2$ Hz, 1H), 3.71 (d, $J = 3.7$ Hz, 4H), 2.16 (ddd, $J = 15.9, 12.4, 2.9$ Hz, 2H), 1.84 (d, $J = 13.3$ Hz, 2H), 1.70 (d, $J = 13.7$ Hz, 3H), 1.38 – 1.20 (m, 3H), OH not observed; ^{13}C NMR (126 MHz, CDCl_3): δ 170.0, 157.0, 140.7, 139.6, 134.7, 132.9, 130.0, 128.7, 127.7, 127.4, 65.9, 52.0, 49.0, 46.5, 29.5, 26.0, 25.1, 15.3; HRMS: exact mass calculated for $[\text{M}+\text{H}]^+$ ($\text{C}_{24}\text{H}_{27}\text{N}_2\text{O}_4$) requires m/z 407.1971, found m/z 407.1970.

Compound 59: 2-(4-(6-((3-isopropyl-2,4-dioxoimidazolidin-1-yl)methyl)pyridin-3-yl)phenyl)acetic acid



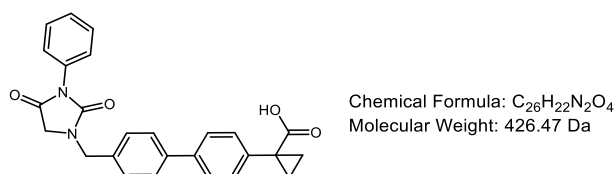
Prepared according to general procedure B using 1,1-((5-bromopyridin-2-yl)methyl)-3-isopropylimidazolidine-2,4-dione (**68**, 0.2 g, 0.64 mmol), methyl 2-(4-(4,4,5,5-tetramethyl-1,3,2-dioxaborolan-2-yl)phenyl)acetate (0.21 g, 0.77 mmol), 2'(dimethylamino)-2-biphenyl-palladium(II)chloride dinorbonylphosphine complex (5 mol%, 18 mg, 0.03 mmol), K_3PO_4 (0.41 g, 1.93 mmol), 1,4-dioxane (4 mL), H_2O (1 mL), LiOH (18 mg, 0.44 mmol) to afford the desired product as a white amorphous solid (28 mg, 12%). ν_{max} (neat): 1701, 1174, 1134 cm^{-1} ; ^1H NMR (500 MHz, CDCl_3): δ 9.02 (d, $J = 1.7$ Hz, 1H), 8.35 (dd, $J = 8.2, 2.0$ Hz, 1H), 8.06 (br.s, 1H), 7.80 (d, $J = 8.3$ Hz, 1H), 7.58 (d, $J = 8.2$ Hz, 2H), 7.44 (d, $J = 8.1$ Hz, 2H), 4.96 (s, 2H), 4.35 (sept, $J = 7.0$ Hz, 1H), 3.99 (s, 2H), 3.73 (s, 2H), 1.43 (d, $J = 6.9$ Hz, 6H); ^{13}C NMR (126 MHz, CDCl_3): δ 174.9, 169.5, 157.5, 151.1, 142.2, 141.4, 138.8, 135.9, 133.1, 131.0, 127.5, 125.8, 50.3, 44.8, 44.6, 40.5, 19.7; HRMS: exact mass calculated for $[\text{M}+\text{H}]^+$ ($\text{C}_{20}\text{H}_{22}\text{N}_3\text{O}_4$) requires m/z 368.1605, found m/z 368.1624.

Compound 60: 2-(4-(6-((3-cyclohexyl-2,4-dioxoimidazolidin-1-yl)methyl)pyridin-3-yl)phenyl)acetic acid



Prepared according to general procedure B using 1-((5-bromopyridin-2-yl)methyl)-3-cyclohexylimidazolidine-2,4-dione (**69**, 0.2 g, 0.57 mmol), methyl 2-(4-(4,4,5,5-tetramethyl-1,3,2-dioxaborolan-2-yl)phenyl)acetate (0.19 g, 0.68 mmol), 2'-(dimethylamino)-2-biphenyl-palladium(II)chloride dinorbonylphosphine complex (5 mol%, 16 mg, 0.03 mmol), K₃PO₄ (0.36 g, 1.71 mmol), 1,4-dioxane (4 mL), H₂O (1 mL), LiOH (14 mg, 0.36 mmol) to afford the desired product as a white powder (60 mg, 24%). MPt: 151 – 153 °C; ν_{\max} (neat): 3360, 1699, 1114 cm⁻¹; ¹H NMR (500 MHz, CDCl₃): δ 9.00 (s, 1H), 8.34 (dd, *J* = 8.3, 1.6 Hz, 1H), 8.04 (br.s, 1H), 7.80 (d, *J* = 8.3 Hz, 1H), 7.57 (d, *J* = 8.1 Hz, 2H), 7.44 (d, *J* = 8.1 Hz, 2H), 4.96 (s, 2H), 3.99 (s, 2H), 3.92 (tt, *J* = 12.3, 3.8 Hz, 1H), 3.72 (s, 2H), 2.11 (qd, *J* = 12.5, 3.2 Hz, 2H), 1.83 (d, *J* = 13.5 Hz, 2H), 1.67 (t, *J* = 14.1 Hz, 3H), 1.37 – 1.15 (m, 3H); ¹³C NMR (101 MHz, CDCl₃): δ 175.1, 169.6, 157.6, 151.0, 142.1, 141.4, 138.8, 136.0, 133.0, 131.0, 127.5, 125.9, 52.4, 50.3, 44.8, 40.5, 29.4, 26.0, 25.1; HRMS: exact mass calculated for [M+H]⁺ (C₂₃H₂₆N₃O₄) requires *m/z* 408.1923, found *m/z* 408.1917.

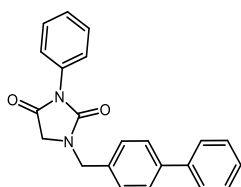
Compound 61: 1-(4'-((2,4-dioxo-3-phenylimidazolidin-1-yl)methyl)-[1,1'-biphenyl]-4-yl)cyclopropane-1-carboxylic acid



Prepared according to general procedure B using 1-(4-bromobenzyl)-3-phenylimidazolidine-2,4-dione (**64**, 0.2 mg, 0.57 mmol), methyl 1-(4-(4,4,5,5-tetramethyl-1,3,2-dioxaborolan-2-yl)phenyl)cyclopropane-1-carboxylate (0.19 g, 0.68 mmol), Pd₂(dba)₃ (1 mol%, 5 mg, 0.01 mmol), K₃PO₄ (0.22 g, 1.04 mmol) and PCy₃ (2.4 mol%, 4 mg, 0.01 mmol), 1,4-dioxane (1.3 mL), H₂O (0.7 mL), and LiOH (19 mg, 0.45 mmol) to afford the desired product as a white amorphous solid

(70 mg, 29%). ν_{\max} (neat): 3143, 1712, 1452, 1172 cm^{-1} ; ^1H NMR (500 MHz, CDCl_3) δ 7.61 (d, $J = 8.2$ Hz, 2H), 7.53 (d, $J = 8.3$ Hz, 2H), 7.50 – 7.36 (m, 9H), 4.68 (s, 2H), 4.12 (q, $J = 7.1$ Hz, 2H), 3.95 (s, 2H), 1.64 (q, $J = 3.9$ Hz, 2H), 1.25 (s, 1H); ^{13}C NMR (126 MHz, CDCl_3) δ 174.5, 168.7, 141.1, 139.2, 134.2, 131.9, 131.0, 129.2, 128.9, 128.2, 127.8, 126.9, 126.1, 61.1, 49.2, 46.8, 28.9, 24.9, 16.6, 14.3; HRMS: exact mass calculated for $[\text{M}+\text{H}]^+$ ($\text{C}_{26}\text{H}_{23}\text{N}_2\text{O}_4$) requires m/z 427.1652, found m/z 427.1650.

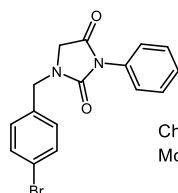
Compound 62: 1-([1,1'-biphenyl]-4-ylmethyl)-3-phenylimidazolidine-2,4-dione



Chemical Formula: $\text{C}_{22}\text{H}_{18}\text{N}_2\text{O}_2$
Molecular Weight: 342.40 Da

Prepared according to general procedure B using 1-(4-bromobenzyl)-3-phenylimidazolidine-2,4-dione (**64**, 0.18 g, 0.52 mmol), (4,4,5,5-tetramethyl-1,3,2-dioxaborolan-2-yl)benzene (0.12 g, 0.57 mmol), $\text{Pd}_2(\text{dba})_3$ (1 mol%, 5 mg, 0.01 mmol), K_3PO_4 (0.19 g, 0.89 mmol), PCy_3 (2.4 mol%, 4 mg, 0.01 mmol), 1,4-dioxane (1.3 mL), H_2O (0.7 mL) to afford the desired product as a white solid (84 mg, 47%). MPt: 162 – 164 $^\circ\text{C}$; ν_{\max} (neat): 1710, 1419, 1244 cm^{-1} ; ^1H NMR (400 MHz, CDCl_3): δ 7.64 – 7.57 (m, 4H), 7.50 – 7.35 (m, 10H), 4.69 (s, 2H), 3.96 (s, 2H); ^{13}C NMR (101 MHz, CDCl_3) δ 168.8, 155.8, 141.6, 140.6, 134.3, 131.9, 129.2, 129.0, 129.0, 128.3, 128.0, 127.7, 127.3, 126.2, 49.2, 46.9; HRMS: exact mass calculated for $[\text{M}+\text{H}]^+$ ($\text{C}_{22}\text{H}_{19}\text{N}_2\text{O}_2$) requires m/z 343.1441, found m/z 343.1440

Compound 64: 1-(4-bromobenzyl)-3-phenylimidazolidine-2,4-dione

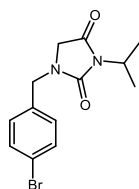


Chemical Formula: $\text{C}_{16}\text{H}_{13}\text{BrN}_2\text{O}_2$
Molecular Weight: 345.20 Da

Prepared according to general procedure A using methyl 2-((4-bromobenzyl) amino) acetate (0.4 g, 1.55 mmol), CH_2Cl_2 (38 mL), phenyl isocyanate (0.30 mL, 3.08 mmol), and $\text{CF}_3\text{CO}_2\text{H}$ (3.16 mL, 41 mmol) to afford the desired product as a yellow amorphous solid (0.34 g, 60%). ν_{\max} (neat): 1647, 1228 cm^{-1} ; ^1H NMR

(400 MHz, CDCl₃): δ 7.55 – 7.50 (m, 2H), 7.50 – 7.34 (m, 5H), 7.23 – 7.18 (m, 2H), 4.60 (s, 2H), 3.90 (s, 2H); ¹³C NMR (101 MHz, CDCl₃): δ 168.5, 155.8, 134.4, 132.4, 131.7, 130.1, 129.2, 128.3, 126.2, 122.5, 49.1, 46.5; HRMS: exact mass calculated for [M+H]⁺ (C₁₆H₁₄BrN₂O₂) requires m/z 345.0233, 347.0213 found m/z 345.0239, 347.0216. (⁷⁹Br:⁸¹Br, 1:1)

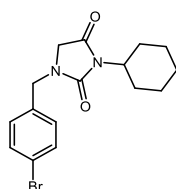
Compound 65: 1-(4-bromobenzyl)-3-isopropylimidazolidine-2,4-dione



Chemical Formula: C₁₃H₁₅BrN₂O₂
Molecular Weight: 311.18 Da

Prepared according to general procedure A using methyl 2-((4-bromobenzyl) amino) acetate (**76**) (0.38 g, 1.47 mmol), CH₂Cl₂ (35 mL), isopropyl isocyanate (0.29 mL, 2.93 mmol), TFA (2.71 mL, 33.81 mmol) to afford the desired product as a yellow amorphous solid (0.3 g, 65%). ν_{\max} (neat): 1697, 1180 cm⁻¹; ¹H NMR (400 MHz, CDCl₃): δ 7.50 (d, J = 8.4 Hz, 2H), 7.13 (d, J = 8.5 Hz, 2H), 4.48 (s, 2H), 4.34 (sept, J = 6.9 Hz, 1H), 3.65 (s, 2H), 1.43 (d, J = 7.0 Hz, 6H); ¹³C NMR (126 MHz, CDCl₃) δ 170.2, 156.9, 134.5, 132.3, 130.0, 122.4, 49.0, 46.3, 44.5, 19.7; HRMS: exact mass calculated for [M+Na]⁺ (C₁₃H₁₅BrN₂O₂Na) requires m/z 333.0209, 335.0189 found m/z 333.0209, 335.0186. (⁷⁹Br:⁸¹Br, 1:1) Consistent with previously reported data.¹⁴⁰

Compound 66: 1-(4-bromobenzyl)-3-cyclohexylimidazolidine-2,4-dione

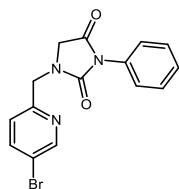


Chemical Formula: C₁₆H₁₉BrN₂O₂
Molecular Weight: 351.24 Da

Prepared according to general procedure A using methyl 2-((4-bromobenzyl) amino) acetate (**76**) (0.4 g, 1.55 mmol), CH₂Cl₂ (35 mL), cyclohexyl isocyanate (0.39 mL, 3.08 mmol), TFA (2.75 mL, 35.7 mmol) to afford the desired product as a yellow amorphous solid (0.24 g, 44%). ν_{\max} (neat): 2937, 1761, 1691 cm⁻¹; ¹H NMR (400 MHz, CDCl₃) δ 7.49 (d, J = 8.3 Hz, 2H), 7.13 (d, J = 8.3 Hz, 2H), 4.48 (s, 2H), 3.92 (tt, J = 12.4, 4.0 Hz, 1H), 3.65 (s, 2H), 2.14 (qd, J = 12.3, 3.0 Hz, 2H), 1.84 (d, J = 13.5 Hz, 2H), 1.69 (d, J = 10.5 Hz, 2H), 1.28 (m, 4H); ¹³C NMR (101 MHz, CDCl₃) δ 169.7, 157.0, 134.8, 132.3, 130.0, 122.4, 52.1, 48.9, 46.3, 29.5, 26.0, 25.1;

HRMS: exact mass calculated for $[M+H]^+$ ($C_{15}H_{20}BrN_3O_2$) requires m/z 351.0703, 353.0682 found m/z 351.0706, 353.0685. (^{79}Br : ^{81}Br , 1:1)

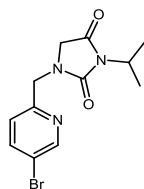
Compound 67: 1-((5-bromopyridin-2-yl)methyl)-3-phenylimidazolidine-2,4-dione



Chemical Formula: $C_{15}H_{12}BrN_3O_2$
Molecular Weight: 346.18 Da

Prepared according to general procedure A using methyl 2-((4-bromobenzyl) amino) acetate (**77**) (0.4 g, 1.54 mmol), CH_2Cl_2 (35 mL), phenyl isocyanate (0.34 mL, 3.07 mmol), and TFA (2.73 mL, 35.42 mmol) to afford the desired product as a yellow amorphous solid (0.15 g, 28%). ν_{max} (neat): 1172, 1170 cm^{-1} ; 1H NMR (400 MHz, $CDCl_3$) δ 8.66 (d, $J = 2.2$ Hz, 1H), 7.85 (dd, $J = 8.3, 2.3$ Hz, 1H), 7.50 – 7.35 (m, 5H), 7.28 (d, $J = 2.7$ Hz, 1H), 4.72 (s, 2H), 4.18 (s, 2H); ^{13}C NMR (101 MHz, $CDCl_3$) δ 168.9, 156.1, 154.0, 150.9, 139.9, 131.8, 129.2, 128.3, 126.1, 123.9, 120.2, 50.3, 47.7; HRMS ($C_{15}H_{13}^{79}BrN_3O_2$) $[M+ H^+]$ 346.0186, found $[M+ H^+]$ 346.0188

Compound 68: 1-((5-bromopyridin-2-yl) methyl)-3-isopropylimidazolidine-2,4-dione

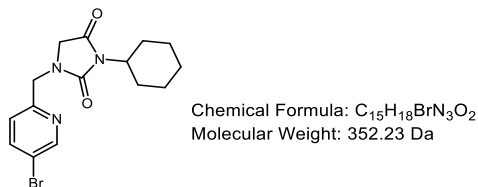


Chemical Formula: $C_{12}H_{14}BrN_3O_2$
Molecular Weight: 312.17 Da

Prepared according to general procedure A using methyl 2-(((5-bromopyridin-2-yl) methyl) amino) acetate (**77**) (0.4 g, 1.54 mmol), CH_2Cl_2 (15 mL), isopropyl isocyanate (0.3 mL, 3.07 mmol), and TFA (2.73 mL, 35.42 mmol) to afford the desired product as a yellow amorphous solid (0.28 g, 58%). ν_{max} (neat): 1703, 1460 cm^{-1} ; 1H NMR (400 MHz, $CDCl_3$): δ 8.61 (d, $J = 1.9$ Hz, 1H), 7.81 (dd, $J = 8.3, 2.4$ Hz, 1H), 7.19 (d, $J = 8.3$ Hz, 1H), 4.60 (s, 2H), 4.33 (sept, $J = 6.9$ Hz, 1H), 3.89 (s, 2H), 1.42 (d, $J = 7.0$ Hz, 6H); ^{13}C NMR (101 MHz, $CDCl_3$): δ 170.0, 157.2, 154.4, 150.8, 139.9, 123.7, 120.1, 50.0, 47.5, 44.3, 19.8; HRMS: exact mass calculated for

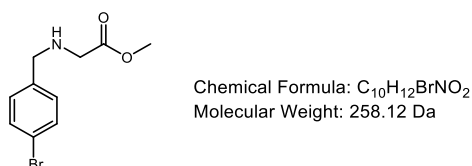
$[M+H]^+$ ($C_{12}H_{15}BrN_3O_2$) requires m/z 312.0342, 314.0322, found m/z 312.0345, 314.0322. (^{79}Br : ^{81}Br , 1:1)

Compound 69: 1-((5-bromopyridin-2-yl)methyl)-3-cyclohexylimidazolidine-2,4-dione:



Prepared according to general procedure A using methyl 2-(((5-bromopyridin-2-yl)methyl) amino) acetate (**77**) (0.4 g, 1.54 mmol), CH_2Cl_2 (15 mL), cyclohexyl isocyanate (0.39 mL, 3.07 mmol) and TFA (2.73 mL, 35.42 mmol) was added and the solution stirred for 2 h to afford the desired product as a yellow amorphous solid (0.4 g, 74%). ν_{max} (neat): 2927, 1751, 1618, 1539 cm^{-1} ; 1H NMR (400 MHz, $CDCl_3$): δ 8.59 (d, $J = 2.3$ Hz, 1H), 7.82 (dd, $J = 8.3, 2.4$ Hz, 1H), 7.27 (d, $J = 9.5$ Hz, 1H), 4.45 (s, 2H), 4.11 (s, 2H), 3.70 – 3.56 (m, 1H), 1.89 – 1.84 (m, 2H), 1.69 – 1.62 (m, 2H), 1.59 – 1.53 (m, 1H), 1.41 – 1.29 (m, 2H), 1.21 – 1.13 (m, 3H); ^{13}C NMR (101 MHz, $CDCl_3$): δ 171.1, 158.0, 156.2, 150.3, 139.8, 124.1, 119.9, 54.1, 52.1, 49.5, 33.5, 25.8, 24.7; HRMS: exact mass calculated for $[M+H]^+$ ($C_{15}H_{19}BrN_3O_2$) requires m/z 352.0655, 354.0635, found m/z 352.0650, 354.0628. (^{79}Br : ^{81}Br , 1:1)

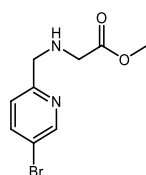
Compound 76: Methyl 2-((4-bromobenzyl) amino) acetate



To a round-bottomed flask was added 4-bromobenzaldehyde (0.5 g, 2.7 mmol), glycine methyl ester hydrochloride (0.34 g, 2.7 mmol), EtOH (7.5 mL), NEt_3 (0.73 mL, 78.3 mmol) under N_2 and stirred at 50 °C for 1h. EtOH was removed and the residue was redissolved in MeOH (7.5 mL) and cooled to 0° C. $NaBH_4$ (0.11 g, 2.97 mmol) was added portion wise and the reaction mixture stirred for 2 h at room temperature. After this time the reaction was concentrated to dryness and H_2O (20 mL) added. The suspension was extracted using CH_2Cl_2 (2 x 25 mL) before The organics were then collected, washed with brine (15 mL), dried (hydrophobic frit),

and concentrated under vacuum to give a residue that was purified by silica gel chromatography to afford the desired product as a clear yellow oil (0.46 g, 66%). ν_{\max} (neat): 3230, 2017, 1057 cm^{-1} ; ^1H NMR (400 MHz, CDCl_3): δ 7.44 (d, $J = 8.4$ Hz, 2H), 7.20 (d, $J = 8.4$ Hz, 2H), 3.75 (s, 2H), 3.72 (s, 3H), 3.39 (s, 2H), 1.96 (s, 1H); ^{13}C NMR (101 MHz, CDCl_3): δ 172.2, 138.0, 131.2, 129.3, 120.3, 51.9, 51.2, 49.2; HRMS: exact mass calculated for $[\text{M}+\text{H}]^+$ ($\text{C}_{10}\text{H}_{13}\text{BrNO}_2$) requires m/z 258.0124, 260.0104, found m/z 258.0127, 260.0103. (^{79}Br : ^{81}Br , 1:1); Consistent with previously reported data.¹⁴¹

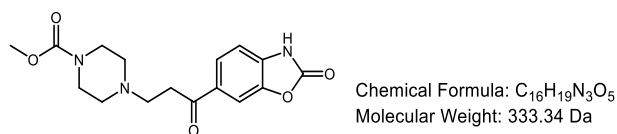
Compound 77: Methyl 2-(((5-bromopyridin-2-yl) methyl) amino) acetate



Chemical Formula: $\text{C}_9\text{H}_{11}\text{BrN}_2\text{O}_2$
Molecular Weight: 259.10 Da

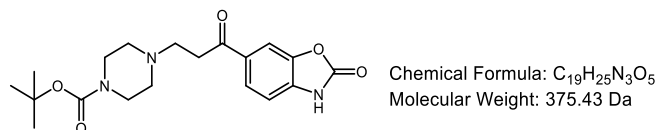
To a round-bottomed flask was added glycine methyl ester hydrochloride (1.23 g, 9.8 mmol) and MeOH (10 mL). NEt_3 (1.16 mL, 8.3 mmol) was added with stirring. The resulting solution was added dropwise to a solution of 5-bromopicolinaldehyde (0.91 g, 4.9 mmol) in MeOH (15 mL) under N_2 . After 30 min $\text{NaBH}(\text{OAc})_3$ (2.49 g, 11.7 mmol) was added portion wise. The reaction mixture was stirred for 16 h at room temperature. After this time the reaction was quenched using saturated NaHCO_3 (40 mL) and the suspension was extracted using CH_2Cl_2 (2 x 25 mL). The organics were then collected, washed with brine (25 mL), dried (hydrophobic frit), and concentrated under vacuum to give a residue that was purified by silica gel chromatography to afford the desired product as a clear yellow oil (1.09 g, 85%). ν_{\max} (neat): 1735, 1207 cm^{-1} ; ^1H NMR (400 MHz, CDCl_3): δ 8.62 (d, $J = 2.2$ Hz, 1H), 7.78 (dd, $J = 8.3, 2.4$ Hz, 1H), 7.27 (d, $J = 9.0$ Hz, 1H), 3.92 (s, 2H), 3.74 (s, 3H), 3.48 (s, 2H), NH not observed; ^{13}C NMR (101 MHz, CDCl_3): δ 171.7, 156.4, 150.4, 139.3, 123.9, 119.4, 53.3, 52.1, 49.5; HRMS: exact mass calculated for $[\text{M}+\text{H}]^+$ ($\text{C}_9\text{H}_{12}^{79}\text{BrN}_2\text{O}_2$) requires m/z 259.0077, found m/z 259.0078

Compound 97: Methyl 4-(3-oxo-3-(2-oxo-2,3-dihydrobenzo[d]oxazol-6-yl)propyl)piperazine-1-carboxylate



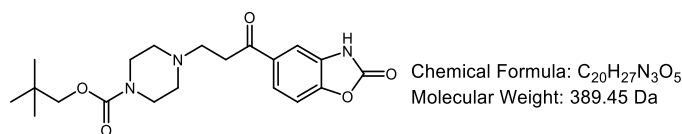
Prepared according to general procedure K at 80 °C using 6-(3-chloropropanoyl)benzo[d]oxazol-2(3*H*)-one (**116**, 0.25 g, 1.11 mmol), MeCN (5 mL), Et₃N (0.17 mL, 1.22 mmol), methyl piperazine-1-carboxylate (0.18 g, 1.22 mmol) to give the desired product as a white solid (0.19 g, 50%). MPt: 140 – 141 °C; ν_{\max} (neat): 1774, 1687, 1168 cm⁻¹; ¹H NMR (400 MHz, DMSO-*d*₆) δ 7.87 – 7.83 (m, 2H), 7.18 (d, *J* = 8.6 Hz, 1H), 3.58 (s, 3H), 3.39 – 3.29 (m, 4H), 3.18 (t, *J* = 7.2 Hz, 2H), 2.70 (t, *J* = 7.1 Hz, 2H), 2.45 – 2.32 (m, 4H), NH not observed; ¹³C NMR (101 MHz, DMSO-*d*₆) δ 197.5, 154.6, 153.8, 143.4, 135.2, 130.9, 125.0, 109.3, 108.8, 78.7, 52.9, 52.4, 35.4, 28.0; HRMS: exact mass calculated for [M+H]⁺ (C₁₆H₁₉N₃O₅) requires *m/z* 334.1397, found *m/z* 334.1395

Compound 98: *tert*-Butyl 4-(3-oxo-3-(2-oxo-2,3-dihydrobenzo[d]oxazol-6-yl)propyl)piperazine-1-carboxylate



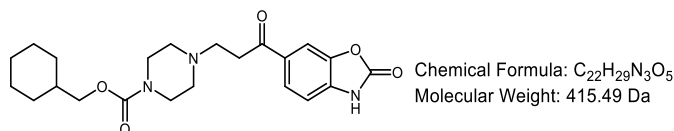
Prepared according to general procedure K at 80 °C using 6-(3-chloropropanoyl)benzo[d]oxazol-2(3*H*)-one (**116**, 1 g, 4.43 mmol), MeCN (15 mL), Et₃N (0.68 mL, 4.88 mmol), *tert*-butyl piperazine-1-carboxylate (0.91 g, 4.88 mmol) to afford the desired product as a white solid (1.07 g, 65%). MPt: 145 – 144 °C; ν_{\max} (neat): 1772, 1764, 1168 cm⁻¹; ¹H NMR (400 MHz, DMSO-*d*₆) δ 7.85 (td, *J* = 4.2, 1.6 Hz, 2H), 7.17 (d, *J* = 8.5 Hz, 1H), 3.31 – 3.25 (m, 4H), 3.17 (t, *J* = 7.2 Hz, 2H), 2.68 (t, *J* = 7.2 Hz, 2H), 2.41 – 2.31 (m, 4H), 1.39 (s, 9H), NH not observed; ¹³C NMR (101 MHz, DMSO-*d*₆) δ 197.6, 154.6, 153.7, 143.3, 135.1, 130.9, 125.1, 109.3, 108.8, 78.7, 52.9, 52.4, 35.4, 28.0, 2xC isochronous; HRMS: exact mass calculated for [M+H]⁺ (C₁₉H₂₅N₃O₅) requires *m/z* 376.1867, found *m/z* 376.1866; Consistent with previously reported data.¹¹⁷

Compound 99: Neopentyl 4-(3-oxo-3-(2-oxo-2,3-dihydrobenzo[d]oxazol-6-yl)propyl)piperazine-1-carboxylate



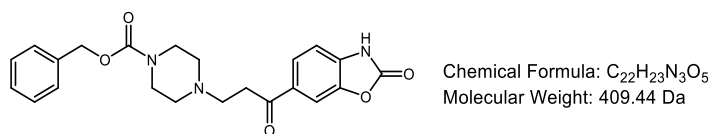
Prepared according to procedure E at 80 °C using 1-(*tert*-butyl) 4-neopentyl piperazine-1,4-dicarboxylate (**122**, 0.18 g, 0.6 mmol), TFA:CH₂Cl₂ (1:1, 2 mL), MeCN (3 mL), Et₃N (0.16 mL, 1.2 mmol), 6-(3-chloropropanoyl)benzo[d]oxazol-2(3*H*)-one (**116**, 0.12 g, 0.53 mmol) to afford the desired product as clear gum (0.07 g, 35%). MPt: 124 – 126 °C; ν_{\max} (neat): 1776, 1686, 1433, 1242 cm⁻¹; ¹H NMR (500 MHz, DMSO) δ 7.90 – 7.82 (m, 2H), 7.18 (d, *J* = 8.7 Hz, 1H), 3.71 (s, 2H), 3.52 – 3.30 (m, 6H), 3.18 (t, *J* = 7.2 Hz, 2H), 2.74 – 2.67 (m, 2H), 2.40 (t, *J* = 7.2 Hz, 2H), 0.90 (s, 9H), NH not observed; ¹³C NMR (101 MHz, DMSO-*d*₆) δ 197.4, 154.6, 143.4, 135.1, 130.9, 125.0, 109.4, 108.8, 74.0, 73.8, 52.9, 52.4, 43.3, 35.4, 31.3, 26.2; HRMS: exact mass calculated for [M+H]⁺ (C₂₀H₂₇N₃O₅) requires *m/z* 390.2023, found *m/z* 390.2025

Compound 100: Cyclohexylmethyl 4-(3-oxo-3-(2-oxo-2,3-dihydrobenzo[d]oxazol-6-yl)propyl)piperazine-1-carboxylate



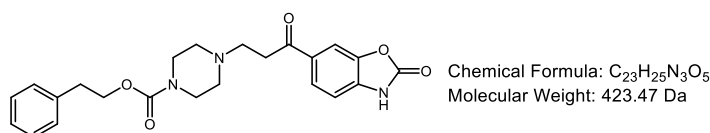
Prepared according to procedure E at 80 °C using 1-(*tert*-butyl) 4-(cyclohexylmethyl) piperazine-1,4-dicarboxylate (**123**, 0.2 g, 0.61 mmol), TFA:CH₂Cl₂ (1:1, 2 mL), MeCN (3 mL), Et₃N (0.17 mL, 1.23 mmol), 6-(3-chloropropanoyl)benzo[d]oxazol-2(3*H*)-one (**122**, 0.13 g, 0.56 mmol) to afford the desired product as clear gum (0.02 g, 10%). ν_{\max} (neat): 2928, 1768, 1675, 1450, 1135 cm⁻¹; ¹H NMR (500 MHz, DMSO-*d*₆) δ 12.19 (s, 1H), 7.94 – 7.86 (m, 2H), 7.26 (d, *J* = 8.1 Hz, 1H), 4.20 – 3.91 (m, 2H), 3.86 (d, *J* = 6.5 Hz, 2H), 3.64 – 3.37 (m, 5H), 3.33 – 3.02 (m, 4H), 1.70 (d, *J* = 11.0 Hz, 4H), 1.66 – 1.55 (m, 2H), 1.30 – 1.08 (m, 4H), 0.97 (q, *J* = 11.7 Hz, 2H); ¹³C NMR (101 MHz, DMSO-*d*₆) δ 195.1, 154.5, 154.3, 143.4, 135.4, 130.2, 125.5, 109.6, 109.1, 70.3, 51.1, 50.8, 36.8, 32.6, 29.1, 25.9, 25.2; HRMS: exact mass calculated for [M+H]⁺ (C₂₂H₃₀N₃O₅) requires *m/z* 416.2180, found *m/z* 416.2180

Compound 101: Benzyl 4-(3-oxo-3-(2-oxo-2,3-dihydrobenzo[d]oxazol-6-yl)propyl)piperazine-1-carboxylate



Prepared according to general procedure K at 80 °C using 6-(3-chloropropanoyl)benzo[d]oxazol-2(3H)-one (**116**, 0.3 g, 1.33 mmol), MeCN (15 mL), Et₃N (0.2 mL, 1.46 mmol), benzyl piperazine-1-carboxylate (0.28 mL, 1.46 mmol) to give the desired product as a white solid (30 mg, 6%). MPt: 105 – 104 °C; ν_{\max} (neat): 1764, 1705, 1246 cm^{-1} ; ¹H NMR (400 MHz, DMSO) δ 11.99 (s, 1H), 7.87 – 7.84 (m, 2H), 7.40 – 7.29 (m, 5H), 7.18 (d, J = 8.7 Hz, 1H), 5.07 (s, 2H), 3.40 – 3.35 (m, 4H), 3.18 (t, J = 7.5 Hz, 2H), 2.69 (t, J = 7.2 Hz, 2H), 2.42 – 2.39 (m, 4H); ¹³C NMR (126 MHz, DMSO) δ 197.5, 154.7, 154.3, 143.4, 136.9, 135.2, 130.9, 128.4, 127.8, 127.5, 125.0, 109.4, 108.8, 66.1, 52.8, 52.3, 43.4, 35.4; HRMS: exact mass calculated for [M+H]⁺ (C₂₂H₂₃N₃O₅) requires m/z 410.1710, found m/z 410.1710; No data previously reported.⁶⁷

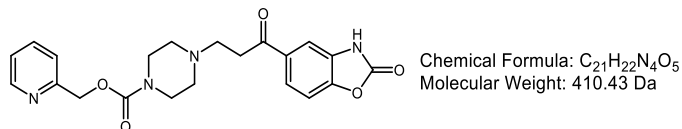
Compound 102: Phenethyl 4-(3-oxo-3-(2-oxo-2,3-dihydrobenzo[d]oxazol-6-yl)propyl)piperazine-1-carboxylate



Prepared according to procedure E at 80 °C using 1-(*tert*-butyl) 4-phenethyl piperazine-1,4-dicarboxylate (**125**, 0.2 g, 0.6 mmol), TFA:CH₂Cl₂ (1:1, 2 mL), MeCN (3 mL), Et₃N (0.17 mL, 1.2 mmol), 6-(3-chloropropanoyl)benzo[d]oxazol-2(3H)-one (**116**, 0.12 g, 0.54 mmol) to afford the desired product as yellow gum (0.05 g, 23%). ν_{\max} (neat): 3405, 1675, 1202, 1132 cm^{-1} ; ¹H NMR (500 MHz, DMSO-*d*₆) δ 7.97 – 7.80 (m, 2H), 7.36 – 7.28 (m, 2H), 7.28 – 7.20 (m, 4H), 4.23 (t, J = 6.7 Hz, 2H), 3.60 – 3.46 (m, 2H), 3.47 – 3.29 (m, 4H), 3.26 (d, J = 5.8 Hz, 2H), 3.10 (dd, J = 14.5, 7.3 Hz, 2H), 2.90 (t, J = 6.7 Hz, 2H), 2.74 (s, 2H), NH not observed; ¹³C NMR (101 MHz, DMSO-*d*₆) δ 195.2, 154.0, 143.1, 137.8, 135.0, 130.3, 128.5, 128.0, 126.0, 124.8, 109.2, 108.6, 65.5, 50.9, 45.9, 42.2, 40.8, 34.5, 1XC not observed; HRMS: exact

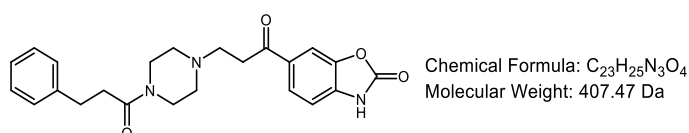
mass calculated for $[M+H]^+$ ($C_{23}H_{26}N_3O_5$) $[M+H]^+$ requires m/z 424.1867, found m/z 424.1863; No data previously reported.⁶⁷

Compound 103: Pyridin-2-ylmethyl 4-(3-oxo-3-(2-oxo-2,3-dihydrobenzo[d]oxazol-5-yl)propyl)piperazine-1-carboxylate



Prepared according to procedure E at 80 °C using 1-(*tert*-butyl) 4-(pyridin-2-ylmethyl) piperazine-1,4-dicarboxylate (**124**, 0.15 g, 0.47 mmol), TFA:CH₂Cl₂ (1:1, 2 mL), MeCN (3 mL), Et₃N (0.13 mL, 0.1 mmol), 6-(3-chloropropanoyl)benzo[d]oxazol-2(3*H*)-one (**116**, 0.1 g, 0.44 mmol) to afford the desired product as clear gum (0.03 g, 19%). MPt: 134 –135 °C; ν_{max} (neat): 1681, 1421, 1240 cm⁻¹; ¹H NMR (500 MHz, DMSO-*d*₆) δ 12.21 (s, 1H), 8.58 (d, J = 4.1 Hz, 1H), 7.96 – 7.75 (m, 3H), 7.47 (d, J = 7.8 Hz, 1H), 7.38 (dd, J = 7.1, 5.3 Hz, 1H), 7.26 (d, J = 8.1 Hz, 1H), 5.20 (s, 2H), 4.26 – 4.07 (m, 2H), 3.60 – 3.50 (m, 6H), 3.38 – 3.09 (m, 4H); ¹³C NMR (126 MHz, DMSO-*d*₆) δ 194.9, 155.7, 154.3, 153.8, 148.7, 143.3, 137.4, 135.3, 130.1, 125.1, 123.1, 121.5, 109.5, 108.9, 67.1, 51.0, 50.8, 32.5, 2xC isochronous; HRMS: exact mass calculated for $[M+H]^+$ ($C_{21}H_{23}N_4O_5$) requires m/z 411.1674, found m/z 411.1664

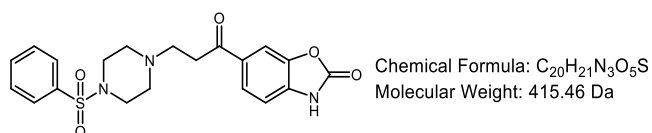
Compound 104: 6-(3-(4-(3-Phenylpropanoyl)piperazin-1-yl)propanoyl)benzo[d]oxazol-2(3H)-one



Prepared according to procedure E at 80 °C using *tert*-butyl 4-(3-phenylpropanoyl)piperazine-1-carboxylate (**136**, 0.2 g, 0.63 mmol), TFA:CH₂Cl₂ (1:1, 2 mL), MeCN (3 mL), Et₃N (0.17 mL, 1.24 mmol), 6-(3-chloropropanoyl)benzo[d]oxazol-2(3*H*)-one (**116**, 0.13 g, 0.56 mmol) to afford the desired product as yellow gum (0.03 g, 12%). ν_{max} (neat): 1766, 1613, 1444 cm⁻¹; ¹H NMR (500 MHz, CDCl₃) δ 7.83 (dd, J = 8.2, 1.3 Hz, 1H), 7.79 (d, J = 1.2 Hz, 1H), 7.31 – 7.26 (m, 2H), 7.24 – 7.15 (m, 3H), 7.11 (d, J = 8.2 Hz, 1H), 3.68 – 3.61 (m, 2H), 3.45 – 3.34 (m, 2H), 3.14 (t, J = 7.2 Hz, 2H), 3.03 – 2.94 (m, 2H), 2.83 (t, J =

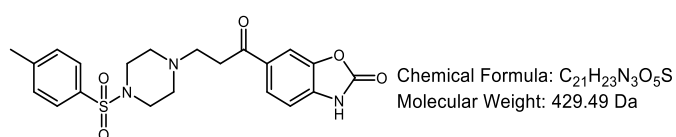
7.2 Hz, 2H), 2.66 – 2.60 (m, 2H), 2.52 – 2.43 (m, 2H), 2.41 – 2.35 (m, 2H), NH not observed; ^{13}C NMR (126 MHz, $\text{DMSO-}d_6$) δ 197.2, 170.1, 154.6, 143.4, 141.4, 135.0, 131.0, 128.5, 128.4, 126.0, 125.3, 109.6, 109.1, 52.7, 52.3, 44.4, 40.6, 33.9, 30.9; HRMS: exact mass calculated for $[\text{M}+\text{H}]^+$ ($\text{C}_{23}\text{H}_{25}\text{N}_3\text{O}_4$) requires m/z 408.1918, found m/z 408.1917

Compound 105: 6-(3-(4-(Phenylsulfonyl)piperazin-1-yl)propanoyl)benzo[d]oxazol-2(3H)-one



Prepared according to procedure E at 80 °C using *tert*-butyl 4-(phenylsulfonyl)piperazine-1-carboxylate (**137**, 0.2 g, 3.06 mmol), TFA: CH_2Cl_2 (1:1, 2 mL), MeCN (3 mL), Et_3N (0.16 mL, 1.13 mmol), 6-(3-chloropropanoyl)benzo[d]oxazol-2(3H)-one (**116**, 0.17 g, 0.51 mmol) to afford the desired product as white solid (0.07 g, 35%). MPt: 222 – 223 °C; ν_{max} (neat): 1766, 1675, 1448, 1169 cm^{-1} ; ^1H NMR (500 MHz, $\text{DMSO-}d_6$) δ 12.13 (s, 1H), 7.97 – 7.55 (m, 6H), 7.35 – 7.13 (m, 2H), 3.93 (t, $J = 6.2$ Hz, 2H), 3.54 (t, $J = 6.2$ Hz, 2H), 3.51 – 3.39 (m, 6H), 3.15 – 3.07 (m, 2H); ^{13}C NMR (101 MHz, $\text{DMSO-}d_6$) δ 195.3, 154.4, 143.4, 135.4, 135.2, 133.8, 130.6, 129.7, 127.7, 125.2, 109.5, 109.0, 50.5, 45.7, 43.3, 8.6; HRMS: exact mass calculated for $[\text{M}+\text{H}]^+$ ($\text{C}_{20}\text{H}_{22}\text{N}_3\text{O}_5\text{S}$) requires m/z 416.1275, found m/z 416.1271

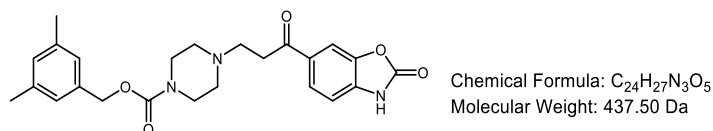
Compound 106: 6-(3-(4-Tosylpiperazin-1-yl)propanoyl)benzo[d]oxazol-2(3H)-one



Prepared according to procedure E at 80 °C using *tert*-butyl 4-tosylpiperazine-1-carboxylate (**138**, 0.2 g, 0.59 mmol), TFA: CH_2Cl_2 (1:1, 2 mL), MeCN (3 mL), Et_3N (0.14 mL, 1.03 mmol), 6-(3-chloropropanoyl)benzo[d]oxazol-2(3H)-one (**116**, 0.11 g, 0.47 mmol) to afford the desired product as white solid (0.17 g, 82%). MPt: 219 – 221 °C; ν_{max} (neat): 1796, 1683, 1349, 1165 cm^{-1} ; ^1H NMR (500 MHz, $\text{DMSO-}d_6$) δ 7.84 – 7.77 (m, 2H), 7.61 (d, $J = 8.0$ Hz, 2H), 7.45 (d, $J = 7.9$ Hz, 2H), 7.16 (d, $J =$

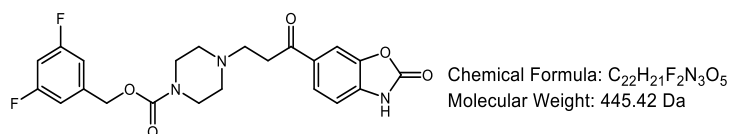
8.1 Hz, 1H), 3.41 – 3.25 (m, 4H), 3.11 (t, $J = 6.9$ Hz, 2H), 2.86 – 2.78 (m, 4H), 2.66 (t, $J = 6.9$ Hz, 2H), 2.41 (s, 3H), NH not observed; ^{13}C NMR (101 MHz, $\text{DMSO-}d_6$) δ 197.4, 154.5, 143.8, 143.3, 135.0, 131.6, 130.9, 129.8, 127.7, 125.0, 109.4, 108.9, 52.3, 51.5, 45.9, 35.4, 21.1; HRMS: exact mass calculated for $[\text{M}+\text{H}]^+$ ($\text{C}_{21}\text{H}_{24}\text{N}_3\text{O}_5\text{S}$) requires m/z 430.1431, found m/z 430.1431

Compound 107: 3,5-Dimethylbenzyl 4-(3-oxo-3-(2-oxo-2,3-dihydrobenzo[*d*]oxazol-6-yl)propyl)piperazine-1-carboxylate



Prepared according to procedure E at 80 °C using 1-(*tert*-butyl)4-(3,5-dimethylbenzyl) piperazine-1,4-dicarboxylate (**127**, 0.2 g, 0.57 mmol), TFA: CH_2Cl_2 (1:1, 2 mL), MeCN (3 mL), Et_3N (0.16 mL, 1.15 mmol), 6-(3-chloropropanoyl)benzo[*d*]oxazol-2(3*H*)-one (**116**, 0.12 g, 0.52 mmol) to afford the desired product as white solid (20 mg, 7%). MPt: 196 – 197 °C; ν_{max} (neat): 1763, 1673, 1452, 1142 cm^{-1} ; ^1H NMR (500 MHz, $\text{DMSO-}d_6$) δ 7.93 – 7.87 (m, 2H), 7.26 (d, $J = 8.1$ Hz, 1H), 7.02 – 6.93 (m, 3H), 5.04 (s, 2H), 3.68 – 3.32 (m, 12H), 2.28 (s, 6H), NH not observed; ^{13}C NMR (101 MHz, $\text{DMSO-}d_6$) δ 195.0, 154.4, 154.1, 143.3, 137.5, 136.2, 135.3, 130.1, 129.4, 125.6, 125.2, 109.5, 109.0, 66.8, 51.1, 50.8, 42.4, 32.6, 30.6, 20.8; HRMS: exact mass calculated for $[\text{M}+\text{H}]^+$ ($\text{C}_{24}\text{H}_{27}\text{N}_3\text{O}_5$) requires m/z 438.2023, found m/z 438.2018; No data previously reported.⁶⁷

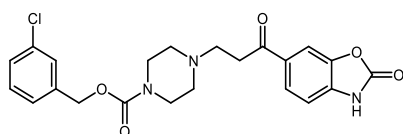
Compound 108: 3,5-Difluorobenzyl 4-(3-oxo-3-(2-oxo-2,3-dihydrobenzo[*d*]oxazol-6-yl)propyl)piperazine-1-carboxylate



Prepared according to procedure E at 80 °C using 1-(*tert*-butyl)4-(3,5-difluorobenzyl) piperazine-1,4-dicarboxylate (**128**, 0.2 g, 0.56 mmol), TFA: CH_2Cl_2 (1:1, 2 mL), MeCN (3 mL), Et_3N (0.14 mL, 1.01 mmol), 6-(3-chloropropanoyl)benzo[*d*]oxazol-2(3*H*)-one (**116**, 0.1 g, 0.46 mmol) to afford the desired product as clear gum (0.03 g, 14%). ν_{max} (neat): 3451, 1772, 1623, 1264 cm^{-1} ; ^1H NMR (400 MHz, MeOD) δ 7.92 (dd, $J = 8.2, 1.6$ Hz, 1H), 7.83 (d, $J = 1.4$ Hz, 1H), 7.17 (d, $J = 8.2$ Hz,

1H), 7.08 – 6.76 (m, 3H), 5.14 (s, 2H), 3.69 – 3.48 (m, 4H), 3.29 – 3.19 (m, 2H), 2.86 (t, $J = 7.1$ Hz, 2H), 2.59 – 2.51 (m, 4H), NH not observed; ^{13}C NMR (101 MHz, MeOD) δ 199.0, 164.6 (d, $^1J_{\text{C-F}} = 247.8$ Hz), 157.1, 156.4, 145.5, 142.7, 136.7, 132.9, 126.5, 111.3 (d, $^2J_{\text{C-F}} = 26.0$ Hz), 110.5, 110.1, 104.0 (t, $^2J_{\text{C-F}} = 25.7$ Hz), 66.8, 54.2, 53.8, 46.1, 44.7, 36.5, 1xC not observed, under solvent; ^{19}F NMR (376 MHz, DMSO- d_6) δ -73.48 (s, 2F); HRMS: exact mass calculated for $[\text{M}+\text{H}]^+$ ($\text{C}_{22}\text{H}_{22}\text{F}_2\text{N}_3\text{O}_5$) requires m/z 446.1522, found m/z 446.1517; No data previously reported.⁶⁷

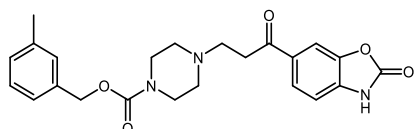
Compound 109: 3-Chlorobenzyl 4-(3-oxo-3-(2-oxo-2,3-dihydrobenzo[d]oxazol-6-yl)propyl)piperazine-1-carboxylate



Chemical Formula: $\text{C}_{22}\text{H}_{22}\text{ClN}_3\text{O}_5$
Molecular Weight: 443.88 Da

Prepared according to procedure E at 80 °C using 1-(*tert*-butyl)4-(3-chlorobenzyl) piperazine-1,4-dicarboxylate (**129**, 0.19 g, 0.54 mmol), TFA: CH_2Cl_2 (1:1, 2 mL), MeCN (3 mL), Et_3N (0.1 mL, 0.73 mmol), 6-(3-chloropropanoyl)benzo[d]oxazol-2(3*H*)-one (**116**, 0.08 g, 0.33 mmol) to afford the desired product as white gum (17 mg, 12%). ν_{max} (neat): 1763, 1676, 1448, 1196 cm^{-1} ; ^1H NMR (500 MHz, DMSO- d_6) δ 7.94 – 7.83 (m, 2H), 7.50 – 7.31 (m, 4H), 7.23 (d, $J = 8.0$ Hz, 1H), 5.14 (s, 2H), 3.67 – 3.61 (m, 2H), 3.52 (t, $J = 6.7$ Hz, 2H), 3.46 – 3.35 (m, 2H), 3.32 – 3.17 (m, 4H), 3.19 – 3.10 (m, 2H), NH not observed; ^{13}C NMR (126 MHz, DMSO- d_6) δ 154.8, 154.5, 143.9, 139.6, 135.8, 130.8, 129.9, 128.4, 126.7, 125.6, 109.9, 109.4, 66.4, 52.0, 51.7, 43.0, 41.6, 3xC not observed; HRMS: exact mass calculated for $[\text{M}-\text{H}]^-$ ($\text{C}_{22}\text{H}_{21}\text{ClN}_3\text{O}_5$) $[\text{M}-\text{H}]^-$ requires m/z 442.1167, found m/z 442.1175; No data previously reported.⁶⁷

Compound 110: 3-Methylbenzyl 4-(3-oxo-3-(2-oxo-2,3-dihydrobenzo[d]oxazol-6-yl)propyl)piperazine-1-carboxylate

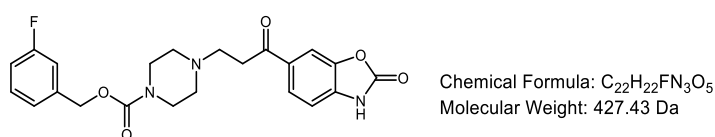


Chemical Formula: $\text{C}_{23}\text{H}_{25}\text{N}_3\text{O}_5$
Molecular Weight: 423.47 Da

Prepared according to procedure E at 80 °C using 1-(*tert*-butyl)4-(3-methylbenzyl) piperazine-1,4-dicarboxylate (**130**, 0.2 g, 0.6 mmol), TFA: CH_2Cl_2 (1:1, 2 mL), MeCN (3 mL), Et_3N (0.15 mL, 1.08 mmol), 6-(3-chloropropanoyl)benzo[d]oxazol-2(3*H*)-one

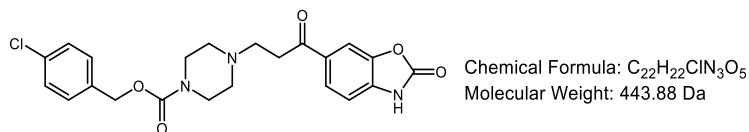
(**116**, 0.11 g, 0.49 mmol) to afford the desired product as clear oil (11 mg, 5%). ν_{\max} (neat): 1761, 1683, 1428, 1245 cm^{-1} ; ^1H NMR (500 MHz, CDCl_3) δ 8.02 – 7.91 (m, 2H), 7.44 – 7.39 (m, 2H), 7.33 – 7.27 (m, 3H), 5.26 (s, 2H), 3.72 – 3.65 (m, 4H), 3.37 – 3.25 (m, 1H), 3.27 – 3.14 (m, 1H), 3.07 – 2.98 (m, 2H), 2.74 – 2.59 (m, 4H), 2.52 (s, 3H), NH not observed; ^{13}C NMR (126 MHz, CDCl_3) δ 197.2, 155.6, 155.5, 144.2, 138.3, 136.6, 134.5, 132.1, 129.0, 128.8, 128.6, 125.4, 125.1, 109.8, 109.6, 67.5, 53.3, 45.7, 43.8, 36.1, 21.5; HRMS: exact mass calculated for $[\text{M}+\text{H}]^+$ ($\text{C}_{23}\text{H}_{26}\text{N}_3\text{O}_5$) requires m/z 424.1867, found m/z 424.1865

Compound 111: 3-Fluorobenzyl 4-(3-oxo-3-(2-oxo-2,3-dihydrobenzo[*d*]oxazol-6-yl)propyl)piperazine-1-carboxylate



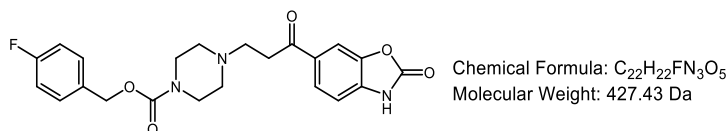
Prepared according to procedure E at 80 °C using 1-(*tert*-butyl) 4-(3-fluorobenzyl) piperazine-1,4-dicarboxylate (**131**, 0.20 g, 0.59 mmol), TFA: CH_2Cl_2 (1:1, 2.00 mL), MeCN (3.00 mL), Et_3N (0.16 mL, 1.18 mmol), 6-(3-chloropropanoyl)benzo[*d*]oxazol-2(3*H*)-one (**116**, 0.12 g, 0.54 mmol) to afford the desired product as a colourless oil (7 mg, 3%). ν_{\max} (neat): 3457, 1768, 1690, 1431, 1249 cm^{-1} ; ^1H NMR (500 MHz, CDCl_3) δ 7.90 – 7.82 (m, 2H), 7.34 (td, $J = 7.9, 5.8$ Hz, 1H), 7.14 (dd, $J = 8.1, 4.2$ Hz, 2H), 7.10 – 6.99 (m, 2H), 5.15 (s, 2H), 3.57 (t, $J = 5.1$ Hz, 4H), 3.21 (t, $J = 7.1$ Hz, 2H), 2.92 (t, $J = 7.1$ Hz, 2H), 2.60 – 2.48 (m, 4H), NH not observed; ^{13}C NMR (101 MHz, CDCl_3) δ 196.3, 162.4 (d, $^1J_{\text{C-F}} = 246.3$ Hz), 154.5, 154.4, 143.5, 138.6, 133.1, 131.7, 129.6 (d, $^3J_{\text{C-F}} = 8.2$ Hz), 124.8, 122.7, 114.4 (d, $^2J_{\text{C-F}} = 21.2$ Hz), 114.1 (d, $^2J_{\text{C-F}} = 21.8$ Hz), 109.3, 108.8, 65.8, 52.6, 52.4, 43.2, 35.4; ^{19}F NMR (376 MHz, $\text{DMSO-}d_6$) δ -73.45 (s, 1F); HRMS: exact mass calculated for $[\text{M}+\text{H}]^+$ ($\text{C}_{22}\text{H}_{23}\text{FN}_3\text{O}_5$) $[\text{M}+\text{H}]^+$ requires m/z 428.1616, found m/z 428.1612; No data previously reported.⁶⁷

Compound 112: 4-Chlorobenzyl 4-(3-oxo-3-(2-oxo-2,3-dihydrobenzo[d]oxazol-6-yl)propyl)piperazine-1-carboxylate



Prepared according to procedure E at 80 °C using 1-(*tert*-butyl) 4-(4-chlorobenzyl) piperazine-1,4-dicarboxylate (**132**, 0.2 g, 0.56 mmol), TFA:CH₂Cl₂ (1:1, 2 mL), MeCN (3 mL), Et₃N (0.16 mL, 1.17 mmol), 6-(3-chloropropanoyl)benzo[d]oxazol-2(3*H*)-one (**116**, 0.12 g, 0.53 mmol) to afford the desired product as white solid (0.24 g, 95%). MPt: 143 – 144 °C; ν_{\max} (neat): 3457, 1768, 1696 cm⁻¹; ¹H NMR (500 MHz, DMSO-*d*₆) δ 7.88 – 7.83 (m, 2H), 7.45 – 7.35 (m, 4H), 7.19 (d, *J* = 8.2 Hz, 1H), 5.07 (s, 2H), 3.41 – 3.34 (m, 4H), 3.23 – 3.16 (m, 2H), 2.75 – 2.64 (m, 2H), 2.45 – 2.39 (m, 4H), NH not observed; ¹³C NMR (126 MHz, DMSO-*d*₆) δ 197.9, 155.0, 154.7, 143.8, 136.4, 135.5, 132.9, 131.5, 129.9, 128.9, 125.5, 109.8, 109.4, 65.8, 53.3, 52.8, 43.9, 35.9; HRMS: exact mass calculated for [M+H]⁺ (C₂₂H₂₃ClN₃O₅) requires *m/z* 444.1321, found *m/z* 444.1319; No data previously reported.⁶⁷

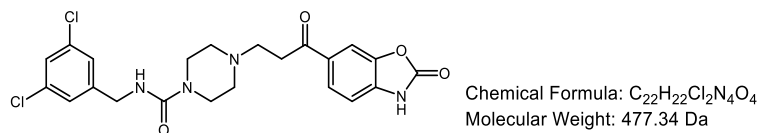
Compound 114: 4-Fluorobenzyl 4-(3-oxo-3-(2-oxo-2,3-dihydrobenzo[d]oxazol-6-yl)propyl)piperazine-1-carboxylate



Prepared according to procedure E at 80 °C using 1-(*tert*-butyl) 4-(4-fluorobenzyl) piperazine-1,4-dicarboxylate (**134**, 0.18 g, 0.53 mmol), TFA:CH₂Cl₂ (1:1, 2 mL), MeCN (3 mL), Et₃N (0.16 mL, 1.12 mmol), 6-(3-chloropropanoyl)benzo[d]oxazol-2(3*H*)-one (**116**, 0.12 g, 0.51 mmol) to afford the desired product as white solid (0.05 g, 21%). MPt: 191– 192 °C; ν_{\max} (neat): 1766, 1681, 1437, 1206 cm⁻¹; ¹H NMR (500 MHz, DMSO-*d*₆) δ 7.92 – 7.87 (m, 2H), 7.48 – 7.43 (m, 2H), 7.23 (dt, *J* = 15.1, 8.5 Hz, 3H), 5.11 (s, 2H), 3.66 – 3.45 (m, 4H), 3.53 – 3.32 (m, 8H), NH not observed; ¹³C NMR (101 MHz, DMSO-*d*₆) δ 195.1, 161.9 (d, ¹*J*_{C-F} = 243.8 Hz), 154.5, 154.1, 143.4, 135.5, 132.8, 132.8, 130.2 (d, ³*J*_{C-F} = 8.6 Hz), 125.3, 115.4 (d, ²*J*_{C-F} = 21.4 Hz), 109.6, 109.0, 66.2, 51.1, 50.8, 40.7, 32.6; ¹⁹F NMR (376 MHz, DMSO-*d*₆)

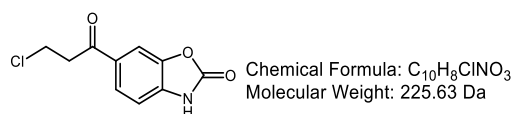
δ -73.74 (s, 1F); HRMS: exact mass calculated for $[M+H]^+$ ($C_{22}H_{23}FN_3O_5$) requires m/z 428.1616, found m/z 428.1613; No data previously reported.⁶⁷

Compound 115: *N*-(3,5-dichlorobenzyl)-4-(3-oxo-3-(2-oxo-2,3-dihydrobenzo[*d*]oxazol-6-yl)propyl)piperazine-1-carboxamide



Prepared according to procedure E at 80 °C using *tert*-butyl 4-((3,5-dichlorobenzyl)carbamoyl)piperazine-1-carboxylate (**135**, 0.2 g, 0.42 mmol), TFA:CH₂Cl₂ (1:1, 2 mL), MeCN (3 mL), Et₃N (0.14 mL, 1.03 mmol), 6-(3-chloropropanoyl)benzo[*d*]oxazol-2(3*H*)-one (**116**, 0.11 g, 0.47 mmol) to afford the desired product as white solid (0.16 g, 32%). MPt: 144 – 145 °C; ν_{max} (neat): 3299, 1766, 1543, 1258 cm⁻¹; ¹H NMR (500 MHz, DMSO-*d*₆) δ 7.90 – 7.83 (m, 2H), 7.39 (s, 1H), 7.32 – 7.28 (m, 2H), 7.21 (d, *J* = 8.1 Hz, 1H), 5.69 (s, 1H), 4.25 (d, *J* = 5.7 Hz, 2H), 3.62 – 3.54 (m, 2H), 3.53 – 3.45 (m, 2H), 3.30 – 3.14 (m, 2H), 3.15 – 2.90 (m, 6H), NH not observed; ¹³C NMR (101 MHz, DMSO-*d*₆) δ 157.0, 154.5, 145.3, 143.4, 135.2, 133.8, 130.4, 126.2, 126.0, 125.2, 109.5, 109.0, 51.4, 42.8, 42.4, 41.5, 40.5, 1xC not observed; HRMS: exact mass calculated for $[M+H]^+$ ($C_{22}H_{23}Cl_2N_4O_4$) requires m/z 477.0191, found m/z 477.1084; No data previously reported.⁶⁷

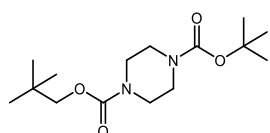
Compound 116: 6-(3-Chloropropanoyl)benzo[*d*]oxazol-2(3*H*)-one



To a round-bottomed flask was added AlCl₃ (18.54 g, 140.6 mmol) and DMF (6 mL) was added dropwise at 0 °C. The exothermic mixture turned grey and vigorous bubbling ensued. After 15 min 3-chloropropanoyl chloride (2.13 mL, 22.2 mmol) was added followed by benzo[*d*]oxazol-2(3*H*)-one (2.5 g, 18.5 mmol) portion wise at 0° C. The reaction was heated to 70 °C and stirred for 2 h. The reaction mixture solution was cooled and poured onto ice (300 g) and the precipitate filtered. The crude material was washed with H₂O, dried under vacuum and recrystallized from

EtOH (10 mL) to afford the desired product as a yellow crystalline solid (2.84 g, 68%). MPt: 162 – 161 °C; ν_{\max} (neat): 1764, 1660 cm^{-1} ; ^1H NMR (400 MHz, DMSO- d_6) δ 12.07 (s, 1H), 7.88 – 7.83 (m, 2H), 7.20 (d, J = 8.8 Hz, 1H), 3.92 (t, J = 6.3 Hz, 2H), 3.53 (t, J = 6.3 Hz, 2H); ^{13}C NMR (101 MHz, DMSO- d_6) δ 195.2, 154.3, 143.3, 135.1, 130.5, 125.1, 109.4, 108.9, 40.4, 39.5; HRMS: exact mass calculated for $[\text{M}+\text{H}]^+$ ($\text{C}_{10}\text{H}_8\text{ClNO}_3$) requires m/z 226.0265, found m/z 226.0265; Consistent with previously reported data.¹¹⁷

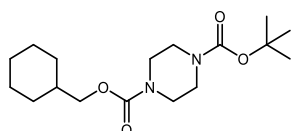
Compound 122: 1-(*tert*-Butyl) 4-neopentyl piperazine-1,4-dicarboxylate



Chemical Formula: $\text{C}_{15}\text{H}_{28}\text{N}_2\text{O}_4$
Molecular Weight: 300.40 Da

Prepared according to general procedure C using 2,2-dimethylpropan-1-ol (0.24 g, 2.68 mmol), CDI (0.52 g, 2.68 mmol), DMF (2 mL), *tert*-butyl piperazine-1-carboxylate (0.5 g, 2.68 mmol) afford the desired product as a white solid (0.44 g, 54%). MPt: 134 – 135 °C; ν_{\max} (neat): 1685, 1423, 1234 cm^{-1} ; ^1H NMR (500 MHz, CDCl_3) δ 3.79 (s, 2H), 3.53 – 3.33 (m, 8H), 1.46 (s, 9H), 0.94 (s, 9H); ^{13}C NMR (126 MHz, CDCl_3) δ 155.8, 154.8, 80.3, 75.1, 43.7, 31.7, 28.5, 26.6, 2xC isochronous; HRMS: exact mass calculated for $[\text{M}+\text{NH}_4]^+$ ($\text{C}_{15}\text{H}_{28}\text{N}_2\text{O}_4\text{NH}_4$) requires m/z 318.2387, found m/z 318.2386

Compound 123: 1-(*tert*-Butyl) 4-(cyclohexylmethyl) piperazine-1,4-dicarboxylate

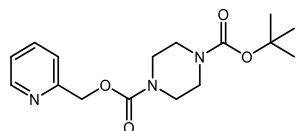


Chemical Formula: $\text{C}_{17}\text{H}_{30}\text{N}_2\text{O}_4$
Molecular Weight: 326.44 Da

Prepared according to general procedure C using cyclohexylmethanol (0.2 mL, 1.61 mmol), CDI (0.31 g, 1.77 mmol), DMF (3 mL), *tert*-butyl piperazine-1-carboxylate (0.3 g, 1.61 mmol) to afford the desired product as a white solid (0.3 g, 57%). MPt: 67 – 69 °C; ν_{\max} (neat): 2922, 2852, 1684, 1424 cm^{-1} ; ^1H NMR (400 MHz, DMSO- d_6) δ 3.82 (d, J = 6.5 Hz, 2H), 3.34 – 3.30 (m, 8H), 1.77 – 1.54 (m, 6H), 1.42 (s, 9H), 1.28 – 1.08 (m, 3H), 1.04 – 0.90 (m, 2H); ^{13}C NMR (101 MHz, DMSO- d_6) δ 154.7, 153.8, 79.1, 69.9, 43.1, 36.9, 29.1, 28.0, 26.0, 25.2, 2xC

isochronous; HRMS: exact mass calculated for $[M+NH_4]^+$ ($C_{17}H_{30}N_2O_4NH_4$) requires m/z 344.2544, found m/z 344.2544; Consistent with previously reported data.¹⁴²

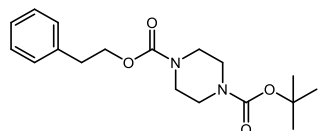
Compound 124: 1-(*tert*-Butyl) 4-(pyridin-2-ylmethyl) piperazine-1,4-dicarboxylate



Chemical Formula: $C_{16}H_{23}N_3O_4$
Molecular Weight: 321.38 Da

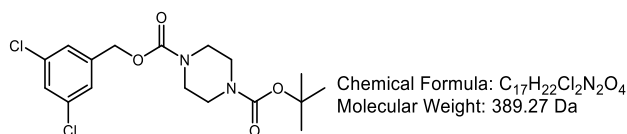
Prepared according to general procedure C using pyridin-2-ylmethanol (0.29 g, 2.68 mmol), CDI (0.52 g, 2.68 mmol), DMF (2.00 mL), *tert*-butyl piperazine-1-carboxylate (0.50 g, 2.68 mmol) to afford the desired product as a white solid (0.65 g, 76%). MPt: 95 – 96 °C; ν_{max} (neat): 1678, 1419, 1228 cm^{-1} ; 1H NMR (500 MHz, $CDCl_3$) δ 8.58 (d, $J = 4.4$ Hz, 1H), 7.68 (td, $J = 7.7, 1.7$ Hz, 1H), 7.33 (d, $J = 7.8$ Hz, 1H), 7.24 – 7.17 (m, 1H), 5.25 (s, 2H), 3.54 – 3.38 (m, 8H), 1.45 (s, 9H); ^{13}C NMR (126 MHz, $CDCl_3$) δ 156.5, 155.1, 154.7, 149.6, 136.9, 136.8, 122.9, 121.7, 80.3, 68.0, 43.9, 28.5; HRMS: exact mass calculated for $[M+H]^+$ ($C_{16}H_{24}N_3O_4$) requires m/z 322.1761, found m/z 322.1761

Compound 125: 1-(*tert*-Butyl) 4-phenethyl piperazine-1,4-dicarboxylate

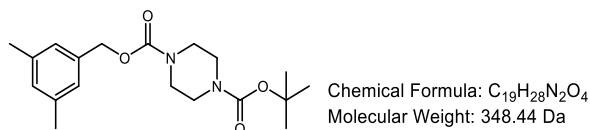


Chemical Formula: $C_{18}H_{26}N_2O_4$
Molecular Weight: 334.42 Da

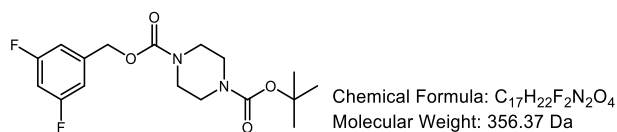
Prepared according to general procedure C using 2-phenylethan-1-ol (0.32 mL, 2.68 mmol), CDI (0.85 g, 5.24 mmol), DMF (4 mL), *tert*-butyl piperazine-1-carboxylate (0.5 g, 2.68 mmol) to afford the desired product as a white solid (0.67 g, 79%). MPt: 87 – 88 °C; ν_{max} (neat): 2975, 2868, 1683, 1230 cm^{-1} ; 1H NMR (500 MHz, $DMSO-d_6$) δ 7.43 – 7.18 (m, 5H), 4.20 (t, $J = 6.8$ Hz, 2H), 3.32 – 3.26 (m, 8H), 2.91 – 2.86 (m, 2H), 1.40 (s, 9H); ^{13}C NMR (101 MHz, $DMSO-d_6$) δ 154.4, 153.8, 138.2, 128.9, 128.3, 126.3, 79.1, 65.6, 43.1, 34.8, 28.0, 2xC isochronous; HRMS: exact mass calculated for $[M+NH_4]^+$ ($C_{18}H_{26}N_2O_4NH_4$) $[M+NH_4]^+$ requires m/z 352.2231, found m/z 352.2231; No data previously reported.¹⁴³

Compound 126: 1-(*tert*-Butyl) 4-(3,5-dichlorobenzyl) piperazine-1,4-dicarboxylate

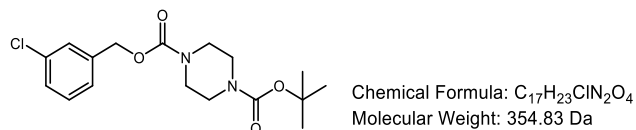
Prepared according to general procedure C using (3,5-dichlorophenyl)methanol (2 g, 11.3 mmol), CDI (1.83 g, 11.3 mmol), DMF (15 mL), *tert*-butyl piperazine-1-carboxylate (1.89 g, 10.17 mmol) to afford the desired product as a white solid (37 mg, 54%). MPt: 114 – 115 °C; ν_{\max} (neat): 1678, 1228 cm⁻¹; ¹H NMR (400 MHz, CDCl₃) δ 7.31 (t, *J* = 1.8 Hz, 1H), 7.22 (d, *J* = 1.8 Hz, 2H), 5.08 (s, 2H), 3.53 – 3.35 (m, 8H), 1.47 (s, 9H); ¹³C NMR (101 MHz, DMSO-*d*₆) δ 154.1, 153.8, 141.1, 134.1, 133.8, 127.5, 126.3, 124.9, 79.2, 64.9, 61.6, 43.3, 28.0; HRMS: exact mass calculated for [M+NH₄OAC]⁺ (C₁₇H₂₆O₄N₃Cl₂) requires *m/z* 406.1295, found *m/z* 406.1293; Consistent with previously reported data.¹¹⁷

Compound 127: 1-(*tert*-Butyl) 4-(3,5-dimethylbenzyl) piperazine-1,4-dicarboxylate

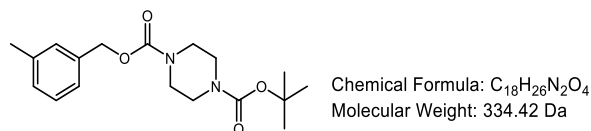
Prepared according to general procedure C using (3,5-dimethylphenyl)methanol (0.39 mL, 2.68 mmol), CDI (0.52, 2.95 mmol), DMF (3 mL), *tert*-butyl piperazine-1-carboxylate (0.5 g, 2.68 mmol) to afford the desired product as a colourless oil (0.93 g, 54%). ν_{\max} (neat): 2921, 1688, 1415, 1228 cm⁻¹; ¹H NMR (400 MHz, CDCl₃) δ 7.15 – 7.09 (m, 1H), 7.00 – 6.97 (m, 2H), 5.09 (s, 2H), 3.51 – 3.38 (m, 8H), 2.34 (s, 6H), 1.49 (s, 9H); ¹³C NMR (101 MHz, CDCl₃) δ 155.4, 154.6, 138.3, 136.4, 129.9, 126.0, 80.3, 67.6, 43.8, 28.5, 21.4, 2xC isochronous; HRMS: exact mass calculated for [M+NH₄]⁺ (C₁₉H₂₈N₂O₄NH₄) requires *m/z* 366.2387, found *m/z* 366.2387

Compound 128: 1-(*tert*-Butyl) 4-(3,5-difluorobenzyl) piperazine-1,4-dicarboxylate

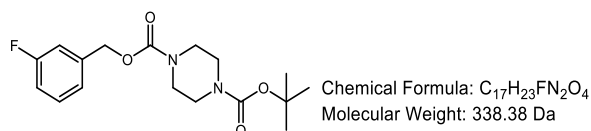
Prepared according to general procedure C (3,5-difluorophenyl)methanol using (0.16 mL, 1.34 mmol), CDI (0.18 g, 1.48 mmol), DMF (2 mL), *tert*-butyl piperazine-1-carboxylate (0.25 mg, 1.34 mmol) to afford the desired product as a white solid (0.48 g, 57%). MPt: 116 – 117 °C; ν_{\max} (neat): 1690, 1243, 1109 cm⁻¹; ¹H NMR (400 MHz, DMSO-*d*₆) δ 7.27 – 7.05 (m, 3H), 5.11 (s, 2H), 3.45 – 3.33 (m, 8H), 1.41 (s, 9H); ¹³C NMR (101 MHz, DMSO) δ 162.5 (d, ¹J_{C-F} = 246.3 Hz), 162.3 (d, ¹J_{C-F} = 246.8 Hz), 154.1, 153.8, 141.5, 110.4 (d, ²J_{C-F} = 25.6 Hz), 103.2 (t, ²J_{C-F} = 25.7 Hz), 79.2, 65.1, 43.4, 28.1; ¹⁹F NMR (471 MHz, DMSO-*d*₆) δ -109.66 (s, 2F); HRMS: exact mass calculated for [M+NH₄]⁺ (C₁₇H₂₂F₂N₂O₄NH₄) requires *m/z* 374.1886, found *m/z* 374.1878

Compound 129: 1-(*tert*-Butyl) 4-(3-chlorobenzyl) piperazine-1,4-dicarboxylate

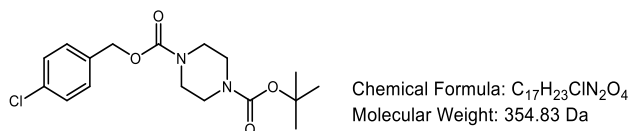
Prepared according to general procedure C using (3-chlorophenyl)methanol (0.19 mL, 1.61 mmol), CDI (0.31 g, 1.77 mmol), DMF (3 mL), *tert*-butyl piperazine-1-carboxylate (0.30 g, 1.61 mmol) to afford the desired product as a colourless oil (0.19 g, 34%). ν_{\max} (neat): 2977, 1691, 1413, 1225 cm⁻¹; ¹H NMR (500 MHz, CDCl₃) δ 7.38 – 7.32 (m, 1H), 7.32 – 7.27 (m, 2H), 7.26 – 7.20 (m, 1H), 5.11 (s, 2H), 3.62 – 3.30 (m, 8H), 1.47 (s, 9H); ¹³C NMR (101 MHz, CDCl₃) δ 154.4, 154.1, 138.0, 133.9, 129.3, 127.8, 127.4, 125.4, 79.7, 65.9, 43.2, 27.9, 2xC isochronous; HRMS: exact mass calculated for [M+NH₄]⁺ (C₁₇H₂₃ClN₂O₄NH₄) requires *m/z* 372.1685, found *m/z* 372.1682

Compound 130: 1-(*tert*-Butyl) 4-(3-methylbenzyl) piperazine-1,4-dicarboxylate

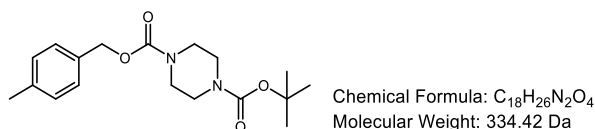
Prepared according to general procedure C using *m*-tolylmethanol (0.2 mL, 1.61 mmol), CDI (0.31 g, 1.77 mmol), DMF (3 mL), *tert*-butyl piperazine-1-carboxylate (0.3 g, 1.61 mmol) to afford the desired product as a colourless oil (0.21 g, 41%). ν_{\max} (neat): 2975, 1691, 1412, 1224 cm⁻¹; ¹H NMR (500 MHz, CDCl₃) δ 7.30 – 7.25 (m, 2H), 7.18 – 7.13 (m, 2H), 5.13 (s, 2H), 3.56 – 3.40 (m, 8H), 2.38 (s, 3H), 1.49 (s, 9H); ¹³C NMR (101 MHz, CDCl₃) δ 154.8, 154.2, 137.7, 135.9, 128.4, 128.3, 128.0, 124.6, 79.7, 66.9, 43.2, 27.9, 20.9, 2xC isochronous; HRMS: exact mass calculated for [M+NH₄]⁺ (C₁₈H₂₆N₂O₄NH₄) requires *m/z* 352.2231, found *m/z* 352.2231

Compound 131: 1-(*tert*-Butyl) 4-(3-fluorobenzyl) piperazine-1,4-dicarboxylate

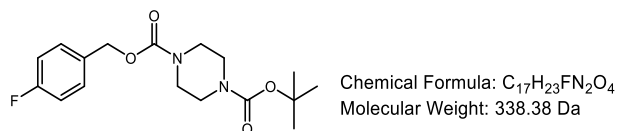
Prepared according to general procedure C using (3-fluorophenyl)methanol (0.17 mL, 1.61 mmol), CDI (0.31 g, 1.77 mmol), DMF (3 mL), *tert*-butyl piperazine-1-carboxylate (0.3 g, 1.61 mmol) to afford the desired product as a white solid (0.48 g, 87%). MPt: 87 – 88 °C; ν_{\max} (neat): 2976, 1694, 1426 cm⁻¹; ¹H NMR (400 MHz, DMSO-*d*₆) δ 7.62 – 7.32 (m, 1H), 7.33 – 6.88 (m, 3H), 5.12 (s, 2H), 3.75 – 3.00 (m, 8H), 1.42 (s, 9H); ¹³C NMR (101 MHz, DMSO-*d*₆) δ 162.1 (d, ¹J_{C-F} = 243.7 Hz), 154.2, 153.6, 139.7, 130.4 (d, ³J_{C-F} = 8.6 Hz), 123.4, 114.6 (d, ²J_{C-F} = 21.0 Hz), 114.1 (d, ²J_{C-F} = 21.7 Hz), 79.1, 65.5, 43.2, 28.0; ¹⁹F NMR (471 MHz, DMSO-*d*₆) δ -113.16 (s, 1F); HRMS: exact mass calculated for [M+ NH₄]⁺ (C₁₇H₂₄FN₂O₄) requires *m/z* 356.1980, found *m/z* 356.1977.

Compound 132: 1-(*tert*-Butyl) 4-(4-chlorobenzyl) piperazine-1,4-dicarboxylate

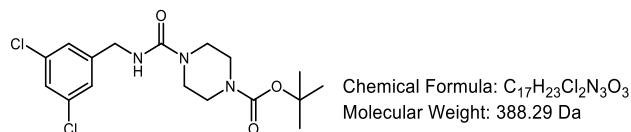
Prepared according to general procedure C using (4-chlorophenyl)methanol (0.19 g, 1.34 mmol), CDI (0.26 g, 1.48 mmol), DMF (2 mL), *tert*-butyl piperazine-1-carboxylate (0.25 mg, 1.34 mmol) to afford the desired product as a white solid (0.48 g, 72%). MPt: 111 – 112 °C; ν_{\max} (neat): 1692, 1362, 1238 cm⁻¹; ¹H NMR (500 MHz, DMSO-*d*₆) δ 7.43 (d, *J* = 8.5 Hz, 2H), 7.39 (d, *J* = 8.5 Hz, 2H), 5.08 (s, 2H), 3.52 – 3.32 (m, 8H), 1.40 (s, 9H); ¹³C NMR (101 MHz, CDCl₃) δ 154.3, 153.8, 135.8, 132.5, 129.5, 128.4, 79.2, 65.5, 43.2, 28.0, 2xC isochronous; HRMS: exact mass calculated for [M+Na]⁺ (C₁₇H₂₃ClN₂O₄Na) requires *m/z* 377.1239, found *m/z* 377.1234; No data previously reported data.⁶⁷

Compound 133: 1-(*tert*-Butyl) 4-(4-methylbenzyl) piperazine-1,4-dicarboxylate

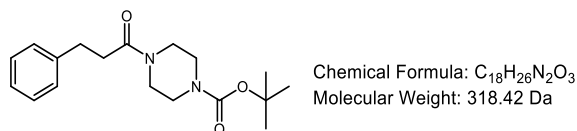
Prepared according to general procedure C using *p*-tolylmethanol (0.2 g, 1.61 mmol), CDI (0.31 g, 1.77 mmol), DMF (4 mL), *tert*-butyl piperazine-1-carboxylate (0.3 g, 1.61 mmol) to afford the desired product as a white solid (0.40 g, 74%). MPt: 114 – 115 °C; ν_{\max} (neat): 1693, 1417, 1224 cm⁻¹; ¹H NMR (400 MHz, DMSO-*d*₆) δ 7.25 (d, *J* = 8.0 Hz, 2H), 7.17 (d, *J* = 7.9 Hz, 2H), 5.03 (s, 2H), 3.41 – 3.25 (m, 8H), 2.29 (s, 3H), 1.40 (s, 9H); ¹³C NMR (101 MHz, CDCl₃) δ 155.4, 154.8, 138.1, 133.6, 129.4, 128.3, 80.3, 67.4, 43.8, 28.5, 21.3, 2xC isochronous; HRMS: exact mass calculated for [M+NH₄]⁺ (C₁₈H₂₅N₂O₄NH₄) requires *m/z* 352.2231, found *m/z* 352.2232

Compound 134: 1-(*tert*-Butyl) 4-(4-fluorobenzyl) piperazine-1,4-dicarboxylate

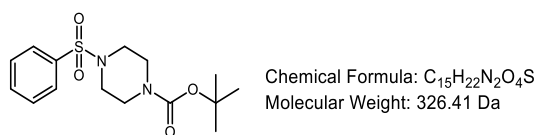
Prepared according to general procedure C using (4-fluorophenyl)methanol (0.15 mL, 1.34 mmol), CDI (0.18 g, 1.48 mmol), DMF (2 mL), *tert*-butyl piperazine-1-carboxylate (0.25 g, 1.34 mmol) to afford the desired product as a white solid (0.2 g, 46%). MPt: 100 – 101 °C; ν_{\max} (neat): 2975, 1694, 1236 cm⁻¹; ¹H NMR (500 MHz, DMSO-*d*₆) δ 7.42 (t, *J* = 8.5 Hz, 2H), 7.19 (t, *J* = 8.5 Hz, 2H), 5.06 (s, 2H), 3.27 – 3.31 (m, 8H), 1.40 (s, 9H); ¹³C NMR (101 MHz, DMSO-*d*₆) δ 184.1 (d, ¹*J*_{C-F} = 238.7 Hz), 154.4, 153.8, 133.1, 130.0 (d, ³*J*_{C-F} = 8.4 Hz), 115.3 (d, ²*J*_{C-F} = 21.2 Hz), 79.2, 65.7, 43.2, 28.0, 2xC isochronous; ¹⁹F NMR (376 MHz, DMSO-*d*₆) δ -114.33 (s, 1F); HRMS: exact mass calculated for [M+NH₄]⁺ (C₁₇H₂₃FN₂O₄NH₄) requires *m/z* 356.1980, found *m/z* 356.1980.

Compound 135: *tert*-Butyl 4-((3,5-dichlorobenzyl)carbamoyl)piperazine-1-carboxylate

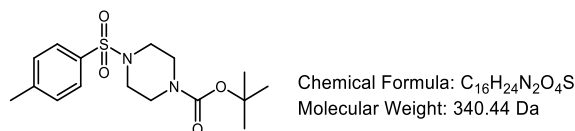
Prepared according to general procedure C using (3,5-dichlorophenyl)methanamine (0.24 g, 1.34 mmol), CDI (0.18 g, 1.48 mmol), DMF (2 mL), *tert*-butyl piperazine-1-carboxylate (0.25 mg, 1.34 mmol) to afford the desired product as a white solid (0.17 g, 32%). MPt: 144 – 145 °C; ν_{\max} (neat): 3334, 1698, 1629, 1534, 1234 cm⁻¹; ¹H NMR (400 MHz, DMSO-*d*₆) δ 7.46 – 7.45 (m, 1H), 7.29 (d, *J* = 1.8 Hz, 2H), 7.23 (t, *J* = 5.8 Hz, 1H), 4.22 (d, *J* = 5.6 Hz, 2H), 3.36 – 3.20 (m, 8H), 1.40 (s, 9H); ¹³C NMR (101 MHz, DMSO-*d*₆) δ 157.2, 153.9, 145.5, 133.8, 126.1, 125.9, 79.1, 43.2, 42.8, 35.8, 28.0; HRMS: exact mass calculated for [M+NH₄]⁺ (C₁₇H₂₃Cl₂N₃O₃NH₄) requires *m/z* 405.1455, found *m/z* 405.1455.

Compound 136: *tert*-butyl 4-(3-phenylpropanoyl)piperazine-1-carboxylate

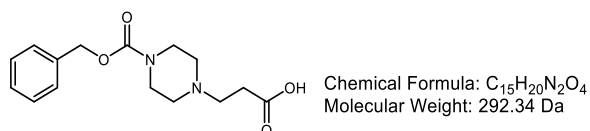
Prepared according to procedure F using 3-phenylpropanoic acid (0.5 g, 3.33 mmol), DIPEA (1.16 mL, 6.66 mmol), COMU (1.43 g, 3.33 mmol), *tert*-butyl piperazine-1-carboxylate (0.62 g, 3.33 mmol), DMF (5 mL) to afford the desired product as white solid (0.52 g, 49%). MPt: 70 – 72 °C; ν_{\max} (neat): 2980, 1684, 1629, 1420, 1240 cm⁻¹; ¹H NMR (500 MHz, CDCl₃) δ 7.38 – 7.33 (m, 2H), 7.30 – 7.26 (m, 3H), 3.66 (t, *J* = 5 Hz, 2H), 3.48 – 3.31 (m, 6H), 3.05 (t, *J* = 8 Hz, 2H), 2.70 (t, *J* = 8 Hz, 2H), 1.53 (s, 9H); ¹³C NMR (126 MHz, CDCl₃) δ 170.9, 154.5, 141.1, 128.6, 128.5, 126.3, 80.3, 45.4, 41.4, 35.1, 31.5, 28.4; HRMS: exact mass calculated for [M+H]⁺ (C₁₈H₂₇N₂O₃) [M+H]⁺ requires *m/z* 319.2016, found *m/z* 319.2016; Consistent with previously reported data.¹⁴⁴

Compound 137: *tert*-Butyl 4-(phenylsulfonyl)piperazine-1-carboxylate

Prepared according to procedure D using benzenesulfonyl chloride (0.31 mL, 1.47 mmol), *tert*-butyl piperazine-1-carboxylate (0.25 g, 1.34 mmol), Et₃N (0.23 mL, 1.61 mmol), CH₂Cl₂ (3 mL) to afford the desired product as a white solid (0.24 g, 55%). MPt: 124 – 126 °C; ν_{\max} (neat): 1686, 1431, 1169 cm⁻¹; ¹H NMR (500 MHz, CDCl₃) δ 7.77 (d, *J* = 7.4 Hz, 2H), 7.66 – 7.63 (m, 1H), 7.59 – 7.55 (m, 2H), 3.54 – 3.52 (m, 4H), 3.01 – 2.99 (m, 4H), 1.43 (s, 9H); ¹³C NMR (101 MHz, CDCl₃) δ 154.2, 135.6, 133.2, 129.3, 127.8, 80.5, 45.9, 28.4, 2xC isochronous; HRMS: exact mass calculated for [M+Na]⁺ (C₁₅H₂₂N₂O₄SNa) requires *m/z* 349.1192, found *m/z* 349.1191; Consistent with previously reported data.¹⁴⁵

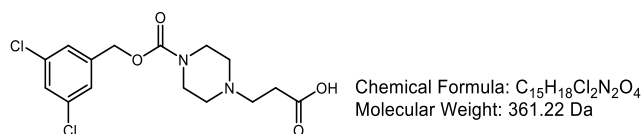
Compound 138: *tert*-Butyl 4-tosylpiperazine-1-carboxylate

Prepared according to procedure D using 4-methylbenzenesulfonyl chloride (0.28 g, 1.47 mmol), *tert*-butyl piperazine-1-carboxylate (0.25 mg, 1.34 mmol), Et₃N (0.23 mL, 1.61 mmol), CH₂Cl₂ (3 mL) to afford the desired product as white solid (0.25 g, 55%). MPt: 159 – 160 °C; ν_{\max} (neat): 1698, 1348, 1167, 942 cm⁻¹; ¹H NMR (500 MHz, CDCl₃) δ 7.63 (d, *J* = 8.2 Hz, 2H), 7.33 (d, *J* = 8.1 Hz, 2H), 3.53 – 3.39 (m, 4H), 3.03 – 2.88 (m, 4H), 2.43 (s, 3H), 1.40 (s, 9H); ¹³C NMR (101 MHz, CDCl₃) δ 154.2, 144.0, 132.5, 129.9, 127.9, 80.4, 45.9, 28.4, 21.6, 2xC isochronous; HRMS: exact mass calculated for [M+Na]⁺ (C₁₆H₂₄N₂O₄SNa) requires *m/z* 363.1349, found *m/z* 363.1350; Consistent with previously reported data.¹⁴⁶

Compound 143: 3-(4-((Benzyloxy)carbonyl)piperazin-1-yl)propanoic acid

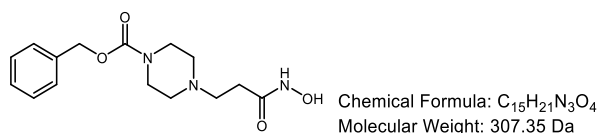
To a round-bottom flask was added benzyl 4-(3-ethoxy-3-oxopropyl)piperazine-1-carboxylate (1.37 g, 4.28 mmol), 1M LiOH:MeOH (1:1, 20 mL) and stirred for 3 h at room temperature. After complete consumption of starting material by TLC analysis the reaction mixture was diluted with EtOAc (15 mL) and acidified with 1M HCl (10 mL). The organics were then collected, dried (hydrophobic frit), and concentrated under vacuum to afford the desired product as a white solid (1.08 g, 86%). MPt: 202 – 203 °C; ν_{\max} (neat): 3410, 2939, 1705 cm⁻¹; ¹H NMR (400 MHz, DMSO-*d*₆) δ 11.61 (br.s, 1H), 7.36 – 7.25 (m, 5H), 5.07 (s, 2H), 4.04 – 3.98 (m, 2H), 3.51 – 3.34 (m, 4H), 3.24 (t, *J* = 7.7 Hz, 2H), 3.19 – 2.99 (m, 2H), 2.84 – 2.80 (m, 2H); ¹³C NMR (101 MHz, DMSO-*d*₆) δ 171.3, 154.1, 136.4, 128.4, 128.0, 127.6, 66.7, 51.0, 50.3, 40.4, 28.3; HRMS: exact mass calculated for [M+H]⁺ (C₁₅H₂₁N₂O₄) requires *m/z* 293.1496, found *m/z* 293.1491.

Compound 144: 3-(4-(((3,5-Dichlorobenzyl)oxy)carbonyl)piperazin-1-yl)propanoic acid



To a round-bottom flask was added ethyl 3-chloropropanoate (0.18 mL, 1.30 mmol), THF (10 mL), Et_3N (0.32 mL, 1.56 mmol), 3,5-dichlorobenzyl piperazine-1-carboxylate (**156**, 0.45 g, 1.56 mmol) and stirred for 16 h at room temperature. The reaction mixture was diluted with H_2O (10 mL) and extracted using EtOAc (25 mL). The organics were combined, dried (hydrophobic frit), and concentrated under vacuum to a residue that was purified using silica gel chromatography (50% EtOAc in petroleum ether) to give the 3,5-dichlorobenzyl 4-(3-ethoxy-3-oxopropyl)piperazine-1-carboxylate as a white solid. The resulting solid (0.17 g, 0.43 mmol) was dissolved in THF: H_2O (3:1, 8 mL) and $LiOH \cdot H_2O$ (0.04 g, 0.85 mmol) and stirred for 4 h at 40 °C. After complete consumption of starting material by TLC analysis the reaction mixture was diluted with EtOAc (15 mL) and acidified with 1 M HCl (5 mL). The organics were collected, dried (hydrophobic frit), and concentrated under vacuum to afford the desired product as a yellow solid (0.17 g, 94%). MPt: 178 – 179 °C; ν_{max} (neat): 2924, 1699, 1415 cm^{-1} ; 1H NMR (400 MHz, $CDCl_3$) δ 7.30 (t, $J = 1.9$ Hz, 1H), 7.21 (d, $J = 1.9$ Hz, 2H), 5.06 (s, 2H), 3.74 – 3.51 (m, 4H), 2.81 (t, $J = 6.3$ Hz, 2H), 2.72 – 2.65 (m, 4H), 2.54 (t, $J = 6.3$ Hz, 2H), OH not observed; ^{13}C NMR (101 MHz, $CDCl_3$) δ 172.9, 154.0, 139.2, 134.7, 127.8, 125.7, 65.3, 52.8, 51.3, 42.5, 29.8; HRMS: exact mass calculated for $[M-H]^-$ ($C_{15}H_{17}Cl_2N_2O_4$) requires m/z 359.0571, found m/z 359.0566.

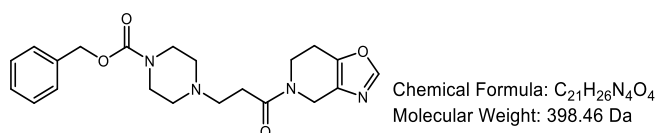
Compound 145: Benzyl 4-(3-(hydroxyamino)-3-oxopropyl)piperazine-1-carboxylate



To a round-bottom flask was added benzyl 4-(3-ethoxy-3-oxopropyl)piperazine-1-carboxylate (0.05 g, 0.16 mmol), anhydrous MeOH (0.25 mL) under N_2 . The flask was purged with N_2 before adding a preformed slurry of $HONH_2 \cdot HCl$ (0.03 g,

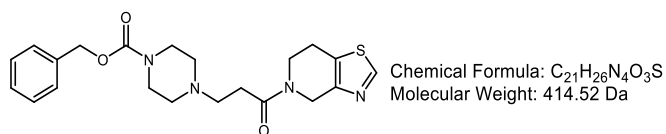
0.47 mmol) and KOH (0.05 g, 0.94 mmol) in MeOH (1 mL). The reaction mixture was stirred for 16 h at 25 °C. The reaction was then neutralized using 3M HCl (3 mL) in CPME and concentrated under vacuum to give a residue. The crude material was dissolved in MeOH:DMSO (1:1, 1 mL) and purified by MDAP to afford the desired product as a white gum (22 mg, 46%). ν_{\max} (neat): 3188, 1695, 1429, 1242 cm^{-1} ; ^1H NMR (400 MHz, $\text{DMSO-}d_6$) δ 10.38 (s, 1H), 8.36 (s, 1H), 7.48 – 7.25 (m, 5H), 5.08 (s, 2H), 3.49 – 3.13 (m, 4H), 2.57 – 2.52 (m, 2H), 2.43 – 2.25 (m, 4H), 2.13 (t, $J = 7.2$ Hz, 2H); ^{13}C NMR (101 MHz, $\text{DMSO-}d_6$) δ 168.1, 154.9, 136.3, 128.6, 128.2, 127.9, 67.6, 53.0, 51.9, 42.1, 28.5; HRMS: exact mass calculated for $[\text{M}+\text{H}]^+$ ($\text{C}_{15}\text{H}_{22}\text{N}_3\text{O}_4$) requires m/z 308.1605 found m/z 308.1602.

Compound 147: Benzyl 4-(3-(6,7-dihydrooxazolo[4,5-c]pyridin-5(4H)-yl)-3-oxopropyl)piperazine-1-carboxylate



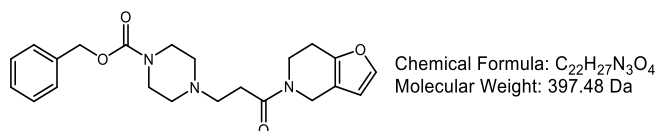
Prepared according to general procedure G using 3-(4-((benzyloxy)carbonyl)piperazin-1-yl)propanoic acid (**143**, 0.15 g, 0.51 mmol), DMF (3 mL), DIPEA (0.27 mL, 1.54 mmol), HATU (0.22 g, 0.51 mmol), 4,5,6,7-tetrahydrooxazolo[4,5-c]pyridine hydrochloride (0.06 mL, 0.51 mmol) to afford the desired product as a colourless gum (10 mg, 5%). ν_{\max} (neat): 3282, 1679, 1429 cm^{-1} ; ^1H NMR (400 MHz, $\text{DMSO-}d_6$) δ 6.59 – 6.43 (m, 5H), 5.49 (dd, $J = 10.2, 1.8$ Hz, 1H), 4.30 (s, 2H), 4.02 (s, 2H), 3.66 (d, $J = 6.4$ Hz, 2H), 3.07 (t, $J = 5.8$ Hz, 1H), 3.00 (t, $J = 5.8$ Hz, 1H), 2.84 – 2.59 (m, 4H), 2.00 – 1.75 (m, 4H), 1.73 – 1.58 (m, 4H); ^{13}C NMR (101 MHz, $\text{DMSO-}d_6$) δ 171.4, 155.1, 151.2, 137.7, 131.3, 128.7, 128.1, 127.8, 66.8, 54.1, 52.8, 44.3, 31.4, 22.9, 2xC not observed, 2xC isochronous; HRMS: exact mass calculated for $[\text{M}+\text{H}]^+$ ($\text{C}_{21}\text{H}_{26}\text{N}_4\text{O}_4$) requires m/z 399.2027, found m/z 399.2035

Compound 147: Benzyl 4-(3-(6,7-dihydrothiazolo[4,5-c]pyridin-5(4H)-yl)-3-oxopropyl)piperazine-1-carboxylate:

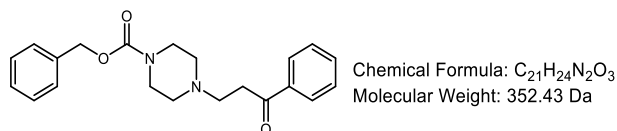


Prepared according to general procedure G using 3-(4-((benzyloxy)carbonyl)piperazin-1-yl)propanoic acid (**143**, 0.15 g, 0.51 mmol), DMF (3 mL), (0.27 mL, 1.54 mmol), HATU (0.2 mg, 0.51 mmol), 4,5,6,7-tetrahydrothiazolo[4,5-c]pyridine, hydrochloride (0.09 g, 0.51 mmol) to afford the desired product as a yellow gum (19 mg, 9%). ν_{\max} (neat): 1639, 1635, 1429 cm⁻¹; ¹H NMR (400 MHz, MeOD) δ 8.35 (s, 1H), 7.47 – 7.23 (m, 5H), 5.15 (d, J = 3.6 Hz, 2H), 3.96 (t, J = 5.9 Hz, 1H), 3.91 (t, J = 5.8 Hz, 1H), 3.62 (s, 4H), 3.07 – 2.70 (m, 10H), 2xH not observed, under solvent; NMR (101 MHz, MeOD) δ 172.2, 156.7, 154.1, 153.9, 138.0, 129.7, 129.4, 129.1, 68.7, 55.0, 53.7, 44.4, 44.0, 41.5, 30.6, 28.4, 1xC not observed; HRMS: exact mass calculated for [M+H]⁺ (C₂₁H₂₇N₄O₃S) requires m/z 415.1798, found m/z 415.1789.

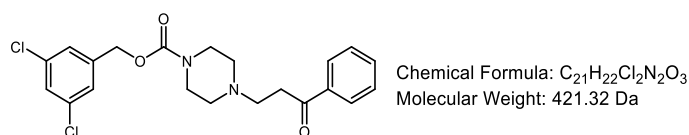
Compound 148: Benzyl 4-(3-(6,7-dihydrofuro[3,2-c]pyridin-5(4H)-yl)-3-oxopropyl)piperazine-1-carboxylate



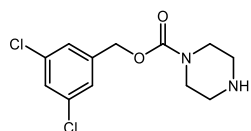
Prepared according to general procedure G using 3-(4-((benzyloxy)carbonyl)piperazin-1-yl)propanoic acid (**143**, 0.15 mg, 0.51 mmol), DMF (3 mL). DIPEA (0.27 mL, 1.54 mmol), HATU (0.2 mg, 0.51 mmol), 4,5,6,7-tetrahydrofuro[3,2-c]pyridine hydrochloride (0.08 g, 0.51 mmol) to afford the desired product as a yellow gum (0.03 g, 14%). ν_{\max} (neat): 1695, 1427 cm⁻¹; ¹H NMR (400 MHz, MeOD) δ 8.29 (s, 1H), 8.12 (d, J = 2.4 Hz, 1H), 7.41 - 7.29 (m, 5H), 5.15 (s, 2H), 4.58 - 4.53 (m, 2H), 3.97 (t, J = 5.7 Hz, 1H), 3.89 (t, J = 5.7 Hz, 1H), 3.64 - 3.55 (m, 4H), 2.99 - 2.92 (m, 2H), 2.91 - 2.71 (m, 8H); ¹³C NMR (101 MHz, DMSO-*d*₆) δ 169.8, 153.9, 147.7, 140.9, 136.5, 127.6, 126.9, 126.7, 114.2, 107.8, 65.6, 53.0, 51.6, 43.1, 42.9, 30.3, 23.0, 2xC isochronous; HRMS: exact mass calculated for [M+H]⁺ (C₂₂H₂₈N₃O₄) requires m/z 398.2074, found m/z 398.2079.

Compound 149: Benzyl 4-(3-oxo-3-phenylpropyl) piperazine-1-carboxylate

Prepared according to general procedure M 3-chloro-1-phenylpropan-1-one (0.25 g, 1.48 mmol), MeCN (12 mL), Et_3N (0.23 mL, 1.63 mmol), benzyl piperazine-1-carboxylate (0.32 mL, 1.63 mmol) to afford the desired product as yellow gum (0.15 g, 29%). ν_{max} (neat): 1681, 1427, 1232 cm^{-1} ; 1H NMR (400 MHz, $CDCl_3$) δ 7.99 – 7.93 (m, 2H), 7.60 – 7.53 (m, 1H), 7.48 – 7.44 (m, 2H), 7.38 – 7.28 (m, 5H), 5.13 (s, 2H), 3.58 – 3.44 (m, 4H), 3.19 (t, $J = 7.3$ Hz, 2H), 2.86 (t, $J = 7.3$ Hz, 2H), 2.59 – 2.35 (m, 4H); ^{13}C NMR (101 MHz, $CDCl_3$) δ 198.9, 155.3, 136.9, 136.7, 133.3, 128.7, 128.6, 128.1, 128.0, 67.2, 53.1, 53.0, 43.8, 36.1; HRMS: exact mass calculated for $[M+H]^+$ ($C_{21}H_{25}N_2O_3$) requires m/z 353.1860, found m/z 353.1855

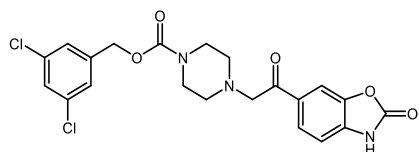
Compound 150: 3, 5-Dichlorobenzyl 4-(3-oxo-3-phenylpropyl)piperazine-1-carboxylate

Prepared according to general procedure K at 80 °C using 3-chloro-1-phenylpropan-1-one (0.25 g, 1.48 mmol), MeCN (12 mL), Et_3N (0.23 mL, 1.63 mmol), 3,5-dichlorobenzyl piperazine-1-carboxylate (**156**, 0.32 mL, 1.63 mmol) to afford the desired product as white solid (1.07 g, 65%). MPt: 195 – 195.5 °C; ν_{max} (neat): 1697, 1670, 1236 cm^{-1} ; 1H NMR (400 MHz, $CDCl_3$) δ 7.97 – 7.94 (m, 2H), 7.60 – 7.53 (m, 1H), 7.50 – 7.43 (m, 2H), 7.36 – 7.29 (m, 2H), 7.22 (d, $J = 1.9$ Hz, 1H), 5.06 (s, 2H), 3.56 – 3.45 (m, 4H), 3.18 (t, $J = 7.2$ Hz, 2H), 2.86 (t, $J = 7.2$ Hz, 2H), 2.55 – 2.42 (m, 4H); ^{13}C NMR (101 MHz, $CDCl_3$) δ 198.9, 154.7, 140.2, 137.0, 135.1, 133.3, 128.7, 128.2, 128.1, 126.2, 65.6, 53.2, 52.9, 44.0, 36.2; HRMS: exact mass calculated for $[M+H]^+$ ($C_{21}H_{22}Cl_2N_2O_3$) requires m/z 421.1080, found m/z 421.1077.

Compound 156: 3,5-Dichlorobenzyl piperazine-1-carboxylate

Chemical Formula: C₁₂H₁₄Cl₂N₂O₂
Molecular Weight: 289.16 Da

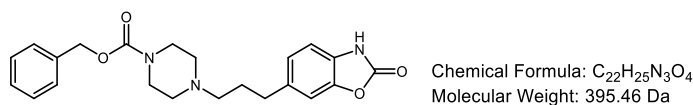
To a round-bottom flask was added 1-(*tert*-butyl) 4-(3,5-dichlorobenzyl) piperazine-1,4-dicarboxylate (**126**, 1 g, 2.57 mmol), 3 M HCl in MeOH (15 mL) and stirred for 16 h at room temperature. The reaction mixture was quenched with saturated NaHCO₃ (15 mL) and extracted using EtOAc. The organics were combined, dried (hydrophobic frit), and concentrated under vacuum to afford the desired product as a white solid (1.27 g, quantitative yield). MPt: 190 – 191 °C; ν_{\max} (neat): 1714, 1697, 1240, 1566 cm⁻¹; ¹H NMR (500 MHz, DMSO-*d*₆) δ 9.40 (s, 1H), 7.57 (t, *J* = 1.9 Hz, 1H), 7.46 (d, *J* = 1.8 Hz, 2H), 5.10 (s, 2H), 3.64 (br s, 4H), 3.12 – 3.05 (m, 4H); ¹³C NMR (101 MHz, DMSO-*d*₆) δ 153.9, 140.8, 134.0, 127.5, 126.3, 65.1, 42.1, 2xC isochronous; HRMS: exact mass calculated for [M+H]⁺ (C₁₂H₁₅Cl₂N₂O₂) requires *m/z* 289.0505, found *m/z* 289.0503; Consistent with previously reported data.¹¹⁷

Compound 164: 3,5-Dichlorobenzyl 4-(2-oxo-2-(2-oxo-2,3-dihydrobenzo[*d*]oxazol-6-yl)ethyl)piperazine-1-carboxylate

Chemical Formula: C₂₁H₁₉Cl₂N₃O₅
Molecular Weight: 464.30 Da

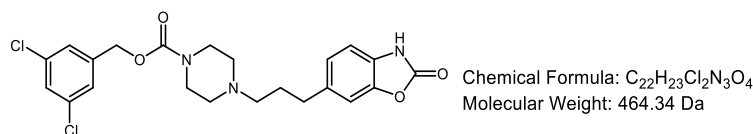
Prepared according to general procedure M using 6-(2-chloroacetyl)benzo[*d*]oxazol-2(3*H*)-one (**172**, 0.2 g, 0.95 mmol), MeCN (18 mL), Et₃N (0.16 mL, 1.13 mmol), 3,5-dichlorobenzyl piperazine-1-carboxylate (**156**, 0.3 g, 1.04 mmol) to give the desired product as a yellow gum (0.2 g, 46%). ν_{\max} (neat): 2980, 1770, 1681, 1444, 1236 cm⁻¹; ¹H NMR (500 MHz, DMSO) δ 12.05 (s, 1H), 7.91 – 7.83 (m, 2H), 7.56 (t, *J* = 1.9 Hz, 1H), 7.42 (d, *J* = 1.8 Hz, 2H), 7.18 (d, *J* = 8.5 Hz, 1H), 5.08 (s, 2H), 3.86 (s, 2H), 3.51 – 3.34 (m, 4H), 2.54 – 2.50 (m, 4H); ¹³C NMR (101 MHz, DMSO-*d*₆) 193.9, 154.8, 154.7, 143.3, 136.0, 133.9, 130.2, 128.0, 127.6, 127.4, 124.3, 109.3, 66.8, 63.7, 52.6, 50.2, 43.1,; HRMS: exact mass calculated for [M+H]⁺ (C₂₁H₂₀Cl₂N₃O₅) requires *m/z* 464.0771, found *m/z* 464.0775; No data previously reported.⁶⁷

Compound 165: Benzyl 4-(3-(2-oxo-2,3-dihydrobenzo[d]oxazol-6-yl)propyl)piperazine-1-carboxylate



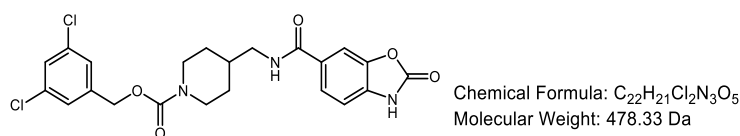
Prepared according to general procedure K at 80 °C using 6-(3-chloropropyl)benzo[d]oxazol-2(3H)-one (**173**, 0.16 g, 0.76 mmol), MeCN (3 mL), Et_3N (0.12 mL, 0.83 mmol), benzyl piperazine-1-carboxylate (0.16 mL, 0.83 mmol) to afford the desired product as a white solid (33 mg, 15%). MPt: 135 – 133 °C; ν_{max} (neat): 1676, 1230 cm^{-1} ; 1H NMR (400 MHz, $CDCl_3$) δ 7.45 – 7.30 (m, 5H), 6.98 (d, J = 8.1 Hz, 1H), 6.92 (s, 1H), 6.79 (d, J = 1.8 Hz, 1H), 6.64 (dd, J = 8.1, 1.9 Hz, 1H), 5.15 (s, 2H), 3.63 – 3.36 (m, 10H), 2.66 (t, J = 7.3 Hz, 2H), 2.12 – 1.92 (m, 2H); ^{13}C NMR (101 MHz, $CDCl_3$) δ 155.6, 154.2, 148.4, 139.1, 138.7, 134.7, 127.9, 125.8, 123.6, 122.0, 120.2, 118.9, 65.5, 43.7, 33.5, 33.3, 32.1, 31.5; HRMS: exact mass calculated for $[M+H]^+$ ($C_{22}H_{26}N_3O_4$) requires m/z 396.1918, found m/z 396.1916

Compound 166: 3,5-Dichlorobenzyl 4-(3-(2-oxo-2,3-dihydrobenzo[d]oxazol-6-yl)propyl)piperazine-1-carboxylate



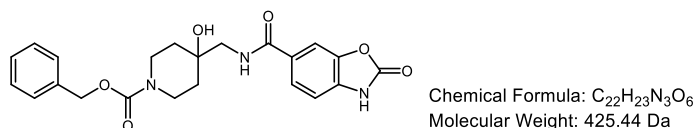
Prepared according to general procedure K at 80 °C using 6-(3-chloropropyl)benzo[d]oxazol-2(3H)-one (**173**, 0.2 g, 0.94 mmol), MeCN (6 mL), Et_3N (0.15 mL, 1.04 mmol), 3,5-dichlorobenzyl piperazine-1-carboxylate (**156**, 0.3 g, 1.04 mmol) to afford the desired product as a yellow gum (25 mg, 11%). ν_{max} (neat): 2924, 1764, 1423, 1226 cm^{-1} ; 1H NMR (400 MHz, $CDCl_3$) δ 7.35 (t, J = 1.9 Hz, 1H), 7.26 (d, J = 1.9 Hz, 2H), 6.92 (d, J = 8.0 Hz, 1H), 6.85 (d, J = 2.0 Hz, 1H), 6.72 – 6.68 (m, 2H), 5.12 (s, 2H), 3.64 – 3.55 (m, 8H), 3.55 – 3.48 (m, 2H), 2.71 (t, J = 7.3 Hz, 2H), 2.14 – 1.95 (m, 2H); ^{13}C NMR (101 MHz, $CDCl_3$) δ 155.6, 154.2, 148.4, 139.1, 138.7, 134.7, 127.9, 125.8, 123.6, 122.0, 120.2, 118.9, 65.5, 43.7, 33.3, 31.5, 2xC not observed; HRMS: exact mass calculated for $[M+3H]^+$ ($C_{22}H_{26}Cl_2N_3O_4$) $[M+3H]^+$ requires m/z 466.1295, found m/z 466.1290.

Compound 167: 3,5-Dichlorobenzyl 4-((2-oxo-2,3-dihydrobenzo[d]oxazole-6-carboxamido)methyl)piperidine-1-carboxylate



Prepared according to general procedure J using *tert*-butyl 4-((2-oxo-2,3-dihydrobenzo[d]oxazole-6-carboxamido)methyl)piperidine-1-carboxylate (**175**, 0.3 g, 0.8 mmol), TFA:CH₂Cl₂ (1:1, 2 mL), (3,5-dichlorophenyl)methanol (1.42 g, 0.80 mmol), CDI (0.13 g, 0.8 mmol), DMF (2.5 mL) to afford the desired product as a yellow gum (40 mg, 10%). ν_{\max} (neat): 3276, 3166, 1772, 1679, 1220 cm⁻¹; ¹H NMR (400 MHz, DMSO-*d*₆) δ 7.78 – 7.71 (m, 2H), 7.63 (s, 1H), 7.56 (t, *J* = 2.0 Hz, 1H), 7.41 (d, *J* = 1.9 Hz, 2H), 7.15 (d, *J* = 8.1 Hz, 1H), 5.07 (s, 2H), 4.01 (d, *J* = 13.2 Hz, 2H), 3.32 (s, 2H), 3.17 (t, *J* = 6.3 Hz, 2H), 1.81 – 1.67 (m, 3H), 1.18 – 0.98 (m, 2H), NH not observed; ¹³C NMR (151 MHz, DMSO-*d*₆) δ 165.4, 154.5, 154.0, 143.0, 141.4, 134.0, 132.8, 128.4, 127.3, 126.1, 123.6, 109.1, 108.2, 64.5, 44.6, 43.5, 40.1, 35.6; HRMS: exact mass calculated for [M+H]⁺ (C₂₂H₂₂Cl₂N₃O₅) [M+H]⁺ requires *m/z* 478.0923, found *m/z* 478.0931.

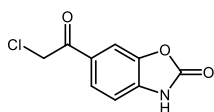
Compound 168: Benzyl 4-hydroxy-4-((2-oxo-2,3-dihydrobenzo[d]oxazole-6-carboxamido)methyl)piperidine-1-carboxylate



Prepared according to general procedure F using 2-oxo-2,3-dihydrobenzo[d]oxazole-6-carboxylic acid (**182**, 0.07 g, 0.38 mmol), DMF (2 mL), DIPEA (0.13 mL, 0.76 mmol), COMU (0.16 g, 0.38 mmol), benzyl 4-(aminomethyl)-4-hydroxypiperidine-1-carboxylate (0.1 g, 0.38 mmol) to yield the desired product as a white solid (19 mg, 12%). MPt: 205 – 206 °C; ν_{\max} (neat): 1778, 1674, 1433 cm⁻¹; ¹H NMR (500 MHz, DMSO-*d*₆) δ 11.90 (s, 1H), 8.28 (s, 1H), 7.79 (s, 1H), 7.74 (d, *J* = 8.1 Hz, 1H), 7.38 – 7.24 (m, 5H), 7.15 (d, *J* = 8.1 Hz, 1H), 5.05 (s, 2H), 4.71 (s, 1H), 3.75 (d, *J* = 12.9 Hz, 2H), 3.29 (s, 2H), 3.21 – 3.05 (m, 2H), 1.45 (s, 4H); ¹³C NMR (101 MHz, DMSO-*d*₆) δ 166.1, 166.0, 154.4, 154.4, 143.0, 137.1, 132.9, 128.4, 127.7, 127.4, 123.8, 109.1, 108.4, 69.1, 66.0, 49.4, 39.6, 34.1; HRMS: exact mass

calculated for $[M-H]^-$ ($C_{22}H_{22}N_3O_6$) $[M-H]^-$ requires m/z 424.1514, found m/z 424.1505

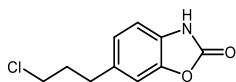
Compound 172: 6-(2-Chloroacetyl)benzo[d]oxazol-2(3H)-one



Chemical Formula: $C_9H_7ClNO_3$
Molecular Weight: 211.60 Da

Prepared according to general procedure H using $AlCl_3$ (12.2 g, 92.51 mmol), DCE (2.5 mL), chloroacetyl chloride (5.86 mL, 74.2 mmol), benzo[d]oxazol-2(3H)-one (5 g, 37 mmol), to afford the desired product as a beige solid (5.48 g, 70%). ν_{max} (neat): 3192, 1935, 1770, 1679, 1613 cm^{-1} ; 1H NMR (400 MHz, $DMSO-d_6$) δ 12.14 (s, 1H), 8.20 – 7.55 (m, 2H), 7.22 (d, $J = 8.1$ Hz, 1H), 5.15 (s, 2H); ^{13}C NMR (101 MHz, $DMSO-d_6$) δ 190.1, 154.3, 143.2, 135.4, 128.4, 125.6, 109.6, 109.3, 47.3; HRMS: exact mass calculated for $[M+H]^+$ ($C_9H_7ClNO_3$) requires m/z 212.0109, found m/z 212.0106; Consistent with previously reported data.¹⁴⁷

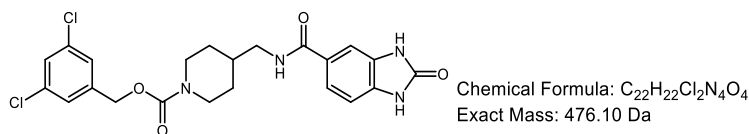
Compound 173: 6-(3-Chloropropyl)benzo[d]oxazol-2(3H)-one



Chemical Formula: $C_{10}H_{10}ClNO_2$
Molecular Weight: 211.65 Da

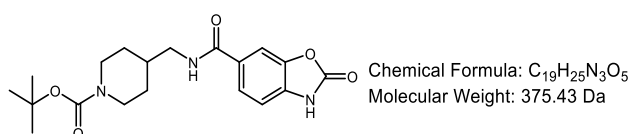
To a round-bottomed flask was added 6-(3-chloropropanoyl)benzo[d]oxazol-2(3H)-one (**116**, 0.5 g, 2.22 mmol). The flask was purged with N_2 before adding TFA (1.73 mL, 22.2 mmol). Triethylsilane (0.72 mL, 4.99 mmol) was added dropwise at 0 °C and the reaction stirred for 48 h at room temperature. The reaction mixture was poured onto ice and the mixture left stirring for 1 h. The precipitate was filtered and washed with H_2O (25 mL) to neutrality. The product was recrystallized in toluene (4 mL) to afford the desired product as a white crystalline solid (0.47 g, 72%). MPt: 106 – 104 °C; ν_{max} (neat): 3076, 1762 cm^{-1} ; 1H NMR (400 MHz, $DMSO-d_6$) δ 11.50 (s, 1H), 7.15 (s, 1H), 7.06 – 6.84 (m, 2H), 3.59 (t, $J = 6.5$ Hz, 2H), 2.73 – 2.68 (m, 2H), 2.22 – 1.82 (m, 2H); ^{13}C NMR (126 MHz, $DMSO-d_6$) δ 154.5, 143.5, 134.7, 128.4, 123.6, 109.4, 44.5, 33.8, 31.9, 1xC not observed; HRMS: exact mass calculated for $[M+H]^+$ ($C_{10}H_{10}ClNO_2$) requires m/z 212.0473, found m/z 212.0472; Consistent with previously reported data.¹³²

Compound 174: 3,5-Dichlorobenzyl 4-((2-oxo-2,3-dihydro-1H-benzo[d]imidazole-5-carboxamido)methyl)piperidine-1-carboxylate



Prepared according to general procedure J using *tert*-butyl 4-((2-oxo-2,3-dihydro-1H-benzo[d]imidazole-5-carboxamido)methyl)piperidine-1-carboxylate (**176**, 0.2 g, 0.73 mmol), TFA:CH₂Cl₂ (1:1, 2 mL), (3,5-dichlorophenyl)methanol (0.1 g, 0.55 mmol), CDI (0.1 g, 0.55 mmol), DMF (2 mL) to afford the desired product as a white solid (0.04 g, 14%). ν_{\max} (neat): 1724, 1676, 1220 cm⁻¹; ¹H NMR (400 MHz, DMSO-*d*₆) δ 10.84 (s, 1H), 10.81 (s, 1H), 8.37 (t, *J* = 5.7 Hz, 1H), 7.57 (t, *J* = 1.8 Hz, 1H), 7.52 (dd, *J* = 8.2, 1.5 Hz, 1H), 7.47 – 7.44 (m, 1H), 7.41 (d, *J* = 1.8 Hz, 1H), 7.36 (d, *J* = 1.9 Hz, 1H), 6.95 (d, *J* = 8.1 Hz, 1H), 5.07 (s, 2H), 4.01 (d, *J* = 12.9 Hz, 2H), 3.14 (t, *J* = 6.1 Hz, 2H), 2.96 – 2.61 (m, 2H), 1.86 – 1.73 (m, 1H), 1.70 (d, *J* = 13.5 Hz, 2H), 1.13 – 1.01 (m, 2H); ¹³C NMR (101 MHz, DMSO-*d*₆) δ 166.4, 155.5, 154.0, 141.4, 134.0, 132.1, 129.4, 127.3, 127.1, 126.0, 124.8, 120.4, 107.5, 64.5, 61.5, 44.5, 43.5, 35.6; HRMS: exact mass calculated for [M+H]⁺ (C₂₂H₂₃Cl₂N₄O₄) requires *m/z* 477.1091, found *m/z* 477.1085.

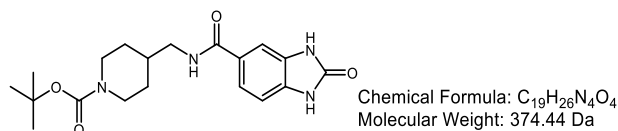
Compound 175: *tert*-Butyl 4-((2-oxo-2,3-dihydrobenzo[d]oxazole-6-carboxamido)methyl)piperidine-1-carboxylate



Prepared according to general procedure F using 2-oxo-2,3-dihydrobenzo[d]oxazole-6-carboxylic acid (**182**, 1.2 g, 6.7 mmol), DMF (10 mL), DIPEA (2.33 mL, 13.4 mmol), COMU (2.87 g, 6.7 mmol), *tert*-butyl 4-(aminomethyl)piperidine-1-carboxylate (1.42 mL, 6.7 mmol) to afford the desired product as a white solid (1.13 g, 45%). MPt: 196.6 – 196.9 °C; ν_{\max} (neat): 1766, 1645, 1427 cm⁻¹; ¹H NMR (500 MHz, MeOD) δ 7.79 – 7.62 (m, 2H), 7.15 (d, *J* = 8.1 Hz, 1H), 4.09 (d, *J* = 13.4 Hz, 2H), 3.28 (d, *J* = 6.9 Hz, 2H), 2.83 – 2.72 (m, 2H), 1.87 – 1.81 (m, 1H), 1.75 (d, *J* = 12.8 Hz, 2H), 1.46 (s, 9H), 1.20 – 1.11 (m, 2H), 2xNH not observed, ¹³C NMR (101 MHz, DMSO-*d*₆) δ 165.4, 154.4, 153.8, 143.0,

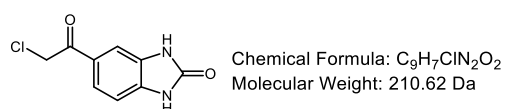
132.8, 128.4, 123.6, 109.1, 108.2, 78.4, 44.6, 35.7, 29.6, 28.1, 1xC not observed; HRMS: exact mass calculated for $[M-H]^-$ ($C_{19}H_{24}N_3O_5$) requires m/z 374.1721, found m/z 374.1713.

Compound 176: *tert*-Butyl 4-((2-oxo-2,3-dihydro-1*H*-benzo[*d*]imidazole-5-carboxamido)methyl)piperidine-1-carboxylate



Prepared according to general procedure F using 2-oxo-2,3-dihydro-1*H*-benzo[*d*]imidazole-5-carboxylic acid (**183**, 0.3 g, 1.68 mmol), DMF (3 mL). DIPEA (0.59 mL, 3.37 mmol), COMU (0.72 g, 1.17 mmol), *tert*-butyl 4-(aminomethyl)piperidine-1-carboxylate (0.36 mL, 1.68 mmol) to afford the desired product as a white solid (0.21 g, 33%). MPt: 203 – 204 °C; ν_{max} (neat): 3290, 2916, 1730, 1680, 1633 cm^{-1} ; 1H NMR (400 MHz, $DMSO-d_6$) δ 8.35 (t, $J = 5.8$ Hz, 1H), 7.51 (dd, $J = 8.2, 1.6$ Hz, 1H), 7.44 (d, $J = 1.4$ Hz, 1H), 6.95 (d, $J = 8.1$ Hz, 1H), 3.92 (d, $J = 12.2$ Hz, 2H), 3.13 (t, $J = 6.2$ Hz, 2H), 2.77 – 2.59 (m, 2H), 1.76 – 1.68 (m, 1H), 1.65 (d, $J = 13.6$ Hz, 2H), 1.39 (s, 9H), 1.09 – 0.92 (m, 2H), 2xNH not observed; ^{13}C NMR (101 MHz, $DMSO-d_6$) δ 166.4, 155.5, 153.9, 132.0, 129.3, 127.1, 120.4, 107.6, 107.5, 78.4, 44.5, 35.8, 29.6, 28.1, 1xC not observed; HRMS: exact mass calculated for $[M+H]^+$ ($C_{19}H_{27}N_4O_4$) requires m/z 375.2027, found m/z 375.2026.

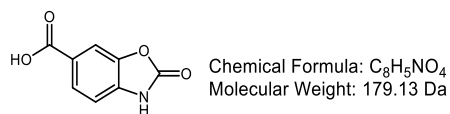
Compound 181: 5-(2-chloroacetyl)-1,3-dihydro-2*H*-benzo[*d*]imidazol-2-one



Prepared according to general procedure H using $AlCl_3$ (1.97 g, 14.91 mmol), DCE (1 mL), chloroacetyl chloride (0.95 mL, 11.93 mmol), 1,3-dihydro-2*H*-benzo[*d*]imidazol-2-one (0.8 g, 5.96 mmol), to afford the desired product as a beige amorphous solid (1.18 g, 94%). 1H NMR (400 MHz, $DMSO-d_6$) δ 11.11 (s, 1H), 10.95 (s, 1H), 7.68 (dd, $J = 8.2, 1.7$ Hz, 1H), 7.50 (d, $J = 1.6$ Hz, 1H), 7.05 (d, $J = 8.2$ Hz, 1H), 5.13 (s, 2H); ^{13}C NMR (101 MHz, $DMSO-d_6$) δ 190.3, 155.4, 134.6, 129.8, 127.1, 122.8, 108.1, 108.1, 47.3; HRMS: exact mass calculated for $[M+H]^+$

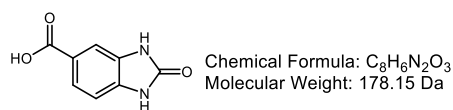
(C₉H₈ClN₂O₂) requires m/z 211.0269, found m/z 211.0268; Consistent with previously reported data.¹⁴⁷

Compound 182: 2-Oxo-2,3-dihydrobenzo[*d*]oxazole-6-carboxylic acid



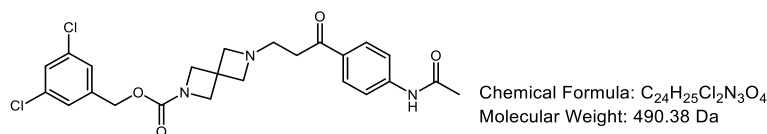
Prepared according to general procedure I using 6-(2-chloroacetyl)benzo[*d*]oxazol-2(3*H*)-one (**172**, 0.4 g, 1.89 mmol), pyridine (4 mL), 2.5M NaOH (4 mL), 1M HCl (10 mL) to afford the desired product as a brown solid (0.3 g, 89%). MPt: 143 – 144 °C, ν_{\max} (neat): 3178, 1683, 1286 cm⁻¹; ¹H NMR (400 MHz, DMSO-*d*₆) δ 12.27 (s, 1H), 7.80 (dd, J = 8.2, 1.5 Hz, 1H), 7.73 (s, 1H), 7.19 (d, J = 8.1 Hz, 1H), OH not observed.; ¹³C NMR (101 MHz, DMSO-*d*₆) δ 166.7, 154.3, 143.0, 134.5, 126.0, 124.4, 110.0, 109.4.; HRMS: exact mass calculated for [M-H]⁻ (C₈H₄NO₄) requires m/z 178.0146, found m/z 178.0146; Consistent with previously reported data.¹⁴⁷

Compound 183: 2-Oxo-2,3-dihydro-1*H*-benzo[*d*]imidazole-5-carboxylic acid



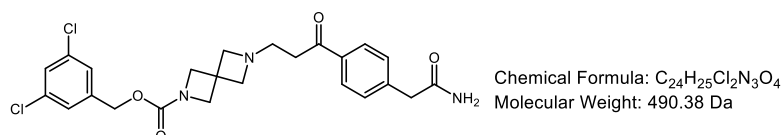
Prepared according to general procedure I using 5-(2-chloroacetyl)-1,3-dihydro-2*H*-benzo[*d*]imidazol-2-one (**181**, 1 g, 4.75 mmol), pyridine (10 mL), 2.5M NaOH (10 mL), 1M HCl (10 mL). The precipitate was filtered to afford the desired product as a brown solid (0.39 g, 37%). MPt: 145 °C (decomposition); ν_{\max} (neat): 3192, 1695, 1303 cm⁻¹; ¹H NMR (400 MHz, DMSO-*d*₆) δ 12.56 (s, 1H), 10.96 (s, 1H), 10.81 (s, 1H), 7.61 (dd, J = 8.2, 1.6 Hz, 1H), 7.46 (s, 1H), 6.98 (d, J = 8.2 Hz, 1H); ¹³C NMR (101 MHz, DMSO-*d*₆) δ 167.5, 155.4, 133.6, 129.5, 122.9, 122.9, 109.2, 107.9; HRMS: exact mass calculated for [M-H]⁻ (C₈H₅N₂O₃) [M-H]⁻ requires m/z 177.0306, found m/z 177.0307; No data previously reported.¹⁴⁸

Compound 188: 3,5-Dichlorobenzyl 6-(3-(4-acetamidophenyl)-3-oxopropyl)-2,6-diazaspiro[3.3]heptane-2-carboxylate



Prepared according to procedure E at 80 °C using 2-(*tert*-butyl) 6-(3,5-dichlorobenzyl) 2,6-diazaspiro[3.3]heptane-2,6-dicarboxylate (**111**, 0.15 g, 0.37 mmol), TFA:CH₂Cl₂ (1:1, 2 mL), MeCN (3 mL), Et₃N (0.05 mL, 0.33 mmol), *N*-(4-(3-chloropropanoyl)phenyl)acetamide (**200**, 0.07 g, 0.30 mmol) to afford the desired product as a yellow gum (27 mg, 17%). MPt: 175 – 176 °C; ν_{\max} (neat): 2945, 1987, 1589, 1409 cm⁻¹; ¹H NMR (400 MHz, DMSO-*d*₆) δ 10.47 (s, 1H), 7.93 (d, *J* = 8.8 Hz, 2H), 7.77 (d, *J* = 8.8 Hz, 2H), 7.57 (t, *J* = 1.7 Hz, 1H), 7.41 (d, *J* = 1.9 Hz, 2H), 5.04 (s, 2H), 4.25 (s, 4H), 4.22 – 4.05 (m, 4H), 3.44 (t, *J* = 6.6 Hz, 2H), 3.37 – 3.32 (m, 2H), 2.10 (s, 3H); ¹³C NMR (101 MHz, DMSO-*d*₆) δ 195.3, 169.0, 155.1, 144.2, 141.2, 134.0, 130.3, 129.3, 127.4, 126.1, 118.2, 64.1, 62.2, 49.1, 33.0, 32.7, 24.1; ¹³C not observed; HRMS: exact mass calculated for [M+H]⁺ (C₂₄H₂₆Cl₂N₃O₄) [M+H]⁺ requires *m/z* 490.1295, found *m/z* 490.1286.

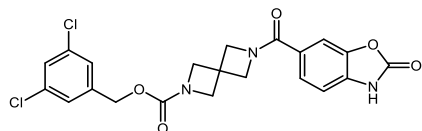
Compound 189: 3,5-Dichlorobenzyl 6-(3-(4-(2-amino-2-oxoethyl)phenyl)-3-oxopropyl)-2,6-diazaspiro[3.3]heptane-2-carboxylate



Prepared according to procedure E at 80 °C using 2-(*tert*-butyl) 6-(3,5-dichlorobenzyl) 2,6-diazaspiro[3.3]heptane-2,6-dicarboxylate (**111**, 0.15 g, 0.37 mmol), TFA:CH₂Cl₂ (1:1, 2 mL), MeCN (3 mL), Et₃N (0.05 mL, 0.33 mmol), 2-(4-(3-chloropropanoyl)phenyl)acetamide (**202**, 0.07 g, 0.30 mmol) to afford the desired product as a white gum (11 mg, 15%). ν_{\max} (neat): 2924, 2854, 1670, 1570, 1414 cm⁻¹; ¹H NMR (400 MHz, CDCl₃) δ 7.93 (d, *J* = 8.3 Hz, 2H), 7.41 (d, *J* = 8.3 Hz, 2H), 7.31 (t, *J* = 1.8 Hz, 1H), 7.21 (d, *J* = 1.8 Hz, 2H), 5.01 (s, 2H), 4.19 (s, 2H), 3.88 (s, 4H), 3.65 (s, 2H), 3.50 (s, 2H), 3.36 – 3.20 (m, 4H). 2xNH not observed; ¹³C NMR (126 MHz, DMSO-*d*₆) δ 171.9, 143.2, 141.7, 134.5, 130.0, 128.4, 127.9, 126.6,

64.7, 64.6, 62.9, 44.7, 42.6, 40.4, 40.3, 31.2, 2xC not observed; HRMS: exact mass calculated for $[M+H]^+$ ($C_{24}H_{26}Cl_2N_3O_4$) requires m/z 490.1295, found m/z 490.1288.

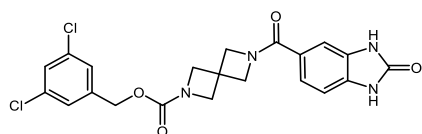
Compound 191: 3,5-Dichlorobenzyl 6-(2-oxo-2,3-dihydrobenzo[d]oxazole-6-carbonyl)-2,6-diazaspiro[3.3]heptane-2-carboxylate



Chemical Formula: $C_{21}H_{17}Cl_2N_3O_5$
Molecular Weight: 462.28 Da

Prepared according to procedure M using 2-(*tert*-butyl) 6-(3,5-dichlorobenzyl) 2,6-diazaspiro[3.3]heptane-2,6-dicarboxylate (**111**, 0.15 g, 0.37 mmol), TFA:CH₂Cl₂ (1:1, 2 mL), 2-oxo-2,3-dihydrobenzo[d]oxazole-6-carboxylic acid (**182**, 0.06 g, 0.33 mmol), DIPEA (0.12 mL, 0.66 mmol), COMU (0.14 g, 0.33 mmol), DMF (1 mL) to afford the desired product as a yellow gum (58 mg, 40%). ν_{max} (neat): 1780, 1703, 1325 cm⁻¹; ¹H NMR (400 MHz, DMSO-*d*₆) δ 11.91 (s, 1H), 7.57 (t, J = 1.9 Hz, 1H), 7.50 (d, J = 1.4 Hz, 1H), 7.46 (dd, J = 8.1, 1.6 Hz, 1H), 7.41 (d, J = 2.0 Hz, 2H), 7.14 (d, J = 8.1 Hz, 1H), 5.03 (s, 2H), 4.56 – 4.39 (m, 2H), 4.27 – 3.98 (m, 6H); ¹³C NMR (101 MHz, DMSO-*d*₆) δ 168.1, 155.2, 154.4, 142.9, 141.1, 134.0, 132.8, 127.4, 126.7, 126.1, 124.1, 109.3, 108.9, 64.1, 62.6, 58.4, 32.6; HRMS: exact mass calculated for $[M+H]^+$ ($C_{21}H_{18}Cl_2N_3O_5$) requires m/z 462.0615, found m/z 462.0618

Compound 192: 3,5-Dichlorobenzyl 6-(2-oxo-2,3-dihydro-1H-benzo[d]imidazole-5-carbonyl)-2,6-diazaspiro[3.3]heptane-2-carboxylate

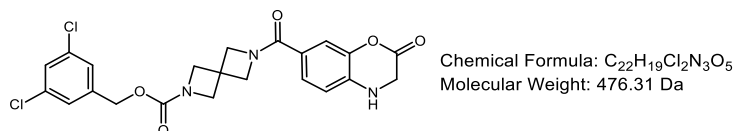


Chemical Formula: $C_{21}H_{18}Cl_2N_4O_4$
Molecular Weight: 461.30 Da

Prepared according to procedure M using 2-(*tert*-butyl) 6-(3,5-dichlorobenzyl) 2,6-diazaspiro[3.3]heptane-2,6-dicarboxylate (**111**, 0.15 g, 0.37 mmol), TFA:CH₂Cl₂ (1:1, 2 mL), 2-oxo-2,3-dihydro-1H-benzo[d]imidazole-5-carboxylic acid (**183**, 0.06 g, 0.33 mmol), DIPEA (0.12 mL, 0.66 mmol), COMU (0.14 g, 0.33 mmol), 3,5-dichlorobenzyl, DMF (1 mL) to afford the desired product as white solid (10 mg, 7%). MPt: 172 – 173 °C; ν_{max} (neat): 1696, 1426, 1327 cm⁻¹; ¹H NMR (400 MHz, DMSO-*d*₆) δ 10.86 (s, 1H), 10.75 (s, 1H), 7.57 (t, J = 1.9 Hz, 1H), 7.41 (d, J = 1.8 Hz, 2H), 7.25 (dd, J = 8.1, 1.5 Hz, 1H), 7.18 (s, 1H), 6.95 (d, J = 8.1 Hz, 1H), 5.03 (s, 2H), 4.54 – 4.01 (m, 8H); ¹³C NMR (126 MHz, DMSO-*d*₆) δ 169.1, 155.3, 155.2, 141.2,

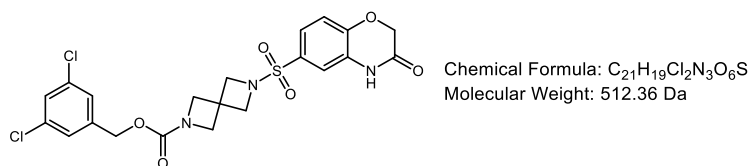
134.0, 132.1, 129.5, 127.4, 126.2, 125.2, 120.9, 108.0, 107.8, 64.1, 34.0, 39.8, 32.7; HRMS: exact mass calculated for $[M-H]^-$ ($C_{21}H_{17}Cl_2N_4O_4$), $[M-H]^-$ requires m/z 459.0632, found m/z 459.0628.

Compound 195: 3,5-Dichlorobenzyl 6-(2-oxo-3,4-dihydro-2H-benzo[*b*][1,4]oxazine-7-carbonyl)-2,6-diazaspiro[3.3]heptane-2-carboxylate



Prepared according to procedure M using 2-(*tert*-butyl) 6-(3,5-dichlorobenzyl) 2,6-diazaspiro[3.3]heptane-2,6-dicarboxylate (**111**, 0.15 g, 0.37 mmol), TFA:CH₂Cl₂ (1:1, 2 mL), benzo[*b*][1,4]oxazine-7-carboxylic acid (**208**, 0.06 g, 0.33 mmol), DIPEA (0.17 mL, 0.2 mmol), COMU (0.14 g, 0.33 mmol), DMF (1 mL) to afford the desired product as a white solid (7 mg, 4%). MPt: 242 °C (decomposed); ν_{max} (neat): 1696, 1435, 1390 cm⁻¹; ¹H NMR (600 MHz, DMSO-*d*₆) δ 10.92 (s, 1H), 7.57 (t, J = 2.0 Hz, 1H), 7.41 (s, 2H), 7.23 (dd, J = 8.1, 1.8 Hz, 1H), 7.16 (s, 1H), 6.93 (d, J = 8.1 Hz, 1H), 5.03 (s, 2H), 4.62 (s, 2H), 4.45 (s, 2H), 4.20 – 4.06 (m, 6H); ¹³C NMR (151 MHz, DMSO-*d*₆) δ 168.3, 165.3, 155.6, 143.2, 141.7, 134.5, 130.2, 128.2, 127.9, 126.7, 122.8, 116.0, 115.9, 79.7, 79.4, 67.2, 64.6, 33.2. ; HRMS: exact mass calculated for $[M+H]^+$ ($C_{22}H_{20}Cl_2N_3O_5$) $[M+H]^+$ requires m/z 476.0775, found m/z 476.0769.

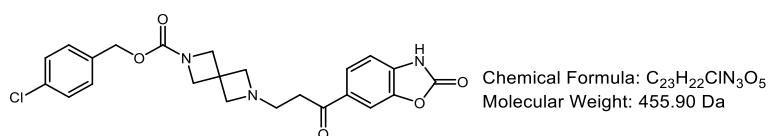
Compound 197: 3,5-Dichlorobenzyl 6-((3-oxo-3,4-dihydro-2H-benzo[*b*][1,4]oxazin-6-yl)sulfonyl)-2,6-diazaspiro[3.3]heptane-2-carboxylate



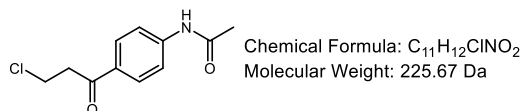
To a round-bottomed flask was added 2-(*tert*-butyl) 6-(3,5-dichlorobenzyl) 2,6-diazaspiro[3.3]heptane-2,6-dicarboxylate (**111**, 0.16 g, 0.4 mmol) and dissolved in TFA:CH₂Cl₂ (1:1, 2 mL). The solution was stirred at room temperature until no starting material remained by TLC analysis. The reaction was concentrated under vacuum to afford amine intermediate TFA salt. The amine intermediate was redissolved in CH₂Cl₂ (2 mL). Et₃N (0.22 mL, 0.29 mmol) and 3-oxo-3,4-dihydro-2H-

benzo[*b*][1,4]oxazine-6-sulfonyl chloride (**205**, 0.03 g, 0.13 mmol) was added and stirred for 16 h at room temperature. The reaction was diluted with EtOAc (5 mL) and washed with H₂O (5 mL). The organics were collected, dried (hydrophobic frit) and concentrated under vacuum to a residue that was purified using silica gel chromatography (70% EtOAc in petroleum ether) to afford the desired product as a white gum (13 mg, 19%). ν_{\max} (neat): 2949, 1698, 1655, 1414, 1151 cm⁻¹, ¹H NMR (400 MHz, CDCl₃) δ 8.76 (s, 1H), 8.02 (d, *J* = 2.1 Hz, 1H), 7.59 (dd, *J* = 8.5, 2.1 Hz, 1H), 7.32 (t, *J* = 1.9 Hz, 1H), 7.21 (d, *J* = 1.9 Hz, 2H), 7.15 (d, *J* = 8.5 Hz, 1H), 5.01 (s, 2H), 4.30 (s, 2H), 4.07 – 3.98 (m, 4H), 3.93 (s, 4H); ¹³C NMR (126 MHz, MeOD) δ 167.6, 157.3, 153.6, 142.0, 136.2, 133.1, 129.9, 129.0, 127.3, 125.3, 122.9, 115.9, 66.2, 61.4, 54.8, 43.9, 33.9; HRMS: exact mass calculated for [M+H₂Cl]⁺ (C₂₁H₂₁Cl₃N₃O₆S), requires *m/z* 548.0211 found *m/z* 548.0205.

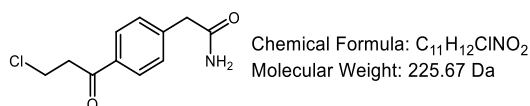
Compound 198: 4-Chlorobenzyl 6-(3-oxo-3-(2-oxo-2,3-dihydrobenzo[*d*]oxazol-6-yl)propyl)-2,6-diazaspiro[3.3]heptane-2-carboxylate



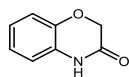
Prepared according to procedure E at 80 °C using 2-(tert-butyl) 6-(4-chlorobenzyl) 2,6-diazaspiro[3.3]heptane-2,6-dicarboxylate (**212**, 0.13 g, 0.36 mmol), TFA:CH₂Cl₂ (1:1, 2 mL), MeCN (1.5 mL), Et₃N (0.1 mL, 0.72 mmol), 6-(3-chloropropanoyl)benzo[*d*]oxazol-2(3*H*)-one (**116**, 0.07 g, 0.33 mmol) to afford the desired product as white solid (98 mg, 61%). MPt: 195 – 196 °C, ν_{\max} (neat): 1707, 1411, 1331 cm⁻¹; ¹H NMR (500 MHz, DMSO) δ 7.81 (d, *J* = 8.1 Hz, 2H), 7.43 (d, *J* = 8.4 Hz, 2H), 7.36 (d, *J* = 8.4 Hz, 2H), 7.16 (d, *J* = 8.1 Hz, 1H), 5.01 (s, 2H), 3.98 (s, 4H), 3.31 (s, 4H), 2.99 (t, *J* = 7.0 Hz, 2H), 2.72 (t, *J* = 6.9 Hz, 2H), NH not observed.; ¹³C NMR (101 MHz, DMSO) δ 197.0, 155.4, 155.2, 143.6, 136.2, 136.0, 132.4, 130.4, 129.5, 128.4, 125.0, 109.4, 108.6, 64.8, 63.4, 53.5, 35.9, 33.3. 1xC not observed; HRMS: exact mass calculated for [M+H]⁺ (C₂₃H₂₂ClN₃O₅H) [M+H]⁺ requires *m/z* 456.1321, found *m/z* 456.1315.

Compound 200: *N*-(4-(3-Chloropropanoyl)phenyl)acetamide

Prepared according to procedure H using AlCl₃ (2.44 g, 18.50 mmol), DCE (4 mL), 3-chloropropanoyl chloride (1.42 mL, 14.8 mmol), *N*-phenylacetamide (1 g, 7.4 mmol), ice (15 g) afford the desired product as a white solid (1.01 g, 61%). MPt: 167.5 – 168 °C; ν_{\max} (neat): 3304, 1670, 1589, 1531, 1176 cm⁻¹; ¹H NMR (400 MHz, DMSO-*d*₆) δ 10.32 (s, 1H), 7.94 (d, *J* = 8.8 Hz, 2H), 7.72 (d, *J* = 8.8 Hz, 2H), 3.91 (t, *J* = 6.3 Hz, 2H), 3.49 (t, *J* = 6.3 Hz, 2H), 2.09 (s, 3H); ¹³C NMR (101 MHz, DMSO-*d*₆) δ 195.4, 169.0, 143.9, 130.9, 129.3, 128.6, 119.0, 118.2, 24.2; HRMS: exact mass calculated for [M+H]⁺ (C₁₁H₁₃ClNO₂) [M+H]⁺ requires *m/z* 226.0629, found *m/z* 226.0631; No data previously reported.¹⁴⁹

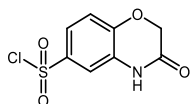
Compound 202: 2-(4-(3-Chloropropanoyl)phenyl)acetamide

To a round-bottomed flask was added AlCl₃ (1.46 g, 11.09 mmol) and DMF (0.5 mL) was added dropwise. The exothermic mixture turned black. After 15 min 3-chloropropanoyl chloride (0.17 mL, 1.78 mmol) was added followed by 2-phenylacetamide (0.2 g, 1.48 mmol). The reaction mixture was heated to 70 °C and stirred for 5 h. The reaction mixture solution was cooled and poured onto ice (5 g) and the precipitate filtered. The crude material was suspended in CH₂Cl₂ (7 mL) and filtered to afford the desired product as an amorphous yellow solid (0.17 g, 50%). ν_{\max} (neat): 3350, 3165, 1666, 1170 cm⁻¹; ¹H NMR (400 MHz, DMSO) δ 7.92 (d, *J* = 8.1 Hz, 2H), 7.55 (s, 1H), 7.41 (d, *J* = 8.0 Hz, 2H), 6.96 (s, 1H), 3.92 (t, *J* = 6.2 Hz, 2H), 3.54 (t, *J* = 6.2 Hz, 2H), 3.47 (s, 2H); ¹³C NMR (126 MHz, DMSO-*d*₆) δ 196.2, 171.9, 129.9, 129.5, 128.6, 126.7, 48.7, 37.0, 31.4; HRMS: exact mass calculated for [M+H]⁺ (C₁₁H₁₃ClNO₂) [M+H]⁺ requires *m/z* 226.0629, found *m/z* 226.0629.

Compound 204: 2*H*-Benzo[*b*][1,4]oxazin-3(4*H*)-one:

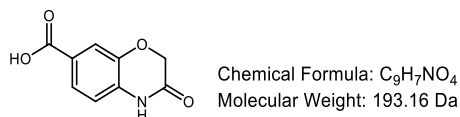
Chemical Formula: C₈H₇NO₂
Molecular Weight: 149.15 Da

To a round-bottom flask was added NaHCO₃ (1.32 g, 15.58 mmol), 2-aminophenol (0.85 g, 7.79 mmol) in THF (20 mL). The reaction mixture was placed under N₂ and cooled to 0 °C before dropwise addition of a solution of chloroacetyl chloride (0.87 mL, 10.9 mmol) in THF (10 mL). The reaction was stirred at room temperature for 5 h. The reaction mixture was then quenched using H₂O (30 mL) and extracted using EtOAc (100 mL). The organics were then collected, dried (hydrophobic frit), and concentrated under vacuum to a solid. The solid was resuspended in CH₂Cl₂ (10 mL) and filtered to afford the desired product as a brown solid (0.76 g, 66%). MPt: 173 – 174 °C; ν_{\max} (neat): 3367, 3151, 1653, 1546, 1458 cm⁻¹; ¹H NMR (400 MHz, DMSO-*d*₆) δ 9.97 (s, 1H), 9.44 (s, 1H), 6.97 (td, *J* = 8.0, 1.5 Hz, 1H), 6.92 – 6.87 (m, 1H), 6.79 (td, *J* = 7.9, 1.5 Hz, 1H), 4.39 (s, 2H); ¹³C NMR (101 MHz, DMSO-*d*₆) δ 164.6, 147.6, 125.6, 124.8, 121.6, 118.9, 115.2, 43.3.; HRMS: exact mass calculated for [M+H]⁺ (C₈H₈NO₂) [M+H]⁺ requires *m/z* 150.0550, found *m/z* 150.0547; Consistent with previously reported data.¹³⁶

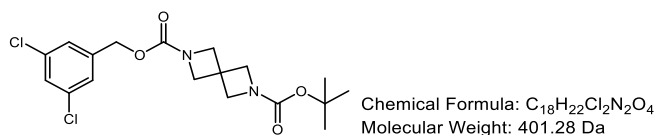
Compound 205: 3-Oxo-3,4-dihydro-2*H*-benzo[*b*][1,4]oxazine-6-sulfonyl chloride

Chemical Formula: C₈H₆ClNO₄S
Molecular Weight: 247.65 Da

To a round-bottomed flask was added was added 2*H*-benzo[*b*][1,4]oxazin-3(4*H*)-on (**204**, 0.25 g, 1.68 mmol). Chlorosulfonic acid (0.33 mL, 5.03 mmol) was added dropwise at 0 °C. The reaction mixture was stirred for 2 h at 0 °C before the reaction was quenched with H₂O. The resulting precipitate was filtered and washed with H₂O (10 mL) to afford the desired product as a pink solid (0.16 g, 40%). MPt: 176 – 178 °C; ν_{\max} (neat): 3213, 1653, 1541, 1166 cm⁻¹; ¹H NMR (400 MHz, DMSO-*d*₆) δ 9.45 (s, 1H), 8.18 (d, *J* = 2.1 Hz, 1H), 7.24 (dd, *J* = 8.4, 2.1 Hz, 1H), 6.83 (d, *J* = 8.3 Hz, 1H), 4.39 (s, 2H); ¹³C NMR (101 MHz, DMSO-*d*₆) δ 164.6, 148.3, 138.1, 124.6, 122.5, 119.5, 114.0, 43.3.; HRMS: exact mass calculated for [M+H]⁺ (C₈H₇ClNO₄S) [M+H]⁺ requires *m/z* 247.9779, found *m/z* 247.9781; No data previously reported.¹⁵⁰

Compound 208: 3-Oxo-3,4-dihydro-2H-benzo[*b*][1,4]oxazine-7-carboxylic acid

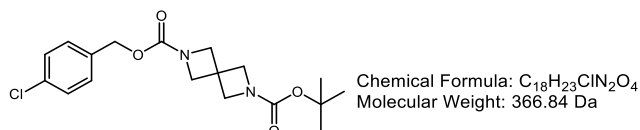
To a round-bottom flask was added NaHCO₃ (0.6 g, 7.06 mmol) and methyl 4-amino-3-hydroxybenzoate (0.59 g, 3.53 mmol) in THF (25 mL). The reaction mixture was placed under N₂ and cooled to 0 °C before dropwise addition of a solution of chloroacetyl chloride (0.39 mL, 4.94 mmol) in THF (10 mL). The reaction mixture was allowed to warm to room temp and left to stir for 16 h before being quenched using H₂O (30 mL) and extracted using EtOAc (100 mL). The organics were collected, dried (hydrophobic frit), and concentrated under vacuum to a solid. The solid was resuspended in CH₂Cl₂:MeOH (1:1, 10 mL) and filtered to afford ester intermediate (**207**, 0.4 g, 55%). The ester (**207**, 0.4 g, 1.93 mmol) was dissolved in THF:H₂O (3:1, 10 mL), LiOH (0.16 mg, 3.86 mmol) was added and the reaction stirred at room temperature until complete consumption of starting material by TLC analysis. The solution was acidified using 1M HCl (5 mL). The resulting precipitate was filtered to afford the desired product as a white solid (0.37 g, quantitative). MPt: 332 – 334 °C; ν_{\max} (neat): 3489, 1692, 1411, 1236 cm⁻¹; ¹H NMR (500 MHz, DMSO-*d*₆) δ 12.78 (s, 1H), 11.02 (s, 1H), 7.56 (dd, *J* = 8.2, 1.7 Hz, 1H), 7.42 (d, *J* = 1.5 Hz, 1H), 6.97 (d, *J* = 8.2 Hz, 1H), 4.64 (s, 2H); ¹³C NMR (101 MHz, DMSO) δ 166.7, 165.1, 142.8, 131.5, 125.5, 124.3, 116.9, 115.7, 66.7; HRMS: exact mass calculated for [M-H]⁻ (C₉H₆NO₄) [M-H]⁻ requires *m/z* 192.0302, found *m/z* 192.0303; Consistent with previously reported data.¹⁵¹

Compound 211: 2-(*tert*-Butyl) 6-(3,5-dichlorobenzyl) 2,6-diazaspiro[3.3]heptane-2,6-dicarboxylate

Prepared according to general procedure C using (3,5-dichlorophenyl)methanol (0.73 g, 4.52 mmol), CDI (0.8 g, 4.52 mmol), DMF (2 mL), *tert*-butyl 2,6-diazaspiro[3.3]heptane-2-carboxylate oxalate (2:1) (1 g, 4.11 mmol) to afford the desired product as a white solid (1.24 g, 75%). ν_{\max} (neat): 2958, 2874, 1703, 1415 cm⁻¹; ¹H NMR (400 MHz, CDCl₃) δ 7.28 (t, *J* = 1.9 Hz, 1H), 7.19 (d, *J* = 1.9 Hz,

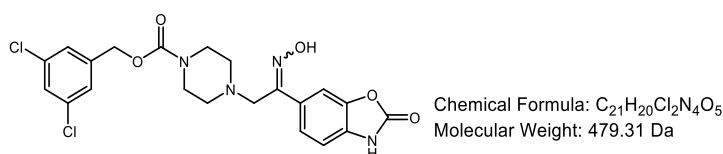
2H), 5.00 (s, 2H), 4.12 (s, 4H), 4.03 (s, 4H), 1.41 (s, 9H); ^{13}C NMR (101 MHz, CDCl_3) δ 155.4, 154.9, 139.3, 134.6, 127.7, 125.7, 79.4, 64.6, 58.9, 32.2, 27.8, 2xC isochronous; HRMS: exact mass calculated for $[\text{M}+\text{Na}]^+$ ($\text{C}_8\text{H}_{22}\text{Cl}_2\text{N}_2\text{O}_4\text{Na}$) requires m/z 425.0819, found m/z 425.0818.

Compound 212: 2-(*tert*-Butyl) 6-(4-chlorobenzyl) 2,6-diazaspiro[3.3]heptane-2,6-dicarboxylate



Prepared according to procedure C using (4-chlorophenyl)methanol (76 mg, 0.53 mmol), CDI (0.1 mg, 0.59 mmol), DMF (2 mL), *tert*-butyl 2,6-diazaspiro[3.3]heptane-2-carboxylate oxalate (2:1) (0.13 mg, 0.53 mmol) to afford the desired product as white solid (0.14 g, 71%); MPt: 145 – 146 °C; ν_{max} (neat): 1692, 1400, 1325, 1089 cm^{-1} ; ^1H NMR (500 MHz, $\text{DMSO}-d_6$) δ 7.43 (d, J = 8.4 Hz, 2H), 7.37 (d, J = 8.4 Hz, 2H), 5.01 (s, 2H), 4.06 (s, 4H), 3.96 (s, 4H), 1.37 (s, 9H); ^{13}C NMR (126 MHz, CDCl_3) δ 155.9, 155.8, 135.0, 134.1, 129.5, 128.7, 79.9, 66.0, 59.6, 32.7, 28.3, 2xC isochronous; HRMS: exact mass calculated for $[\text{M}+\text{Na}]^+$ ($\text{C}_{18}\text{H}_{23}\text{ClN}_2\text{O}_4\text{Na}$) requires m/z 389.1239, found m/z 389.1235.

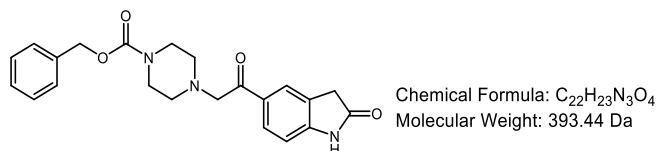
Compound 213: 3,5-Dichlorobenzyl 4-(2-(hydroxyimino)-2-(2-oxo-2,3-dihydrobenzo[*d*]oxazol-6-yl)ethyl)piperazine-1-carboxylate



Prepared according to general procedure M using 3,5-dichlorobenzyl 4-(2-oxo-2-(2-oxo-2,3-dihydrobenzo[*d*]oxazol-6-yl)ethyl)piperazine-1-carboxylate (**164**, 0.2 g, 0.43 mmol), NaOAc (0.04 g, 0.47 mmol), $\text{HONH}_2\cdot\text{HCl}$ (0.33 g, 0.47 mmol), MeOH (3 mL) to afford the desired product as a white solid (21 mg, 14%). MPt: 192 – 194 °C; ν_{max} (neat): 1768, 1697, 1421 cm^{-1} ; ^1H NMR (400 MHz, $\text{DMSO}-d_6$) δ 11.38 (s, 1H), 7.65 – 7.48 (m, 3H), 7.40 (d, J = 1.9 Hz, 2H), 7.07 (d, J = 8.2 Hz, 1H), 5.06 (s, 2H), 3.64 (s, 2H), 3.39 – 3.26 (m, 4H), 2.43 – 2.33 (m, 4H), OH not observed; ^{13}C NMR (101 MHz, $\text{DMSO}-d_6$) δ 163.9, 163.4, 161.7, 152.7, 150.7, 143.5, 140.1, 139.7,

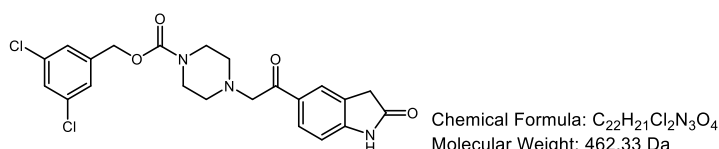
136.8, 135.5, 131.5, 118.6, 116.7, 74.1, 61.9, 59.4, 52.9; HRMS: exact mass calculated for $[M+H]^+$ ($C_{21}H_{22}Cl_2N_4O_5$) $[M+H]^+$ requires m/z 480.0914, found m/z 480.0915.

Compound 216: Benzyl 4-(2-oxo-2-(2-oxoindolin-5-yl)ethyl)piperazine-1-carboxylate



Prepared according to procedure K at 50 °C using 5-(2-chloroacetyl)indolin-2-one (**226**, 0.38 g, 1.67 mmol), MeCN (4 mL), Et_3N (0.26 mL, 1.84 mmol), benzyl piperazine-1-carboxylate (0.36 mL, 1.84 mmol) to give the desired product as a brown amorphous solid (0.37 g, 56%). ν_{max} (neat): 2922, 1682, 1614, 1230, 1114 cm^{-1} ; 1H NMR (500 MHz, $CDCl_3$) δ 7.97 – 7.85 (m, 2H), 7.41 – 7.22 (m, 5H), 6.96 (d, J = 8.2 Hz, 1H), 5.14 (s, 2H), 3.81 (s, 2H), 3.63 – 3.46 (m, 6H), 2.86 – 2.39 (m, 4H), NH not observed; ^{13}C NMR (400 MHz, $CDCl_3$) 194.2, 176.8, 154.2, 146.7, 139.6, 134.6, 130.2, 129.12, 127.7, 125.6, 125.0, 124.3, 108.8, 65.1, 63.6, 52.6, 43.3, 35.3; HRMS: exact mass calculated for $[M+H]^+$ ($C_{22}H_{24}N_3O_4$) $[M+H]^+$ requires m/z 394.1766, found m/z 394.1761.

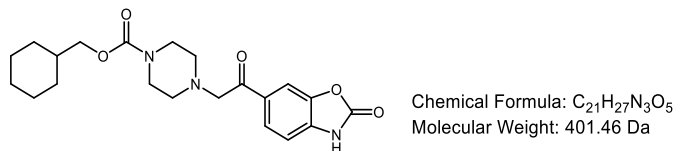
Compound 217: 3,5-Dichlorobenzyl 4-(2-oxo-2-(2-oxoindolin-5-yl)ethyl)piperazine-1-carboxylate



Prepared according to procedure K at 50 °C using 5-(2-chloroacetyl)indolin-2-one (**226**, 0.27 g, 1.28 mmol), MeCN (4 mL), Et_3N (0.39 mL, 2.8 mmol), 3,5-dichlorobenzyl piperazine-1-carboxylate (**156**, 0.41 g, 1.41 mmol) to give the desired product as a brown amorphous solid (0.1 g, 15%). ν_{max} (neat): 2922, 1641, 1233, 789 cm^{-1} ; 1H NMR (400 MHz, $CDCl_3$) δ 8.79 (s, 1H), 7.94 (d, J = 8.7 Hz, 1H), 7.90 (s, 1H), 7.29 (t, J = 1.9 Hz, 1H), 7.22 (d, J = 1.9 Hz, 2H), 6.94 (d, J = 8.2 Hz, 1H), 5.07 (s, 2H), 3.79 (s, 2H), 3.66 – 3.45 (m, 6H), 2.67 – 2.49 (m, 4H); ^{13}C NMR (101 MHz, $CDCl_3$) δ 194.8, 177.4, 154.8, 147.3, 140.2, 135.3, 130.8, 129.8, 128.3, 126.2,

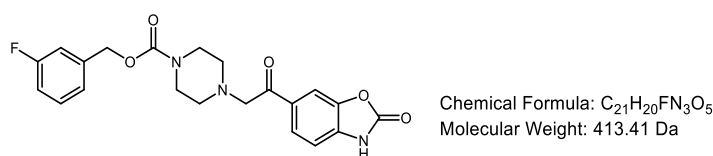
125.6, 124.9, 109.4, 65.7, 64.2, 53.2, 43.9, 36.0; HRMS: exact mass calculated for $[M+H]^+$ ($C_{22}H_{22}Cl_2N_3O_4$) requires m/z 462.0975 found m/z 462.0982

Compound 218: Cyclohexylmethyl 4-(2-oxo-2-(2-oxo-2,3-dihydrobenzo[d]oxazol-6-yl)ethyl)piperazine-1-carboxylate



Prepared according to general procedure E at 50 °C using 1-(*tert*-butyl) 4-(cyclohexylmethyl) piperazine-1,4-dicarboxylate (**123**, 0.48 g, 1.47 mmol), TFA:CH₂Cl₂ (1:1, 2 mL), 6-(2-chloroacetyl)benzo[d]oxazol-2(3*H*)-one (**172**, 0.28 g, 1.3 mmol), MeCN (5 mL), Et₃N (0.2 mL, 1.43 mmol) to give the desired product as a brown gum (0.28 g, 53%). ν_{max} (neat): 2924, 2851, 1765, 1672, 1241 cm⁻¹; ¹H NMR (500 MHz, MeOD) δ 7.96 (dd, J = 8.2, 1.5 Hz, 1H), 7.89 (d, J = 1.2 Hz, 1H), 7.19 (d, J = 8.2 Hz, 1H), 3.97 (s, 2H), 3.91 (d, J = 6.5 Hz, 2H), 3.72 – 3.44 (m, 4H), 2.79 – 2.46 (m, 4H), 1.88 – 1.53 (m, 6H), 1.40 – 1.13 (m, 3H), 1.12 – 0.85 (m, 2H), NH not observed; ¹³C NMR (126 MHz, MeOD) δ 196.3, 157.2, 156.8, 145.3, 136.6, 131.8, 126.6, 110.4, 110.3, 71.9, 64.7, 54.1, 44.5, 38.8, 30.7, 27.5, 26.8; HRMS: exact mass calculated for $[M+H]^+$ ($C_{21}H_{28}N_3O_5$) requires m/z 402.2023, found m/z 402.2018.

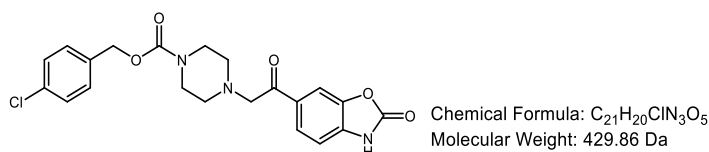
Compound 219: 3-Fluorobenzyl 4-(2-oxo-2-(2-oxo-2,3-dihydrobenzo[d]oxazol-6-yl)ethyl)piperazine-1-carboxylate



Prepared according to general procedure E at 50 °C using 1-(*tert*-butyl) 4-(3-fluorobenzyl) piperazine-1,4-dicarboxylate (**131**, 0.45 g, 1.33 mmol), TFA:CH₂Cl₂ (1:1, 2 mL), 6-(2-chloroacetyl)benzo[d]oxazol-2(3*H*)-one (**172**, 0.25 g, 1.19 mmol), MeCN (5 mL), Et₃N (0.18 mL, 1.31 mmol), 3-fluorobenzyl piperazine-1-carboxylate (0.31 g, 1.31 mmol) to give the desired product as a yellow gum (0.17 g, 34%). ν_{max} (neat): 1768, 1677, 1430, 1238 cm⁻¹; ¹H NMR (500 MHz, MeOD) δ 7.93 (dd, J = 8.2, 1.4 Hz, 1H), 7.87 (d, J = 1.2 Hz, 1H), 7.41 – 7.33 (m, 1H), 7.21 – 7.14 (m, 2H), 7.13

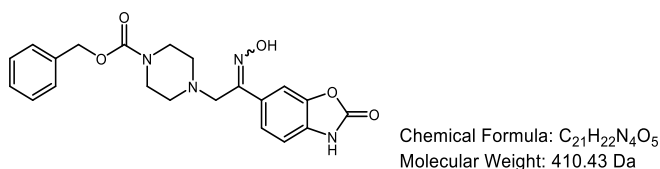
– 7.00 (m, 2H), 5.14 (s, 2H), 3.94 (s, 2H), 3.73 – 3.45 (m, 4H), 2.80 – 2.34 (m, 4H), NH not observed; ^{13}C NMR (126 MHz, DMSO- d_6) δ 196.3, 164.3 (d, $^1J_{\text{C-F}} = 244.8$ Hz), 156.8, 156.7, 145.3, 140.9, 136.6, 131.8, 131.4 (d, $^3J_{\text{C-F}} = 8.1$ Hz), 126.6, 124.5, 115.8 (d, $^2J_{\text{C-F}} = 21.2$ Hz), 115.4 (d, $^2J_{\text{C-F}} = 22.1$ Hz), 110.4, 110.3, 67.5, 64.7, 54.0, 44.6; ^{19}F NMR (471 MHz, Acetone- d_6) δ -114.76 (s, 1F); HRMS: exact mass calculated for $[\text{M}+\text{H}]^+$ ($\text{C}_{21}\text{H}_{21}\text{FN}_3\text{O}_5$) $[\text{M}+\text{H}]^+$ requires m/z 414.1460, found m/z 414.1457.

Compound 220: 4-Chlorobenzyl 4-(2-oxo-2-(2-oxo-2,3-dihydrobenzo[*d*]oxazol-6-yl)ethyl)piperazine-1-carboxylate



Prepared according to general procedure E at 50 °C using 1-(*tert*-butyl) 4-(4-chlorobenzyl) piperazine-1,4-dicarboxylate (**132**, 0.52 g, 1.47 mmol), TFA: CH_2Cl_2 (1:1, 2 mL), 6-(2-chloroacetyl)benzo[*d*]oxazol-2(3*H*)-one (**172**, 0.43 g, 2.04 mmol), MeCN (3 mL), Et_3N (0.31 mL, 2.24 mmol), 4-chlorobenzyl piperazine-1-carboxylate (0.57 g, 2.24 mmol) to give the desired product as a brown gum (0.22 g, 25%). ν_{max} (neat): 2987, 1773, 1693, 1430 cm^{-1} ; ^1H NMR (500 MHz, DMSO- d_6) δ 7.90 – 7.81 (m, 2H), 7.38 (m, 4H), 7.16 (d, $J = 8.1$ Hz, 1H), 5.05 (s, 2H), 4.31 – 3.95 (m, 2H), 3.84 (s, 4H), 3.63 – 3.14 (m, 4H), NH not observed; ^{13}C NMR (126 MHz, DMSO- d_6) δ 166.8, 161.1, 154.4, 143.0, 135.5, 134.5, 129.6, 129.5, 128.4, 126.0, 124.5, 110.0, 109.4, 65.9, 65.6, 44.5, 42.5; HRMS: exact mass calculated for $[\text{M}+\text{H}]^+$ ($\text{C}_{21}\text{H}_{21}\text{ClN}_3\text{O}_5$) $[\text{M}+\text{H}]^+$ requires m/z 430.1163, found m/z 430.1163; No data previously reported.⁶⁷

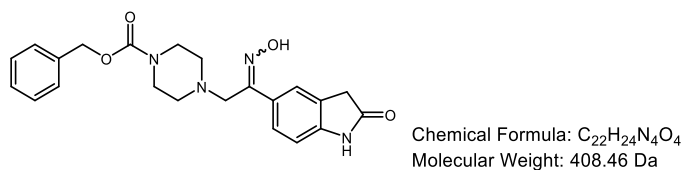
Compound 221: Benzyl 4-(2-(hydroxyimino)-2-(2-oxo-2,3-dihydrobenzo[*d*]oxazol-6-yl)ethyl)piperazine-1-carboxylate



Prepared according to general procedure M using benzyl 4-(2-oxo-2-(2-oxo-2,3-dihydrobenzo[*d*]oxazol-6-yl)ethyl)piperazine-1-carboxylate (**163**, 0.18 g,

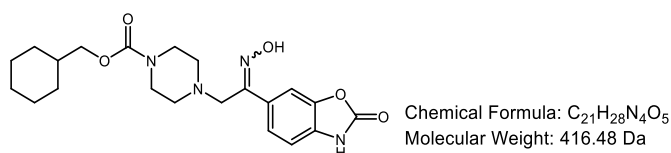
0.46 mmol), NaOAc (0.04 g, 0.5 mmol), HONH₂.HCl (0.04 g, 0.5 mmol), MeOH (3 mL) to afford the desired product as a yellow gum (21 mg, 11%). ν_{\max} (neat): 1670, 1427, 1234 cm⁻¹; ¹H NMR (400 MHz, MeOD) δ 7.72 – 7.56 (m, 1H), 7.38 – 7.29 (m, 5H), 7.06 (d, J = 8.2 Hz, 1H), 5.12 (s, 2H), 3.77 – 3.71 (m, 2H), 3.50 – 3.40 (m, 4H), 2.52 – 2.49 (m, 4H), OH and NH not observed; ¹³C NMR (126 MHz, MeOD) δ 155.8, 155.5, 153.1, 143.9, 136.7, 131.0, 130.8, 128.1, 127.7, 127.5, 122.6, 108.8, 107.6, 66.9, 52.6, 50.3, 43.5; HRMS: exact mass calculated for [M+H]⁺ (C₂₁H₂₂N₄O₅) [M+H]⁺ requires m/z 411.1663, found m/z 411.1668.

Compound 222: Benzyl 4-(2-(hydroxyimino)-2-(2-oxoindolin-5-yl)ethyl)piperazine-1-carboxylate



Prepared according to general procedure M using benzyl 4-(2-oxo-2-(2-oxoindolin-5-yl)ethyl)piperazine-1-carboxylate (**216**, 0.37 g, 0.94 mmol), NaOAc (0.08 g, 1.03 mmol), HONH₂.HCl (0.07 g, 1.03 mmol), MeOH (3 mL) to afford the desired product as a white solid (90 mg, 22%). MPt: 216 – 218 °C; ν_{\max} (neat): 3051, 1706, 1683, 1244 cm⁻¹; ¹H NMR (500 MHz, DMSO-*d*₆) δ 11.22 (s, 1H), 10.47 (s, 1H), 7.90 – 7.42 (m, 2H), 7.43 – 7.03 (m, 5H), 6.79 (d, J = 8.1 Hz, 1H), 5.05 (s, 2H), 3.60 (s, 2H), 3.48 (s, 2H), 3.43 – 3.20 (m, 4H), 2.47 – 2.33 (m, 4H); ¹³C NMR (101 MHz, DMSO-*d*₆) δ 176.4, 154.3, 152.6, 144.1, 136.9, 129.3, 128.4, 127.8, 127.5, 125.9, 125.6, 122.1, 108.6, 66.1, 52.5, 49.9, 43.4, 35.8; HRMS: exact mass calculated for [M+H]⁺ (C₂₂H₂₅N₄O₄) [M+H]⁺ requires m/z 409.1870, found m/z 409.1867.

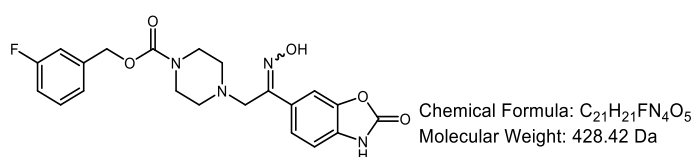
Compound 223: Cyclohexylmethyl 4-(2-(hydroxyimino)-2-(2-oxo-2,3-dihydrobenzo[*d*]oxazol-6-yl)ethyl)piperazine-1-carboxylate



Prepared according to general procedure M using cyclohexylmethyl 4-(2-oxo-2-(2-oxo-2,3-dihydrobenzo[*d*]oxazol-6-yl)ethyl)piperazine-1-carboxylate (**218**, 0.27 g, 0.67 mmol), NaOAc (0.06 g, 0.74 mmol), HONH₂.HCl (0.05 g, 0.74 mmol), MeOH

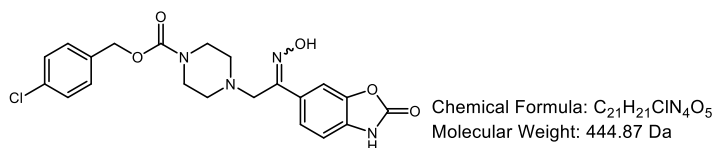
(2 mL) to afford the desired product as a yellow gum (0.19 g, 67%). ν_{\max} (neat): 2928, 2851, 1761, 1436, 1241 cm^{-1} ; ^1H NMR (500 MHz, Acetone- d_6) δ 7.09 (s, 1H), 6.82 – 6.70 (m, 1H), 6.18 (d, J = 8.1 Hz, 1H), 2.93 (m, 2H), 2.56 – 2.43 (m, 4H), 1.66 – 1.51 (m, 4H), 1.22 – 1.11 (m, 1H), 0.88 – 0.60 (m, 7H), 0.42 – 0.14 (m, 3H), 0.14 – 0.04 (m, 2H), NH and OH not observed; ^{13}C NMR (101 MHz, DMSO- d_6) δ 154.4, 152.2, 143.0, 130.2, 121.9, 109.5, 108.8, 108.5, 107.0, 78.8, 69.3, 52.1, 51.8, 49.9, 43.1, 36.6, 28.8, 25.6, 24.8. (343 K); HRMS: exact mass calculated for $[\text{M}+\text{H}]^+$ ($\text{C}_{21}\text{H}_{29}\text{N}_4\text{O}_5$) $[\text{M}+\text{H}]^+$ requires m/z 417.2132, found m/z 417.2128.

Compound 224: 3-Fluorobenzyl 4-(2-(hydroxyimino)-2-(2-oxo-2,3-dihydrobenzo[*d*]oxazol-6-yl)ethyl)piperazine-1-carboxylate



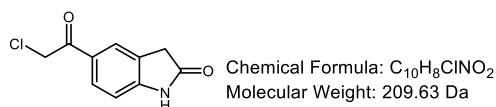
Prepared according to general procedure M using 3-fluorobenzyl 4-(2-(hydroxyimino)-2-(2-oxo-2,3-dihydrobenzo[*d*]oxazol-6-yl)ethyl)piperazine-1-carboxylate (**219**, 0.17 g, 0.41 mmol), NaOAc (0.04 g, 0.45 mmol), $\text{HONH}_2\cdot\text{HCl}$ (0.03 g, 0.45 mmol), MeOH (3 mL) to afford the desired product as a yellow gum (0.18 g, 39%). ν_{\max} (neat): 1754, 1676, 1430, 1240 cm^{-1} ; ^1H NMR (500 MHz, Acetone- d_6) δ 7.97 (s, 1H), 7.68 – 7.56 (m, 2H), 7.46 – 7.29 (m, 1H), 7.24 – 6.98 (m, 4H), 5.09 (s, 2H), 3.72 (s, 1H), 3.52 – 3.16 (m, 4H), 2.67 – 2.36 (m, 3H), 2.01 (dt, J = 4.4, 2.2 Hz, 2H), NH not observed; ^{13}C NMR (126 MHz, DMSO- d_6) δ 154.8 (d, $^1J_{\text{C-F}}$ = 244.7 Hz), 147.1, 144.7, 135.8, 131.4 (d, $^3J_{\text{C-F}}$ = 7.5 Hz), 122.8, 122.7, 121.9 (d, $^4J_{\text{C-F}}$ = 6.6 Hz), 114.9, 114.5, 106.3 (d, $^2J_{\text{C-F}}$ = 21.3 Hz), 105.9 (d, $^2J_{\text{C-F}}$ = 22.2 Hz), 102.0, 100.8, 99.5, 57.9, 53.1, 44.5, 42.2; ^{19}F NMR (471 MHz, Acetone- d_6) δ -114.80 (s, 1F); HRMS: exact mass calculated for $[\text{M}+\text{H}]^+$ ($\text{C}_{21}\text{H}_{22}\text{FN}_4\text{O}_5$) $[\text{M}+\text{H}]^+$ requires m/z 429.1569, found m/z 429.1564

Compound 225: 4-Chlorobenzyl 4-(2-(hydroxyimino)-2-(2-oxo-2,3-dihydrobenzo[d]oxazol-6-yl)ethyl)piperazine-1-carboxylate



Prepared according to general procedure M using 4-chlorobenzyl 4-(2-oxo-2-(2-oxo-2,3-dihydrobenzo[d]oxazol-6-yl)ethyl)piperazine-1-carboxylate (**220**, 0.21 g, 0.49 mmol), NaOAc (0.05 g, 0.54 mmol), HONH₂·HCl (0.04 g, 0.54 mmol), MeOH (3.00 mL) to afford the desired product as a yellow gum (66.00 mg, 30%). ν_{\max} (neat): 1775, 1663, 1433, 1247 cm^{-1} ; ¹H NMR (400 MHz, DMSO-*d*₆) δ 7.66 – 7.51 (m, 2H), 7.46 – 7.29 (m, 4H), 7.07 (d, *J* = 8.3 Hz, 1H), 5.05 (s, 2H), 3.64 (s, 2H), 3.47 – 3.07 (m, 4H), 2.45 – 2.28 (m, 4H), NH and OH not observed; ¹³C NMR (101 MHz, DMSO-*d*₆) δ 154.5, 154.2, 152.3, 143.2, 136.0, 132.4, 130.7, 130.2, 129.4, 128.4, 122.1, 109.2, 107.3, 65.4, 52.4, 50.0, 43.5; HRMS: exact mass calculated for [M+H]⁺ (C₂₁H₂₂ClN₄O₅) [M+H]⁺ requires *m/z* 445.1273, found *m/z* 445.1269

Compound 216: 5-(2-chloroacetyl)indolin-2-one



Prepared according to general procedure H using AlCl₃ (1.98 g, 15.02 mmol), DCE (1 mL), chloroacetyl chloride (0.48 mL, 6.01 mmol), indolin-2-one (0.8 g, 6.01 mmol), to afford the desired product as a brown amorphous solid (1.26 g, 79%). ¹H NMR (400 MHz, DMSO-*d*₆) δ 10.83 (s, 1H), 7.91 – 7.87 (m, 2H), 6.94 (d, *J* = 8.2 Hz, 1H), 5.08 (s, 2H), 3.57 (s, 2H); ¹³C NMR (101 MHz, DMSO-*d*₆) δ 190.2, 176.7, 149.0, 129.7, 127.8, 126.3, 124.5, 108.9, 47.1, 35.4; HRMS: exact mass calculated for [M+H]⁺ (C₁₀H₉ClN₂O₂) requires *m/z* 210.0316, found *m/z* 211.0312; Consistent with previously reported data.¹⁵²

5.3 Biology

5.3.1 PathHunter[®] CHO-K1 EDG2 β -Arrestin Compound Screen Study¹⁰⁶

5.3.1.1 Agonist Mode

Compounds were screened against the PathHunter[®] CHO-K1 EDG₂ cell line (DiscoverX) in agonist mode. DiscoverX reference 1-oleoyl-LPA (dissolved in EtOH) specified for the EDG2 cell line was used as the standard agonist. 5000 cells / well were plated in a 384 well assay plate, in 20 μ L PathHunter[®] Cell Plating Reagent, and incubated overnight to allow cells to attach and grow. Cells were then exposed to 10 μ M compound (1% DMSO) or buffer + 1% DMSO. The stocks of DiscoverX reference LPA are suspended in EtOH: therefore cells were exposed to 10 μ M compound (5% EtOH) or buffer + 5% EtOH. Cells were exposed to compounds for 3 h at room temperature. Following compound incubations, PathHunter[®] Detection Reagent was added and the assay plates were read on an Envision luminometer.

5.3.1.2 Antagonist Mode Screen

Compounds were profiled against the PathHunter[®] CHO-K1 EDG2 (DiscoverX) cell line in antagonist mode. The experiment was run concurrently with the agonist mode test. Cells were exposed to 10 μ M compound (1% final DMSO) or buffer + 1% DMSO for 1 h at 37° C, followed by exposure to 500 nM 1-oleoyl-LPA (0.25% final EtOH) for 3 hours at RT. Control wells were exposed to 500 nM LPA (@ 0.25% final EtOH) + 1% DMSO. Buffer only control wells were exposed to Buffer + 1% DMSO + 0.25% EtOH. The 500 nM agonist challenge dose was based on historical data from the EDG2 cell line. Following compound incubations, PathHunter[®] Detection Reagent was added and the assay plates were read on an Envision luminometer.

5.3.2 Bis-*p*NPP ATX Inhibition Assay

Molecules were tested for their ability to inhibit ATX activity using the Autotaxin Inhibitor Screening Kit (Cayman Chemical) with modifications to the manufacturer's protocol. Briefly, In a 96 well plate 20 ng/mL autotaxin was incubated with 3 mM bis-*p*NPP at 30 °C for 30 min in 50 mM Tris-HCl buffer (pH 8.5) containing 10 mM CaCl₂ and 0.02% triton X. Liberated bis-*p*-nitrophenol was measured using a Wallac Victor2 1420 multilabel counter (Perkin Elmer, Beaconsfield, UK) in absorbance mode at 405 nm. The background was determined by incubating bis-*p*NPP in the

absence of enzyme. Activity of the compounds was determined by subtracting the average background from all results and expressing the compound activity as a percentage of the enzyme-substrate reaction in the absence of compound. PF-8380 in the concentration range of 0.1-300 nM in half log units was included as a standard compound in every assay plate. The potential inhibitors were initially tested against autotaxin at a concentration of 30 μ M; samples which showed inhibition of 70% or greater were considered to be active. Dose response curves, in the concentration range of 30 nM to 30 μ M in half log units, to calculate K_i values were performed on compounds reaching the designated activity threshold. Data was expressed as mean \pm SEM was plotted using Graph Pad Prism Software.

5.3.3 [³H]-Thymidine Incorporation Assay

5.3.3.1 Cell Culture

PC3 (human prostate cancer) cells were kept under conventional cell culture conditions at 37 °C, 5% CO₂.

5.3.3.2 Stimulating Cells

Cells were sub-cultured and grown to 70% confluence in 24 well plates before quiescing for 24 h and then treatment with appropriate stimulus or vehicle (DMSO) for 18 h.

5.3.3.3 [³H]-Thymidine Incorporation

[³H]-Thymidine (9.25 kBq diluted in serum free medium) was added to each well 5 h before the expiry of the 18-20 h period. The medium was aspirated to the radioactive sink. 1 mL ice cold 10% (w/v) trichloroacetic acid (TCA) was added to each well and incubated on ice for 6 min x 3. This precipitates the protein and nuclear material remains stuck to the base of the well. The TCA was aspirated to the radioactive sink and 0.25 mL 0.1% (w/v) SDS/0.3 M NaOH was added to each well (at room temperature). This dissolves the nuclear material. The contents of each well were transferred to separate beta vials. 2 mL scintillant was added to each vial, capped and mixed thoroughly. Each vial was counted in scintillation counter (3 min per sample).

5.3.4 Cytotoxicity Alamar Blue Assay

Compounds were tested for any cytotoxic effects against normal fibroblasts (HS27 cells) and an ovarian carcinoma cell line (A2780). The cytotoxicity was evaluated by using the alamarBlue[®] assay. HS27 cells were incubated in DMEM supplemented with 10% FBS, 2 mM glutamine and 1% penicillin/streptomycin under 5% CO₂ at 37 °C in a humidified incubator. A2780 cells were cultured under the same conditions in RPMI 1640 media with 10% FBS and 1% penicillin-streptomycin. At 70-80% confluency the cells were detached from the culture flasks using Triple[®] Express and seeded in clear 96-well plates at a concentration of 3750 cells per well (A2780 cells) and 7500 cells per well (HS27 cells). The cells were allowed to adhere and equilibrate overnight before addition of compound (diluted in the relevant media). After a further 42 h incubation, 10% Almar Blue[®] was to each well and incubated for 6 h. The resulting fluorescence was measured using a Wallac Victor2 1420 multilabel counter, in fluorescence mode: excitation 560, emission 590. Cells in the absence of compound were considered as 100% viable against which compound treated cells (at a concentration of 30 µM, at least n=2) were compared. 0.1% triton X was used as a negative control. Data was expressed as mean ± SEM and plotted using Graph Pad Prism Software.

5.3.5 High Throughput Physicochemical Measurements¹⁵³

5.3.5.1 CLND Solubility Assay¹⁵⁴

GSK in-house kinetic solubility assay: 5 µL of 10 mM DMSO stock solution diluted to 100 µL with pH7.4 phosphate buffered saline, equilibrated for 1 h at room temperature, filtered through Millipore Multiscreen_{HTS}-PCF filter plates (MSSL BPC). The filtrate is quantified by suitably calibrated flow injection Chemi-Luminescent Nitrogen Detection (CLND). The standard error of the CLND solubility determination is ±30 µM, the upper limit of the solubility is 500 µM when working from 10 mM DMSO stock solution.

5.3.5.2 Artificial Membrane Permeability Assay¹¹⁰

The donor cell contained 2.5 µL of 10 mM sample solution in pH 7.40 phosphate buffer. To enhance solubility, 0.5% hydroxypropyl-cyclodextrin (encapsin) has been added to the buffer. The artificial membrane is prepared from 1.8% phosphatidylcholine and 1% cholesterol in decane solution. The sample

concentration in both the donor and acceptor compartment is determined by LC-MS after 3 h incubation at room temperature. The permeability ($\log P_{app}$) measuring how fast molecules pass through the black lipid membrane is expressed in nm/s. The average standard error of the assay is around ± 30 nm/s and can be higher at the low permeability range.

5.3.5.3 ChromlogD Assay¹¹⁶

The Chromatographic Hydrophobicity Index (CHI) values were measured using reversed phase HPLC column (50 x 2 mm 3 μ M Gemini NX C18, Phenomenex, UK) with fast acetonitrile gradient at starting mobile phase of pH = 7.4. CHI values are derived directly from the gradient retention times by using a calibration line obtained for standard compounds. The CHI value approximates to the volume % organic concentration when the compound elutes. CHI is linearly transformed into ChromlogD by the formula: $\text{ChromlogD} = 0.0857\text{CHI} - 2.00$. The average error of the assay is ± 3 CHI unit or ± 0.25 ChromlogD

6 References

- 1 A. M. Tager, P. LaCamera, B. S. Shea, G. S. Campanella, M. Selman, Z. Zhao, V. Polosukhin, J. Wain, B. a Karimi-Shah, N. D. Kim, W. K. Hart, A. Pardo, T. S. Blackwell, Y. Xu, J. Chun and A. D. Luster, *Nat. Med.*, 2008, **14**, 45–54.
- 2 G. Raghu, D. Weycker, J. Edelsberg, W. Z. Bradford and G. Oster, *Am. J. Respir. Crit. Care Med.*, 2006, **174**, 810–816.
- 3 M. S. Wilson and T. Wynn, *Mucosal Immunol.*, 2009, **2**, 103–121.
- 4 SlideShare, <http://www.slideshare.net/ActionforPF/ipf-webinar-for-the-british-lung-foundation-2012-dr-helen-parfrey>, 2016, 22nd Jan.
- 5 B. G. Kelly, S. S. Lok, P. S. Hasleton, J. J. Egan and J. P. Stewart, *Am. J. Respir. Crit. Care Med.*, 2002, **166**, 510–513.
- 6 M. Whyte, R. Hubbard, R. Meliconi, M. Whidborne, V. Eaton, C. Bingle, J. Timms, G. Duff, A. Facchini, A. Pacilli, M. Fabbri, I. N. Hall, J. Britton, I. N. Johnston and F. D. I. Giovine, *Am. J. Respir. Crit. Care Med.*, 2000, **162**, 755–758.
- 7 A. Datta, C. J. Scotton and R. C. Chambers, *Br. J. Pharmacol.*, 2011, **163**, 141–172.
- 8 C. J. Scotton and R. C. Chambers, *Chest*, 2007, **132**, 1311–1321.
- 9 P. Spagnolo, A. U. Wells and H. R. Collard, *Drug Discov. Today*, 2015, **20**, 514–524.
- 10 H. Sem, *Chest*, 2002, **122**, 286S–289S.
- 11 S. H. Phan, *Proc. Am. Thorac. Soc.*, 2008, **5**, 334–337.
- 12 Y. Qian, M. Hamilton, A. Sidduri, S. Gabriel, Y. Ren, R. Peng, R. Kondru, A. Narayanan, T. Truitt, R. Hamid, Y. Chen, L. Zhang, A. J. Fretland, R. A. Sanchez, K.-C. Chang, M. Lucas, R. C. Schoenfeld, D. Laine, M. E. Fuentes, C. S. Stevenson and D. C. Budd, *J. Med. Chem.*, 2012, **55**, 7920–7939.

- 13 S. R. K. D. M. Walters, *Curr Protoc Pharmacol*, 2008, 5.46.1–5.46.17.
- 14 M. K. A. Moeller, K. Ask, D. Warburton, J. Gauldie, *Int J Biochem Cell Biol.*, 2013, **18**, 1199–1216.
- 15 G. Raghu, H. R. Collard, J. J. Egan, F. J. Martinez, J. Behr, K. K. Brown, T. V Colby, J.-F. Cordier, K. R. Flaherty, J. Lasky, D. Lynch, J. H. Ryu, J. J. Swigris, A. U. Wells, J. Ancochea, D. Bouros, C. Carvalho, U. Costabel, M. Ebina, D. M. Hansell, T. Johkoh, D. S. Kim, T. E. King, Y. Kondoh, J. Myers, N. L. Müller, A. G. Nicholson, L. Richeldi, M. Selman, R. F. Dudden, B. S. Griss, S. L. Protzko and H. J. Schünemann, *Am. J. Respir. Crit. Care Med.*, 2011, **183**, 788–824.
- 16 P. W. Noble, C. Albera, W. Z. Bradford, U. Costabel, M. K. Glassberg, D. Kardatzke, T. E. King, L. Lancaster, S. a. Sahn, J. Szwarcberg, D. Valeyre and R. M. Du Bois, *Lancet*, 2011, **377**, 1760–1769.
- 17 L. Richeldi, R. M. du Bois, G. Raghu, A. Azuma, K. K. Brown, U. Costabel, V. Cottin, K. R. Flaherty, D. M. Hansell, Y. Inoue, D. S. Kim, M. Kolb, A. G. Nicholson, P. W. Noble, M. Selman, H. Taniguchi, M. Brun, F. Le Maulf, M. Girard, S. Stowasser, R. Schlenker-Herceg, B. Disse and H. R. Collard, *N. Engl. J. Med.*, 2014, **370**, 2071–2082.
- 18 M. E. Cho and J. B. Kopp, *Expert Opin. Investig. Drugs*, 2010, **19**, 275–283.
- 19 T. E. King, W. Z. Bradford, S. Castro-Bernardini, E. A. Fagan, I. Glaspole, M. K. Glassberg, E. Gorina, P. M. Hopkins, D. Kardatzke, L. Lancaster, D. J. Lederer, S. D. Nathan, C. A. Pereira, S. A. Sahn, R. Sussman, J. J. Swigris and P. W. Noble, *N. Engl. J. Med.*, 2014, **370**, 2083–2092.
- 20 D. Valeyre, C. Albera, W. Z. Bradford, U. Costabel, T. E. King, J. A. Leff, P. W. Noble, S. A. Sahn and R. M. du Bois, *Respirology*, 2014, **19**, 740–747.
- 21 ANNEX I EMA Europe,
http://www.ema.europa.eu/docs/en_GB/document_library/EPAR_-_Product_Information/human/002154/WC500103049.pdf, 2016, 22 nd Jan.
- 22 F. Hilberg, G. J. Roth, M. Krssak, S. Kautschitsch, W. Sommergruber, U. Tontsch-Grunt, P. Garin-Chesa, G. Bader, A. Zoepfel, J. Quant, A. Heckel

- and W. J. Rettig, *Cancer Res.*, 2008, **68**, 4774–4782.
- 23 H. V. Woodcock, P. L. Molyneaux and T. M. Maher, *Drug Des. Devel. Ther.*, 2013, **7**, 503–510.
- 24 Boehringer Ingelheim Pharmaceuticals Prescribing Information, *Ofev*, 2014, 1–18.
- 25 Ats Board of Directors and Ers Executive Committiee, *Am. J. Respir. Crit. Care Med.*, 2000, **161**, 646–664.
- 26 T. Mutoh, R. Rivera and J. Chun, *Br. J. Pharmacol.*, 2012, **165**, 829–844.
- 27 J. W. Choi, D. R. Herr, K. Noguchi, Y. C. Yung, C.-W. Lee, T. Mutoh, M.-E. Lin, S. T. Teo, K. E. Park, A. N. Mosley and J. Chun, *Annu. Rev. Pharmacol. Toxicol.*, 2010, **50**, 157–186.
- 28 T. Klabunde and G. Hessler, *ChemBioChem*, 2002, **3**, 928–944.
- 29 R. Wattiez and P. Falmagne, *J. Chromatogr. B. Analyt. Technol. Biomed. Life Sci.*, 2005, **815**, 169–178.
- 30 J. Aoki, A. Inoue and S. Okudaira, *Biochim. Biophys. Acta*, 2008, **1781**, 513–518.
- 31 H. Shindou, D. Hishikawa, T. Harayama, K. Yuki and T. Shimizu, *J. Lipid Res.*, 2008, **50**, S46–S51.
- 32 J. E. Chrencik, C. B. Roth, M. Terakado, H. Kurata, R. Omi, Y. Kihara, D. Warshaviak, S. Nakade, G. Asmar-Rovira, M. Mileni, H. Mizuno, M. T. Griffith, C. Rodgers, G. W. Han, J. Velasquez, J. Chun, R. C. Stevens and M. A. Hanson, *Cell*, 2015, **161**, 1633–1643.
- 33 I. González-Gil, D. Zian, H. Vázquez-Villa, S. Ortega-Gutiérrez and M. L. López-Rodríguez, *Med. Chem. Commun.*, 2015, **6**, 13–23.
- 34 C. Lipinski, F. Lombardo, B. W. Dominy and P. J. Feeney, *Adv. Drug Deliv. Rev.*, 2001, **46**, 3–26.
- 35 D. J. Fischer, N. Nusser, T. Virag, K. Yokoyama, D. Wang, D. L. Baker, D. Bautista, L. Parrill and G. Tigyi, *Mol. Pharmacol.*, 2001, **60**, 776–784.

- 36 C. E. Heise, W. L. Santos, M. Schreihofner, B. H. Heasley, Y. V. Mukhin, T. L. Macdonald and K. R. Lynch, *Mol. Pharmacol.*, 2001, **60**, 1173–1180.
- 37 H. Ohta, K. Sato, N. Murata, A. Damirin, E. Malchinkhuu, J. Kon, T. Kimura, M. Tobo, Y. Yamazaki, T. Watanabe, M. Yagi, M. Sato, R. Suzuki, H. Murooka, T. Sakai, T. Nishitoba, D.-S. Im, H. Nochi, K. Tamoto, H. Tomura and F. Okajima, *Mol. Pharmacol.*, 2003, **64**, 994–1005.
- 38 Y. Kihara, H. Mizuno and J. Chun, *Exp. Cell Res.*, 2015, **333**, 171–177.
- 39 J. S. Swaney, C. Chapman, L. D. Correa, K. J. Stebbins, A. R. Broadhead, G. Bain, A. M. Santini, J. Darlington, C. D. King, C. S. Baccei, C. Lee, T. A. Parr, J. R. Roppe, T. J. Seiders, J. Ziff, P. Prasit, J. H. Hutchinson, J. F. Evans and D. S. Lorrain, *J. Pharmacol. Exp. Ther.*, 2011, **336**, 693–700.
- 40 ClinicalTrials.gov,
<https://clinicaltrials.gov/ct2/show/NCT01766817?term=lysophosphatidic+acid&rank=2,%20accessed%202nd%20September>, 2016, 22nd Jan.
- 41 E. Barbayianni, V. Magrioti, P. Moutevelis-Minakakis and G. Kokotos, *Expert Opin. Ther. Pat.*, 2013, **23**, 1123–1132.
- 42 M. L. Stracke, H. C. Krutzsch, E. J. Unsworth, A. Arestad, V. Cioce, E. Schiffmann and L. Liotta, *J. Biol. Chem.*, 1992, **267**, 2524–2529.
- 43 S. Jansen, C. Stefan, J. W. M. Creemers, E. Waelkens, A. Van Eynde, W. Stalmans and M. Bollen, *J. Cell Sci.*, 2005, **118**, 3081–3090.
- 44 C. Stefan, S. Jansen and M. Bollen, *Trends Biochem. Sci.*, 2005, **30**, 542–550.
- 45 A. Giganti, M. Rodriguez, B. Fould, N. Moulharat, F. Cogé, P. Chomarot, J.-P. Galizzi, P. Valet, J.-S. Saulnier-Blache, J. a Boutin and G. Ferry, *J. Biol. Chem.*, 2008, **283**, 7776–7789.
- 46 T. Hashimoto, S. Okudaira, K. Igarashi, K. Hama, Y. Yatomi and J. Aoki, *J. Biochem.*, 2012, **151**, 89–97.
- 47 J. E. Day, T. Hall, L. E. Pegg, T. E. Benson, J. Hausmann and S. Kamtekar, *Acta Cryst*, 2010, **F66**, 1127–1129.

- 48 K. Inoue, N. Tanaka, A. Haga, K. Yamasaki, T. Umeda, Y. Kusakabe, Y. Sakamoto, T. Nonaka, Y. Deyashiki and K. T. Nakamura, *Acta Cryst*, 2011, **F67**, 450–453.
- 49 H. Nishimasu, S. Okudaira, K. Hama, E. Mihara, N. Dohmae, A. Inoue, R. Ishitani, J. Takagi, J. Aoki and O. Nureki, *Nat. Struct. Mol. Biol.*, 2011, **18**, 205–212.
- 50 J. I. Fells, S. C. Lee, Y. Fujiwara, D. D. Norman, K. G. Lim, R. Tsukahara, J. Liu, R. Patil, D. D. Miller, R. J. Kirby, S. Nelson, W. Seibel, R. Papoian, A. L. Parrill, D. L. Baker, R. Bittman and G. Tigyi, *Mol. Pharmacol.*, 2013, **84**, 415–424.
- 51 W. H. Moolenaar and A. Perrakis, *Nat Rev Mol Cell Bioliol*, 2011, **12**, 674–679.
- 52 H. Nishimasu, S. Okudaira, K. Hama, E. Mihara, N. Dohmae, A. Inoue, R. Ishitani, J. Takagi, J. Aoki and O. Nureki, *Nat. Struct. Mol. Biol.*, 2011, **18**, 205–212.
- 53 W. J. Keune, *Unpublished work, Netherlands Cancer Institute*, 2016.
- 54 H. M. H. G. Albers and H. Ovaa, *Chem. Rev.*, 2012, **112**, 2593–2603.
- 55 C. G. Ferguson, C. S. Bigman, R. D. Richardson, L. a van Meeteren, W. H. Moolenaar and G. D. Prestwich, *Org. Lett.*, 2006, **8**, 2023–2026.
- 56 H. Takakusa, K. Kikuchi, Y. Urano, S. Sakamoto, K. Yamaguchi and T. Nagano, *J. Am. Chem. Soc.*, 2002, **124**, 1653–1657.
- 57 L. Van Meeteren, P. Ruurs, E. Christodoulou, J. W. Goding, H. Takakusa, K. Kikuchi, A. Perrakis, T. Nagano and W. H. Moolenaar, *J. Biol. Chem.*, 2005, **280**, 21155–21161.
- 58 D. D. Miller, G. Tigyi, V. Gududura, Y. Fujiwara, D. Baker, M. D. Walker and G. Durgam, *US2006270634A1*, 2006.
- 59 G. Prestwich, G. Tigyi, G. Jiang, G. Zhang, J. Gajewiak, H. Zhang and X. Xu, *WO2008157361A1*, 2008.
- 60 H. Zhang, X. Xu, J. Gajewiak, R. Tsukahara, Y. Fujiwara, J. Liu, J. I. Fells, D.

- Perygin, A. L. Parrill, G. Tigy and G. D. Prestwich, *Cancer Res.*, 2009, **69**, 5441–5449.
- 61 A. L. Parrill, U. Echols, T. Nguyen, T. Pham, A. Hoeglund and D. L. Baker, *Bioorg. Med. Chem.*, 2008, **16**, 1784–1795.
- 62 A. B. Hoeglund, H. E. Bostic, A. L. Howard, I. W. Wanjala, M. D. Best, D. L. Baker and A. L. Parrill, *J. Med. Chem.*, 2010, **53**, 1056–1066.
- 63 H. M. H. G. Albers, L. a. Van Meeteren, D. a. Egan, E. W. Van Tilburg, W. H. Moolenaar and H. Ovaa, *J. Med. Chem.*, 2010, **53**, 4958–4967.
- 64 H. M. H. G. Albers, L. J. D. Hendrickx, R. J. P. Van Tol, J. Hausmann, A. Perrakis and H. Ovaa, *J. Med. Chem.*, 2011, **54**, 4619–4626.
- 65 J. Hausmann, S. Kamtekar, E. Christodoulou, J. E. Day, T. Wu, Z. Fulkerson, H. M. H. G. Albers, L. A. Van Meeteren, L. Van Zeijl, S. Jansen, M. Andries, T. Hall, L. E. Pegg, T. E. Benson, M. Kasiem, K. Harlos, C. Vander Kooi, S. S. Smyth, H. Ovaa, M. Bollen, A. J. Morris and W. H. Moolenaar, *Nat Struct Mol Biol.*, 2011, **18**, 198–204.
- 66 D. Castagna, D. C. Budd, S. J. F. Macdonald, C. Jamieson and A. J. B. Watson, *J. Med. Chem.*, 2016, DOI: 10.1021/acs.jmedchem.5b01599.
- 67 K. Schiemann, M. Seeheom-Jugenheim, A. Schultz, I. Blauket and G.-G. Kober, *Merck US2010222341A1*, 2010.
- 68 J. Gierse, A. Thorarensen, K. Beltey, E. Bradshaw-Pierce, L. Cortes-Burgos, T. Hall, A. Johnston, M. Murphy, O. Nemirovskiy, S. Ogawa, L. Pegg, M. Pelc, M. Prinsen, M. Schnute, J. Wendling, S. Wene, R. Weinberg, A. Wittwer, B. Zweifel and J. Masferrer, *J. Pharmacol. Exp. Ther.*, 2010, **334**, 310–317.
- 69 S. B. Jones, B. H. Norman and L. A. Pfeifer, *Eli Lilly WO2014/143583A1*, 2014.
- 70 V. Furminger, O. R. Hugues, D. M. Legrand, E. Stanley and C. Thomson, *Novartis US2014/0171404A1*, 2014.
- 71 J. Hert, D. Hunziker, P. Mattei, H. Mauser, G. Tang and L. Wang, *Hoffmann-*

- La Roche WO2014/048865A1*, 2014.
- 72 J. R. Roppe, A. T. Parr and J. H. Hutchinson, *Amira Pharm. WO2012166415A1*, 2012.
- 73 J. R. Roppe, A. T. Parr and J. H. Hutchinson, *Amira Pharm. US20130029948 A1*, 2013.
- 74 S. A. Long, A. Thoraesen and M. E. Schnute, *Pfizer WO2013/054185A1*, 2013.
- 75 J. I. Fells, S. C. Lee, D. D. Norman, R. Tsukahara, J. R. Kirby, S. Nelson, W. Seibel, R. Papoian, R. Patil, D. D. Miller, A. L. Parrill, T. C. Pham, D. L. Baker, R. Bittman and G. Tigyi, *FEBS J.*, 2014, **281**, 1017–1028.
- 76 D. H. Johnson, B. M. Shrier, J. S. O. Neal and J. A. Knutzen, *Mol. Pharmacol.*, 2015, **88**, 982–992.
- 77 L. Babiss, M. Clark, D. Keefe, Anthony, M. J. Mulvihill, H. Ni, L. Renzetti, F. Ruebsam, C. Wang, Z. Xie and Y. Zhang, *X-Rx Discov. Inc. WO2015154023*, 2015.
- 78 N. Desroy, B. Heckmann, R. C. X. Brys, A. M. Joncour, C. Peixoto and B. X. Marie, *Galapagos US2015/011872A1*.
- 79 The Biochemical Pharmacology Discussion Group,
<https://www.google.co.uk/url?sa=t&rct=j&q=&esrc=s&source=web&cd=3&cad=rja&uact=8&ved=0ahUKEwih7rPdob3KAhWBiQ8KHaJBDTYQFgggMAI&url=http%3A%2F%2Fwww.nyas.org%2Fasset.axd%3Fid%3Dc49be70c-bc9d-4f07-927a-ec80ef16846d%26t%3D635500174199370000&usg=AFQjCNEaiLVAEy>,
2016, 22nd Jan.
- 80 Galapagos, <http://www.glp.com/glp-1690>, 2016, 22nd Jan.
- 81 T. J. Ritchie and S. J. F. Macdonald, *Drug Discov. Today*, 2009, **14**, 1011–1020.
- 82 ChemAxon, *JCHEM Excel*, 2013, <http://www.chemaxon.com>.
- 83 P. D. Leeson and B. Springthorpe, *Nat. Rev. Drug Discov.*, 2007, **6**, 881–890.

- 84 J. R. Proudfoot, *Bioorganic Med. Chem. Lett.*, 2002, **12**, 1647–1650.
- 85 M. M. Hann, R. Leach and G. Harper, *J. Chem. Inf. Comput. Sci.*, 2001, **41**, 856–864.
- 86 G. Vert and J. Chory, *Dev. Cell*, 2011, **21**, 1179.
- 87 M. M. Hann and T. I. Oprea, *Curr. Opin. Chem. Biol.*, 2004, **8**, 255–263.
- 88 M. P. Gleeson, *J. Med. Chem.*, 2008, **51**, 817–834.
- 89 X. Cao, S. T. Gibbs, L. Fang, H. A. Miller, C. P. Landowski, H. C. Shin, H. Lennernas, Y. Zhong, G. L. Amidon, L. X. Yu and D. Sun, *Pharm Res*, 2006, **23**, 1675.
- 90 M. H. Abraham and J. Le, *J. Pharm. Sci.*, 1999, **88**, 868–880.
- 91 D. A. Horton, G. T. Bourne and M. L. Smythe, *Chem. Rev*, 2003, **103**, 893–930.
- 92 Z. Rankovic and R. Morphy, *Lead Generation Approaches in Drug Discovery*, Wiley, 1st edn., 2010.
- 93 E. J.-G. Anctil and V. Snieckus, *J. Organomet. Chem.*, 2002, **653**, 150–160.
- 94 J. C. Thenmozhiyal, P. T. Wong and W. Chui, *J. Med. Chem.*, 2004, **47**, 1527–1535.
- 95 R. L. Hudkins and P. Doukas, *Bioorganic Med. Chem. Lett.*, 1997, **7**, 979–984.
- 96 M. A. Rogawski and W. Löscher, *Nat. Rev. Neurosci.*, 2004, **5**, 553–564.
- 97 N. Triballeau, C. Peixoto, J. Lefranc, L. Alvey, M. Manioc, C. Housseman, H. Klaassen, K. Van Beeck, F. Namour, D. Minet, E. Van Der Aar, J. Feyen, S. Fletcher, R. Blaque, C. Robin-Jagerschmidt and P. Deprez, *J. Med. Chem*, 2012, **55**, 8236–8247.
- 98 A. Burger, *Prog. Drug Res.*, 1991, **37**, 287–371.
- 99 N. Meanwell, *J. Med. Chem.*, 2011, **54**, 2529–2591.
- 100 A. M. Birch, S. Groombridge, R. Law, A. G. Leach, C. D. Mee and C.

- Schramm, *J. Med. Chem.*, 2012, **55**, 3923–3933.
- 101 A. K. Ghosh and M. Brindisi, *J. Med. Chem.*, 2015, **58**, 2895–2940.
- 102 C. A. de Sa Alves, Fernando R. Barreiro, Eliezer J. Manssour Fraga, *Mini. Rev. Med. Chem.*, 2009, **9**, 782–793.
- 103 N. Kudo, M. Perseghini and G. C. Fu, *Angew. Chem. Int. Ed.*, 2006, **45**, 1282–1284.
- 104 M. Malacria and G. Maestri, *J. Org. Chem.*, 2013, **78**, 1323–1328.
- 105 D. Castagna, E. L. Duffy, D. Semaan, L. C. Young, J. M. Pritchard, S. J. F. Macdonald, D. C. Budd, C. Jamieson and A. J. B. Watson, *Med. Chem. Commun.*, 2015, **6**, 1149–1155.
- 106 DiscoverRx, <https://www.discoverx.com/arrestin>, 2016, 22 March.
- 107 Y. Goldshmit, R. Matteo, T. Sztal, F. Ellett, F. Frisca, K. Moreno, D. Crombie, G. J. Lieschke, P. D. Currie, R. a. Sabbadini and A. Pébay, *Am. J. Pathol.*, 2012, **181**, 978–992.
- 108 L. C. Young, *University of Strathclyde*, 2015.
- 109 M. A. Nouh, M. Abdel, X. X. Wu, H. Okazoe, H. Tsunemori, R. Haba, A. M. M. Abou-Zeid, M. D. Saleem, M. Inui, M. Sugimoto, J. Aoki and Y. Kakehi, *Cancer Sci.*, 2009, **100**, 1631–1638.
- 110 K. Valko, S. Nunhock, C. Bevan, M. Abraham and D. Reynolds, *J. Pharm. Sci.*, 2003, **92**, 2236–2248.
- 111 A. P. Hill and R. J. Young, *Drug Discov. Today*, 2010, **15**, 648–655.
- 112 J. S. Swaney, C. Chapman, L. D. Correa, K. J. Stebbins, R. Bunday, P. C. Prodanovich, P. Fagan, C. S. Baccei, M. Santini, J. H. Hutchinson, T. J. Seiders, T. Parr, P. Prasit, J. F. Evans and D. S. Lorrain, *Br. J. Pharmacol.*, 2010, **160**, 1699–1713.
- 113 B. Brad, N. John, E. Kumaraswamy and S. Scott, *Intermune*, W02313025733A1, 2013.
- 114 K. Eiji, K. Takatoshi, F. Yatu, K. Yatuaka, S. Ryushi, K. Kazuyuki, T. Kazuhiko

- and S. Kazuyuki, *Astellas Pharma*, W02011/037192, 2011.
- 115 R. Zhang and X. Xie, *Acta Pharmacol. Sin.*, 2012, **33**, 372–384.
- 116 R. J. Young, D. V. S. Green, C. N. Luscombe and A. P. Hill, *Drug Discov. Today*, 2011, **16**, 822–830.
- 117 P. D. St-Cœur, D. Ferguson, P. J. Morin and M. Touaibia, *Arch. Pharm. (Weinheim)*, 2013, **346**, 91–97.
- 118 A. C. Anderson, *Chem Biol*, 2003, **10**, 787–797.
- 119 F. Potjewyd, *Unpublished work*, *University of Strathclyde*, 2016.
- 120 Accelrys Software Inc, *Discov. Stud. Model. Environment*, 2007, Release 4.
- 121 *Mol. Oper. Environ. 2013.08*, *Chem. Comput. Gr. Inc*, *Sherbooke St. West, Suite #910*, 2016, Montreal, QC, Canada, H3A 2R7, 2016.
- 122 S. S. A. Shah, G. Rivera and M. Ashfaq, *Mini Rev. Med. Chem.*, 2013, **13**, 70–86.
- 123 G. Patani and E. J. LaVoie, *Chem. Rev.*, 1996, **96**, 3147–3176.
- 124 E. P. Gillis, K. J. Eastman, M. D. Hill, D. J. Donnelly and N. A. Meanwell, *J. Med. Chem.*, 2015, **58**, 8315–8359.
- 125 Alan Kennedy, *University of Strathclyde*, 2014.
- 126 A. El-Faham, R. S. Funosas, R. Prohens and F. Albericio, *Chem. - A Eur. J.*, 2009, **15**, 9404–9416.
- 127 K. Chen, L. Xu and O. Wiest, *J. Org. Chem.*, 2013, **78**, 5051–5055.
- 128 L. Carpino, *J. Am. Chem. Soc.*, 1993, **115**, 4397–4398.
- 129 J. Burkhard and E. M. Carreira, *Org. Lett.*, 2008, **10**, 3525–3526.
- 130 Y. Zheng, C. M. Tice and S. B. Singh, *Bioorg. Med. Chem. Lett.*, 2014, **24**, 3673–3682.
- 131 J. A. Burkhard, B. Wagner, H. Fischer, F. Schuler, K. Müller and E. M. Carreira, *Angew. Chem. Int. Ed.*, 2010, **49**, 3524–3527.

- 132 D. Lesieur, C. Lespagnol and J. Bonnet, *Adir Cie. US005132305A*, 1992.
- 133 G. McMahon, P. C. Tang and L. Sun, *Sugen Inc, US6486185B1*1998, 1998.
- 134 S. Wood, *M. Chem. Thesis, University of Strathclyde*, 2015.
- 135 C. Bissantz, B. Kuhn and M. Stahl, *J. Med. Chem.*, 2010, **53**, 5061–5084.
- 136 H. B. Borate, S. R. Maujan, S. P. Sawargave, M. A. Chandavarkar, S. R. Vaiude, V. A. Joshi, R. D. Wakharkar, R. Iyer, R. G. Kelkar, S. P. Chavan and S. S. Kunte, *Bioorganic Med. Chem. Lett.*, 2010, **20**, 722–725.
- 137 G. A. Jeffrey, *An Introduction to Hydrogen Bonding*, Oxford University Press, 1997.
- 138 J. Hausmann, *Nat. Struct. Mol. Biol.*, 2011, **18**, 198–204.
- 139 W. P. Walters, J. Green, J. R. Weiss and M. Murcko, *J. Med. Chem.*, 2011, **54**, 6405–6416.
- 140 M. Van Der Stelt, J. Cals, S. Broeders-Josten, J. Cottney, A. A. Van Der Doelen, M. Hermkens, V. De Kimpe, A. King, J. Klomp, J. Oosterom, I. Pols-De Rooij, J. De Roos, M. Van Tilborg, S. Boyce and J. Baker, *J. Med. Chem.*, 2011, **54**, 7350–7362.
- 141 M. van der Stelt and J. Cals, *Organon, US2010/0144723A1*, 2010.
- 142 G. S. Bisacchi, W. A. Slusarchyk, U. Treunwe, J. C. Sutton, R. Zahler, S. Seiler, D. R. Kronenthal, M. E. Randazzo, M. D. Schwinden, Z. Xu and Z. Shi, *Bristol-Myers Squibb, US6355324B1*, 20020.
- 143 J. Sutton, S. Bolton and K. Hartl, *Bioorg. Med. Chem. Lett.*, 2002, **12**, 3229–3233.
- 144 Y. Chen, A. Turlik and T. R. Newhouse, *J. Am. Chem. Soc.*, 2016, **138**, 1166–1169.
- 145 P. V Archaryulu, P. K. Dubey, P. Reddy and T. Suresh, *Indian J. Chem.*, 2010, **49**, 923–928.
- 146 J. J. Marugan, W. Zheng, O. Motabar, N. Southall, E. Goldin, W. Westbroek, B. K. Stubblefield, E. Sidransky, R. A. Aungst, W. A. Lea, A. Simeonov, L.

- William and C. P. Austin, *J. Med. Chem.*, 2011, **54**, 1033–1058.
- 147 B. E. Kornberg, R. A. Lewthwaite, D. D. Manning, S. S. Nikam and I. L. Scott, *Warn. Lambert Co. US2003/18021A1*, 2003.
- 148 M. A. Dombroski, M. A. Letavic, K. F. McClure, J. T. Barberia, T. J. Carty, S. R. Cortina, C. Csiki, A. J. Dipesa, N. C. Elliott, C. A. Gabel, C. K. Jordan, J. M. Labasi, W. H. Martin, K. M. Peese, I. A. Stock, L. Svensson, F. J. Sweeney and C. H. Yu, *Bioorg. Med. Chem. Lett.*, 2004, **14**, 919–923.
- 149 V. Gracias, Z. Ji, I. Akritopoulou-Zanze, C. Abad-Zapatero, J. R. Huth, D. Song, P. J. Hajduk, E. F. Johnson, K. B. Glaser, P. A. Marcotte, L. Pease, N. B. Soni, K. D. Stewart, S. K. Davidsen, M. R. Michaelides and S. W. Djuric, *Bioorg. Med. Chem. Lett.*, 2008, **18**, 2691–2695.
- 150 S. Konda, S. Raparathi, K. Bhaskar, R. K. Munaganti, V. Guguloth, L. Nagarapu and D. M. Akkewar, *Bioorg. Med. Chem. Lett.*, 2015, **25**, 1643–1646.
- 151 C. Steeneck, C. Gege, F. Richter, H. Kroth, M. Hochguertel, M. Essers, J. Van Veldhuizen, S. Note and T. Irving, *Atlantos Pharm. Inc US200702155738A1*, 2007.
- 152 J. C. Henise and J. Taunton, *J. Med. Chem.*, 2011, **54**, 4133–4146.
- 153 GSK, *In-house PhysChem Assay, Gunnels Wood Rd, Stevenage SG1 2NY*.
- 154 E. H. Demont, P. Bamborough, C. Chung, P. D. Craggs, D. Fallon, J. Laurie, P. Grandi, C. I. Hobbs, J. Hussain, E. J. Jones, A. Le Gall, D. J. Mitchell, R. K. Prinjha, A. D. Roberts, R. J. Sheppard and R. J. Watson, *ACS Med Chem Lett*, 2014, 1–29.
- 155 S. Anoopkumar-Dukie, J.B. Carey, T. Conere, E. O'Sullivan, F.N. Van Pelt, A. Allshire, *Brit. J. Radiol.*, 2005, **78** (934), 945-947.